Quantitative studies of collective cell migration using novel microstructured molds

Anna-Kristina Marel

München 2013

Quantitative studies of collective cell migration using novel microstructured molds

Anna-Kristina Marel

Dissertation
durchgeführt an der Fakultät für Physik
der Ludwig–Maximilians–Universität
München

vorgelegt von
Anna-Kristina Marel
aus Mainz

München, den 29.11.2013

Erstgutachter: Prof. Dr. Joachim Rädler
Zweitgutachter: Prof. Dr. Erwin Frey
Tag der mündlichen Prüfung: 12.02.2014

Contents

Abstract **ix**

Zusammenfassung **xi**

1 Introduction **1**

The cell is a highly dynamic, viscoelastic material 2
Cells respond sensitively to external forces 3
Mechanical properties of cells can be described by models 3
Collective cell migration is characterized by coordinated motion 4
Micropatterning and image analysis provide insights into migratory processes 5
The dynamics of tissues are sensitively balanced 6

2 Basic Concepts **9**

2.1 Basic Principles of Tissues 9
2.1.1 Epithelial cells line cavities and build specialized barriers 9
The ECM is composed of fibrous proteins and glycosaminoglycans . . . 10
Cell junctions form contacts between cells and from cells to the ECM . 10
2.1.2 Cell division and rearrangement maintain the function of the tissue . . . 11
2.2 Migratory behavior of cells 12
2.2.1 Single cells migrate in a persistent random walk 12
2.2.2 Collective cell migration shows correlated cell motion 13
2.3 Microfabrication techniques 13
2.3.1 Soft lithography to microstructure surfaces 14
Microcontact printing 15
Plasma-induced micropatterning 15
Micromolding in capillaries (MIMIC) 15

3 Microstructured Environments to Control Cellular Behavior **17**

Poly(ethylene glycol) exhibits protein and cell repellent properties . . . 18
PEG-DMA is cross-linked by radical polymerization 18

3.1 PEG-DMA Micromolding in Standard Culture Dishes 19
3.1.1 Three-dimensional microstructures are fabricated by MIMIC 20
3.1.2 Cells are confined by PEG-DMA microstructures 22

4 Expansion Dynamics of Circular Shaped Cell Microcolonies 37
Wound-healing assays are suitable to probe collective cell migration . . 38
4.1 Proliferation and Collective Migration of Small Cell Groups 38

5 Guided Collective Cell Migration in Channels 57
The MDCK cell line is a model system for collective cell migration . . . 59
Collective cell motion is assessed by particle image velocimetry (PIV) . 59
Fick's law describes mass transport along concentration gradients 60
Propagating cell fronts are described by traveling waves 61
Mean square displacement (MSD) of single cell migration 61
The orientation of cell division is determined by the mitotic spindle . . 62
Aspects of tissue behavior are modeled by a mesoscopic particle based approach 63
5.1 Flow and Diffusion in channel-guided cell migration [M1] 64
5.2 Alignment of cell division axes in directed epithelial cell migration [M2] 67

6 Investigation of Single Stem Cell Fate in Microstructured Environments 131
Hematopoietic stem cells differentiate into all types of blood cells 132
6.1 Marker Free Detection of Stem Cell Differentiation by Brownian Motion Analysis in μ-Wells [M3] 133

7 Conclusion and Outlook 151
Voronoi diagrams describe continuous cell layers 151
Functionalized microwells present specialized ligands to stem cells . . . 152
PEG-DMA membranes as templates for semiconductors 153

List of Figures

2.1 Polarization of epithelial cells 11
2.2 Leader cell and finger formation during collective cell migration 14
2.3 Schematic presentation of different micropatterning techniques 16

3.1 PEG-DMA is cross-linked by radical polymerization 19
3.2 Fabrication of PEG-DMA microstructures by MIMIC 20
3.3 SEM images of PEG-DMA structures 21
3.4 MDCK cells are confined in different geometries 22

4.1 Circular microcolonies are released by PEG-DMA lift-off 39
4.2 Viability of small cell groups released from PEG-DMA lift-off 40

5.1 The principles of PIV 60
5.2 The orientation of cell division is determined by the mitotic spindle 63
5.3 A mesoscopic particle model to describe tissue behavior 64
5.4 Invading cell sheets in microchannels 65
5.5 Random motion an diffusive behavior 66
5.6 Time course of a cell division event 67

6.1 Differentiation of hematopoietic stem cells 133

7.1 Cellular networks are described by Voronoi tessellation 152
7.2 Differentiation of stem cells is detected by specialized ligands 153
7.3 Thin PEG-DMA membranes act as templates for pentacene deposition 154

Abstract

Collective cell migration plays a fundamental role in processes such as wound healing, embryogenesis and cancer. Collective migration is defined as coordinated movement of tightly connected cell groups. Cells are linked together via cell junctions that act as interfaces for information transfer and are able to transmit forces across the sheet. This connective network exhibits viscoelastic properties as well as active cell migration and hence represents a from of 'active soft matter'. In order to study the dynamics of moving cell assemblies, cultured epithelial monolayers are frequently used as two-dimensional model systems.

This cumulative dissertation studied the collective migration of cellular systems of finite size which were spatially controlled and guided by microstructured surfaces. To this end, a multifunctional micromolding technique to produce three-dimensional and biocompatible microstructures was developed. The cell-repellent polymer poly(ethylene glycol)-dimethacrylate (PEG-DMA) was cross-linked, forming a free-standing network that predefined the areas of cell adhesion. A standard perti-dish served as substrate and enabled the residue-free removal of the PEG-DMA layer [69]. The foundation of the following projects is given by the introduced micropatterning technique.

In a first application, we investigated the expansion dynamics of small, disk-like cell patches in terms of cell proliferation and area relaxation. Cell groups, consisting of 5 to 23 cells, were released in a lift-off scenario and exponential cell growth was found by analysis of the cell number over time. An initial viscoelastic relaxation of the cell patch was verified by following the overall area over time and the resulting relaxation time was determined to be in the range of the cell doubling time [68].

Next, we analyzed the flow field of cell assemblies invading microchannels, restricting the direction of expansion to one dimension. On short time and length scales, we observed noisy behavior of the system and evaluated the fluctuations in the velocity field and vortex formation events. For longer time scales, however, the overall cell movement resembled a plug-flow with weak boundary conditions and collective diffusion behavior was described by a reaction-diffusion model. In a second manuscript, we investigated the influence of the emerging flow field in the cell layer on the orientation of cell division and showed a clear alignment between the velocity gradient tensor and the cell division axis. These experimental findings were modeled by a mesoscopic particle based approach within the framework of a cooperation.

In a final project, we used microwell arrays to confine stem cells at the single cell level, in order to unravel the heterogeneity of cell decision making during differentiation. The transition of non-adherent granulocyte-macrophage progenitors to adherent macrophages was determined by following the Brownian motion of the trapped cells. This technique enables the label-free detection of individual stem cell fate in more detail without being reliant on fluorescence microscopy.

Zusammenfassung

Kollektive Zellmigration spielt bei Prozessen wie Wundheilung, Embryogenese oder auch Krebs eine wichtige Rolle. Dabei bewegen sich Zellgruppen aus untereinander vernetzten Zellen auf koordinierte Art und Weise fort. Der Kontakt zwischen den Zellen wird durch adhäsive Zellverbindungen aufrechterhalten, die zum einem der Informationsübermittelung und zum anderen der Kraftübertragung dienen. Dieses Netzwerk aus Zellen kann als viskoelastisches Material mit aktiven Elementen betrachtet werden, das in seinen Eigenschaften denen von weicher Materie ähnelt. Die physikalische Beschaffenheit von Zellen und Geweben kann an einem einfachen, zweidimensionalen Modelsystem aus kultivierten Epithelzellen studiert werden. Epithelien zeichnen sich durch eine meist einlagige und polarisierte, zusammenhängende Zellschicht aus.

Diese kumulative Dissertation beschäftigt sich mit dem kollektiven Migrationsverhalten von kleinen Zellsystemen die mit Hilfe von mikrostrukturierter Oberflächen räumlich kontrolliert und geleited werden. Dafür wurde zunächst eine geeignete Methode zur Mikrostrukturierung entwickelt, die durch freistehende, dreidimensionale Polymernetzwerke aus zellabweisendem Material die Zelladhäsion auf dem unbedeckten Untergrund vorherbestimmt. Das Besondere an der vorgestellten Technik ist die Verwendung von handelsüblichen Petrischalen als Substrat und die damit verbundene Möglichkeit des mechanischen und rückstandslosen Entfernens der Polymerschicht zu einem gewünschten Zeitpunkt. Diese vielseitig einsetzbare Methode bildet die strukturelle Basis der folgenden Projekte.

In einer ersten Anwendung wurde die Ausbreitungsdynamik von kleinen, runden Zellverbänden von 5 bis 23 Zellen untersucht, die zunächst in Mikrostrukturen der entsprechenden Geometrie kultiviert und durch anschließendes Abziehen der Begrenzung zur Migration und Proliferation angeregt wurden. Durch Analyse der Flächenausbreitung konnte eine anfängliche viskoelastische Relaxation des Zellhaufens nachgewiesen werden, die durch den komprimierte Zustand der Zellen durch die Strukturierung hervorgerufen und im weiteren Verlauf von Zellproliferation und -migration überlagert wurde. Die resultierende Relaxationszeit lag im Bereich der Verdopplungszeit der verwendeten Zelllinie.

Als nächstes wurden expandierende Zellfronten in Kanälen begrenzt und das Flussverhalten der Zellverbände analysiert. Dabei fiel auf kurzen Zeitskalen das Auftreten von spontaner und ungerichteter Bewegung auf, das durch die Untersuchung des Geschwindigkeits-

feldes und das Vorkommen von Wirbeln nachgewiesen wurde. Auf längeren Zeitskalen konnte ein kolbenströmungsähnliches Verhalten des Zellverbundes gezeigt und das kollektive Diffusionsverhalten mit einem Reaktions-Diffusionsmodell beschrieben werden. Desweitern wurde die Auswirkung des entstehenden Flusses auf die Ausrichtung der Zellteilungsachse untersucht und ein deutlicher Zusammenhang zwischen Orientierung der Achse und des Gradienten des Geschwindigkeitstensors belegt. Die experimentellen Ergebnisse wurden in einer Kooperation mit einer mesoskopischen Simulationsmethode modelliert.
In dem letzten Projekt dieser Arbeit wurde mit Hilfe der entwickelten Mikrostrukturierung eine Plattform zur Einzelzellanalyse etabliert, die insbesondere für seltene und schwer kultivierbare Zellen, wie beispielsweise Stammzellen, interessant ist. Durch Analyse der Brownschen Bewegung von separierten Zellen in Vertiefungen von wenigen Mikrometern Durchmesser konnte der Zeitpunkt der Differenzierung von nicht-adhärenten Vorläuferzellen in adhärente Makrophagen ohne zusätzliche Fluoreszenzmarkierung detektiert werden.

1 Introduction

In their review "Soft Active Matter", Marchetti *et al.* give an overview over the recent experimental and theoretical findings of the young field of active matter [67]. In one sentence, they summarize the main properties of these fascinating materials: "Living systems [...] provide the preeminent example of active matter, exhibiting extraordinary properties such as reproduction, adaptation, spontaneous motion, and dynamical organization including the ability to generate and to respond in a calibrated manner to forces."
What this concerns, among other things, is a physical viewpoint of the properties of the fundamental unit of life, the cell. At first sight, the investigation of cellular processes is subject of biological research. Molecular and cellular biology technologies are able to identify spatiotemporal dynamics inside cells at subcellular or even molecular level, making great progress in particular in the field of genetics dealing with proteins and their interactions. The legitimate question arises: "Does cell biology need physicists?" as picked out as central theme in the paper of Charles Wolgemuth two and a half year ago [141]. Molecular and cellular biology can resolve and quantify chemical pathways, however, even for a single and isolated cellular function such as for instance, cell migration, the complex molecular machinery that drives this particular process, appears incomprehensible. Additionally, genetics disregards the fact that a cell is not a isolated shell filled with proteins; cells interact with their environment producing forces in order to grow or migrate. Physicists may now be able to examine cellular processes at a more functional level and provide the basis for cell modeling [141]. One example of successful physical biology is the analysis of cell motility. By considering actin polymerization that produces the force that pushes the cell front forward as Brownian ratchet mechanism and adhesive forces not as rigid attachment but as viscous drag forces, whole cell simulations were developed to test the mechanism of cell motion theoretically [141].
With this work, we tie in with the topic of cell migration, investigating collective behavior in finite sized, connected epithelial cell assemblies as a link between single cell migration and collective movement of large cell sheets. In order to achieve spatial and temporal control over cell adhesion and motion, a micropatterning method is introduced that is effortless in fabricating microstructured surfaces and includes multifunctional applications. Expanding cell microcultures are investigated from defined geometries as a lift-off scenario and invasion experiments into channels. The focus of this work is determining the growth and migration

behavior and fluid-like properties of small cell assemblies.

The cell is a highly dynamic, viscoelastic material

From a physical point of view, cells have been considered as active biological materials with unusual mechanical properties [29, 55]. Cells are highly dynamic; they crawl, divide and change their shape by stretching and contracting. The basis for cell motility, differentiation and development consists of the ability to continuously remodel the internal cellular structure and thus change the mechanical properties of the cell. Since cells are the building blocks of tissues, the evaluation of the physical characteristics of cell assemblies has attracted attention in recent years. Since 1982, it has been know that certain tissues exhibit viscoelastic properties [117]. The response of cell aggregates to external compression has been measured quantitatively by means of the parallel plate compression apparatus [31]. By alternating compression and relaxation states, Forgacs *et al.* demonstrated that tissues relax as elastic material on short time scales and resemble a viscous fluid on long times scales. This finding was confirmed by the group of Brochard-Wyart who observed a fast elastic deformation of cellular aggregates followed by a viscous flow by aspirating the cells with a micropipette [39]. The described observations happen on time scales of a few seconds. Angelini *et al.* studied a confluent cell monolayer over several hours and found a glass-like behavior of the cell layer for high cell densities [5]. Their two main observations of decreasing cell motility with increasing cell density and the accompanied dynamic heterogeneity are hallmarks for glass transition [34]. The associated relaxation times in the glass-like regime were observed to be in the range of cell division times, exceeding days.

Usually, single cell mechanics are determined by measuring the deformation in response to a force. These measurements can be achieved by a set of various techniques such as atomic force microscopy, traction force microscopy or magnetic bead cytometry [55, 57]. Cells also exhibit nonlinear, viscoelastic properties that depend sensitively on the applied stress. Under mechanical load, the stress relaxation behavior follows a power-law response, hence, for large deformations, the cellular response is in the nonlinear regime and stress-stiffening is observed [55, 57]. All eukaryotic cells are mechanically stabilized by the cytoskeleton that forms the most complex active material that exists in nature. The cytoskeleton network is composed of three main biopolymers - the actin-myosin network, intermediate filaments and microtubules - and diverse collaborating binding proteins and molecular motors that form a dynamic, heterogeneous structure able to deform, contract and remodel. Trepat *et al.* established four universal rules to describe the properties of the cytoskeleton. They prove that cell rheology is scale-free, cells are prestressed, the intracellular diffusion is anomalous and stiffness and dissipation are altered by stretch [128]. The prestress in the cytoskeleton determines the elastic properties of the cell and has an impact on cell adhesion and stress propagation within the cell [55]. Due to their mechanical properties, cells are able to sense external forces, transmit them inside or between cells and to transduce the mechanical response into chemical signaling.

Cells respond sensitively to external forces

Within a cell sheet, individual cells are coupled to adjacent cells and the underlying extracellular matrix by cell junctions [134]. These junctions provide mechanical stability and constitute a platform for information exchange being involved in generating biological signals in response to external stimuli. Generated forces are directly transmitted inside the cell through adherens junctions and focal adhesions to the actin cytoskeleton and stretch, changes in hydrostatic pressure, shear stresses or osmotic forces can be sensed [107]. Due to the processing of external environmental variations in terms of mechanotransduction, cells are able to adapt dynamically, maintaining tensional homeostasis inside the tissue [84]. The emergent spatial pattern of tension fluctuations within the cell sheet, however, determines regions of concentrated cell growth and division [79]. Additionally, cell behavior is affected by the texture of the underlying substrate or rather the extracellular matrix. Cells exert traction forces to the substrate to probe the elastic properties, for instance [35]. Regulation of stem cell fate is one example of mechanical force driven decisions that are influenced by factors such as intracellular tension or elastic properties of the substrate [107].

Mechanical properties of cells can be described by models

The phenomenological rheology of cells including the viscoelastic properties, power-law relaxation and prestress is able to describe the mechanical behavior of cells, however, a mechanistic understanding is not provided. A number of models have been introduced to explain and predict certain aspects of cell mechanics such as the sol-gel hypothesis, the tensegrity model or the soft glassy rheology model [46, 57]. These models concentrate on a specific aspect of cell mechanics while the development of a global, physical model that captures the full phenomenology of cell behavior is still challenging. Sandersius *et al.* modeled active cell dynamics at cell- and tissue-scale, respectively, using an extended subcellular element model. They studied the cellular response to an external mechanical force and local cell movement within an epithelial-like cell sheet and were able to reproduce recent experimental findings [102]. A more conceptional approach for tissue modeling considers individual cells as particles and neglects subcellular mechanisms [8, 25]. Basan *et al.* propose a particle based model that is able to construe mechanical aspects of a spreading epithelial sheet such as the long-range coordination of cell motility, the buildup of tensile stress within the tissue and density-dependent formation and size of swirls [8]. Two dimensional cell sheets can also be described by a vertex model taking cell elasticity, cortical tension and the associated junctional forces as well as cell adhesion into account [27, 59]. The emergent forces are expressed by an energy function and aspired force balance corresponds to local minima.

Collective cell migration is characterized by coordinated motion

One fundamental concept of active matter is the emergence of spontaneous motion [67]. Eukaryotic cells migrate due to crawling or blebbing, exerting forces on the substrate and neighboring cells. Cell migration is a cyclic process of polarization, formation of protrusions and traction sites, contraction and retraction of the rear [98]. During several physiological processes such as vascularization, wound healing or morphogenesis, cells migrate collectively. Collective cell migration is characterized by three hallmarks: firstly, during movement, cells are physically and functionally connected, maintaining the integrity of cell-cell junctions. Second, polarization and organization of the actin cytoskeleton over multiple cell diameters generates traction and protrusion forces that drive cell migration. Lastly, the tissue is structurally modified by migrating cell groups in terms of surface alteration by depositing a basement membrane [33]. Investigating migrating cells in their natural environment is still challenging in terms of imaging and specific manipulation, however, in the case of sheet migration, two dimensional cell cultures of epithelial cells provide a powerful model system to study collective cell migration [100].
Cells within a connected cell sheet exhibit streaming behavior in terms of collectively migration cell groups [41, 122]. Puliafito *et al.* studied single cell and collective behavior in expanding Madin Darby canine kidney (MDCK) cell sheet and demonstrated a density-dependent motion behavior. With increasing cell density, cells became less motile and spontaneously arising large-scaled swirls disappear. The correlation lengths of moving cells decreases up to single cell size and cell motion is reduced to small scale fluctuations [92]. By embedding beads in a polyacrylamid gel that serves as substrate for cell migration, Angelini *et al.* were able to follow substrate deformations due to force transmission across the cell layer. Mechanical coupling of cells is mediated by the substrate deformation patterns over long-distances that also guide collective cell migration. The formation of swirls was also observed, however, swirl size was determined to be essentially dependent on the stiffness of the substrate [4].
Besides studying collective cell migration within continuous cell layers, a prevalent scenario is to introduce a model wound to the sheet in order to trigger spontaneous cell migration. The gap is closed by sheet expansion due to cell migration and proliferation, however, it has been shown that cell proliferation is not necessarily required [89, 100, 133]. By combining the two factors of random motility and proliferation, the moving cell front can be described by a reaction-diffusion equation (Fisher-Kolmogorov). The solutions of the equation imply constant shape traveling wave solutions moving at constant speed. The front speed can be easily determined experimentally and inferences about diffusive behavior and proliferation rate are possible on the basis of this model [103, 109, 113].
Focused observations on the migrating border of expanding cell sheets after wounding reveal a highly nonuniform invasion with considerable roughening of the border [89]. The formation of finger-like columns of motile cells has been described in several works [37, 85, 89, 95].

The cells at the tips of the emerged fingers were named 'leader cells' and feature distinct characteristics of highly motile cells such as a polarized morphology and a higher migration velocities. Leader cells move normal to the free boundary at constant speed exerting forces to several cell rows behind leading to correlated motion with correlation lengths up to 200 µm[85]. A cell density gradient is established within the finger and cell morphology is changed over increasing distances with increasing finger length suggesting mechanical tension along the protrusion. Reffay *et al.* performed photoablation experiments finding a retraction of the newly generated borders. Further evidences for the development of a complex stress field are orientated cell division axis and polarity within the finger [95]. In general, each individual cell tends to align with the direction of the maximal local stress, this phenomenon of guided motion has been introduced as plithotaxis [123]. Since plithotaxis necessitates mechanical force transmission from cell-to-cell across several cell diameters, it emerges as intrinsic property of a cell assembly [38, 127]. The arising question concerning the driving forces for cell sheet expansion includes on one hand the hypothesis of the buildup of an internal pressure by cell proliferation that pushes cells outwards and the pulling forces of leader cells dragging following cell rows on the other hand. Trepat *et al.* addressed this question by measuring the traction forces of a growing epithelial cell sheet. They suggest a global tug-of-war mechanism that integrates a global contractile tension in the tissue. The state of tensile stress is balanced by traction forces exerted by each cell on the substrate via cell adhesion junctions [38, 129]. Basan *et al.* were able to quantitatively reproduce these findings using a particle based model and showed that the tensile stress is caused by long-range alignment of motility forces [8].
The described observations give clear evidence of the significance of the transmission of physical forces within cell sheet. Directionality and effectiveness of migratory behavior are controlled by emerging mechanical stresses, however, the propagation of slow mechanical waves are qualified to trigger mechanotransduction and thereby serves as connection between physical forces and intracellular signaling [111].

Micropatterning and image analysis provide insights into migratory processes

Cell migration is a complex mechanism and studying special aspects of this dynamic process requires the ability to exert control over certain parameters. By varying surface properties such as stiffness or presented proteins for instance, cellular responses can be analyzed in term of adhesion strength or motility. Micropatterning methods, in general, are specialized tools providing spatial and temporal control over cell adhesion by presenting defined adhesion sites surrounded by cell-repellent materials. Cellular microarrays enable high throughput experiments under the same conditions and usually with small volumes [18, 145]. For cell migration experiments in two dimensions, micropatterning techniques have shown steady progress in terms of controlling size, geometry and invasiveness. By means of barrier assays and lift-off scenarios, a model wound can be generated without injuring cells at the border and creating spatial gradients in the composition of the extracellular matrix which both has an impact on

the migratory behavior [80, 97, 127].
Moving cell fronts can be followed by time-lapse microscopy, however, subsequent image analysis is necessary to gain deeper insights into the underlying processes. Cell displacement can be measured by tracking single cells or performing particle image velocimetry (PIV) analysis [89, 131, 133] and correlated motion can be examined by automated algorithms [115]. Fluorescence microscopy enables following detailed cellular processes by labeling specific organelles with fluorescent dyes. A further powerful approach is the combination of surface modification and fluorescence microscopy as demonstrated by Trepat *et al.* who used fluorescent beads embedded in a polyacrylamide gel to monitor cell traction forces that correspond to the displacement of the beads [129].

The dynamics of tissues are sensitively balanced

In migrating cell sheets, during wound healing cells proliferate and the growing cell mass contributes to close the gap. In a healthy tissue, however, cell proliferation and apoptosis is sensitively balanced, maintaining a state of homeostasis. Stem cells serve as a cell pool supplying the tissue with specialized cells of different functions. Puliafito *et al.* investigated the transition from the low cell density regime of freely proliferating cells to a dense and fully differentiated epithelial monolayer by following MDCK populations over up to three weeks [92]. They observed an inhibition of cell division, reduction in cell motility and cell areas over time, leading to mitotic arrest for cell areas below a certain threshold. Nowadays, this complex process of growth regulation is termed "contact inhibition", which is misleading to some extent, because the original meaning of contact inhibition as introduced by Abercrombie and Heaysman in 1954 refers to the arrest of locomotion of animal cells which are in contact with one another [1, 118]. Recently, Jacques Prost coined the concept of homeostatic pressure which arises as mechanical stress that cells experience by expanding against the surrounding tissue and reaches homeostasis when cell division and apoptosis are balanced [9, 71]. In the work of Basan *et al.*, homeostatic pressure is suggested as an experimentally accessible variable that allows the determination of the metastatic potential of early tumor growth [9] which has been discussed controversially by experts [71]. Brú *et al.* investigated the tumor contours of growing brain tumors and found evidence of a relation of super-rough profiles and malignity [15, 119]. Tumor modeling based on mechanical assumptions has attracted wide interest and given insights into the expansion kinetics of tumor growth [12, 17].

The scope of this work was to investigate the migratory behavior of cell assemblies of finite size in defined spatial pattern. In order to achieve spatial and temporal control over cell groups, we developed a micropatterning method based on micromolding in capillaries (MIMIC). The cell-repellent polymer poly(ethylene glycol)-dimethacrylate (PEG-DMA) was shaped by a polydimethylsiloxane (PDMS) mold forming three dimensional microstructures after cross-linking. The usage of standard petri-dishes as substrate enabled the residue-free removal of the

PEG-DMA layer in a lift-off scenario. The detailed preparation of PEG-DMA microstructures and the manifold application options were published in publication P1 [69] and summarized in chapter 3.
In chapter 4, we explored the expansion dynamics of small, disk-like cell groups which were able to migrate uniformly in all directions. Cells patches were arranged in a spatial pattern of widely separated microwells and grown to confluence. The mechanical release of the cell patches initiated a expansion of the colony that initially was dominated by an elastic relaxation of the cells. The typical relaxation time was determined to be in the range of the cell division rate. Further expansion was driven by proliferation and formation of leader cells that occurred on several sides of the patch, inducing a tug-of-war between leaders existing in parallel. The findings were published in publication 2 [68].
In this first project, we were able to characterize the extensive behavior of area relaxation and cell growth. The underlying mechanism of directed motility, however, were still less understood. Thus, in the next step, we focused on the flow field of migrating cell sheets investigating the flow characteristics of cell assemblies. We restricted the direction of growth to one dimension using the developed microfabrication technique. The growing cells were guided by three dimensional PEG-DMA channels, creating migrating cell sheets of three to twenty cell widths. A density gradient from the invading cell front towards the bulk developed and directed flow of the cell layer was monitored. We found a homogenous flow, however, an increase in velocity towards the front as well as weak slip boundaries were observed. On short time scales, the system exhibited noisy behavior as revealed by analysis of the velocity field and vorticity formation. We showed that on longer time scales, the expansion of the cell front was described by a reaction-diffusion model as previously discussed in literature. The flow behavior of confined cell sheets in channels is presented in manuscript 1. In a second manuscript, we investigated the influence of the emerging flow field on cell division events. In a isotropic environment, cells divide in any direction, however, the occurrence of flow leads to symmetry breaking in the system. We found a clear alignment of the orientation of the division axis with the velocity gradient tensor. The scenario of flowing cells sheets were compared with confined confluent monolayers in order to distinguish the impacts of flow and interface behavior due to the PEG-DMA walls. In cooperation with a theoretical soft matter group, we were able to model our experimental findings with a mesoscopic particle based approach. The results of both, experimental observations and theoretical modeling of invading cell sheets in channels are collected in manuscript 2. Chapter 5 summarizes the outcome of the two questions concerning flow behavior on short and long time scales and impact of emerging forces on the orientation of cell division axis, respectively.
The last chapter of this work presents a further application of the developed micopatterning method. PEG-DMA microwells were used to trap individual stem cells in order to study the heterogeneity of stem cell fate on the single cell level. A label-free method was introduced that determines the transition of non-adherent granulocyte-macrophage progenitors to adherent

macrophages by following the Brownian motion of cells inside the wells. The preliminary results are described in manuscript 3.
Finally, three ongoing projects are shortly introduced in the outlook section of this work.

2 Basic Concepts

In order to study and understand fundamental biological processes, model systems that provide low complexity are used. Cell migration, for instance, is involved in many crucial phenomena such as embryogenesis, wound healing or vascularization. The investigation of individual aspects of this highly regulated process is facilitated by separating cells from the living organism. In the case of cell migration, especially collective cell migration, epithelial tissues are an excellent system to study physical properties of moving cell assemblies. Epithelial cells are tightly connected by cell-junctions and rest on a thin layer of extracellular matrix. Furthermore, most epithelial cell lines grow in monolayers and thus provide a perfect two dimensional model of a cell sheet. In general, cells respond sensitive to their environments. By modifying the properties of the underlying substrate, cell adhesion behavior can be influenced. Hence, microstructured surfaces are used to guide and control cell growth as well as cell migration.

2.1 Basic Principles of Tissues

Tissues are organisations of cells into cooperative assemblies in multicellular organisms [3]. The tissue of vertebrates can be grouped in four different types: nervous, muscle, epithelial and connective tissue. In general, a tissue is composed of cells and the extracellular matrix (ECM). Cells adhere to the ECM via focal adhesions, which thereby provides structural support for the tissue. The cells themselves are linked together by means of cell junctions that can transmit forces between cells or cells and the ECM.

2.1.1 Epithelial cells line cavities and build specialized barriers

Epithelial tissues line all internal cavities and cover the external surfaces of the body. The principle functions of epithelial tissue is to protect the interior of the organism from external impacts, to regulate the exchange of molecules between cavity and tissue, as well as the secretion of hormones and the provision of sensation. By closely linking cells together, a strong barrier separating compartments is achieved. Thereby, cells carry the mechanical load themselves, transmitting forces through strong intracellular protein filaments that are attached to the neighboring cell via specialized junctions in the plasma membrane. The epithelial sheet rests on the basal lamina, which is part of the ECM. Nutrients must be

provided via diffusion from the underlying tissue or the cavity due to absent vascularization. Epithelial cells are polarized in terms of morphology and orientation. The apical surface is free and exposed to the lumen while the basal membrane is connected to the basal lamina. The lateral domains are in close contact with adjacent cells and contain several types of cell-cell junctions.

The ECM is composed of fibrous proteins and glycosaminoglycans

The extracellular matrix is a complex meshwork of macromolecules. Fibrous proteins like fibronectin, laminin or collagen as well as glycosaminoglycans are components of the ECM. The ingredients are produced inside the cells and secreted locally by exocytosis. In the case of epithelial tissues, the underlying ECM is a thin layer called basal lamina. The basal lamina is mainly composed of collagen and proteoglycans containing specialized proteins like laminin that provides adhesion sites for integrins and therefore links the ECM to the cell membrane. It also acts as selective barrier preventing contact the epithelial sheet and migrating fibroblast from the underlying connective tissue while macrophages or lymphocytes are allowed to pass. Furthermore, the basal lamina supplies a scaffold for tissue regeneration after injury by guiding cell migration.

Cell junctions form contacts between cells and from cells to the ECM

Epithelial cell layers serve as interfacial tissues controlling the exchange of metabolites, proteins and cells from one compartment to the other. The cells are tightly connected by cell junctions to ensure the barrier function of the tissue. In general, three categories for cell junctions can be distinguished: occluding junctions that form a selective permeability barrier between cells, anchoring junctions that connect adjacent cells or components from the ECM to actin or intermediate filaments and communication junctions that allow small molecules to pass directly from cell to cell [134]. An overview of cell junctions in epithelial cells is given in Figure 2.1.

The apilcal and basolateral domain is separated by tight junctions that are localized close to the entrance of the intercellular cleft. Tight junctions form a diffusion barrier for lipids and proteins within the plasma membrane and hence maintain a polar distribution of proteins between the domains. Furthermore, the exchange of metabolites and chemical cues is restricted so that chemical gradients can be established.

To provide mechanical stiffness, cells are connected by anchoring junctions that form strong structures linking the tension-bearing filaments of the cytoskeleton with the ECM or the neighboring cell. Adherens junctions connect bundles of actin filaments from cell to cell, forming a continuous adhesion belt right underneath the tight junctions. Desmosomes on the other hand link intermediate filaments together. In both cases, transmembrane proteins (cadherins) from each cell membrane stick to their corresponding extracellular domain. The

intracellular parts are joined with the cytoskeleton via adapter proteins. Through this, local mechanical stress can be distributed into the whole cell layer in order to reduce the impact on a single cell. Another type of anchoring junctions are focal adhesions and hemidesmosomes. They are responsible for the binding to the ECM via integrin mediated contacts. Here, the adhesion sites are connected to the filaments of the cytoskeleton via adapter proteins as well. Gap junctions serve as a direct communication link between adjacent cells. Transmembrane proteins form channels from one cell to the other allowing small molecules to pass directly from cytoplasm to cytoplasm. Therefore, cells are coupled both metabolically and electrically.

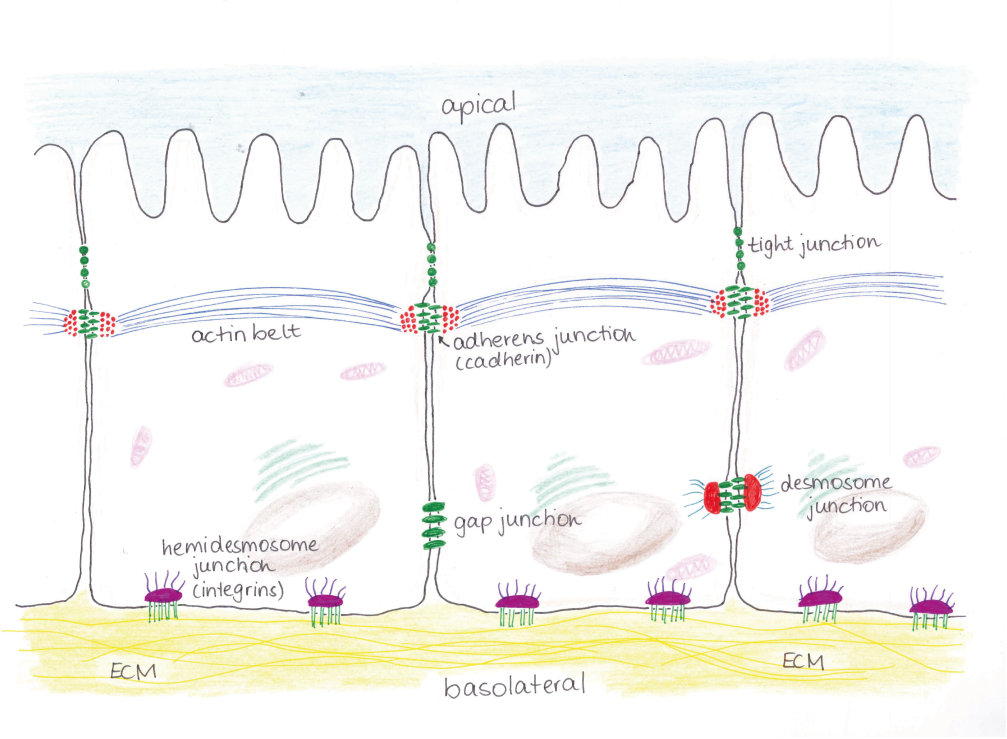

Figure 2.1: Cell junctions and actin belts in epithelial cell sheets. *Cells are connected to adjacent cells by tight junctions, adherens junctions, desmosomes and gap junctions. Each type of junction performs a special task like building a selective barrier, transmitting forces by linking filaments of the cytoskeleton together or providing of communication pathways. The adhesion to the underlying basal lamina is performed by hemidesmosomes and focal adhesions that connect the ECM to actin and intermediate filaments respectively, by integrin binding.*

2.1.2 Cell division and rearrangement maintain the function of the tissue

Although epithelia are robust tissues that perform important functions such as selective barriers, secretion and sensation, they are highly dynamic structures. Cells are stitched together by characteristic cell junctions. The junctions can be remodeled or deformed under the control of the local balance of force transmission and adhesion. A short-term external stress leads to elastic deformation of the tissue, preserving the integrity of the epithelium. When the cell

layer is stressed for longer time scales such as hours, the tissue show a fluid-like behavior. Cells rearrange cell-cell contacts and move in a diffusive manner. Therefore, the plasticity and fluid behavior of epithelial tissue is enabled by active remodeling of cell junctions [40]. The integrity of a tissue is assured by continual cell replacement, cell division events and programmed cell death called apoptosis. Nonetheless, the organization and function of the tissue must be preserved during renewal. The orientation of the cell division is biased by the topology of the cell and its neighbors. Cell adhesion points, as well as the apico-basal polarity, are maintained during division. The formation of new cellular junctions and the control of their length is an active process that involves many cells of the tissue. Due to increasing tissue pressure by cell movements, external compression or increasing cell density, live cell extrusion takes place to keep the steady state called homeostasis. In the process, cell junctions are partly removed followed by the formation of a supracellular actomyosin ring between the cells remaining within the tissue. By contraction of the ring, the loosened cell is excluded. Hence, the removal of junctions is an active and collective process to maintain the homeostatic state of the tissue [40].

2.2 Migratory behavior of cells

Cell migration plays an important role in plenty of biological phenomena and is a highly regulated process. Cells migrate during embryogenesis, in wound healing and as part of the immune response. Tissues are shaped, vascularized and maintained by migrating cells. Unfortunantely, this process is also involved in pathological processes like metastasis, as well as chronic inflammatory and vascular diseases. Cell migration can occur at single cell level but in many cases collective cell migration in which cells migrate in tightly or loosely associated groups is observed [100].

2.2.1 Single cells migrate in a persistent random walk

The movement of cells over surfaces, meaning the extracellular matrix or the surface of other cells under physiological conditions and artificial substrates in cell culture respectively, is a repetitive process of extension, adhesion, contraction and detachment. Crawling cells are polarized, developing a cell front and a rear. First, a protrusion is formed in direction of the movement and binds to the surface via adhesion sites . These protrusions can be lamellipodia, filopodia or pseudopodia, depending on the cell type. The cell body contracts towards the new adhesion sites while the rear retracts and detaches from the surface. On the level of molecular biology, this process involves many connected biochemical pathways and protein players like integrins, actin and myosin filaments. From the physical point of view, the cell must exert significant forces to overcome the viscous resistance emerging when a body is moving close to a solid surface. Furthermore, traction forces enable the cell to pull the cell body.

Examples of single cells migrating in animals are immune cells or germ cells. In culture, fibroblast are a commonly used model system. This cell type develops lamellipodia and reaches speeds around 40 µm/h by crawling [14]. The cells follow a sinuous track over the surface, describing a random walk. The motion is normally biased, however, either by chemical attractants or even substrate topology. This guided movement involves correlations between successive step orientations and is named a persistent random walk [19]. Cell migration can also be directed intrinsically. To characterize both, intrinsic and external directed cell migration, velocity and directional persistence is needed [86].

2.2.2 Collective cell migration shows correlated cell motion

During many processes such as vascularization, morphogenesis and wound closure cells move together. The term of collective cell migration refers to loosely or closely associated migrating cell groups. Epithelial cell lines are good model systems to study sheet migration under 2D tissue culture conditions. These cells maintain strong cell-cell adhesion and migrate in a coordinated manner in direction of the sheet front. Wound healing assays are an easily accessible platform to study cellular behavior at the migrating cell front as well as emerging traction or pulling forces within the cell layer. In these, an unperturbed, confluent monolayer is wounded by scratching or removal of a physical barrier. The newly available surface is sufficient to trigger the migration of adjacent cell rows. The cells at the front are automatically polarized and become actively motile. A few specialized cells called 'leader cells' are formed and start to migrate at constant velocity perpendicular to the border (Fig. 2.2 a) These cells show noticeable morphological transformation: leader cells are larger and spread out showing an active ruffling lamellipodium [89]. Due to the directed and active motion, cells are influenced and pulled by the leader cells even across several rows. Through this, so-called fingers are developed migrating at higher velocity than the average velocity within the monolayer as shown in Figure 2.2 b. The cells migrate in a highly coordinated manner showing correlation lengths up to 200 µm for MDCK II cells [85]. Another aspect in cell sheet expansion is proliferation that leads to an increase of the internal pressure within the tissue pushing the cells outwards by creation of new mass. Recent studies have shown, however, that cell proliferation is not coercively necessary for gap closure [100].

2.3 Microfabrication techniques

The recent ability to easily produce microstructured surfaces accounts for increasing interest of the field of quantitative biology to use such devices for biological questions. Individual cells can be manipulated by selective surface modifications at nano- and micron level and the extracellular environment becomes shapeable. The basis for cellular-patterning in general, is the creation of alternating surfaces of non-fouling parts that prevent cell or protein adsorption and adhesive islands where cells like to attach. The development of simple and low

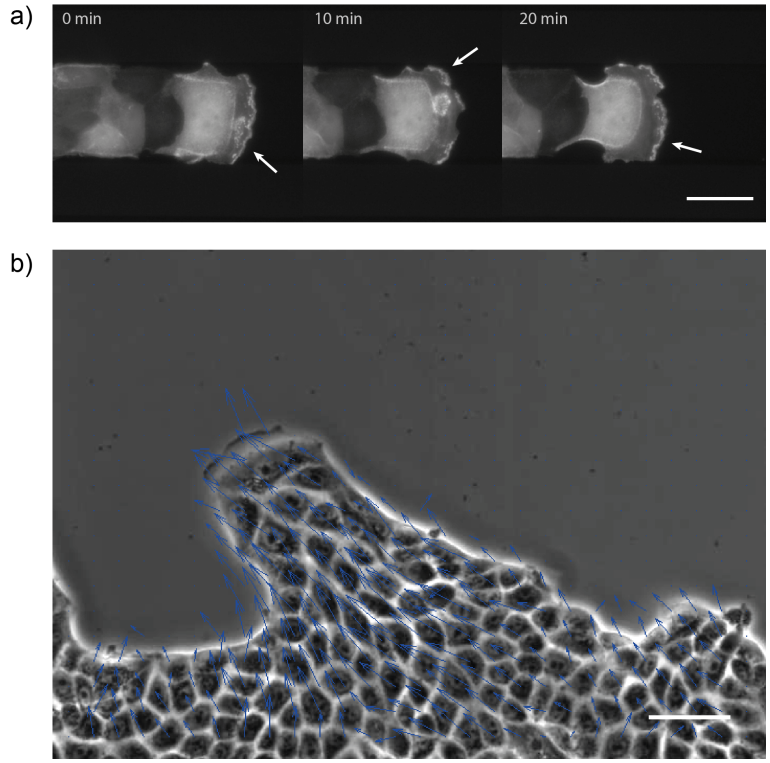

Figure 2.2: Leader cell occurrence and finger formation during collective cell migration. *(a) A fully developed leader cell show active ruffling lamellipodia visualized by labeled actin fibers (see arrows). (b) An expanding MDCK II cell sheet forms finger-like structures guided by a leader cell. The following cells migrate in highly directed manner as demonstrated by the flow field (blue arorws). Both scale bars corresponds to 50 µm.*

cost microfabrication techniques make the tools accessible for biological studies in terms of biochemical assays, cell-based microarrays and high-throughput screening [18, 48, 139, 145].

2.3.1 Soft lithography to microstructure surfaces

The term 'soft lithography' was coined by George Whitesides in 1997 [146] who wanted to develop alternative microfabrication methods that are independent from photolithographic processes that exhibit appreciable disadvantages like limited feature size or the requirement of sophisticated facilities. Soft lithography includes several techniques that all, at one fabrication stage, use an elastomeric ("soft") material to produce micropatterend surfaces. In most cases, the elastomer used is polydimethylsiloxane (PDMS) that is cast against a master to create a perfect replica. In general, the master is still fabricated by conventional photolithography. Thereto, a silicon substrate covered with a thin layer of a photoresist is partially illuminated by UV light through a chrome mask or a patterned transparent polymeric sheet. After developing, the structured silicon wafers are usually silanized to ensure proper detachment of the PDMS. After this treatment, the master can be used many times. The elastomeric molds

are prepared by mixing the PDMS with the curing agent, degassing the mixture and pouring it on the surface of the master. After thermal curing, the PDMS is removed and can be applied to several micropatterning techniques such as replica molding, microcontact printing, micromolding in capillaries, stencil-assisted patterning or plasma-induced micropatterning. A short overview for selected techniques is given is Fig. 2.3.

Microcontact printing

The technique of microcontact printing (μCP) was adapted to biological applications in 1994 by Singhvi et al. [114]. The principle is similar to the potato printing technique well known by all children. Instead of shaping a potato and printing colors to a piece of paper, μCP uses a PDMS mold to transfer various kinds of inks to the substrate. For this, the topographically shaped PDMS stamp is incubated with a solution of the chosen ink, such as proteins, small biomolecules, cells or even alkanthiols that produce self-assembled monolayers (SAMs) on metal surfaces. The attached ink is transferred from the raised structures of the stamp to the substrate by conformal contact. Due to the elastic properties of the PDMS, the contact is facilitated and the pattering of non-planar surfaces renders possible. In order to fabricate cellular arrays, proteins like fibronectin or collagen are used as ink and printed on glass or polystyrene surfaces. Cell adhesion in between the patterns can be avoid by backfilling procedures with passivation agents such as polyethylene glycol (PEG) derivatives or bovine serum albumin (BSA).

Plasma-induced micropatterning

Surfaces can also be pattered by selective plasma treatment. This method called plasma-induced or plasma-initiated micropatterning was introduced by Langowski in 2005 [60]. Here, a PDMS stamp or membrane is used to protect parts of initially hydrophobic surfaces like polystryene or PDMS. The sample is exposed to oxygen plasma and uncovered regions become hydrophilic while protected areas remain hydrophobic. Cells prefer to adhere to hydrophilic surfacs and can be confined by the differences in hydrophobicity alone. The patterned surface can be further functionalized with proteins or other inks that absorb either to hydrophilic or hydrophobic areas depending on their characteristics.

Micromolding in capillaries (MIMIC)

The micromolding in capillaries method in combination with PDMS stamps as master was established in the group of George Whitesides [91]. Here, a PDMS stamp with a relief structure building an open network is placed in conformal contact with the surface. A droplet of a low-viscosity prepolymer is spotted in front of the open end of the PDMS mold so that the liquid is drawn spontaneously into the channels by capillary action. After curing the prepolymer into a solid, the mold is removed leaving free standing microstructures behind.

The PDMS network can be filled with various materials like curable polymers (by UV light or thermally), biological macromolecules or liposome suspensions [52, 144]. With this method, three-dimensional microstructures with variable heights depending on the given features of the PDMS mold can be produced. Cells can be separated both by the physical barrier and the chemical properties of the utilized material. There are functionalized PEG derivatives, for instance, that can be crosslinked under UV illumiantion and exhibit the cell repelling properties of PEG.

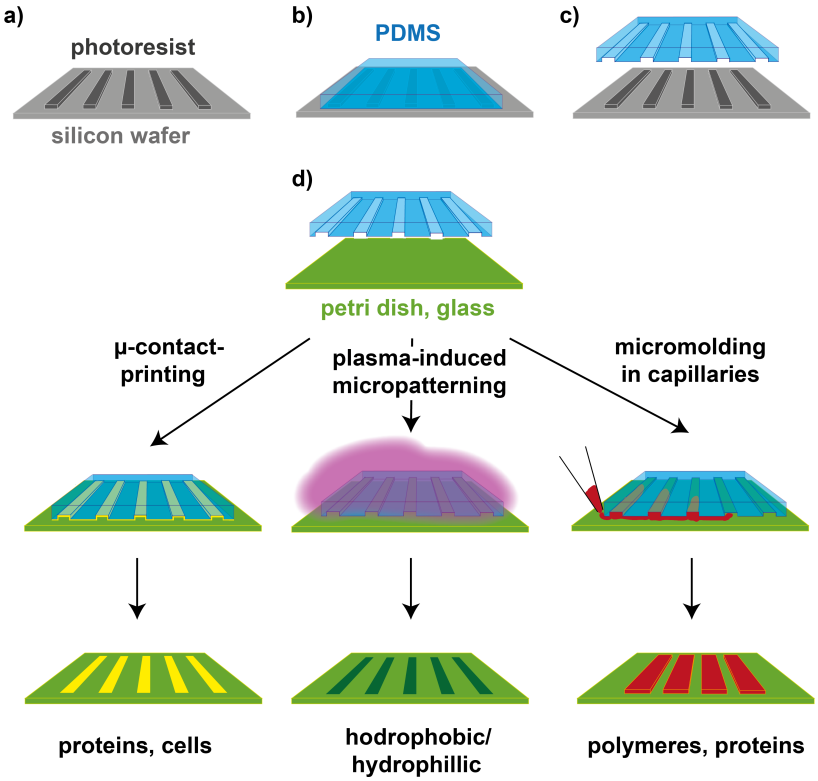

Figure 2.3: Soft lithography to form micropatterned surfaces. *(a) A silicon wafer is covered by a photoresist layer that is partially developed. (b) The microstructures are molded by the elastomer PDMS. (c) The PDMS replica can be easily peeled off the master and acts as template for different micropatterning methods to structure surfaces such as petri dishes or glass (d). The PDMS mold can transfer attached inks like proteins or cells to the substrate creating spatially separated patterns. The surface can be hydrophilized by plasma activation, while the areas protected by the PDMS stamp remain in their original state. Furthermore, the PDMS mold can act as template to deposit polymers, lipids or proteins which where placed by capillary forced induced flow.*

3 Microstructured Environments to Control Cellular Behavior

Cells are the building blocks of life and although they are the smallest unit classified as a living thing, they exhibit remarkable complexity. To unravel the molecular interplay of biochemical pathways, the interaction between cells themselves or the mechanisms of cell responses to environmental stimuli, living-cell assays have been developed. Three prerequisites have to be fulfilled for performing cell based studies: the cells have to survive outside the organism, the external delivery of stimuli is supposed to be controllable and the ability to measure the resulting cellular response has to be given [145]. For quantitative cell studies, the possibility of high-throughput screening is of great interest. In particular, the application of small volumes to reduce the consumption of reagents and the feasible usage of small cell numbers in cases of limited availability like primary patient samples for instance, are conditions worth pursuing. Microscaled systems provide these capacities and are highly recommended for living-cell based assays.

In the field of microtechnology, new ways of producing microstructured surfaces have been developed [136]. The different techniques of soft lithography for instance, offer a simple route for sample production without specialized facilities [144]. Microcontact printing is a well-know method to transfer proteins or cells from a 'soft' PDMS stencil to a chosen substrate [53]. The interspaces between the pattern are usually backfilled with PEG or PEG derivatives to avoid protein or cell adhesion [26]. A further technique is micromolding in capillaries (MIMIC) or capillary force lithography (CFL) [120, 144]. Here, a PDMS mold features the negative structures of the desired pattern. It is brought in close contact to the surface and filled with a liquid polymer. The filling process is driven by capillary action due to the pressure difference between the hydraulically connected regions. The prepolymer is cured either thermally or via UV light and the PDMS mold is removed. The resulting structures are free-standing and the bottom equals that of the original substrate. The generally used substrates for MIMIC are functionalized glass surfaces [54, 56, 75]. For cell culture, however, biologist have relied heavily on lab ware made of polystyrene over the past fifty years [11]. Hence, the standard cell behavior observations are from platforms such as petri dishes or cell culture flasks. From this perspective, microstructured devices on standard cell culture dishes become more attractive for biologists in order to support direct comparability.

In any case, the basic structure of a surface that is able to separate cells spatially is the alternating provision of adhesion sites and cell-repellent areas. To promote cell adhesion, proteins or components of the ECM are used to mimic natural cell environments. To prevent unspecific binding of proteins or other biomolecules, the highly biocompatible polymer poly(ethylene glycol) or poloxamers, also known as Pluronics®, are the most widely accepted systems.

Poly(ethylene glycol) exhibits protein and cell repellent properties

Poly(ethylene glycol) (PEG) is the most widely used polymer for biotechnical and biomedical applications. Due to its good biocompatibility, PEG is used in drug delivery, to cover surfaces in order to achieve protein and cell resistance or as immunosensor [42]. PEG is a linear, neutral polyether with the structure H-(O-CH_2-CH_2)$_n$-OH. The polymer is available in a wide range of molecular weights: from a few hundred up to approximately 20,000 g/mol. For molecular weights under 1000 g/mol, PEG is a viscous colorless liquid that turns to waxy white solids for higher weights. It is soluble in water and most organic solvents and hence described as amphiphilic. Poly(ethylene glycol) is considered a non-toxic agent, although it has been reported that small PEG's with molecular weights under 400 g/mol may exhibit slight toxicity [16]. For the main part, the non-fouling properties of PEG is a result of its highly mobile chains more than its hydrophilicity. The polymer chains possesses a high conformational flexibility and perform rapid motions. Thereby, PEG molecules show a large exclusion volume in water and are heavily hydrated. As a result, other macromolecules are rejected due to the 'exclusion effect' or 'steric stabilization effect'. Additionally, the conformational degrees of freedom for the polymer chains are drastically reduced by approaching particles and causes an entropically driven repulsion. This is true for both PEG in its free form or grafted onto a flat surface [43]. The immobilization of PEG-layers on surfaces can be achieved by covalent binding. Usually, the polymer is modified at the terminal hydroxy group and bound to functionalized surfaces. The derivatization reactions are manifold and includes methods to prepare PEG derivatives with bromide, amine, sulfonate or aldehyde. Further PEG derivatives such as poly(ethylene glycol)-dimethacrylate (PEG-DMA), poly(ethylene glycol)-diacrylate (PEG-DA) or star-PEG are functionalized at both ends of the polymer. They can be cross-linked among themselves forming three-dimensional networks.

PEG-DMA is cross-linked by radical polymerization

Poly(ethylene glycol)-dimethacrylate (PEG-DMA) is a PEG derivative that is functionalized with a methacrylate group at both ends (see Fig. 3.1). For our microstructure fabrication, we use short PEG chains so that the molecule has an overall molecular weight of 550 g/mol. The methacrylate groups can be cross-linked by photopolymerization. The reaction is started by a light sensitive compound called photoinitiator, in our case 2-hydroxy-2-methylpropiophenone.

The initiator responds sensitive to a specific wavelength and undergoes photocleavage forming highly reactive radicals. These radicals starts the polymerization reaction by attacking a monomer and forming of a new radical. The polymer chain propagates until termination or depletion of monomer supply. Termination occurs by combination of radicals either of two growing chains or a polymer chain with an initiator radical. The process is illustrated in Figure 3.1.

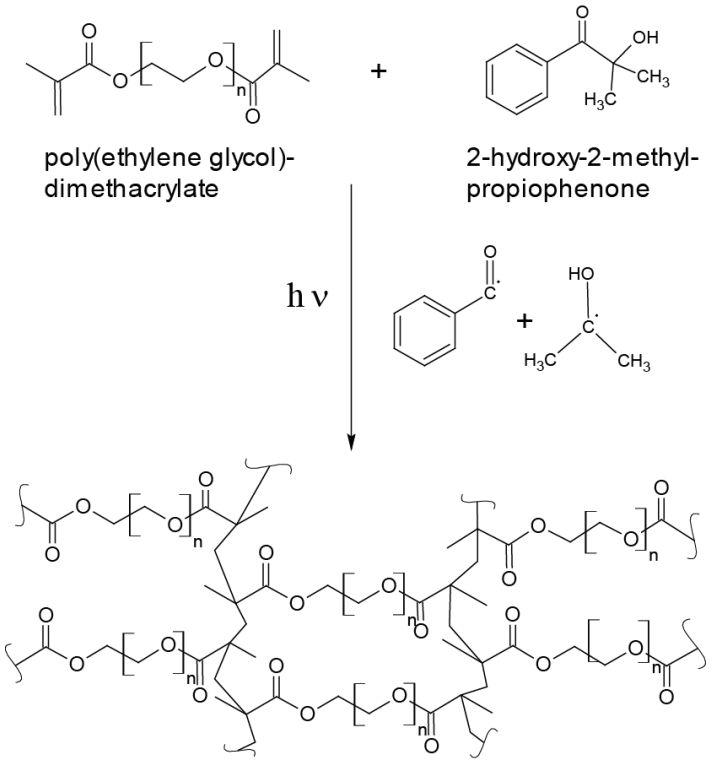

Figure 3.1: Poly(ethylene glycol)-dimethacrylate (PEG-DMA) is cross-linked by radical polymerization forming three-dimensional networks. *A mixture of PEG-DMA and the photoinitiator 2-hydroxy-2-methylpropiophenone is exposed to UV light. By breaking the photoinitiator into radicals, the polymerization reaction is started. The functional groups of the PEG-DMA are cross-linked forming a three-dimensional network.*

3.1 Arraying Cell Cultures Using PEG-DMA Micromolding in Standard Culture Dishes [P 1]

In order to execute spatial control over cell adhesion, a robust micropatterning process was developed. Using the photopolymerizable PEG derivative PEG-DMA in combination with the micromolding in capillaries method, three-dimensional microstructures were prepared. Beside the straightforwardness, the major advantage of the fabrication process is the direct patterning of the plastic surface without prior modification. The size and geometry of the microstructures are arbitrary within the limits of master fabrication, however, widely spaced

microwells were achieved by inserting pillars around the wells to prevent sagging of the PDMS mold. Cells were confined to small cell groups or even the single cell level. In addition, this technique allowed further applications, such as templates for plasma-induced micropatterning or removable layers for lift-off scenarios. The different applications are described in detail in publication 1 [P 1].

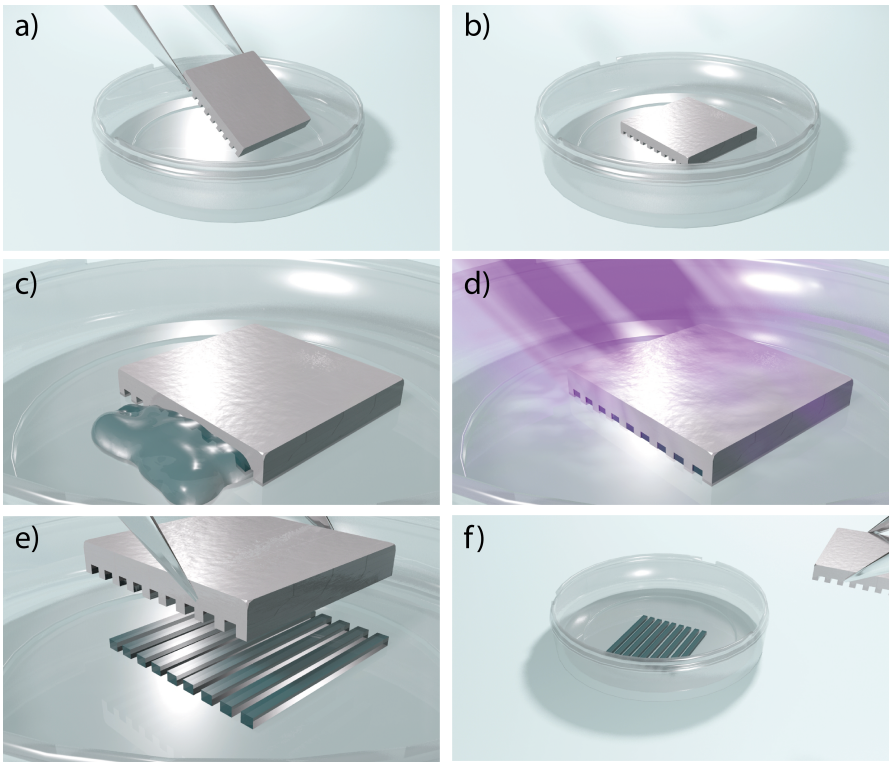

Figure 3.2: Fabrication of PEG-DMA microstructures on ibidi μ-dishes by the MIMIC method. *(a,b) A PDMS mold is placed in closed contact with the substrate by tweezers and filled by capillary force induced flow with the polymer solution (c). (d) The PEG-DMA is cross-linked by UV radiation. (e, f) The PDMS mold is removed and the PEG-DMA microstructures are ready for use in cell experiments. [The images are part of a movie describing the whole preparation process. The movie was generated by Christoph Hohmann and all images are copyrighted by Nanosystems Initiative Munich (NIM).]*

3.1.1 Three-dimensional microstructures are fabricated by MIMIC

The fabrication steps of three-dimensional microstructures by means of the MIMIC method are illustrated in Figure 3.2.

A PDMS mold was cut with sharp razor blades in a way that an open network is formed. The PDMS was activated by argon plasma to enhance its hydrophilicity. As previously described [112], the hydrophilic surface treatment facilitated the proper filling of the mold wiht the slightly hydrophilic PEG-DMA. Immediately after plasma treatment, the PDMS mold was carefully brought into conformal contact with the substrate (Fig. 3.2 a). As substrates,

several plastics were tested: cell culture labware from Greiner (Greiner, Frickenhausen, Germany), Nunc (Nunc, Roskilde, Denmark) and ibidi µ-dishes (ibidi, Martinsried, Germany). The PEG-DMA layer stably attached to all dishes, however, ibidi µ-dishes were used for cell experiments. The preparation of microstructures on glass slides was also possible but showed no permanence under liquids at all, with the PEG-DMA layer detaching quickly from the substrate. This effect was utilized for fabricating thin PEG-DMA membranes as templates for plasma-induced micropatterning as described in publication 1. After checking the proper attachment of the PDMS mold to the substrate (Fig. 3.2 b), a droplet of freshly prepared PEG-DMA prepolymersolution containing 2 % v/v of the photoinitiator 2-hydroxy-2-methylpropiophenone was deposited in front of the open network of the PDMS stencil. Several concentrations of the photoinitiator were added, however, lower concentrations resulted in incomplete polymerization of the PEG-DMA. The mixture of polymer and initiator was spontaneously pulled into the PDMS network by force induced flow (Fig. 3.2 c). For proper microstructure preparation, it was advisable to use as little prepolymer solution as possible to prevent overfilling and formation of brinks around the mold. The photopolymerization reaction was initiated by UV illumination with a wavelength from 185-546 nm (Fig. 3.2 d). After 10 min of UV-ozone treatment, the PDMS mold was removed (Fig. 3.2 e, f) and the sample was stored at 50 °C over night.

For better illustration of the obtained structures, images from scanning electron microscopy were taken. As demonstrated in Figure 3.3, the PEG-DMA microstructures exhibited clear edges and geometries. The bottom of the channels and the microwells respectively, were pure petri -dishes and PEG-DMA free. Hence, it was assured that cells will adhere on the unaffected plastic surface.

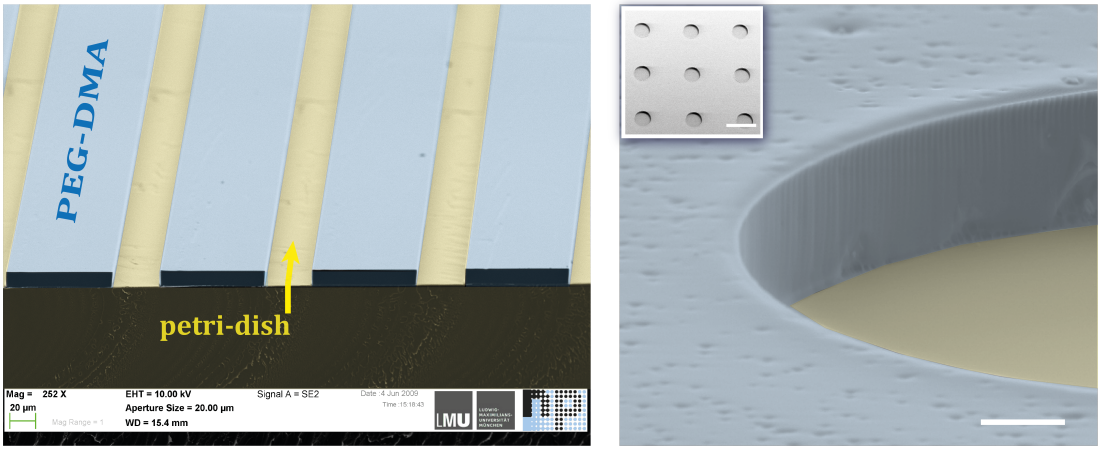

Figure 3.3: SEM images of different PEG-DMA microstructures. *The PEG-DMA layer (indicated by slightly blue inking) attaches to the surface (yellow inking). The SEM images clearly show that the bottom of the microstructures is free of PEG-DMA and cells therefore adhere directly to the petri-dish. Scale bars correspond to 20 µm (right image) and 500 µm (insert), respectively.*

3.1.2 Cells are confined by PEG-DMA microstructures

The PEG-DMA microstructures were sterilized with 80 % ethanol and washed with phosphate buffered saline (PBS) before cell seeding. In general, the cell suspension was seeded over the whole petri-dish. Cells settled down on the structures and adhere to the PEG-DMA free areas. Remaining cells on top of the PEG-DMA layer did not attach to the non-fouling surface and stayed in a rounded up state. By thermal fluctuations and diffusion, some cells were flushed into the cavities of the structures and remained at the perti-dish bottom. The rest of the non-sticking cells underwent apoptosis since adhesion to a scaffold is crucial for epithelial cell survival. Redundant cell were eliminated by gently washing with cell culture medium.
As shown in Figure 3.4, MDCK cells were spatially controlled by any geometry of the PEG-DMA pattern. Cells were cultured over several days within the microstructures and grown to confluence. In order to assure cell viability, cells were grown in PEG-DMA mircowells and treated with the LIVE/DEAD cell Viability Assay Kit (Invitrogen, Carlsbad, CA, USA). For this, C_{12}-resazurin is reduced by metabolically active cells to red-fluorescent C_{12}-resorufin. The second, green-fluorescent dye SYTOX Green is cell-impermeant and exclusively stains cells with compromised plasma membranes. Hence, metabolic active cells can easily be distinguished from apoptotic or necrotic cells due to the emitted fluorescence. An example of experimental results is given in Publication 1. Several cell lines like fibroblasts (3T3), human hepatocarcinoma cell line (Huh 7) or nonadherent murine erythroleukemia (MEL) cells were grown in PEG-DMA microstructures and all showed strong confinement by the PEG-DMA (data not shown).

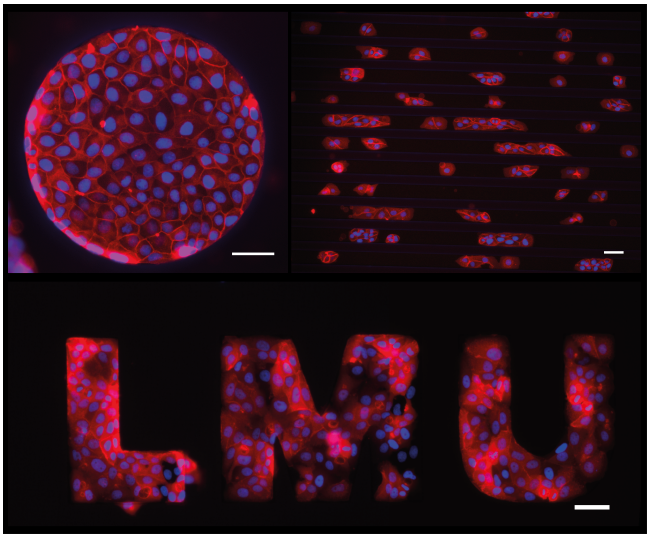

Figure 3.4: Epithelial cells are confined by PEG-DMA microstructures. *MDCK cells grow within PEG-DMA microstructures of various geometries. The cell line stably expresses eGFP-labeled lifeact that binds to the actin cytoskeleton. The nuclei are stained after fixation with 4,6-Diamidin-2-phenylindol (DAPI). All scale bars correspond to 50 µm.*

Publication 1 [P1]

Arraying Cell Cultures Using PEG-DMA Micromolding in Standard Culture Dishes

Anna-Kristina Marel[1], Susanne Rappl[1],Alicia Piera Alberola[1] and Joachim Oskar Rädler[1]

[1]Fakultät für Physik, Ludwig-Maximilians-Universität, Geschwister-Scholl-Platz 1, 80539 München, Germany

published in:

Macromolecular Bioscience, Vol. 13, Issue 5, 2013, 595-602.
DOI: 10.1002/mabi.201200400

Volume 13 • Number 5 • May 2013 www.mbs-journal.de

Macromolecular Bioscience

Impact Factor: 3.9

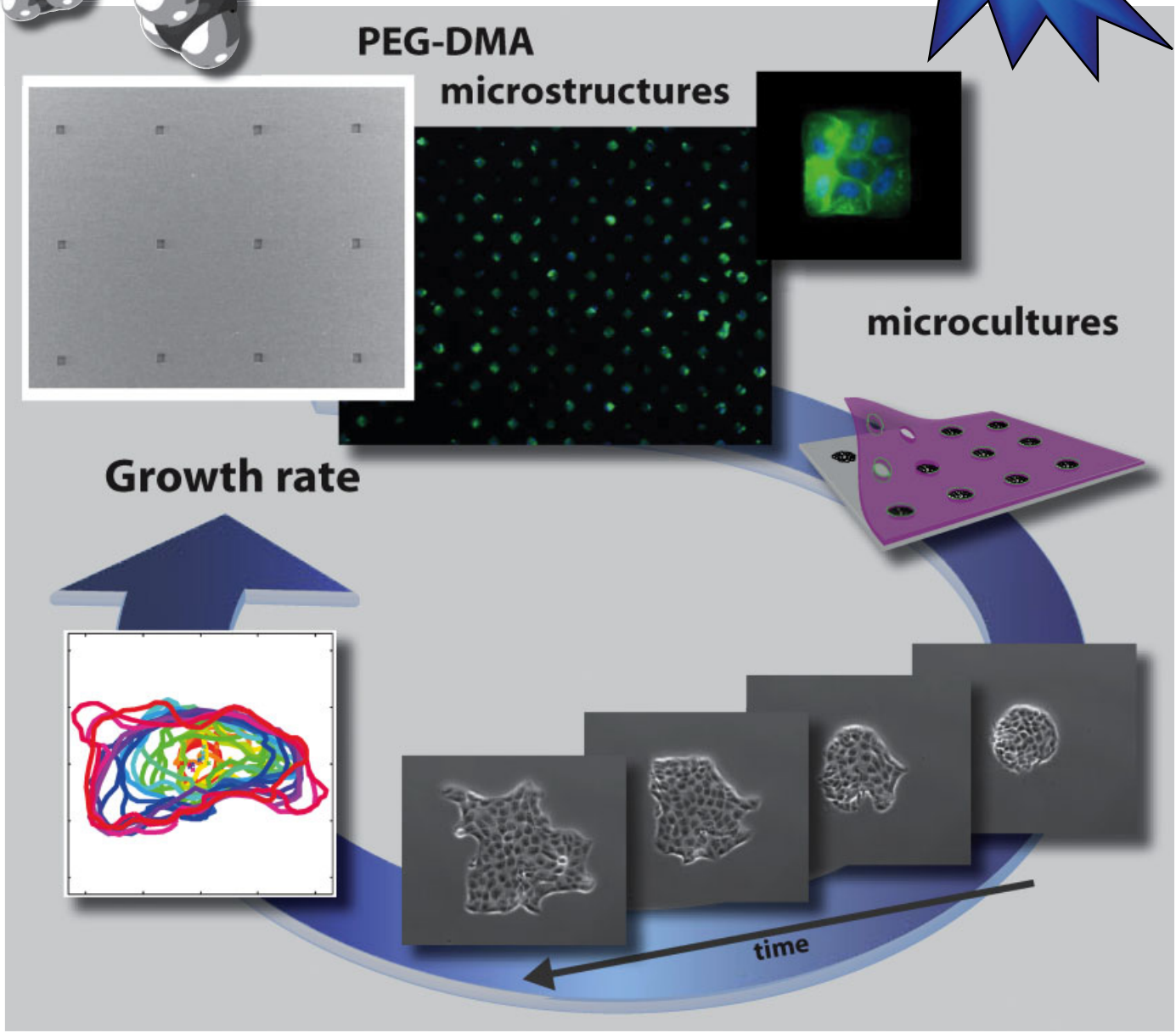

5/2013

WILEY-VCH

Arraying Cell Cultures Using PEG-DMA Micromolding in Standard Culture Dishes[a]

Anna-Kristina Marel, Susanne Rappl, Alicia Piera Alberola, Joachim Oskar Rädler*

A robust and effortless procedure is presented, which allows for the microstructuring of standard cell culture dishes. Cell adhesion and proliferation are controlled by three-dimensional poly(ethylene glycol)-dimethacrylate (PEG-DMA) microstructures. The spacing between microwells can be extended to millimeter size in order to enable the combination with robotic workstations. Cell arrays of microcolonies can be studied under boundary-free growth conditions by lift-off of the PEG-DMA layer in which the growth rate is accessible via the evolution of patch areas. Alternatively, PEG-DMA stencils can be used as templates for plasma-induced patterning.

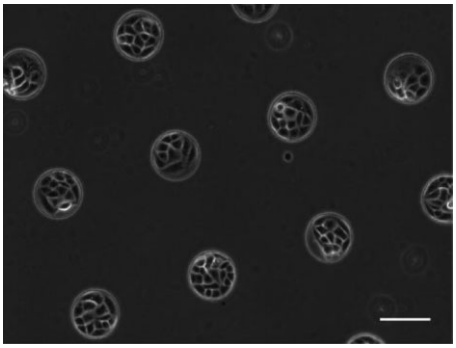

1. Introduction

Microstructures have become increasingly interesting for applications in the field of quantitative biology.[1,2] The development and improvement of specialized methods that yield highly reproducible construction of precise and functional structures at the micro- and nanoscale has seen a steady progression during the last years. The ability to control the behavior of cells both spatially and temporally opens up the possibility for parallel studies of single cells in artificial arrays,[3] while cell-arrays allow the collection of broad statistics on the fate of identically prepared cells under the same conditions.[4] In particular the dynamics of single cells can be assessed using time-lapse microscopy. A number of versatile techniques to produce micropattern arrays, such as soft lithography, photochemistry, inkjet printing, or dip-pen nanolithography have been investigated.[5–10] Cell microarrays are for instance used for high-throughput screening of chemical and genomic libraries or studies of cell-surface interactions.[4,11–13] Arrays of single cells have been created by microcontact printing and internal cellular organization such as polarization, cell division axis, or minimal needed adhesive area for cell survival has been investigated.[14–16] Microstructured hydrogels mimic artificial stem cell niches and enable long-term observation and high throughput screening.[17,18] Furthermore, microstructured surfaces enable the measurement of mechanical forces exerted by cells.[19,20] Cells can also be dynamically confined and released by thin elastomeric membranes[21] and this lift-off technique is used to perform co-culture experiments[22] or even create model wounds in order to analyze collective cell migration.[23–25] Plasma-induced micropatterning is an alternative method to confine cells by chemical surface modification.[26,27] In addition to single cell analysis having been performed, migratory behavior has been investigated on such surfaces.[28,29] However, despite numerous reported applications, microengineered systems are still not yet extensively accepted or widely adopted for cellular studies. Reasons for the limited usage of such devices are that they are mostly complicated and incompatible with existing laboratory techniques or instrumentation.[2,30]

To control cell adhesion in order to separate cells, a structured surface with non-fouling areas and adhesive

A.-K. Marel, S. Rappl, Dr. A. Piera Alberola, Prof. J. O. Rädler
Fakultät für Physik, Ludwig-Maximilians-Universität,
Geschwister-Scholl-Platz 1, 80539 München, Germany
E-mail: joachim.raedler@physik.lmu.de

[a] **Supporting Information** is available from the Wiley Online Library or from the author.

DOI: 10.1002/mabi.201200400

islands is needed. Polyethylene glycol (PEG) and derivates like PEG-dimethacrylate (DMA), PEG-DA, or Star PEG are suitable polymers for passivating surfaces in micropatterning techniques.[31,32] PEG-DMA can be cross-linked by radical polymerization forming a three-dimensional network. Due to the hydrophilic nature of the PEG chains, the polymer resists the adsorption of proteins and builds a barrier against cell adhesion. By curing PEG-DMA against a polydimethylsiloxane (PDMS) mold, microwells for stem cell culture[33,34] or even structures on the nanolevel can be produced.[35] Bottom-free microstructures are achieved by applying the MIMIC (micromolding in capillaries) method.[36–38] However, since PEG-DMA layers do not stably attach to the commonly used glass surfaces, a preceding functionalization such as silanization is necessary. This technique produces a substrate with entirely new characteristics concerning cellular behavior. The major problem of these modifications and substrates itself is the need of extensive tests concerning biocompatibility, cytotoxicity, or cell viability. A direct solution is to prepare microstructures on top of established materials that are used in cell culture, such as the thermoplastic polystyrene.[2]

Here, we present a robust protocol to prepare PEG-DMA microstructures directly on top of standard cell culture petri dishes. We show that PEG-DMA structures can be used as a microwell to control the size, shape, and separation distance of adhesion sites. In particular, single cells but also groups of cells can be arrayed. The concept of microcultures enables mimicking connective tissue with countable cell numbers. Studying microcultures is a new and interesting approach to gain profound insights into proliferation, migration, and toxicity processes in more detail. The control over spatial alignment enables the combination of automated read-out and image analysis of highly parallelized experiments. To study arrayed microcultures that can freely migrate and proliferate, a removable confinement like in standard lift-off scenarios is required. The presented protocol of preparing microstructures allows a mechanical detachment of the PEG-DMA layer. For long-term experiments, an adequate distance between the growing microcultures is needed in order to ensure unhindered patch expansion. We demonstrate an experimental approach to enlarge the well spacing to arbitrary size. Furthermore, PEG-DMA structures can act as templates for plasma-induced micropatterning allowing the formation of cellular micropatterns by chemical surface modification. With the described method, we present a straight forward protocol to produce microstructured surfaces on standard cell culture petri dishes. The preparation does not require complicated chemistry or specialized lab equipment. Consequently, the combination of the highly compatible surface, effortless preparation, and manifoldness makes the presented technique widely accessible for biological research.

2. Experimental Section

2.1. Master Fabrication by Soft Lithography

The photoresist template for PDMS molding was fabricated by conventional photolithography under clean room conditions. The process is described in detail in Supporting Information section.

In case a clean room is not accessible, a master can be purchased from associated institutes.[39,40]

2.2. PEG-DMA Micromolding on Plastic Dishes

Polydimethylsiloxane (PDMS) prepolymer solution (Sylgard 184, Dow Corning, USA) is carefully mixed with the curing agent in a 10:1 ratio w/w and degassed under vacuum conditions for 15 min. The mixture is deposited on top of the master and again degassed for 15 min to avoid the formation of bubbles. After degassing, the polymer is cured at 70 °C for 4 h. The molded stamp is then peeled off and cut in a way so that the structures form a network with open ends. The PDMS is activated by argon plasma (Diener Electronic, Nagold, Germany) for 30 s with the structures facing upwards. Immediately after the treatment, the stamp is placed upside down in close contact with a cell culture dish. A solution of PEG-DMA ($\overline{M}_n = 550$) containing 2% v/v of the photoinitiator 2-hydroxy-2-methylpropiophenone (both purchased from Sigma–Aldrich, Germany) is freshly prepared. Detailed information about the molecular weight of PEG-DMA is given in Supporting Information section. A drop is deposited in front of the open ends of the trimmed micromold so that the structures are filled spontaneously by capillary force induced flow. To assure a homogeneous filling of the PDMS mold it is important to deposit the PEG-DMA prepolymer solution immediately after hydrophilic treatment. An additional effect of careful plasma treatment is the stable attachment of the stamp to the surface which prevents slipping of the PDMS. Only minimal amounts of PEG-DMA should be used: from experience, 1 μl are enough to fill 0.5 cm × 0.5 cm of microstructures. The polymerization of PEG-DMA is initiated by the use of an UV-ozone cleaning system (UVOH 150 LAB, FHR, Ottendorf, Germany) with a wavelength ranging from 185–546 nm and a power of $>50\ mW \cdot cm^{-2}$ for 10 min. Finally, the PDMS stamp is peeled off and the resulting structures of cross-linked PEG-DMA are placed in a drying oven (Binder GmbH, Tuttlingen, Germany) overnight at 50 °C. Samples were sterilized with 80% ethanol for 5 min, washed three times with PBS and used immediately for cell experiments. The single steps of preparation are illustrated in Figure 1A.

2.3. Plasma-Induced Micropattering

PEG-DMA membranes were fabricated following the protocol for preparing PEG-DMA microstructures with the only difference being that the substrate was replaced with a glass slide. After curing the structures overnight, a droplet of water was placed at the rim of the PEG-DMA. The spreading droplet detached the layer from the glass surface so that the membrane can be easily isolated. The dried stencil was then brought into contact with an untreated hydrophobic ibidi μ-dish (ibidi, Martinsried, Germany), where it attached spontaneously. The sample was exposed to low-pressure oxygen plasma for 2 min (40 W, $5\ cm^3 \cdot min^{-1}$ at 25 °C and 2 bar, Femto, Diener). After plasma activation, the petri dish was immediately placed under the clean bench and the stencil was removed manually.

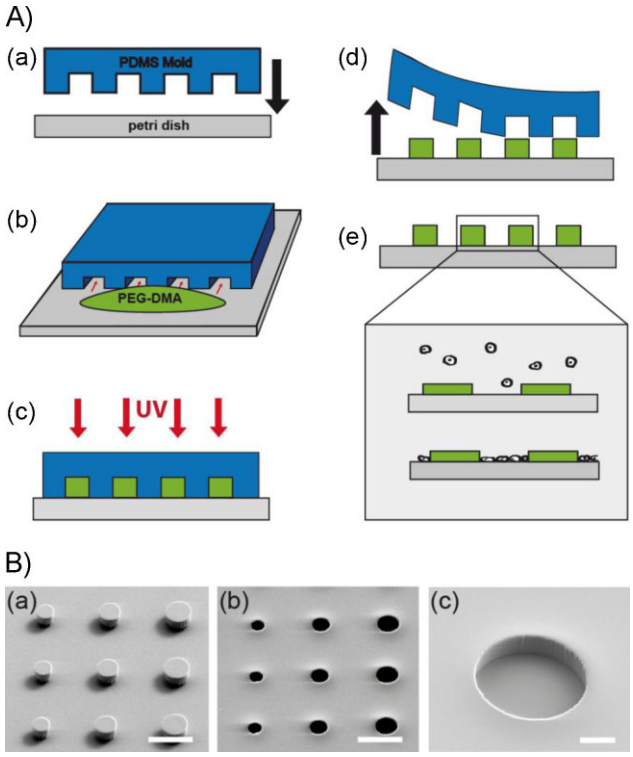

Figure 1. Preparation steps of PEG-DMA microstructures with the MIMIC method on standard cell culture dishes. (A) The trimmed PDMS mold is placed in close contact with the substrate (a) and filled by capillary force induced flow with the liquid polymer (b). The PEG-DMA is cross-linked by UV radiation (c). The mold is removed (d) and cells can be seeded onto the structures (e). (B) SEM images of a PDMS mold with different sizes of cylinders [scale bar: 50 μm (a)], and corresponding PEG-DMA microstructures [scale bars: 50 μm (b) and 20 μm (c)].

To promote cell adhesion on the hydrophilic areas, the dishes were filled with cell medium 20 min before cell seeding.

2.4. Fibronectin Coating

Human fibronectin (Biochrom, Berlin, Germany) was labeled using the Alexa Fluor 488 Protein Labeling Kit (Invitrogen, Carlsbad, CA, USA) by following the instructions. PEG-DMA microwells were incubated with 400 μl of a 50 $\mu g \cdot ml^{-1}$ solution of labeled fibronectin for 30 min at room temperature under light protection. The sample was rinsed three times with buffer and carefully dried with a gentle flow of nitrogen.

2.5. Cell Lines and Culture Conditions

Madin-Darby canine kidney cells (MDCK II, ATCC no. CRL-2936) were obtained from American Type Culture Collection (ATCC) and grown in Minimum Essential Medium supplemented with 10% fetal bovine serum (FBS) and 10 mM L-glutamine. Double transfected MDCK II cells with lifeact and H2B were kindly provided by Dr. Wedlich-Söldner of the Max Planck Institute of Biochemistry. MDCK II lifeact/H2B cells were grown in Dulbecco's Modified Eagle Medium, supplemented with 10% FBS, 20 mM L-glutamine, high-glucose level ($4.5 g \cdot l^{-1}$) and $110 mg \cdot l^{-1}$ pyruvate. Both cell lines were cultured at 37 °C in a humidified atmosphere, 5% CO_2 level. Cells were grown to 70–80% confluence, trypsinized and centrifuged at 1 000 rpm for 3 min. The cell pellet was resuspended in cell medium and cells were seeded on top of freshly prepared PEG-DMA structures.

2.6. Visualization of the Plasma Membrane and DNA

For plasma membrane imaging, cells were stained with CellMask Orange plasma membrane stain (Invitrogen, Carlsbad, CA, USA). Cells were incubated with the dye using a $5 \mu g \cdot ml^{-1}$ concentration for 5 min, rinsed three times with buffer and fixed in a 3.75% formaldehyde solution for 10 min. Again, the sample was rinsed three times with buffer. Finally, DNA was stained using a $1 \mu g \cdot ml^{-1}$ 4′,6-diamidino-2-phenylindole (DAPI) solution.

2.7. Viability Test

Cell viability was determined with the LIVE/DEAD cell Vitality Assay Kit (Invitrogen, Carlsbad, CA, USA). Cells were incubated with Leibovitz's L15 cell culture medium (Invitrogen, Carlsbad, CA, USA) containing 1 μM C_{12}-resazurin and 20 nM SYTOX Green stain for 15 min at in 37 °C in an atmosphere of 5% CO_2. The solution was diluted with 400 μl PBS and the sample was directly visualized under a Nikon Eclipse Ti microscope. Metabolic active cells were stained red while dead cells were stained green.

2.8. Microscopy

Optical and fluorescence images were obtained by using an epifluorescence motorized Nikon Eclipse Ti microscope equipped with a temperature-controlled mounting frame and a CCD camera (model Clara E from Andor Technology). Image acquisitions were controlled through μ-Manager open source software. For living cell image acquisition, temperature was controlled by an ibidi heating stage (ibidi GmbH, Martinsried, Germany) to maintain a constant 37 °C. Cells were grown in CO_2 independent Leibovitz's L15 medium, supplemented with 10% FBS.

2.9. Scanning Electron Microscopy (SEM)

The qualitative surface analysis was carried out with a LEO DSM 982 scanning electron microscope with an acceleration voltage of 8 kV. The samples were sputtered with a 10 nm thick gold layer at room temperature before scanning to prevent the sample from charging during the scanning process.

3. Results and Discussion

3.1. PEG-DMA Microwells for Single Cell- or Microculture-Arrays

Microfabricated environments allow one to spatially separate, shape and control the adhesion of cells.[34,41,42]

In this work, we demonstrate that cells are controlled by three-dimensional PEG-DMA microstructures and confined by the physical boundaries. The obtained microstructures are precise replica from the PDMS mold as indicated in Figure 1B. Typically, we prepare microstructures with a height of 10–20 μm and a diameter of the wells ranging from 15–300 μm. Cellular behavior is strongly influenced by the properties of the substrate.[43–45] As indicated in literature PEG-DMA structures are prepared on glass surfaces in most cases by whatever specialized surface functionalization like silanization or layer-by-layer deposition of charged polymers is required.[33,34,37,38,42] Here, we demonstrate a preparation using cell culture dishes as substrate. Hence, it is possible to perform experiments in a microstructured environment that is otherwise absolutely identical to standard cell culture conditions and therefore supports direct comparability. Additionally, no further surface modification to enhance cell adhesion is necessary. In our experiments, we use ibid μ-dishes with ibiTreat or hydrophobic bottoms (ibidi, Martinsried, Germany) but we achieve the same reproducibility of the microstructures on Greiner (Greiner, Frickenhausen, Germany) or Nunc (Nunc, Roskilde, Denmark) products. Cells were seeded on top of the freshly prepared structures. For example, a PEG-DMA array with microwells of 100 μm diameter and a spacing of 50 μm is filled by 500 μl cell suspension of MDCK II cells with a cell density of 400 000 cells · ml^{-1}. Four hours after cell seeding, we observe a Gauss distribution from 1 to 21 cells per well, with an average probability of 6 cells per well. Only less than 2% of the wells are unoccupied. The bottom of one well is completely covered typically by 9 cells and more. Depending on the initial cell density in the wells, the time of reaching a confluent monolayer can last several days depending on growth behavior of the cell line. Cells are trapped in the PEG-DMA wells by diffusive motion for small spacing intervals such as 50–100 μm. With increasing distances, cells remaining on top of the PEG-DMA surface appear more frequently. These cells round up and do not adhere to the surface. Thus, they can be easily removed by gentle washing with medium. Figure 2A shows various shaped small cell groups whose geometry is predetermined by the confinement. To ensure the non-toxic and biocompatible properties of PEG-DMA microwells, we investigated the viability of MDCK II cells 24 h after cell seeding. Using the LIVE/DEAD cell Vitality Assay Kit, we show that cells constrained by the PEG-DMA layer do not show any metabolic changes compared to free growing cells as indicted by same fluorescence level. This is in good agreement with previously reported data reporting that PEG-DA microstructures[46] as well as PEG-DMA hydrogels[47] are non-cytotoxic. Figure 2B shows metabolic active cell in the microstructures as indicated by the red fluorescence of C_{12}-resorufin. Cells remaining on top of the PEG-DMA structures rounded up and show apoptotic behavior. As indicated in Figure 2B (see insert), apoptotic cells are stained with SYTOX Green due to permeable cell membranes. To control cell adhesion a selective functionalization of the well bottoms with proteins like fibronectin or collagen can be performed according to standard protocols of incubation and washing for culture dishes. Figure 3A shows an array of PEG-DMA microstructures with labeled fibronectin

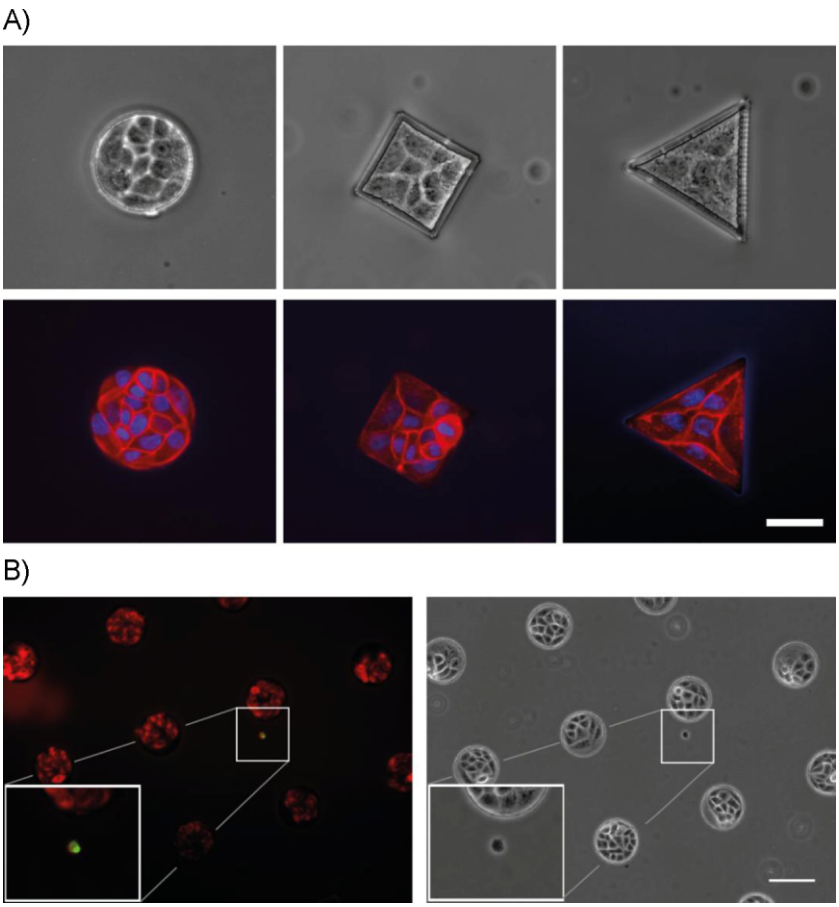

Figure 2. (A) PEG-DMA microwells of various shapes loaded with MDCK II cells. The shape of the cell groups is controlled by the geometry of the confinement. Cell membranes (red) were labeled with CellMask Orange and the nuclei were stained with DAPI (blue). Scale bar corresponds to 50 μm. (B) Proof of cell viability in PEG-DMA microwells. Red fluorescence of C_{12}-resorufin indicates metabolically active MDCK II cells. Single cells remaining on top of the PEG-DMA array (see insert) show apoptotic behavior (scale bar: 100 μm).

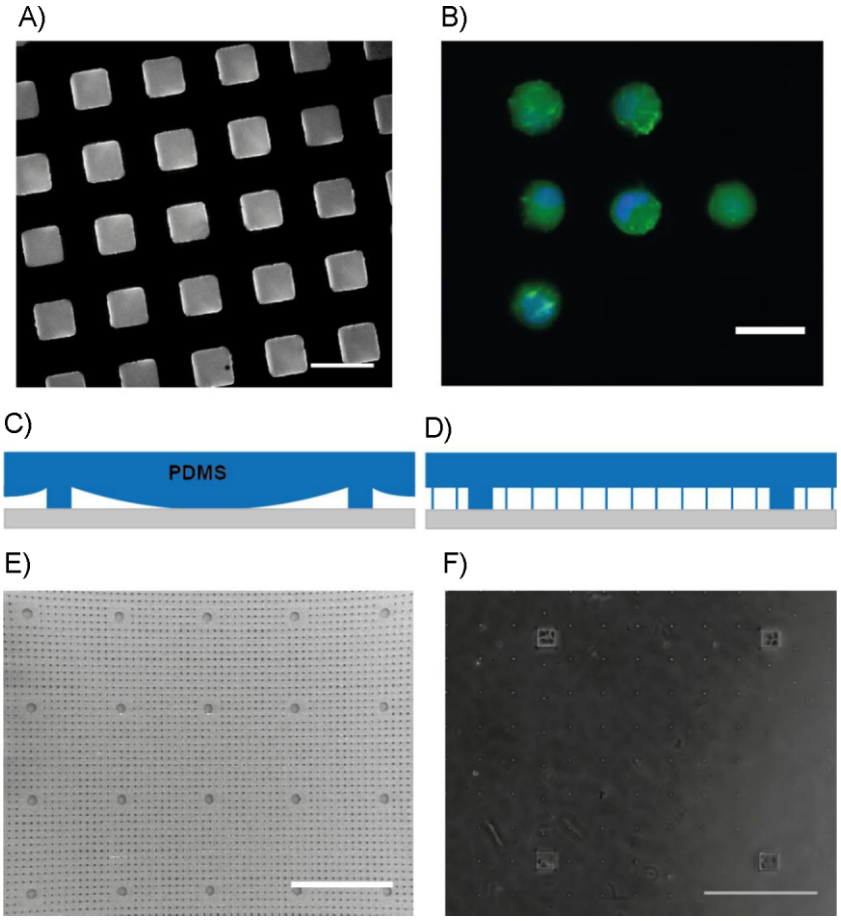

Figure 3. Fabrication of PEG-DMA arrays for microcultures. (A) Fluorescence micrograph demonstrating the selective adsorption of fibronectin (scale bar corresponds to 100 μm). (B) Single MDCK II cells are trapped in the PEG-DMA microwells as indicated by stable transfection of histone H2B (blue) and lifeact (green). The scale bar corresponds to 25 μm. (C) Extension of the lattice spacings to macroscopic (mm) dimensions causes problems due to sagging of the PDMS mold. (D,E) Inclusion of micro pillars in the PDMS mold prevents sagging as indicated by the SEM image (scale bar: 1 mm). (F) Phase contrast image of widely spaced microcultures (scale bar: 500 μm).

covering the adhesive areas. The size of the microwells can be scaled down to single cell level. Figure 3B shows single confined MDCK II cells as verified by nucleus staining. Thus, with the presented method, we can create arrays of microenvironments where cells can be trapped and remain viable. Nevertheless, the optical properties of the surface are relevant as well, particularly for fluorescence microscopy. With the MIMIC method the wells are prepared without a PEG-DMA layer on the bottom. Therefore, fluorescence imaging is not disturbed by background auto-fluorescence signals from the structuring material. Furthermore, the structured surfaces are suitable for observation with a magnification, such as with standard 100× objectives that have a short working distance. Note that in this specific case, culture dishes with thin plastic bottom are required for high quality imaging (e.g., ibidi μ-slides).

3.2. Widely Spaced Microstructures

The combination of microstructured surfaces that spatially control cell adhesion with robotic workstations for high-throughput analysis is promising. Since most automated systems have lower precision, widely separated adhesion fields are necessary for addressability. Furthermore, fluorescence intensity analysis of single wells without disturbing fluorescence signal from neighboring wells is an interesting task. The spacing of microwells is not arbitrary however, as the distance is limited by the PDMS mold. Since PDMS is a bendable material, sagging is a problem which has been discussed in literature.[48,49] For very low aspect ratios, the PDMS bends and comes into contact with the substrate (Figure 3C), and therefore leads to discontinuous PEG-DMA structures. The stiffness of cured PDMS can be controlled by varying the crosslinking density, however.[41] In general, a 10:1 w/w ratio of prepolymer to crosslinker is used. By trend, we mix slightly higher ratios such as 11:1 w/w since softer PDMS molds appeared to seal more effectively to the surface than stiffer ones. For the preparation of PEG-DMA structures it is important that the stamp is in close contact with the surface therefore avoiding slipping of the PDMS and unintended wetting of the surface with the PEG-DMA polymer. We overcame this problem by inserting an array of small pillars around the desired structure (Figure 3D). The diameter is chosen in a way so that the resulting holes in the PEG-DMA layer are too small for cell penetration. Figure 3E shows an SEM image of a widely spaced PEG-DMA microwell. For better illustration, these structures exhibit pillars of a diameter of 20 μm and a spacing of 50 μm. However, the resulting holes are large enough to trap MDCK II cells. To achieve well-separated cell colonies as shown in Figure 3F, a pillar field with 50 μm spacing and 7 μm diameter was used. In this way, arbitrary structures' dimensions can be achieved and implemented in automated workstations.

3.3. Arraying of Boundary-Free Microcultures by PEG-DMA Lift-Off

In the previous section, culturing of adherent cells in microwells up to confluence was shown. Cells can be

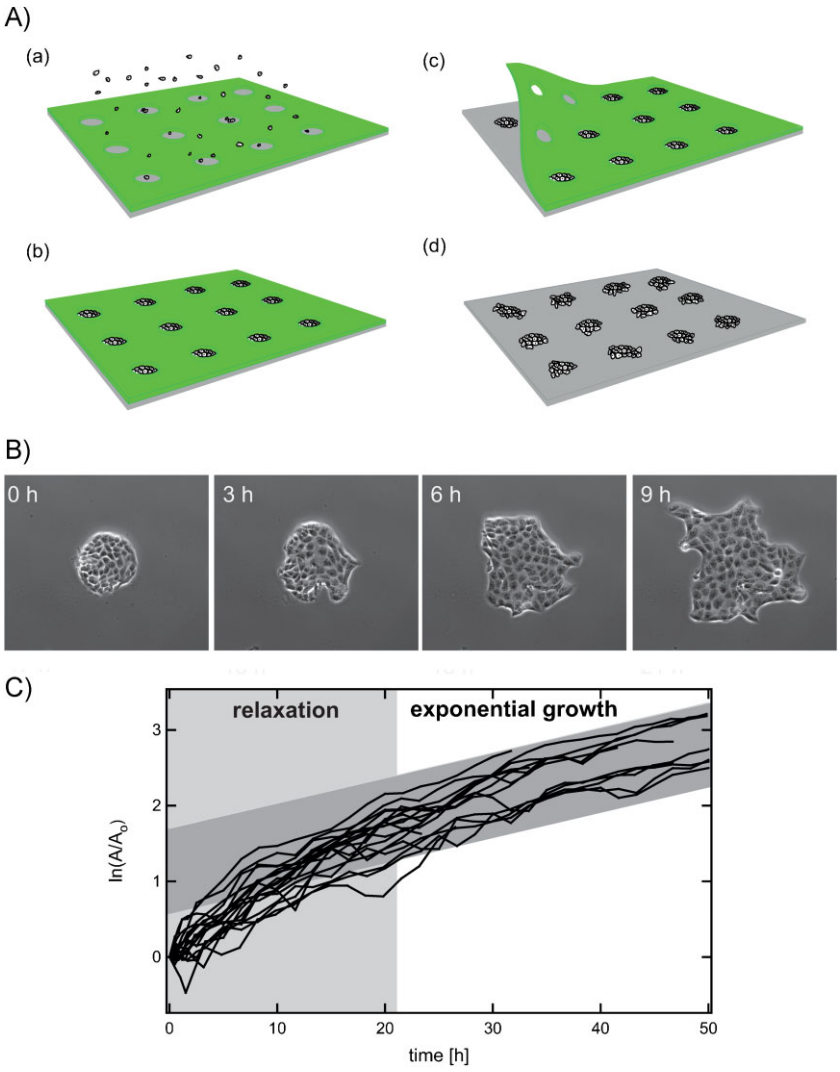

Figure 4. Positioning of boundary-free microcultures in arrays. (A) Cells were seeded and cultured in PEG-DMA microwells (a,b). The confinement can be removed mechanically (c) and free-standing microcultures of defined positions were obtained (d). (B) The microcultures can be followed by time lapse microscopy over several days. (C) The evolution of the overall area shows exponential growth after a relaxation time of one doubling time.

further cultured for two additional doubling times in the microwells. Beyond that, the confluent cell monolayer overgrows and the cells show sickly appearance, however, a boundary-free array of growing cell patches enables longer observation time of healthy cells. The release of confluent cell layers can be achieved by stencil assisted patterning. For this purpose, thin PDMS membranes as well as metal-based grids are used,[6,50] though demanding fabrication as well as difficult handling of these stencils can be limiting factors for biological applications.[21,22,50,51] We demonstrate that connective cell microcultures can be observed over several days with the described method by lift-off the PEG-DMA microstructures. For this purpose, PEG-DMA microstructures were fabricated as described in the experimental section on ibiTreat μ-dishes. The cells were cultured in the microstructures until a confluent monolayer is reached. The cell density varies from well to well due to the cell seeding process as mentioned in 3.1. Then, the PEG-DMA layer was mechanically removed. To facilitate the detachment of the structure, the cell medium is taken off aside from a thin film to protect the cells against drying. The PEG-DMA stencil is grabbed by tweezers and lifted off the surface. Leftover material is eliminated by gently washing the sample with medium. The single steps of the procedure are illustrated in Figure 4A. The removal of the boundaries enables free expansion and growth of the microcultures on the newly available surface of the petri dish. Initially, the resulting cell microcolonies feature the geometry of the PEG-DMA well and are spatially aligned in an array. The interface of propagating cell microcultures shows dynamic instabilities and the cell patch contour roughens over time. Phenomena like leader cells can be observed just like in wound healing scenarios.[23,24,52] The cells start to cover the whole free surface and growing microcultures meet each other after some time. To enable long-term experiments, an adequate spacing between the cell patches is required to ensure unhindered area enlargement. As described in the previous section, we obtain widely spaced microstructures by inclusion of small pillar fields around the underlying structure. The growing microcultures can be followed by time-lapse microscopy as demonstrated by the time series in Figure 4B. Figure 4C shows exemplary time traces of area evolution of small cell patches from the same experiment. In previous work, we investigated the area and cell number evolution of small cell patches.[52] We observed an exponential cell number growth while the total area expands initially faster than exponentially. This phenomenon is due to the fact that the initial cell density is exaggerated in the confining PEG-DMA microwells. When cells are released, the cell density relaxes with a characteristic relaxation time in the order of the cell doubling time. Nevertheless, since the contour and hence the area of the cell

microculture can be followed by image analysis tools,[53] growth rates of each single cell patch can be readily determined during the course of a time-lapse experiment. This feature of microcultures might be an important advantage over ordinary cell culture experiments in cases where cell growth rates might be related to other observables in the time-lapse study. In addition, since parallelized microculture experiments allow assessment of many cell microcultures under the same conditions, improved statistics and accuracy of growth rates and changes is achievable.

3.4. Preparation of PEG-DMA Membranes as Templates for Plasma-Induced Patterning

As an alternative to the physical separation and confinement of cells by three-dimensional microstructures, surfaces can be chemically treated to create a cellular pattern. In plasma-induced patterning a partially covered surface is exposed to low-pressure plasma. Due to the changes of surface hydrophobicity, cells adhere exclusively on areas exposed to the plasma. We use thin PEG-DMA membranes to perform low-pressure plasma-induced micropatterning on cell culture dishes. For this, the microstructures were prepared on a glass surface to enable a facile and neat detachment of the membrane, following the same protocol as described in the experimental section. Since the PEG-DMA layer shows a very low adhesive strength on glass under liquids, we remove the microstructures by pipetting a single droplet of distilled water at the border of the structures. After a few minutes, the membrane is completely detached. Following this, the membrane is dried with a gentle flow of nitrogen. The PEG-DMA layer seals spontaneously against the plastic surface when it is brought in close contact as demonstrated in Figure 5A. After plasma treatment, the areas exposed to the plasma turn hydrophilic whereas the protected parts stay hydrophobic. The PEG-DMA template is removed and cells are seeded on top of the surface (Figure 5B). The cells adhere to the hydrophilic part of the substrate corresponding to the cutout of the PEG-DMA layer and therefore the shape of the cell pattern is predefined by the geometry of the adhesive island as shown in Figure 5C. In contrast to the three-dimensional microwells where the cells are constricted beyond a confluent state, structures from plasma-induced patterning allow the cells to leave the confinement. The separation between cell patches is more based on preference toward the hydrophilic surface than on repellent properties of the hydrophobic one. Thus this chemical confinement is weaker in comparison to the physical PEG-DMA barrier. However, PEG-DMA stencils can be reused several times to produce microstructures from plasma-induced patterning.

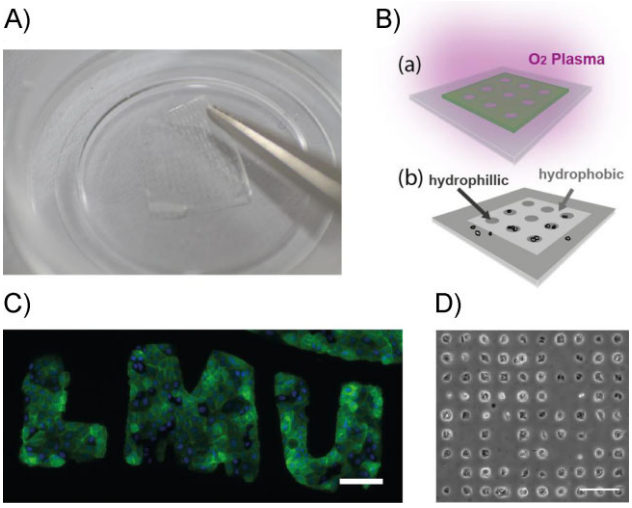

Figure 5. PEG-DMA stencils as templates for plasma-induced micropatterning. (A) A thin PEG-DMA stencil seals spontaneously on an ibidi μ-dish. (B) By the use of low-pressure oxygen plasma, the exposed areas become hydrophilic while the protected surface stays hydrophobic (a). After removal of the PEG-DMA template, cells can attach to the chemically modified surface (b). (C, D) Stable transfected MDCK II (H2B and lifeact) cells are confined in pattern from plasma-induced micropatterning (scale bars: 100 μm).

4. Conclusion

We have presented a detailed protocol for the fabrication of three-dimensional PEG-DMA microstructures on standard cell culture dishes. Cells were confined in single cell arrays or small cell groups. Widely spaced microwells were achieved by inserting a pillar field to prevent the PDMS stamp from sagging. In particular, we created arrays of free-growing microcultures by mechanical removal of the PEG-DMA layer in a lift-off scenario. We showed in time lapse experiments that growth rates are accessible in good approximation through evaluation of total area evolution. PEG-DMA stencils can act as templates for plasma-induced micropatterning where cells were confined by chemical surface modification. In all presented applications, cells were grown on standard cell culture dishes. Thereby a direct comparison to routine experiments is rendered possible without the need to consider the influence of entirely new surface properties to cellular behavior. PEG-DMA based microarrays present a versatile platform to study cellular responses of single cells or microcultures in parallelized experiments with large potential for quantitative biology.

Acknowledgements: We would like to thank Christoph Klingner and Dr. Wedlich-Söldner for the kind supply of stable transfected MDCK cell lines. Financial support by the Deutsche Forschungsgemeinschaft (DFG) via SFB 1032, the Excellence Cluster "Nano-

systems Initiative Munich (NIM)" and the Center for NanoScience (CeNS) is gratefully acknowledged.

Received: November 5, 2012; Revised: January 18, 2013; Published online: March 4, 2013; DOI: 10.1002/mabi.201200400

Keywords: adhesion; biological applications of polymers; microstructure; photopolymerization; plastics

[1] D. B. Weibel, W. R. Diluzio, G. M. Whitesides, *Nat. Rev. Microbiol.* **2007**, *5*, 209.
[2] E. Berthier, E. W. K. Young, D. Beebe, *Lab Chip* **2012**, *12*, 1224.
[3] M. Thery, *J. Cell Sci.* **2010**, *123*, 4201.
[4] M. L. Yarmush, K. R. King, *Annu. Rev. Biomed. Eng.* **2009**, *11*, 235.
[5] R. S. Kane, S. Takayama, E. Ostuni, D. E. Ingber, G. M. Whitesides, *Biomaterials* **1999**, *20*, 2363.
[6] D. Falconnet, G. Csucs, H. M. Grandin, M. Textor, *Biomaterials* **2006**, *27*, 3044.
[7] J. Fink, M. Théry, A. Azioune, R. Dupont, F. Chatelain, M. Bornens, M. Piel, *Lab Chip* **2007**, *7*, 672.
[8] D. E. J. Anderson, M. T. Hinds, *Ann. Biomed. Eng.* **2011**, *39*, 2329.
[9] X. Zhou, F. Boey, F. Huo, L. Huang, H. Zhang, *Small* **2011**, 2273.
[10] Z. Nie, E. Kumacheva, *Nat. Mater.* **2008**, *7*, 277.
[11] A. L. Hook, H. Thissen, N. H. Voelcker, *Trends Biotechnol.* **2006**, *24*, 471.
[12] F. Xu, J. Wu, S. Wang, N. G. Durmus, U. A. Gurkan, U. Demirci, *Biofabrication* **2011**, *3*, 034101.
[13] H. Shin, *Biomaterials* **2007**, *28*, 126.
[14] M. Théry, V. Racine, M. Piel, A. Pépin, A. Dimitrov, Y. Chen, J.-B. Sibarita, M. Bornens, *Proc. Natl. Acad. Sci. USA* **2006**, *103*, 19771.
[15] M. Théry, V. Racine, A. Pépin, M. Piel, Y. Chen, J.-B. Sibarita, M. Bornens, *Nat. Cell Biol.* **2005**, *7*, 947.
[16] C. S. Chen, *Science* **1997**, *276*, 1425.
[17] M. P. Lutolf, H. M. Blau, *Adv. Mater.* **2009**, *21*, 3255.
[18] S. Gobaa, S. Hoehnel, M. Roccio, A. Negro, S. Kobel, M. P. Lutolf, *Nat. Methods* **2011**, *8*, 949.
[19] X. Trepat, M. R. Wasserman, T. E. Angelini, E. Millet, D. A. Weitz, J. P. Butler, J. J. Fredberg, *Nat. Phys.* **2009**, *5*, 426.
[20] J. Fu, Y.-K. Wang, M. T. Yang, R. A. Desai, X. Yu, Z. Liu, C. S. Chen, *Nat. Methods* **2010**, *7*, 733.
[21] E. Ostuni, R. Kane, C. S. Chen, D. E. Ingber, G. M. Whitesides, *Langmuir* **2000**, *16*, 7811.
[22] D. Wright, B. Rajalingam, S. Selvarasah, M. R. Dokmeci, A. Khademhosseini, *Lab Chip* **2007**, *7*, 1272.
[23] M. Poujade, E. Grasland-Mongrain, A. Hertzog, J. Jouanneau, P. Chavrier, B. Ladoux, A. Buguin, P. Silberzan, *Proc. Natl. Acad. Sci. USA* **2007**, *104*, 15988.
[24] L. Petitjean, M. Reffay, E. Grasland-Mongrain, M. Poujade, B. Ladoux, A. Buguin, P. Silberzan, *Biophys. J.* **2010**, *98*, 1790.
[25] M. Huergo, M. Pasquale, A. Bolzán, A. Arvia, P. González, *Phys. Rev. E* **2010**, *82*, 1.
[26] A. Ohl, K. Schro, *Surf. Coat. Technol.* **1999**, *119*, 820.
[27] J.-H. Kim, S. Seo, J. Min, *J. Biotechnol.* **2011**, *155*, 308.
[28] Q. Cheng, S. Li, K. Komvopoulos, *Biomaterials* **2009**, *30*, 4203.
[29] M. Junkin, P. K. Wong, *Biomaterials* **2011**, *32*, 1848.
[30] M. Charnley, M. Textor, A. Khademhosseini, M. P. Lutolf, *Integr. Biol.* **2009**, *1*, 625.
[31] J. Groll, Z. Ademovic, T. Ameringer, D. Klee, M. Moeller, *Biomacromolecules* **2005**, *6*, 956.
[32] A. Revzin, R. J. Russell, V. K. Yadavalli, W. G. Koh, C. Deister, D. D. Hile, M. B. Mellott, M. V. Pishko, *Langmuir* **2001**, *17*, 5440.
[33] H.-C. Moeller, M. K. Mian, S. Shrivastava, B. G. Chung, A. Khademhosseini, *Biomaterials* **2008**, *29*, 752.
[34] J. M. Karp, J. Yeh, G. Eng, J. Fukuda, J. Blumling, K.-Y. Suh, J. Cheng, A. Mahdavi, J. Borenstein, R. Langer, A. Khademhosseini, *Lab Chip* **2007**, *7*, 786.
[35] P. Kim, D. H. Kim, B. Kim, S. K. Choi, S. H. Lee, A. Khademhosseini, R. Langer, K. Y. Suh, *Nanotechnology* **2005**, *16*, 2420.
[36] E. Kim, Y. Xia, G. M. Whitesides, *Lett. Nat.* **1995**, *376*, 581.
[37] H.-W. Shim, J.-H. Lee, T.-S. Hwang, Y. W. Rhee, Y. M. Bae, J. S. Choi, J. Han, C.-S. Lee, *Biosens. Bioelectron.* **2007**, *22*, 3188.
[38] H.-M. Song, C-S. *Korean J. Chem. Eng.* **2008**, *25*, 1467.
[39] Institut für Mikrotechnik, Mainz, Germany Online. **2012**. Available from URL www.imm-mainz.de.
[40] Micro Resist Technology GmbH. Berlin, Germany Online. **2012**. Available from URL www.microresist.de (accessed February 2013).
[41] M. Ochsner, M. R. Dusseiller, H. M. Grandin, S. Luna-Morris, M. Textor, V. Vogel, M. L. Smith, *Lab Chip* **2007**, *7*, 1074.
[42] H. Kim, R. E. Cohen, P. T. Hammond, D. J. Irvine, *Adv. Funct. Mater.* **2006**, *16*, 1313.
[43] R. G. Flemming, C. J. Murphy, G. A. Abrams, S. L. Goodman, P. F. Nealey, *Biomaterials* **1999**, *20*, 573.
[44] C. J. Bettinger, R. Langer, J. T. Borenstein, *Angew. Chem. Int. Ed.* **2009**, *48*, 5406.
[45] M. M. Stevens, J. H. George, *Science* **2005**, *310*, 1135.
[46] A. Revzin, R. G. Tompkins, M. Toner, *Langmuir* **2003**, *19*, 9855.
[47] K. Arcaute, B. K. Mann, R. B. Wicker, *Ann. Biomed. Eng.* **2006**, *34*, 1429.
[48] B. E. Delamarche, H. Schmid, B. Michel, *Adv. Mater.* **1997**, 741.
[49] C. Y. Hui, A. Jagota, Y. Y. Lin, E. J. Kramer, *Langmuir* **2002**, *18*, 1394.
[50] A. Folch, B. H. Jo, O. Hurtado, D. H. Beebe, M. Toner, *J. Biomed. Mater. Res.* **2000**, *52*, 346.
[51] R. J. Jackman, D. C. Duffy, O. Cherniavskaya, G. M. Whitesides, *Langmuir* **1999**, *15*, 2973.
[52] A.-K. Marel, A. Piera Alberola, J. O. Rädler, *Biophys. Rev. Lett.* **2012**, *7*, 15.
[53] A. Puliafito, L. Hufnagel, P. Neveu, S. Streichan, A. Sigal, D. K. Fygenson, B. I. Shraiman, *Proc. Natl. Acad. Sci. USA* **2012**, *109*, 739.

Supporting Information

for *Macromol. Biosci.*, DOI : 10.1002/mabi.201200400

Master Fabrication by Soft Lithography

Anna-Kristina Marel, Susanne Rappl and Joachim Oskar Rädler *

Protocol for Master Fabrication

The photo mask was designed using the layout editor software CleWin Version 4 (WieWeb Software, Hengelo, Netherlands). The layout was printed by Zitzmann GmbH (Eching, Germany), a company which is specialized for plotting transparencies with a resolution up to 64.000 dpi. The use of lithography transparencies for micro-scaled structuring is an expedient alternative to an expensive chromium mask.

The master for PDMS replication was created using the negative photo resist SU-8 (Microchem, distributed by MicroResist Techology, Berlin, Germany). Three-inch silicon wafers (100_P type, Si-Mat, Landsberg/Lech, Germany) served as substrates.

To enhance the adhesion of the resist, the SiO_2 was removed from the surface of the Si-Wafer by dipping the wafers in a 20% solution of hydrofluoric acid (BASF-Ätzmischung AF 87,5-12,5). As soon as all of the acid rolled off the wafer, the SiO_2 was removed. The wafer was rinsed with MilliQ water and blown dry with nitrogen. Directly after the acid treatment, 1 ml of the adhesive agent TI-Prime (MicroChemicals GmbH, Ulm, Germany) was poured on top of the wafer. The covered wafer was spin-coated at 5000 rpm for 30 sec, after progressive acceleration, and baked it for 2 min at 120 °C.

By spin coating 1 ml of SU-8 10 photo resist at 1,000 r.p.m. for 32 sec, with an acceleration step of 500 r.p.m. for 5 sec, a 30 µm high photo resist layer was achieved. The spin speed determines the height of the final structures. To avoid friction in the resist layer, there was a rest period of 30 min. Next, the wafer was baked at 65°C for 3 min, followed by a second

heating step at 95°C for 7 min. The wafer was then exposed to UV-illumination in a mask aligner (Süss MicroTec, Garching, Germany) through the lithographic transparency, which was stabilized by a quartz glass blank. The exposure time depended on to the type and the size of the structures. In our case, the exposure time was in the range of 40 - 100 sec with an exposure output of 4.1 mW/cm^2.

The next step was to cross-link the exposed portions of the film by a progressive post exposure bake (1 min at 65 °C and 2 min at 85-90 °C, with a slow cooling down to room temperature). The wafer was developed in a mr-Dev 600 developer (micro resist technology GmbH, Germany) for approximately 4 min until all non-crosslinked parts were dissolved. The structured wafer was then rinsed with isopropanol and blown dry with nitrogen. Finally, the wafer was baked at 160 °C for 15 min followed by a slow cool down to ensure a high mechanical standard of the microstructures.

Silanization of the Structured Waver with 1H,1H,2H,2H-perfluorooctyltrichlorosilane

To ensure proper PDMS modling, the resist master was silanized. Vapor deposition of a fluorosilane (1H, 1H, 2H, 2H-perfluorooctyltrichlorosilane, ABCR, Germany) was achieved under vacuum for one hour. Due to the passivation of the wafer by silanization, the master can be used many times.

Molecular Weight of PEG-DMA

PEG-DMA can be purchased in a wide range of molecular weights (from Mn = 330 to 6000, Sigma-Aldrich, Germany). The properties of the polymer such as cross-linking ratio, viscosity, swelling behavior, protein adsorption and cell adhesion all depend on its chain length. Moeller[1] found for PEG-DA (poly(ethylene glycol)-diacrylate) that a decreasing average MW lowers the resistance to protein and cell attachment. Furthermore, for high molecular weight polymers, the structures became unstable in aqueous solutions since the polymer tends to swell. Whereas shorter chain lengths resist this effect due to higher cross-

linking densities and remain in their original shape.[2,3] We use a PEG-DMA polymer with a molecular weight of 550 to achieve an optimal agreement between stability and surface properties. Its low viscosity enables a fast and efficient filling of the PDMS mold and its inertness to PDMS ensures a complete detachment of the mold after the formation of the microstructures.

[1] H.-C. Moeller, M. K. Mian, S. Shrivastava, B. G. Chung, A. Khademhosseini, *Biomaterials* **2008**, *29*, 752.

[2] H.-W. Shim, J.-H. Lee, T.-S. Hwang, Y. W. Rhee, Y. M. Bae, J. S. Choi, J. Han, C.-S. Lee, *Biosens. Bioelectron.* **2007**, *22*, 3188.

[3] P. Kim, H. E. Jeong, A. Khademhosseini, K. Y. Suh, *Lab Chip* **2006**, *6*, 1432.

4 Expansion Dynamics of Circular Shaped Cell Microcolonies

During numerous biological processes such as wound healing, morphogenesis, sprouting and branching, cells migrate collectively. This highly regulated process comprises coordinated cell motion as well as dynamic remodeling at single cell level, including formation or breakup of cell junctions. The description of the global properties of connective tissue remains a great challenge in biophysical modeling. Recently, cells and tissue have been depicted as visocelastic material [55]. For spherical cell aggregates under mechanical deformation, a complex viscoelastic behavior has been reported [31, 39]. On short time scales, tissues relax like an elastic material, however, for long term deformation, cells aggregates flow like a viscous liquid. This is not very astonishing when the viscoelastic properties of most cellular components such as cytoplasm, microtubules or actin filaments are taken into account. Several approaches of measuring the surface tension of tissues have been performed such as micropipette aspiration technique [39], compression by parallel plates [32] or deformation under centrifugal forces [87]. The resulting elastic stress is quickly dissipated by the tissue and is followed by a longer viscous flow that includes processes like cellular rearrangements. The measured relaxation times, however, are in the order of seconds or minutes, respectively. Further work predicts relaxation processes at the time scale of cell division and death [5, 93]. Ranft *et al.* showed that cell division events as well as apoptosis induce a dynamic remodeling of the tissue in terms of liquid like behavior. A two dimensional system has been studied by Angelini *et al.*. They analyzed cell motion within a confluent epithelial sheet and found a cell density dependent flow behavior of the tissue, leading them to the assumption of a transition to a glass-like state of the monolayer for high cell densities that is associated to the time scale of cell division time.

A further aspect of cell migration captures single cell motion. Single cells migrate in the context of immune response or during metastasis, however, single cell migration within a connected cell sheet has also been investigated [92]. An interesting question deals with the transition of single cell behavior to coordinated movement of several cells and the associated changes in cellular properties. The investigation of small cell colonies of finite size could lead to new insights of the migratory behavior of cells. Furthermore, small systems with countable cell numbers are convenient for direct comparability of experimental finding and theoretical

models. On this note, we analyzed the expansion of small cell patches from defined circular geometries [68]. The technical problem of preparing free-growing cell assemblies of the same geometry was challenged by a lift-off scenario of PEG-DMA microstructures.

Wound-healing assays are suitable to probe collective cell migration

In order to study the dynamics of collective cell migration, various techniques have been developed [97]. Wound healing assays are a simple approach to create a migrating cell front by providing a new, unoccupied surface which is sufficient to trigger cell migration [89]. Model wounds can be created by mechanical, chemical, optical or electrical impacts, however, some of these methods causes injuries at the boundary of the cell layer. The simplest way of introducing a cell-free region within a confluent monolayer is by mechanical scratching [63]. Another mechanical wounding is performed by punching the cell layer with a stamp. Both methods produce a surface with debris of destroyed cells and the extracellular matrix. An unaffected surface is produced by solid barriers that prevent cell adhesion at the covered area. The physical barrier usually consists of a biocompatible material such as Teflon [90] or PDMS [89]. The cells are seeded around the block and grown to confluence. After lifting-off the barrier, the cell layer starts to close the emerging gap. By stencil assisted patterning, the inverse scenario is created: islands of cells on a free surface are formed after stencil removal [30, 82, 142, 143]. Here, the challenge is to produce thin, robust and perforated membranes that exhibit structures of micron size.

4.1 Proliferation and Collective Migration of Small Cell Groups Released from Circular Patches [P2]

In our paper [P2], the proliferation and expansion of small cell cohorts were monitored in order to investigate the intrinsic characteristics leading to area expansion. Cell microcolonies were shaped by removable PEG-DMA mircostructures. Once the bottom of the microwells were covered by cells, the PEG-DMA layer was mechanically removed. The expansion of the released cell groups was followed by time lapse microscopy (see Fig. 4.1).
The described lift-off scenario is similar to stencil assisted patterning methods known from earlier literature [26]. In this process, a flexible membrane with through-holes is sealed onto the surface prior to cell seeding and thus protects the covered area from cell adhesion. The methods for fabricating stencils made of silicon, parylene-C or PDMS are variable, ranging from photolithography and dry etching [143], over microfluidic approaches [30] to spin coating. The challenge is to produce a membrane of reasonable height meaning a maximum of a few hundred microns for comfortable handling. Using removable PEG-DMA microstructures was an elegant technique, since first off, the height of the structures was easily controllable by the height of the used PDMS mold, ans additionally cells were not damaged by the bar-

rier as consequence of the non-fouling properties of PEG-DMA. As described in the work of Nikolić and coworkers [80], the peeling-off of a PDMS membrane causes an injured cell boundary that influences the migratory behavior of the cell sheet. To ensure that removal of PEG-DMA structures leaves an intact cell layer behind, viability tests on freshly released cell patches were performed. As demonstrated in Fig. 4.2, a few cells showed apoptotic or necrotic behavior demonstrated by the green fluorescence of the dye SYTOX Green that only penetrates into damaged cells. The majority of the cells were metabolically active as indicated by red fluorescence of C_{12}-resorufin.

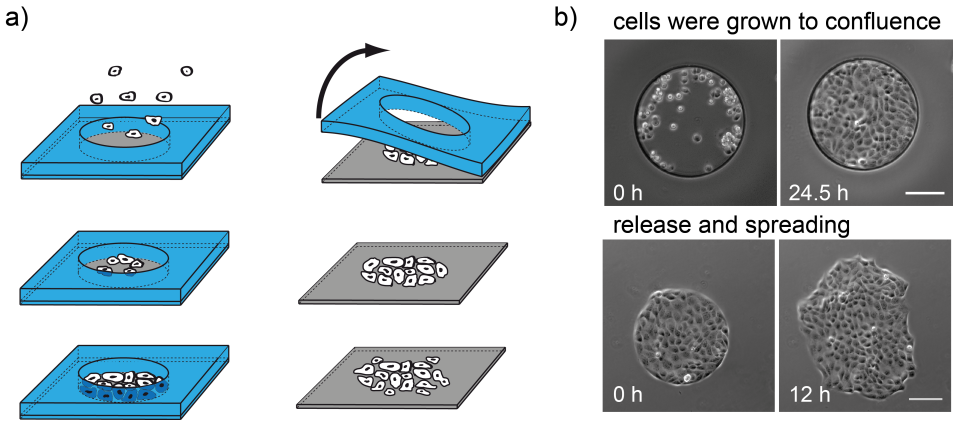

Figure 4.1: Small, circular cell patches are shaped by PEG-DMA microstructures and released by lift-off. *(a) A schematic diagram of the experimental procedure: MDCK cells were seeded on top of the PEG-DMA structures and grown to confluence. The PEG-DMA layer was removed and the cell group expanded by proliferation and migration. (b) Cellular behavior was followed by time-lapse microscopy. As indicated by the brightfield images, cells were perfectly confined by the physical barrier. Cell grew normally within the structures and were released once they reached a confluent monolayer. The microcolony grew by occupying the new surface. Scale bars corresponds to 100 µm.*

Cells groups were arrayed by widely spaced PEG-DMA microstructures. Due to inhomogeneous seeding, wells possessed different but countable numbers of cells at the time of lifting-off the PEG-DMA layer. The analysis of cell number evolution showed exponential cell growth with a growth rate reasonable for MDCK cells, as expected. The standard procedure of growth rate determination for adherent cell lines is repetitive trypsination and cell counting either by a hemocytometem or electrical cell counters. Park et al. introduced a very specific micro-electro-mechanical system to measure individual cell growth rates and mass evolution [83]. On the basis of the created well defined system, we were able to show that growth rates are also accessible by following the total area evolution of the cell patch. The area growth is due to cell proliferation, however, a systematic deviation of area evolution from exponential growth had to be taken into account due to the early phase of expansion. This variance is more pronounced for cell patches with higher starting cell densities and caused by compression

of the cell group prior to lifting-off the PEG-DMA layer. The observation could be confirmed by analysis of area per cell over time showing that the area per cell is shifted to higher values and the distribution broadened over time. By combining elastic area relaxation and cell division, the area evolution was described exactly and served as a basis for correct growth rate determination. With our model, the identification of growth rates from area evolution is rendered possible, which is of great interest because it provides the opportunity of calculating growth behavior for the actual cell population without interference. The viscoelastic behavior of small cell colonies was determined by analyzing the evolution of cell density. We found the resulting relaxation time to be in the same order as the measured doubling time. Therewith, we were able to determined experimentally an intrinsic relaxation behavior relying on the time scale of cell division. In the theoretical work of Ranft *et al.*, they assume that the relaxation time of the tissue is set by the rate of cell division and apoptosis [93].
Since the microcolonies showed active cell migration, leader cell formation and roughening of the border of the cell sheet were observed. Due to the circular shape of the cell assemblies, leader cells developed in any direction and often in parallel. The following cells were polarized, however, the emerging forces resembled a tug-of-war scenario caused by the short distances from one patch side to the other and therefore between the individual leader cells. The dynamic border instabilities and phenomena like finger formation where cells move in a highly coordinated manner are described in a physical model by Mark *et al.* [70]. They consider the first cell row a continuous one dimensional, active membrane with elastic properties such as curvature and surface tension. A further approach to characterizing propagating cell fronts in both tumor growth and sheet expansion is the analysis of the fractal dimension of interfaces as performed by Huergo *et al.* or Brú *et al.* [49, 119]. The systems investigated by these methods were exclusively large and multicellular, while in contrast, our microcolonies consisted of less than 80 cells. Although border instabilities were observed, the created cell groups seemed to be too small in size as to be analyzed by the described methods.

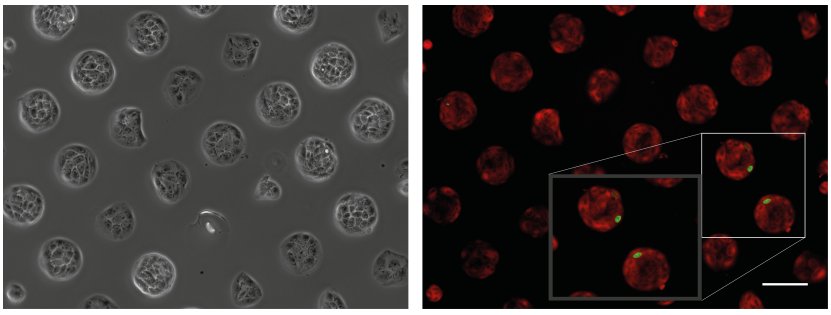

Figure 4.2: The removal of PEG-DMA microstructures shows little impact on the border cells. *The brightfield image shows perfectly circular shaped microcolonies for wells where cells have reached confluence before lift-off. All cells exhibit clear red fluorescence due to active metabolism except two cells showing apoptotic or necrotic behavior indicated by the green fluorescent signal (see insert).*

Publication 2 [P2]

Proliferation and Collective Migration of Small Cell Groups Released from Circular Patches

Anna-Kristina Marel[1], Alicia Piera Alberola[1] and Joachim Oskar Rädler[1]

[1]Fakultät für Physik, Ludwig-Maximilians-Universität,
Geschwister-Scholl-Platz 1, 80539 München, Germany

published in:

Biophysical Reviews and Letters, Vol. 7, Issue 12, 2012, 15-28.
DOI: 10.1142/S1793048012500026

Biophysical Reviews and Letters
Vol. 7, Nos. 1 & 2 (2012) 15–28

DOI: 10.1142/S1793048012500026

World Scientific
www.worldscientific.com

PROLIFERATION AND COLLECTIVE MIGRATION OF SMALL CELL GROUPS RELEASED FROM CIRCULAR PATCHES

A.-K. MAREL, A. PIERA ALBEROLA and J. O. RÄDLER
Fakultät für Physik
Ludwig-Maximilians-Universität
Geschwister-Scholl-Platz 1, D-80539 München, Germany

Received 30 November 2011
Revised 17 March 2012
Published 7 May 2012

Collective cell migration is a key element in morphogenesis, cancer formation and wound healing. The multicellular dynamics of epithelial cell layers were studied in experiment and theory over the last years. Yet little is known about cell patches of finite size that should lead over from single cell behavior to collective motion. Here we study the migration and proliferation of small assemblies of epithelial cells (5-23 cells initially). Cells are released at defined time using removable poly(ethylene glycol)-dimethlacrylate (PEG-DMA) stencils with circular apertures, wherein cells were seeded. Using time-lapse microscopy we determine cell number, cell patch area and shape of multiple patches in parallel. We confirm exponential growth in cell number but find the area of the patches expanding faster than exponential in the early phase. The area is, however, well-described if cell proliferation is superimposed by elastic area dilation assuming that the cell groups were initially compressed. The elastic relaxation time is of the same order as the measured doubling time. Furthermore, analysis of the center-of-mass movement of the patches reveals bursts of directed motion, which coincide with asymmetric cell growth. In these cases the contours of the patches seem to result from a tug-of-war like scenario of opposing leader cells.

Keywords: Collective cell migration; microstructured surfaces; relaxation.

1. Introduction

Collective cell migration is a hallmark of morphogenesis in embryonic development, cancer formation and wound healing. During the process of developing or refurnishing shape, the dynamic remodeling of tissue is a central element of biological organisms. In contrast, shape persistence and mechanical load capacity is an attribute of full-grown tissue. In fact, cellular rearrangements in tissue are tightly controlled by biochemical signals mediated by cytokines and cell-cell contact. Yet mechanical aspects play an important role, leading to universal constraints that

any remodeling process needs to fulfill. Recently, much effort has been made to develop a framework describing the global properties of connective tissue. It is generally accepted that tissue on short time scales can be described as a viscoelastic material[1–3] and that the morphology of many, but not all, naturally occurring tissues is well approximated by a foam-like structure.[4] In the case of two-dimensional cell layers, the tissue structure is well-described by a mathematical vertex model. Recently, the polygonal distribution of epithelia cell layers in drosophila wing disks has been correctly reproduced based on a vertex model including cell elasticity, cell-cell adhesion and cortical tension.[5] In contrast, at long time scales, i.e., periods longer than cell division, tissue appears dynamic.

In development, remodeling is also frequently accompanied by controlled cell death. In a recent work, a minimal model of tissue dynamics has been established,[2] which assumes that cells reorganize solely by cell division and apoptosis. The model predicts a homeostatic state for tissue where cell division and apoptosis balance and derives viscoelastic properties. Furthermore, experiments following the velocity fields in migrating epithelia sheets exhibit long-range correlations in collectively migrating epithelia cells.[6–9] A tightly connected cell association exhibits glass-like behavior with multicellular groups migrating collectively over a broad range of length scales and times.[7] Phenomenologically different types of collective motion are specified like sheet movement, sprouting and branching.[10] In particular a prominent feature in spreading epithelia fronts is the formation of an elongated finger guided by so-called leading cells, which appear to have a distinct phenotype.[6,11,12] Within the finger a distinctly coordinated flow of cells following the leader cell is observed. However there are no experiments that investigate the transition from single cell migration to collective migration and questions regarding the dynamics of small groups of cells (cohorts) in collective motion have not been addressed yet.

Early attempts to systematically measure cell migration *in vitro* used the so-called scratch assay,[13] where a confluent cell monolayer is scratched with a pipette tip to create a wound. During wound closure, the mean velocity of the spreading cell layer is determined. However, little control over the shape or size of the scratch is given by this method. Border cells can be damaged and influence migration. In recent years microstructured surfaces have been developed to control cell process such as proliferation and differentiation.[14–16] Stencil-assisted patterning, in which a stiff or flexible membrane is employed to shape and separate regions for cell adhesion, can be used to create cellular micropatterns on homogenous substrates.[17,18] Such microstructured membranes can be easily peeled off without cell damage. This lift-off technique has recently been used by Poujade *et al.* to study collective cell migration from an initial stripe conformation. Other techniques to generated controlled cell interfaces are removable barriers.[19] or chemical micropatterning and photochemical initiation.[20,21] An important difference in migration from small circular cell patterns is the fact that the total number of initial cells is countable in contrast to the unmanageably high cell numbers of most migration assays. In order

to compare spreading experiments with theory, a small system with a countable number of cells is convenient.

In this article, we investigate collective cell migration from micro-cell-patches consisting of a small number of Madin-Darby canine kidney (MDCK) cells (typically 5-23). Using a lift-off method, we create in the order of 20 to 50 disk-like proliferating cell patches in a parallelized assay. For each patch we measure the total cell area and the total number of cells as a function of time using time-lapse microscopy. This method allows the generation of precisely circularly shaped cell populations with controllable cell densities. We find exponential growth in the number of cells, while the cell density exhibits a universal relaxation behavior with a relaxation time close to the doubling time. Furthermore, we study the center-of-mass motion of cell patches, which exhibits bursts of directed motion.

2. Materials and Methods

2.1. *Preparation of PEG-DMA structures*

3-D microstructures were fabricated based on the micromolding in capillaries (MIMIC) method reported by Shim *et al.*[22] The master is prepared by conventional soft lithography protocols. Polydimethylsiloxane (PDMS) preploymer solution is mixed carefully with the crosslinker in a 10:1 ratio (w/w) (Sylgard 184, Dow Corning, USA) and degassed under vacuum for 15 min. After deposition on top of the master, the whole device is again exposed to vacuum and subsequently cured at 70°C for 4 hours. The resulting PDMS stamp is peeled off the master and cut at the end of the structures forming a network with open ends. Then, it is activated by argon plasma (Diener Electronic, Nagold, Germany) for 30s, the structures facing upwards. Accordingly, the PDMS mold is placed upside down in close contact with a cell culture dish. A solution of PEG-DMA (MW = 550) containing 2% of the photoinitiator 2-hydroxy-2-methylpropiophenone (both purchased from Sigma-Aldrich, Germany) is freshly prepared under light protection and a drop is spotted in front of the open ends of the trimmed micromold. The channels are filled spontaneously by capillary action. The prepolymer is cured by the use of the UV-Ozone UVOH 150 LAB (FHR, Ottendorf, Germany) for 10 min. At last the PDMS is peeled off and the resulting structures are placed in a drying oven (Binder GmbH, Tuttlingen, Germany) overnight at 50°C. Samples were sterilized in 80% ethanol for 10 min, washed three times with Phosphate-Buffered Saline (PBS) and used immediately.

2.2. *Initiation of cell spreading by removal of the PEG-DMA layer*

Cells were cultured under normal conditions to the point where confluence is reached. Then the media is taken off except for a thin liquid film that defends the cells from drying out. The PEG-DMA layer is carefully detached using forceps. Following this, the sample is rinsed with cell media or PBS.

2.3. *Cell culture and deposition*

MDCK II cells were grown in Minimum Essential Medium supplemented with 10% fetal bovine serum (FBS) and 10 mM L-Glutamine at 37°C in a humidified atmosphere, 5% CO_2 level. Cells were grown to confluence, trypsinized and centrifuged at 1000 rpm for 3 min. The cell pellet was resuspended in cell medium and cells were seeded on top of freshly prepared PEG-DMA structures.

2.4. *Microscopy*

Optical and fluorescence images were obtained by using an epifluorescence motorized Nikon Eclipse Ti microscope equipped with a temperature-controlled mounting frame and a CCD CoolSNAP HQ monochrome camera. Acquisitions were controlled through μ-Manager open source software. For living cell image acquisition, temperature is controlled by an ibidi heating stage (ibidi GmbH, Martinsried, Germany) to 37°C. Cells were grown in CO_2 independent Leibovitz's L15 cell culture medium, supplemented with 10% FBS. The time interval for time lapse acquisition was 10 min.

2.5. *Image analysis*

The contours of cell patches as observed in brightfield microscopy are discerned by tracing the outlines with ImageJ software.[23] Coordinates were transferred to Matlab (MathWorks) and time resolved area dynamics were calculated using custom scripts.

2.6. *PIV analysis*

The velocity field of the patches was mapped by PIV analysis using the MatPIV software package[24] for Matlab (MathWorks Inc.).[25,26] The time delay between analyzed images was 10 min. The windows shifting technique was used, starting off with 64×64 large images and ending with 16×16 after 3 iterations. The overlap of the interrogation region was 50%.

3. Results

3.1. *Spreading epithelia cell patches: Area and cell density evolution*

Microstructured PEG-DMA surfaces were fabricated to create stencils that allow the release of many equally sized cell patches at the same time. The PEG-DMA structures are directly formed on top of petri dishes by micromolding into capillaries (MIMIC) using a PDMS stamp as template. After curing the polymer and removing the PDMS stamp, we obtain a cell repellent 3-D structured surface as shown in Fig. 1(a) (see also the Materials and Methods section). Cells are seeded out to grow in the adhesive areas, while non-adherent cells on the pegylated areas are rinsed off.

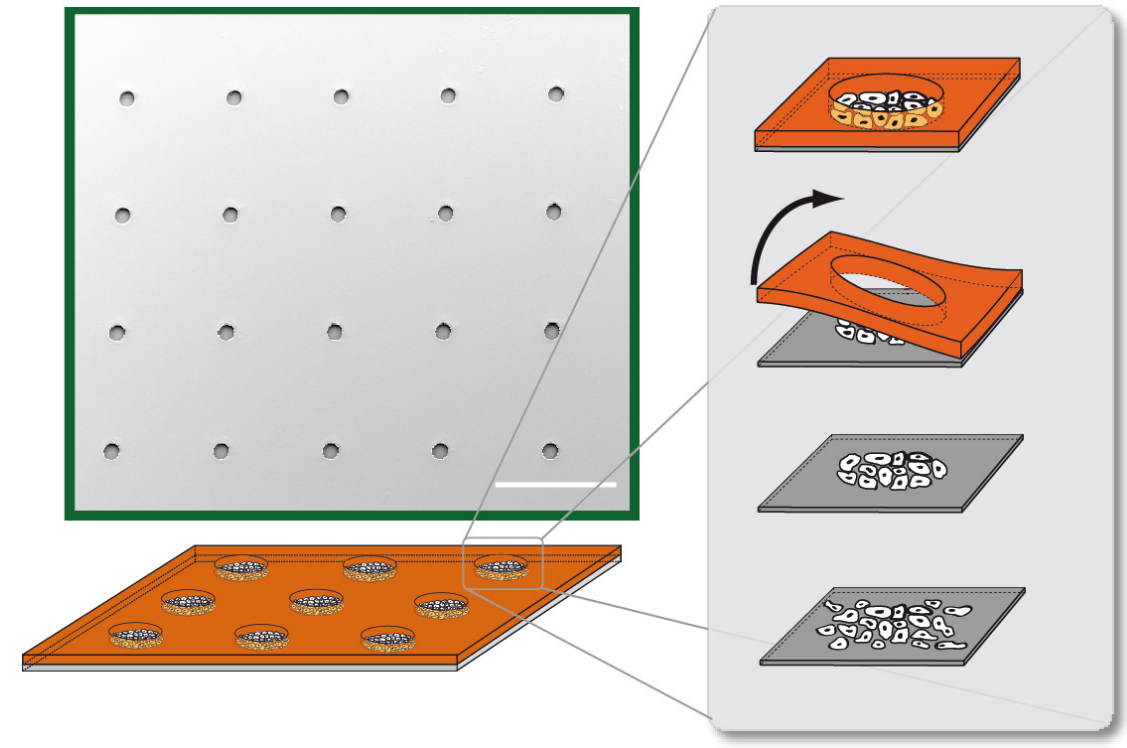

(a)

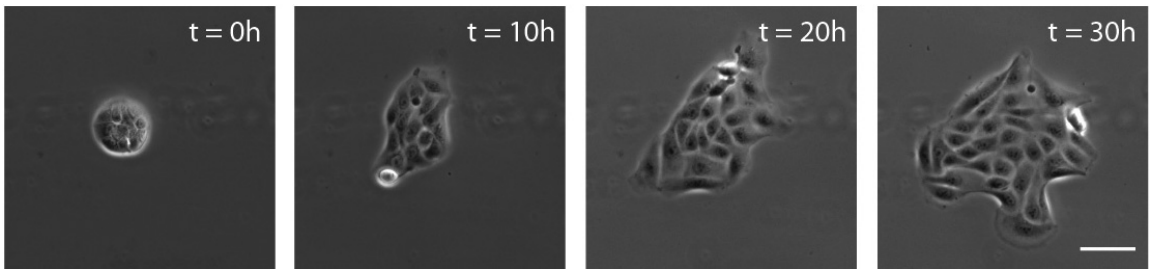

(b)

Fig. 1. (a) A schematic diagram for the removal of the PEG-DMA structures. After cell seeding and culture up to the desired cell density, the PEG-DMA layer can be removed mechanically. The emerging cell pattern has a well defined contour. Several experiments can be carried out in parallel due to the array character of the system (see image from scanning electron microscopy, green box. Scale bar corresponds to 500 μm). (b) Time evolution of a released cell population (scale bar corresponds to 100 μm).

The culture is grown to confluence in the confined PEG-DMA free areas. Typically 24 hours after cell deposition, the migration experiment is initiated by removal of the PEG-DMA layer. This time point is defined as the starting time point, t_0. The growth of the released cell patches is monitored by time-lapse microscopy taking images every 10 min up to a maximum of 68 hours (Fig. 1(b)). Observation time was determined once the cells come into contact with neighboring cell patches or drop out of the cameras field of view. The resulting brightfield images are analyzed

by ImageJ open software[23] measuring the absolute area, cell number and contour of the cell patches. Note that the initial number of cells per patch varies due to the random seeding process. The cell groups contain between 5 and 23 cells when they are released and start to proliferate. We measured the evolution of the cell number in 18 patches as shown in Fig. 2(a). The linear increase in the logarithmic representation confirms the well-known exponential growth

$$N(t) = N_0 \cdot e^{\lambda t}, \tag{1}$$

with an average growth rate $\lambda = 0.032 \pm 0.004\,\mathrm{h}^{-1}$ corresponding to a doubling time $t_D = 21.5 \pm 2.6\,\mathrm{h}$, in good agreement with literature values.[27] Note that there are no systematic deviations as a function of the initial cell number, N_0, which is encoded in the gray scale of the traces. Dark traces correspond to high starting cell numbers, bright traces to smaller ones.

Next, we analyze the evolution of the area of the cellular patches, which is shown in Fig. 2(b). Here we observe a small but systematic deviation from exponential growth in the early phase of migration. The deviation is more pronounced for cell patches with higher initial cell numbers than for small cell number patches as seen in Fig. 2(b). An obvious explanation is the assumption that the area per cell, $a(t) = A(t)/N(t)$, is not constant over time. We assume that cells at high cell density in a confined geometry are more compressed than cells at low number density. When the physical boundaries are removed cell patches will partly expand by viscoelastic relaxation. We use an exponential ansatz to describe the area dilation per cell, $a(t)$, assuming a single relaxation time τ_r,

$$a(t) = a_\infty - \Delta a \cdot e^{-t/\tau_r}, \tag{2}$$

where a_∞ is the longtime average area per cell and Δa describes the difference between a_∞ and the initial area per cell a_0. The model assumes that every cell has the same area. It is clear, however, that cell-to-cell variability exists in multicellular systems. Figure 3 shows the distribution of single cell areas. At time zero, directly after the removal of the PEG-DMA layer, the distribution for the patches is very narrow. Over time a shift to higher areas and a broadening of the distribution is observed. It is difficult to obtain a compelling statistic since the system studied here consists of only a small number of cells, but the observed systematic trend in the distribution supports our assumption of a well-defined average cell area.

We now reconsider the time evolution of the total area of the proliferating cell patches. Since both the area per cell and the cell number change with time, we obtain:

$$A(t) = [a_0 + \Delta a \cdot (1 - e^{\frac{-t}{\tau_r}})] \cdot N_0 \cdot e^{\lambda t}. \tag{3}$$

Equation (3) should describe the area expansion correctly, if the passive viscoelastic expansion is independent from cell growth based on cell division. Figure 2(c) shows the logarithmic curve of $A(t)$ divided through $a(t)$ and the

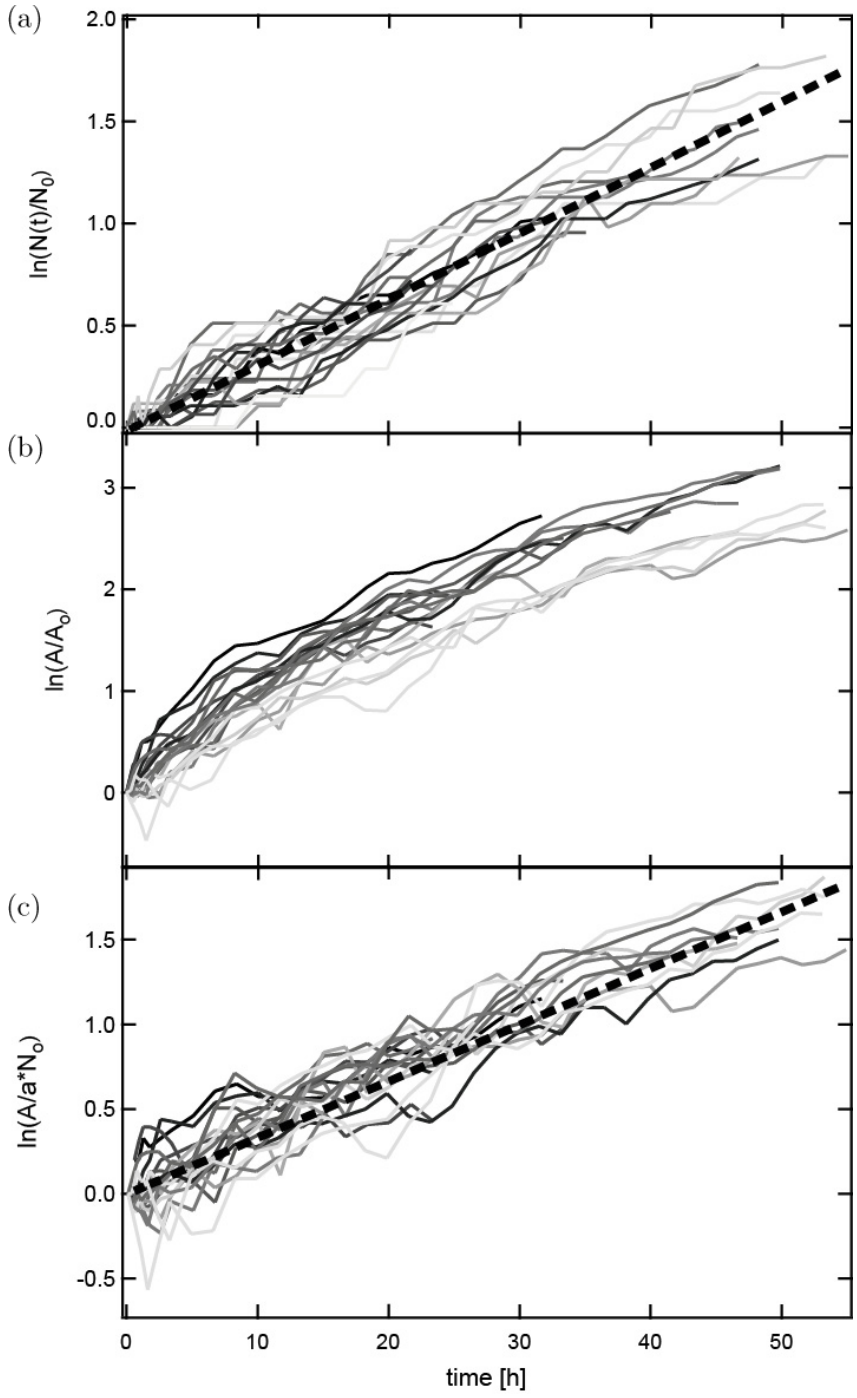

Fig. 2. Cell growth behavior for small cell colonies from 5 to 23 cells. (a) Time evolution of cell number on a logarithmic scale. An exponential cell growth with a calculated doubling time $t_d = 21.5 \pm 2.6\,\mathrm{h}$ is observed. (b) The area dilation shows a non-exponential time curve mainly in the first 10 hours. High starting cell numbers show a stronger slope in the beginning than smaller ones. This can be explained by more intense viscoelastic compression due to high cell densities. (c) Corrected time course of area evolution by dividing the total patch area through $a(t)$ times the initial cell number. A doubling time of $t_d = 20.8 \pm 3.8\,\mathrm{h}$ is calculated. Bright traces correspond to small cell numbers, dark traces to higher ones. The average slope of linear fits is monitored by the dashed line (for colored graph see online version).

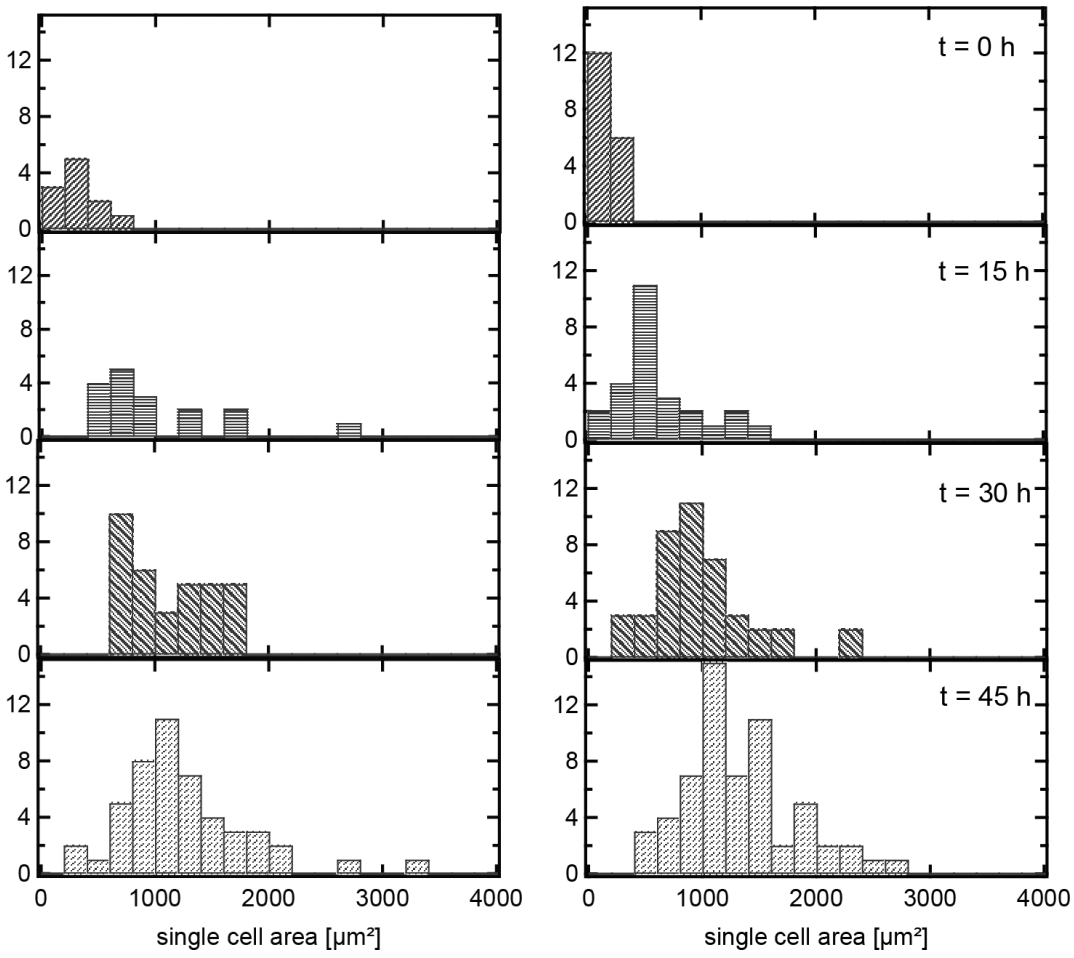

Fig. 3. Evolution of the distribution of single cell areas over time. The data are taken from patches with different starting cell numbers ((a) 11 cells and (b) 18 cells). The histograms show a shift and broadening of the distributions with time.

accordant initial cell number. The exponential growth of the patches is clearly distinguishable. We fitted the traces linearly and take the mean of the slopes (indicated by the dashed line in Fig. 2(c)). The calculated doubling time $t_D = 20.8 \pm 3.8\,\mathrm{h}$ is again in the same range as indicated in literature.

Since the area per cell changes over time, the connected relaxation time of the whole system can be determined by studying the time course of cell density as shown in Fig. 4. The squeezed cell populations expand due to viscoelastic relaxation to a mean value of the area per cell of $a_\infty = 1903 \pm 155\,\mu\mathrm{m}^2$. The calculated relaxation time from the averaged density curve is $\tau_R = 25.7 \pm 14\,\mathrm{h}$ and hence is of the same order as the cell doubling time. Moreover, we find that the relaxation time is independent from the initial cell density (see insert of Fig. 4).

As seen in Fig. 5, we find a heterogeneous evolution of contours ranging from a nearly symmetric expansion growth to an evolution with an apparently preferred direction. In order to obtain more information about the motion of the cell groups we

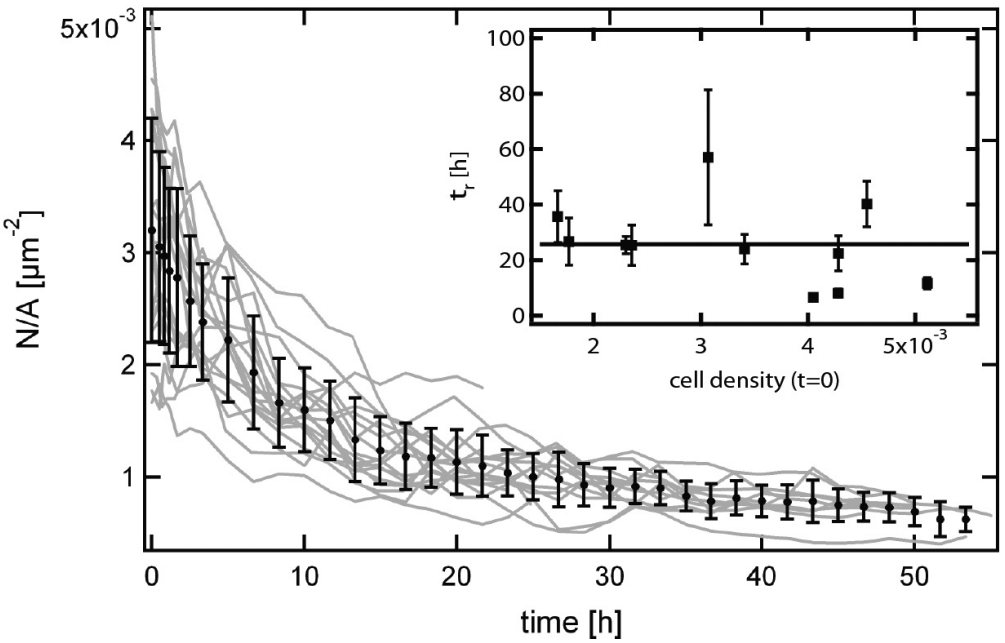

Fig. 4. Time dependant course of cell densities. The relaxation time τ_r and the mean value of the area per cell for the relaxed state of the patch a_∞ can be calculated as fit parameters. Gray traces correspond to experimental data; the averaged values are monitored in black dots. Fit parameters are estimated to be $\tau_r = 25.7 \pm 14\,\mathrm{h}$ and $a_\infty = 1903.1 \pm 155 \mu\mathrm{m}^2$. The insert show the calculated relaxation time for single traces. The relaxation is independent from the initial cell density.

analyze the center-of-mass movement (Fig. 6). The exemplary trace of the centroid (Fig. 6(a)) shows periods of long distance motion as well as phases where the centroid stays roughly stationary. This behavior can also be followed by plotting the squared displacement against time (Fig. 6(c)). The patches that exhibit a strong shift of the center-of-mass start to migrate 5 hours after removal of the PEG-DMA layer and the last movement ends 27 hours later. In this time range these cohorts consist of 9 to 30 cells with a cell density of 0.0006 to 0.00115 cells per $\mu\mathrm{m}^2$. With increasing mass, the colonies seem to stabilize and the center-of-mass motion is restricted.

The question arises what kind of movement drives small cell populations. Is it a long-range correlated collective motion where all cells in the patch move in the same direction or is the patch movement the sum of many statistically independent cell movements? We analyzed different patches with huge centroid displacements at the time of the longest drift by Particle Image Velocitmetry (PIV). Only in rare cases do we find a correlated motion of neighboring cells that would correspond to homogenous viscoelastic relaxation. There is strong evidence for active dynamics of the cellular motion within the patches (Fig. 6(b)). It appears that multiple transient leader cells emerge at the rim of the patch and act in opposite directions in our small system. The leader cells are characterized by a fully spread out morphology with an active ruffling lamellipodium at the front side as described in literature.[11,28,29] In our experiments, in contrast to collectively migrating epithelial cell fronts in

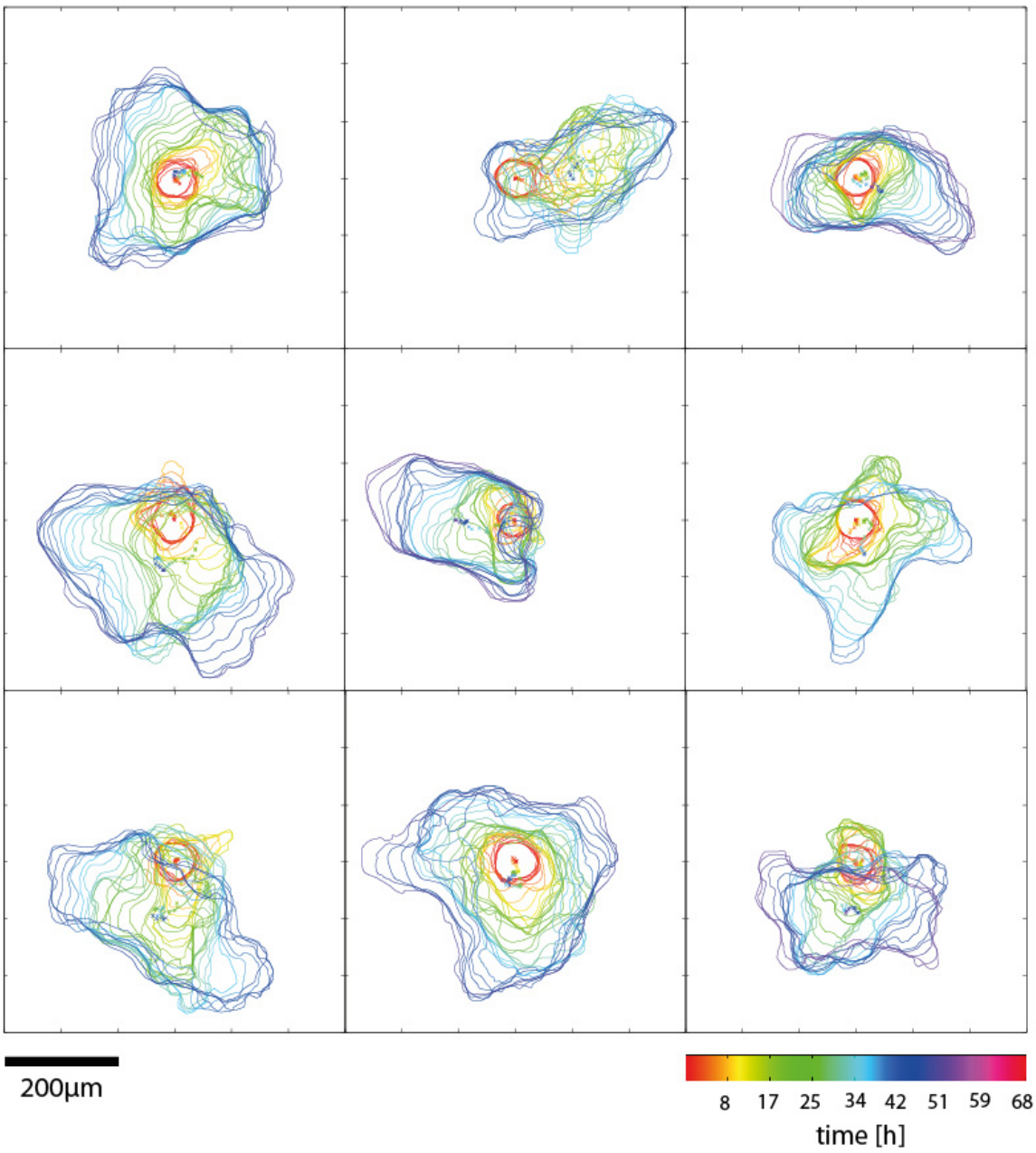

Fig. 5. The evolution of exemplary cell patch contours. Growth behavior with almost stable center-of-mass is observed as well as asymmetric growth with a distinct centroid movement.

large epithelia layers, no fully extended fingers are developed. Yet the leader cells are found to be followed by neighboring cells over short distance. Secondly, while in migrating cell sheet fronts leader cells and finger formation occurs in the same direction even towards the released surface and perpendicular to the sheet, here in small circular cell groups cells strive in all directions. In fact, leader cells emerge all around the patch border and often several (in some cases up to four) active leader cells are seen at the same time. Figure 7 shows exemplary contours with marked leader cells. Each of the leader cells seeks to migrate perpendicular to

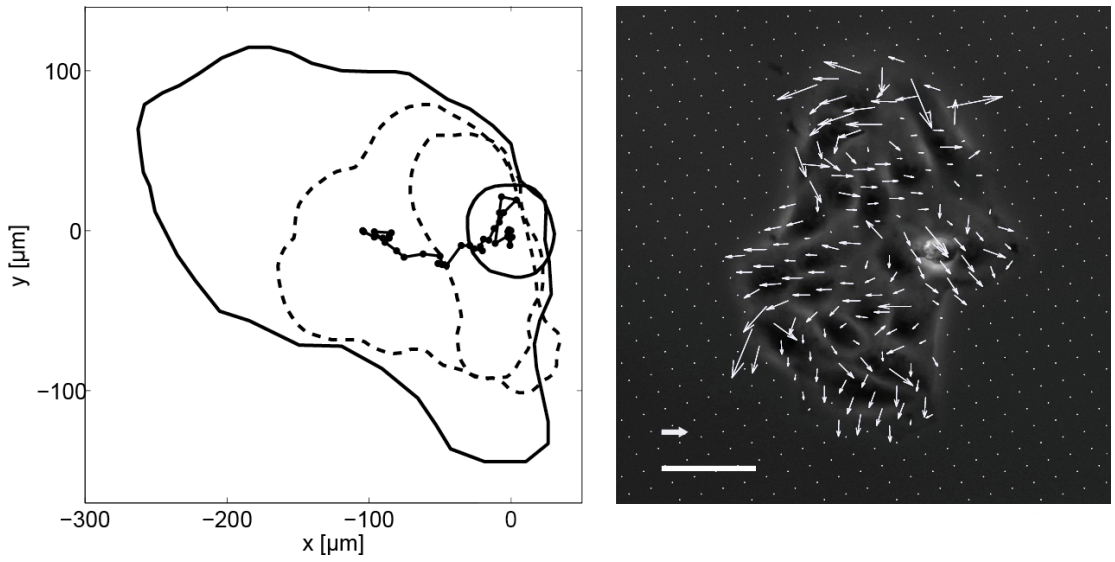

(a) (b)

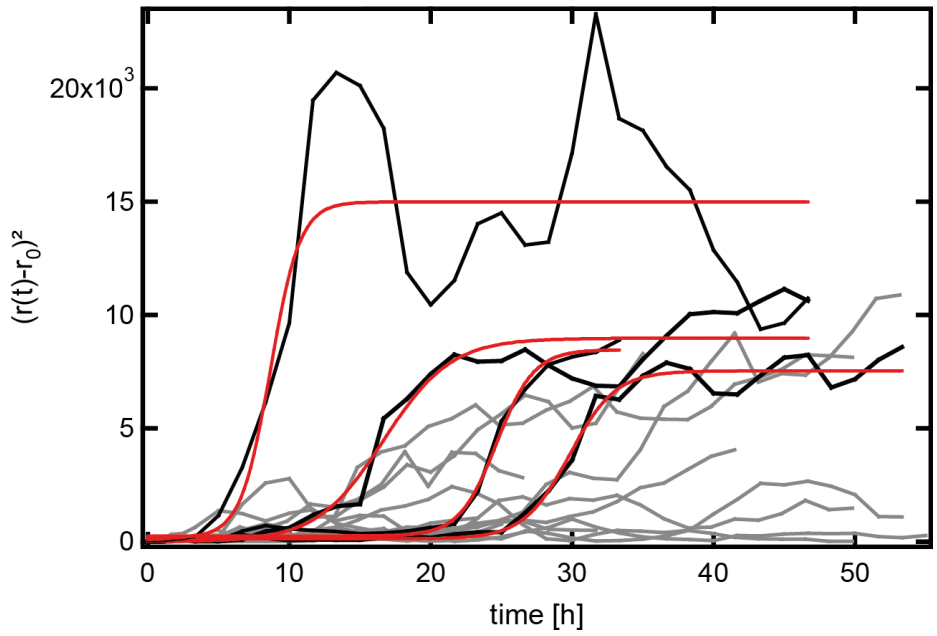

(c)

Fig. 6. Center-of-mass displacement during cell migration. (a) The trace of the centroid shows temporary broad shifts and periods of nearly stationary fluctuations. (b) Velocity field measurements indicate short-range correlation from the leader cells to the rows behind (scale bar, 50 μm, arrow 1 $\mu\text{m} \cdot \text{h}^{-1}$). (c) Following the squared displacement of the centroid over time, distinct changes can be monitored due to jumps in the curve over 3 to 5 time points.

the cell interface hence pull on the patch in opposing directions, a scenario that resembles a tug-of-war of leader cells in two dimensions. Since leader cells have a limited lifetime the observed fluctuations in the center-of-mass motion is a result of the competition of opposing leader cells showing no preferred direction over longer time periods.

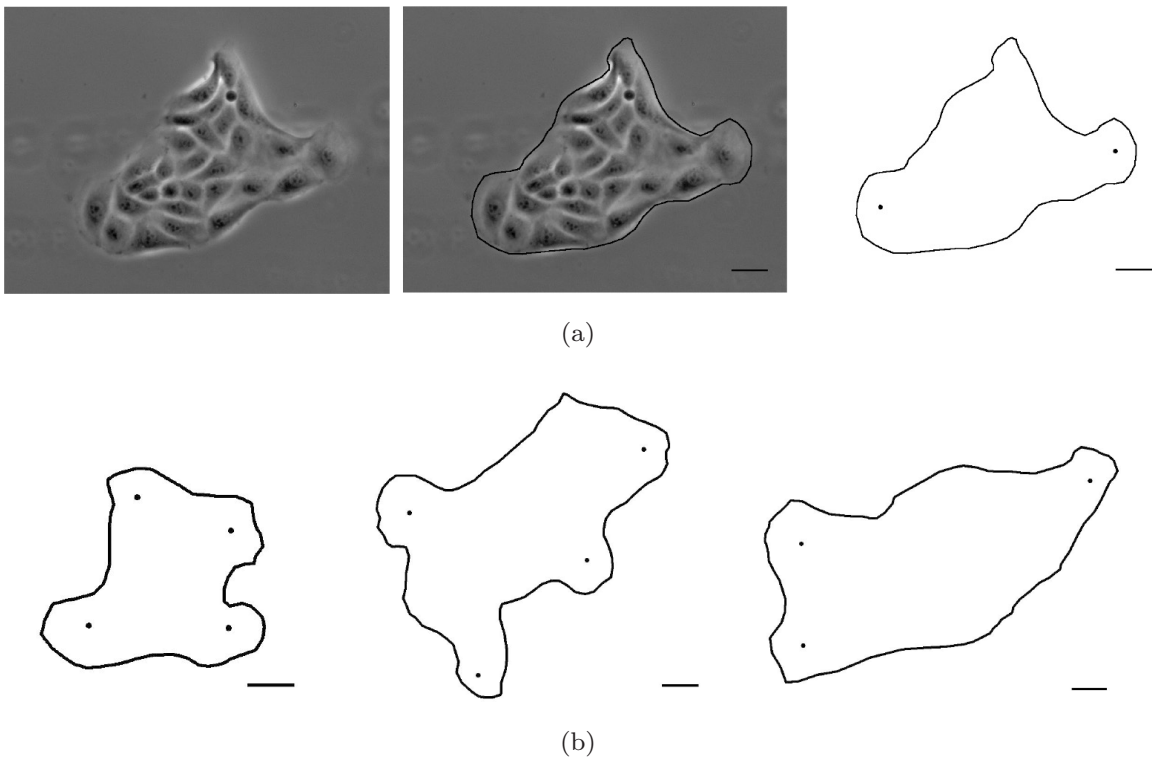

Fig. 7. (a) Active leader cells as well as the patch outline are marked in the brightfield image. (b) Exemplary contours with leader cells from different cell colonies at different times (scale bar corresponds to 50 μm).

An alternative scenario for center-of-mass displacement is motion purely based on cell division and relaxation. For small cell numbers the area reduction of a single cell in the mitotic phase can lead to a shift of the center-of-mass of the entire cell patch. Such events can be found at early stages of the experiment. With increasing patch size, however, the impact of such events should be averaged out statistically. Hence it appears that cell division contributes to the center-of-mass fluctuations but the dominating mechanism behind the observed abrupt patch displacements are clearly linked to the role of leader cells.

4. Conclusion

In this article, we used a lift-off technique to create small disk-like cell patches and investigated the area evolution of the patches as cells proliferated. We showed that the data fall onto a universal curve, if elastic area dilation and cell division are combined. The key finding is that the area relaxation time is independent from the initial cell density and is of the same order as the doubling time. The relaxation of tissues has been discussed intensively.[2,5,30,31] Farhadifar *et al.* perform laser ablation experiments where they cut boundaries between two cells. The observed local relaxation time was in the order of seconds. This technique was also used to study tension forces of the actin cytoskeleton of single cells.[31] In a recent theoretical study, Ranft *et al.* investigated the dynamics of multicellular tissue based on the

assumption that tissue remodeling occurs by cell division and apoptosis. One of the main findings was that tissue effectively behaves like a viscoelastic fluid with the relaxation time set by the rates of cell division and apoptosis. Our data report to our knowledge for the first time on experiments measuring the viscoelastic relaxation of a two-dimensional cell patch. Hence it is noteworthy that the relaxation time found in the experiment is of the same order as the cell doubling time as predicted. We also described the center-of-mass motion and the morphology of the cell patches. We interpret the distinct bursts in the centroid displacements as a result of a tug-of-war mechanism of opposing leader cells. This hypothesis needs further investigation but seems reasonable within the current understanding of cell behavior at the border of migrating epithelia cells.

From a technical point of view, our lift-off method is a stencil-based assay as introduced by Poujade *et al.*[6,11] However, using the particular PEG-DMA chemistry we can create very small cell groups that can be released from the confinement without damage of the border cells. The method provides excellent spatial control and allows the preparation of structures smaller that $10\,\mu$m. In general, defined initial cell states as for migration studies can be created by means of artificial microenvironments. For quantitative studies and modeling of tissue it is important that migration studies are rendered reproducible and quantifiable. Furthermore microstructured surfaces can not only be used to set the initial time of cell migration but also be used to confine the cell migration itself aiming to scrutinize the complex flow behavior of cell growth.

Acknowledgments

We would like to thank Susanne Rappl for technical help in the master fabrication. Financial support by the Excellence Cluster 'Nanosystems Initiative Munich (NIM)' and the Center for NanoScience (CeNS) is gratefully acknowledged.

References

1. G. Forgacs, R. Foty, Y. Shafrir and M. Steinberg, *Biophysical Journal* **74**, 2227 (1998).
2. J. Ranft, M. Basan, J. Elgeti, J.-F. Joanny, J. Prost and F. Jülicher, *Proceedings of the National Academy of Sciences of the United States of America* **107**, 3 (2010).
3. K. Guevorkian, M.-J. Colbert, M. Durth, S. Dufour and F. Brochard-Wyart, *Physical Review Letters* **104**, 218101 (2010).
4. T. Hayashi and R. W. Carthew, *Nature* **431**, 647 (2004).
5. R. Farhadifar, J.-C. Röper, B. Aigouy, S. Eaton, F. Jülicher and J.-Christian Ro, *Current Biology* **17**, 2095 (2007).
6. L. Petitjean, M. Reffay, E. Grasland-Mongrain, M. Poujade, B. Ladoux, A. Buguin and P. Silberzan, *Biophysical Journal* **98**, 1790 (2010).
7. T. E. Angelini, E. Hannezo, X. Trepat, M. Marquez, J. J. Fredberg and D. A. Weitz, *Proceedings of the National Academy of Sciences of the United States of America* 1 (2011).
8. X. Trepat, M. R. Wasserman, T. E. Angelini, E. Millet, D. A. Weitz, J. P. Butler and J. J. Fredberg, *Nature Physics* **5**, 426 (2009).

9. T. E. Angelini, E. Hannezo, X. Trepat, J. J. Fredberg and D. A. Weitz, *Physical Review Letters* **104**, 1 (2010).
10. P. Rørth, *Annual Review of Cell and Developmental Biology* **25**, 407 (2009).
11. M. Poujade, E. Grasland-Mongrain, A. Hertzog, J. Jouanneau, P. Chavrier, B. Ladoux, A. Buguin and P. Silberzan, *Proceedings of the National Academy of Sciences of the United States of America* **104**, 15988 (2007).
12. M. Reffay, L. Petitjean, S. Coscoy, E. Grasland-Mongrain, F. Amblard, A. Buguin and P. Silberzan, *Biophysical Journal* **100**, 2566 (2011).
13. C.-C. Liang, A. Y. Park and J.-L. Guan, *Nature Protocols* **2**, 329 (2007).
14. D. Falconnet, G. Csucs, H. M. Grandin and M. Textor, *Biomaterials* **27**, 3044 (2006).
15. D. B. Weibel, W. R. Diluzio and G. M. Whitesides, *Nature Reviews Microbiology* **5**, 209 (2007).
16. G. Kumar, B. Chen, C. C. Co and C.-C. Ho, *Experimental Cell Research* **317**, 1340 (2011).
17. A. Folch, B. H. Jo, O. Hurtado, D. J. Beebe and M. Toner, *Journal of Biomedical Materials Research* **52**, 346 (2000).
18. E. Ostuni, R. Kane, C. S. Chen, D. E. Ingber and G. M. Whitesides, *Langmuir* **16**, 7811 (2000).
19. M. Huergo, M. Pasquale, A. Bolzán, A. Arvia and P. González, *Physical Review E* **82**, 1 (2010).
20. J. Fink, M. Théry, A. Azioune, R. Dupont, F. Chatelain, M. Bornens and M. Piel, *Lab on a Chip* **7**, 672 (2007).
21. Y. Kikuchi, J. Nakanishi, H. Nakayama, T. Shimizu, Y. Yoshino, K. Yamaguchi, Y. Yoshida and Y. Horiike, *Chemistry Letters* **37**, 1062 (2008).
22. H.-W. Shim, J.-H. Lee, T.-S. Hwang, Y. W. Rhee, Y. M. Bae, J. S. Choi, J. Han and C.-S. Lee, *Biosensors & Bioelectronics* **22**, 3188 (2007).
23. W. S. Rasband, http://rsbweb.nih.gov/ij/ (2008).
24. J. K. Sveen, MatPIV available at http://folk.uio.no/jks/matpiv/ (2006).
25. M. Raffel, C. E. Willert, S. T. Wereley, J. Kompenhans, C. Willert, S. Wereley, W. Merzkirch, D. Rockwell and C. Tropea, *Particle Image Velocimetry* (Springer Berlin Heidelberg, Berlin, Heidelberg, 2007), pp. 97–121.
26. R. J. Adrian, *Experiments in Fluids* **39**, 159 (2005).
27. ATTC at http://www.lgcstandards-atcc.org/
28. H. Haga, C. Irahara, R. Kobayashi, T. Nakagaki and K. Kawabata, *Biophysical Journal* **88**, 2250 (2005).
29. T. Omelchenko, J. M. Vasiliev, I. M. Gelfand, H. H. Feder and E. M. Bonder, *Proceedings of the National Academy of Sciences of the United States of America* **100**, 10788 (2003).
30. M. Bock, A. K. Tyagi, J.-U. Kreft and W. Alt, *Bulletin of Mathematical Biology* **72**, 1696 (2010).
31. S. Kumar, I. Z. Maxwell, A. Heisterkamp, T. R. Polte, T. P. Lele, M. Salanga, E. Mazur and D. E. Ingber, *Biophysical Journal* **90**, 3762 (2006).

5 Guided Collective Cell Migration in Channels

Although tissues consist of connected cell assemblies, they are highly dynamic, with regulated processes such as cell division and death as well as cell rearrangement fundamental to maintaining the tissue's function. Cells can migrate within the tissue showing correlated movements. Single-layer cell sheets like they occur naturally for epithelial tissues, are suitable model systems to study collective dynamics *in vitro*. A prime example, the canine, epithelial Madin-Darby Canine Kidney (MDCK) cell line, is prevalent in literature for biophysical questions [47, 101, 129]. The most commonly used approach to induce collective cell migration is the generation of an artificial wound within the cell layer. Formerly, cells were physically removed from the confluent monolayer by scratching with, for instance, a pipette tip [63, 66], razor blade [104] or Teflon spatula [20], whereas, nowadays alternative physical, chemical, electrical or optical methods for introducing model wounds have been developed [97]. Here, some of the methods even allow the creation of new cell-free regions without injuring the border cells of the confluent layer [69, 80]. In all cases, cell migration and proliferation is triggered by the free surface and cells spontaneously start to close the formed gap. The dynamics of cell movements and interactions can be followed by time-lapse microscopy, however, a subsequent analysis of the obtained image material is required. A recently introduced method to map collective cell motion by visualizing the emerging velocity field is particle image velocimetry (PIV) [4, 85, 89, 95, 131]. Originally stemming from the analysis of hydrodynamics, PIV is a simple technique based on the cross-correlation of successive images divided into small interrogation windows. All visible features of typically brightfield images are assessed and the overall motion of the migrating sheet is described, however, no information about individual cell displacement is obtained. Another aspect of collective cell migration, in particular in wound healing assays, is the spatiotemporal displacement of the cell front. In general, the expansion of the cell layer is driven by both active cell motion and proliferation that leads to growing cell mass. The two components are included in the standard continuum model based on the Fisher-Kolmogorov equation (see eq. 5.4). In this equation, the expansion of a cell population is described by a combination of random cell motion (expressed as a diffusion coefficient) and logistic growth. Predicted solutions include traveling wave solutions of constant shape and speed meaning that the propagation cell front takes the form of a traveling wave.

The velocity of the cell front is determined by a combination of the diffusion coefficient and the growth rate of the cell population. The model was used to estimate the diffusive behavior of cells within a monolayer assuming that the Fisher-Kolmogorov equation is valid for cellular systems since continuous front displacement was experimentally observed [65, 109, 110]. An independent determination of the diffusivity parameter, however, is missing in these cases. Although the collective diffusion of cells is still hard to extract from experimental findings, single cell motion can be directly addressed by individual cell tracking. The cell trajectories can be analyzed in terms of their mean square displacement (MSD) and the single cell diffusion can be calculated according to the linear relation between diffusion coefficient and MSD (see eq.5.6) [122]. The mean square displacement $\langle r^2 \rangle$ describes the mean of the squared distances between the position of the cell at times t_0 and it's actual position at time t:

$$\langle r^2 \rangle = \left\langle [x\,(t+t_0) - x(t_0)]^2 + [y\,(t+t_0) - y(t_0)]^2 \right\rangle \tag{5.1}$$

where $\langle ... \rangle$ indicates a combined average over all starting times t_0 and cell trajectories. The linear relation between MSD and diffusion coefficient can only applied to scenarios of normal diffusion. Further information about cell migration within a confluent cell layer is gained by correlating adjacent individual cell traces [122, 130, 133]. By means of this, coupled motion of cell groups and their persistence according to direction and velocity correlations were documented. Collective cell motion within an expanding cell population, however, is subject to changing conditions. Cell proliferation lead to increasing cell density and therefore affects the properties of the cell sheet. Naturally, cell proliferation is inhibited when a maximal cell density is reached leading over into the state of homeostasis. This process is also known as 'contact inhibition'. With increasing cell density, the average migration speed has been shown to decrease and diffusive motion is reduced [5]. The individual cell shape fluctuates at low densities and becomes stable towards a rounded shape with increasing cell density, which influences the correlation length of coordinated motion [4]. Increasing cell density is a direct result of regular cell division events. The division axis and therefore the positioning of the daughter cells are influenced by cell shape, cell polarity and the spatial distribution of the extracellular matrix [74, 96, 124, 125].

Still, it is a great challenge to develop mechanical models that consider the described and highly dynamic properties of cell assemblies. This includes cell-cell interaction leading to collective migration or diffusive motion, cell proliferation and density changes having to be taken into account as well as cell-substrate interactions that guide cell migration and even the orientation of cell division. Usually, the models focus on one particular point in cell mechanics, describing cell sheets as vertex model [27] or in a particle based approach [8] among others.

Although multiple tools for analyzing and controlling collective cell motion have been investigated, the underlying mechanisms are less understood. The question concerning the driving

forces of directed motion are not trivially to answer. In their review, Trepat *et al.* discussed the cellular interaction and force transmission in collective cell migration [127]. They conclude that cells tends to migrate in the direction of the smallest shear stress which is identical to the greatest normal stress according to a phenomenon called plithotaxis [123]. Cell are able to generate long-range gradients of intercellular tension, transmitting forces through cellular junctions. The mechanical connectivity is required for plithotaxis which for this reason is an emergent property of the cell group. Another scenario at a macroscopic level may consider cells as particles diffusing along developed density gradients. How can cells sense such gradients mechanically, only interacting with adjacent neighbors?
In the first manuscript [M1] attached to this chapter, we investigated the flow behavior of growing cell sheets by confining the cell layer in three-dimensional PEG-DMA mircochannels. The direction of expansion was restricted by the barriers, creating a flow field along the channel. By focusing on diffusion behavior at single cell and collective level, respectively, we explored the fluid-like properties of the cell layer, probing the applicability of the traveling wave model for our system. In a second manuscript [M2], we analyzed the influence of the emerging flow field on the orientation of cell divisions, comparing our results with the predictions of a model working with a particle based approach.

The MDCK cell line is a model system for collective cell migration

The Madin-Darby Canine Kidney (MDCK) cell line was isolated in 1958 from the kidney of an apparently normal adult female cocker spaniel by S.H. Madin and N.B. Darby. The cells grow in a continuous monolayer with an average cell area of 180 μm^2 and 6-10 μm height at confluent level [7, 135]. They form a polarized epithelium and exhibit tight cell junctions as well as strong adhesion to the substrate. Cell division is usually within the epithelial plane and both daughter cells remain within the monolayer [96]. The doubling time of MDCK cells is documented to be approximately 22 hours [6].
Since MDCK cells migrate and grow as connective tissue that is strictly organized in a monolayer, the tissue forms an attractive model system to study fundamental processes of cell motion. In particular, the mechanical aspects of collective cell migration have been examined in experiments with MDCK cells [89, 92, 95, 131].

Collective cell motion is assessed by particle image velocimetry (PIV)

Particle image velocimetry (PIV) is a pattern matching method that allows the quantitative measurement of velocity vectors from the displacement of particles. Originally, PIV was developed to study the characteristics of turbulent flow [2]. Turbulence takes place on a wide range of physical scales and occurs randomly even at high velocities. A feasible technique has to deal with these features, and PIV was optimized to rise to this challenge. The standard and basic PIV system uses a pulsed laser to illuminate particles in the micron range that

have been seeded with uniform density. Images are usually recorded by interline-transfer PIV video cameras. For evaluation, images are divided into interrogation windows, typically with a certain overlap. By cross-correlating successive images, the displacement field of particles is obtained. Velocity fields are calculated by including information about frame rate and image scale (see Fig.5.1). PIV analysis is still a routine technique used in hydrodynamics. Recently, PIV has been used in biological contexts such as mapping the coordinated motions of bacteria [24] or detection of pulling forces during invasion of single cells in three dimensional environments [88]. A further newly formed application is the analysis of migrating cell sheets. Poujade *et al.* showed that collective cell motion can be followed by PIV analysis. They used brightfield images of a connected MDCK layer and were able to extract the local velocity field solely by the contrast of the intracellular textures. The additional use of tracer particles was not required, however, information about individual cell movement cannot be obtained by the PIV method.

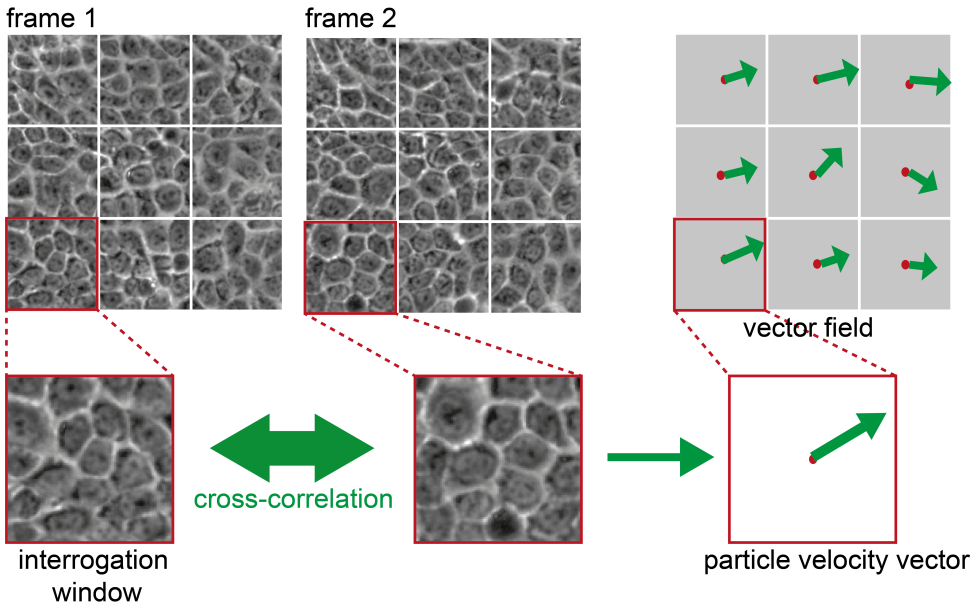

Figure 5.1: Velocity fields are obtained by particle image velocimetry (PIV) analysis. *The frames are divided into interrogation windows. Conspicuous structures are cross-correlated to the following frame and combined in an average vector. By specifying frame rate and scale, a velocity field is created over the whole frame. (The time interval between the shown brightfield images is larger than the typically used 10 min in order to clarify the principle of the method.)*

Fick's law describes mass transport along concentration gradients

Fick's first law is the linear relation between diffusive flux and a concentration gradient for steady state conditions and was introduced in 1855 by Adolf Fick [28]. The term "gradient" specifies the spatial variation of the concentration field and the equation postulates a flux going from areas of high concentration to areas of low concentration. For one spatial dimension,

Fick's first law is given by:

$$J = -D\frac{\partial c}{\partial x} \tag{5.2}$$

where J is the flux and D the diffusion coefficient. The concentration gradient over the position x is given by $\partial c/\partial x$. The right direction of the particle flux is assured by the minus sign. Flux is, for a two dimensional situation, the number of particles crossing a plane with area A per unit time and can be also expressed by equation 5.3:

$$J = c \cdot v \tag{5.3}$$

where c is the concentration of particles and v the local velocity.

Propagating cell fronts are described by traveling waves

Traveling waves are patterns that move trough an extended elastic medium in an uninterrupted fashion. The wave travels away from a source and transports energy while moving. Traveling wave solutions with a constant shape that moves at constant speed are given for the Fisher-Kolmogorov equation 5.4. This relation was recently used to describe spreading cell fronts [65, 77, 103, 109]. The equation consists of a diffusive term specifying random cell motion and a second part takening logistic growth into account:

$$\frac{dc}{dt} = \underbrace{D\frac{\partial^2 c}{\partial x^2}}_{\text{diffusive component}} + \underbrace{\lambda c\left[1 - \frac{c}{K}\right]}_{\text{logistic growth}} \tag{5.4}$$

where c is the cell density, t is time and x the position. D represents the diffusion term analogous to the diffusion in Fick's law. The growth rate of the cell line is given by λ and K is equal to the maximal cell density that can be reached in homeostasis named carrying-capacity density. The shape and velocity v of the propagating cell front is dependent on the size of K and λ and follows equation 5.5:

$$v = \sqrt{4D\lambda} \tag{5.5}$$

This correlation has been used to determine the cellular diffusion coefficient from experimentally determined growth rates and cell front displacements, however, the obtained diffusion coefficient does not refer to single cell movement but rather gives a sense of collective cell motion.

Mean square displacement (MSD) of single cell migration

The simplest approach to describe single cell migration is to consider the motion as diffusive in the sense of Brownian motion or random walk. The diffusion coefficient D is related to the

mean squared displacement $\langle r^2 \rangle$ in two dimensions by :

$$\langle r^2 \rangle = 4Dt \tag{5.6}$$

Experimentally, the square of the displacement of a particle at successive times t relative to the position of the particle at different times t_0 is monitored. The MSD is then yielded by averaging the squared displacement of many particles.
Cell migration, however, is considered to be biased and shows a certain correlation between successive steps in size and direction. In this particular case of motion named persistence random walk, the persistence time T_p has to be taken into account by relating the MSD to the diffusion coefficient as documented in equation 5.7:

$$\langle r^2 \rangle = 4D \left[t - T_p \left(1 - e^{-t/T_p} \right) \right] \tag{5.7}$$

The persistence time describes the time scale on which the direction of sequent steps is preserved. Hence, for periods much longer than the persistence time, cell motion remains accessible by the simple relation of diffusion and MSD as mentioned in equation 5.6.

The orientation of cell division is determined by the mitotic spindle

Cell division leads to increasing cell number within a tissue and by subsequent cell growth to the expansion of the tissue's volume. During the cell cycle, the DNA is replicated and organized in chromosomes. The duplicated chromosomes are lined up to the spindle microtubules and pulled toward the spindle pole while being separated into two daughter chromosomes. New nuclei are formed and the cytoplasm is divided by a contractile actin ring. Depending on the orientation of the cleavage planes, the tissue can be expanded in a particular direction to create a new form. In epithelial tissue, the orientation of cell division decides if both daughter cells remain within the cell layer or one is pushed outward (see Fig. 5.2) These processes plays an important role during morphogenesis such as placenta formation or uterus preparation for embryo implantation [22]. So far, the position of the mitotic spindle is assumed to determine the orientation of the cell division, since the cytokinesis always takes place transversely to the former spindle axis. Besides chemical signaling systems, the mitotic spindle is predicted to be able to self-organize due to mechanical forces. In 1884, Oscar Hertwig proposed a simple rule, also referred to as the "long axis rule" [45] which was popularized by Edmund Wilson [140]: "The axis of the spindle lies in the longest axis of the protoplasmic mass, and division therefore tends to cut this axis transversely". By following this rule, cells division lead to a reduction of forces associated by emerging distortions within the tissue and a strong alignment of the cell division axis with the local force field [124]. The force field generated during finger formation at the border of a migrating cell sheet is therefore an plausible example for cell division orientation due to mechanical tension [95].

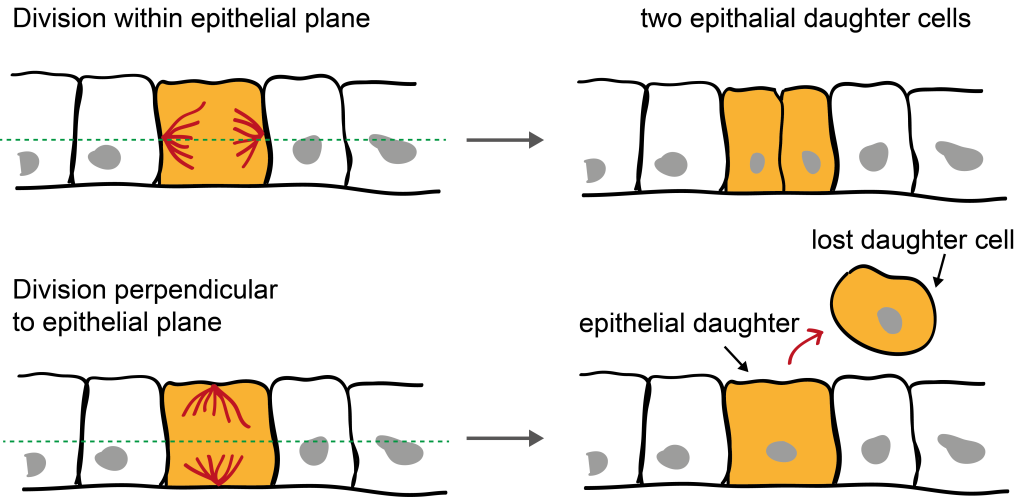

Figure 5.2: The position of the mitotic spindle defines the orientation of cell division. *The cleavage plane can be either in the plane of the epithelium (green dotted line) or perpendicular to the plane. Thus, the position of the mitotic spindle decides if the two daughter cells remain within the epithelium leading to two dimensional growth or one is lost either apically or basally.*

Aspects of tissue behavior are modeled by a mesoscopic particle based approach

The mechanical characteristics of tissue can be modeled by a mesoscopic particle approach. This kind of model is more focused on the meso- and macroscopic dynmaics of tissue, respectively, than on describing single cell processes. In the model, a single cell is represented by two particles interacting via repulsive forces. Cell growth corresponds to the expansion of particle distance due to this repulsion. By a certain threshold in size R_{div}, cell division is introduced and occurs at a rate k_{div}. The two daughter cells are placed at a small distance r_{div} with one occupying the position of the mother particle (see Fig.5.3). Cell death is considered to occur rarely in experiments and hence is set to zero in the simulations. Cell adhesion to the substrate is modeled by a friction force that is proportional to the cell velocity. Cell-cell interaction includes a volume exclusion part preventing two cells from occupying the same position as well as the description of cell-cell adhesion forming a continuous monolayer. Both is expressed by a force that is repulsive at short and attractive at intermediate distances. Long-range friction or fluctuations within the tissue are addressed by dissipative particle dynamics (DPD) that locally conserve momentum. Since cells migrate actively in a certain direction, active motility forces against the substrate are taken into account. The orientation of the motility force is described by a simple stochastic model assuming that cells switch between a motile and a nonmotile state at constant rate k_{mot}. In the motile state, cell are able to exert motility forces in a randomly choosen direction. The rate from the nonmotile to the motile state depends on the orientation of the cell relative to it's velocity and is defined as k^+ when the motility force $\vec{m}$ and the velocity $\vec{v}$ are aligned and k^- when both are antiparallel, where typically $k^- > k^+$.

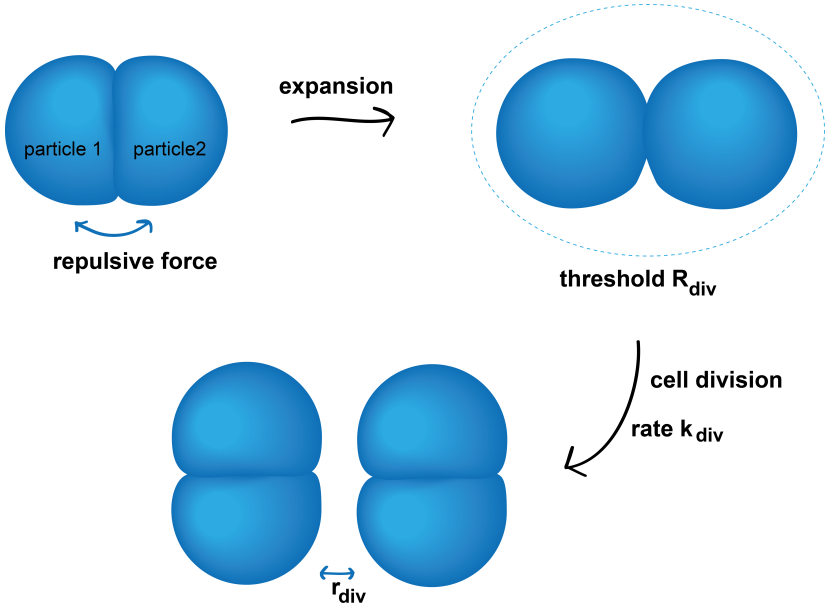

Figure 5.3: Cells are represented by two particles in the mechanical simulation model. *One cell consists of two narrow particles that exhibit repulsive forces between each other, leading to cell growth. By reaching a certain threshold in size R_{div}, cells divide at a rate k_{div}. The two daughter particles are placed at the distance r_{div}.*

5.1 Flow and Diffusion in channel-guided cell migration [M1]

In this work [M1], we deal with the pivotal question of the mechanism underlying directed collective cell migration. In order to gain insights into the process of collective motion, we investigated the flow profile of directed cell sheet expansion and the emergence of large- and short-scale noise. Oriented movement of the cell sheet was achieved by confining the propagating cell front in three-dimensional poly(ethylene glycol)-dimethacrylate (PEG-DMA) channels of different widths (100-300 µm). MDCK cells were seeded in front of the PDMS mold that remains on top of the freshly prepared PEG-DMA microstructures, protecting the channels from cell adhesion. The grown monolayer provided a reservoir of cells with a sharp edge at the PDMS. By removal of the stamp, the channels were opened and the released cell expanded towards the channel entrances. The measurement was started once the cells entered the confinement. Both, brightfield and fluorescence images were taken in a time-lapse microscopy setup. We observed a linear propagation of the leading edge at constant speed, independent of the channel width with an average velocity $v = 22 \pm 5$ µm/h. Simultaneously, a cell density gradient developed along the channel with increasing densities in direction of the bulk. We used stably transfected MDCK cells with fluorescently labeled 2B histones resulting in a bright and sharply defined signal of the cell nucleus. By detecting the nuclei, we determined the local cell density for every time point of the measurement (see Fig. 5.4).

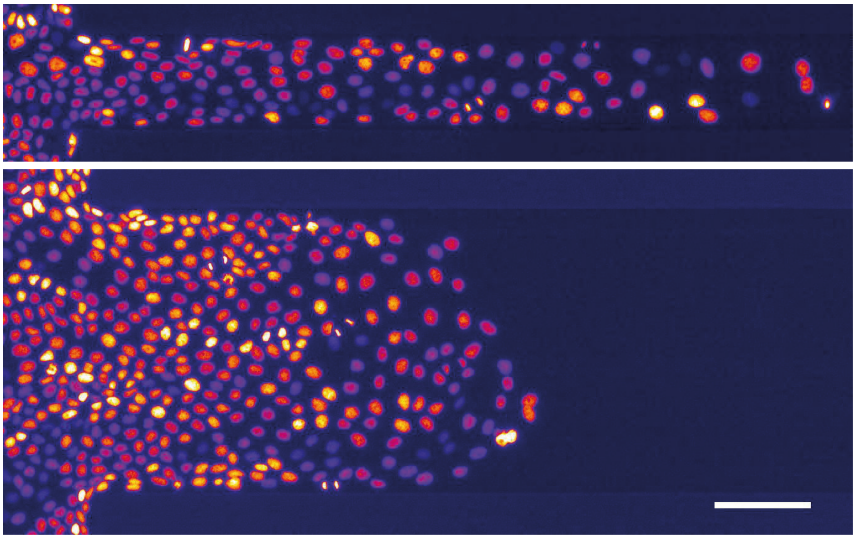

Figure 5.4: Invading cell sheets in microchannels of different widths. *MDCK cells migrate collectively into PEG-DMA microchannels. The developing density gradient is clearly visible due to the fluorescently labeled cell nuclei (scale bar corresponds to 100 μm).*

The flow field of the invading MDCK cells was evaluated by particle image velocimetry (PIV) analysis. The originally velocity fields obtained by cross-correlating two subsequent images showed strong spatial and temporal fluctuations. By both coarse-graining and temporal averaging, the flow field smoothed out to a directional flow with increasing velocities towards the leading edge. The flow profile perpendicular to the channel's direction provided a flat plug-flow like shape with decreasing velocities for the two adjacent cell rows at the walls implying week boundary slip conditions.

The direction of the plug-flow like invasion of the cell sheets was consistent with the developed density gradient. In the next step, we applied the Onsager reciprocal relations or, more detailed, a relation in analogy to Fick's first law, to our system, respectively, in order to describe the collective transport along the channels (see Fig. 5.5). The analysis was limited to the bulk of the cell layer to avoid the influence of boundary effects, and yields an effective collective diffusion coefficient $D_c = 1200 \pm 500$ μm^2/h. At the same time, an underlying drift flux was detected that was in accordance with a drift migration velocity of 9 ± 1 μm/h.

In this approach, however, growth based on proliferation is totally neglected. The propagation of the cell front can also be described by reaction-diffusion models taking diffusion like motility and cell proliferation by logistic growth into account. We fitted the observed averaged density profiles with the analytical solution of the Fisher-Kolmogorow equation. The resulting collective diffusion coefficient $D_c = 1140 \pm 120$ μm^2/h agreed well with the value obtained by analysis of the cell density flux.

The described behavior of plug-flow like invasion and collective transport, however, referred to long-range and time averaged scenarios. At short-scales, the observed motion appeared much more noisy. We analysed the lifetime and frequency of occurrence of swirl-like coordi-

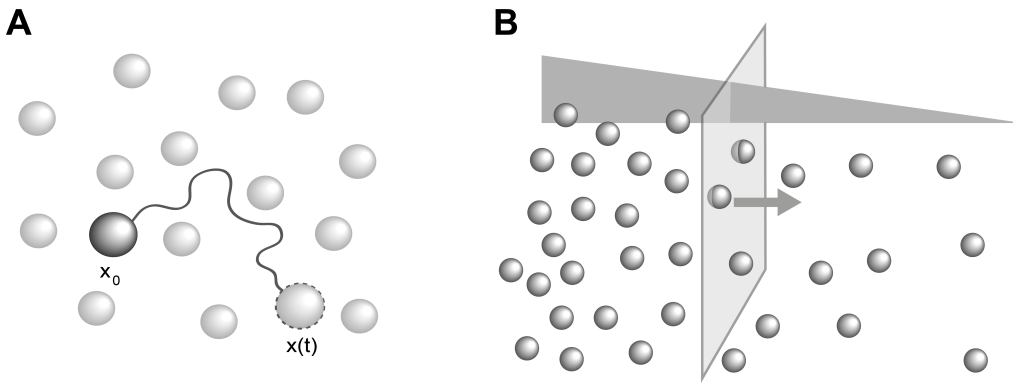

Figure 5.5: The concept of random motion and diffusive behavior of particles. *(A) A particle moves with an unpredictable direction and covers a certain distance in a given time. (B) The diffusive motion of spheres is directed along a density gradient resulting in a density flux.*

nated cell migration by calculating of vorticity maps. In order to evaluate the influence of directed motion on vortex formation, we compared the measurements of invading cell fronts to a scenario of resting cell sheets in the same confinement by uniformly seeding cells over the whole channel resulting in a confluent monolayer without borders. In the case of resting tissue, a strong cell density dependance of vortex formation was observed. With increasing cell densities, the occurrence of coordinated rotational cell migration was drastically reduced. Interestingly, we found that vorticities emerged to a considerably lesser extent in flowing cell sheets in areas of similar cell densities suggesting that directed cell flow suppressed the formation of vorticities.

By focusing on the migration behavior of individual cells, we addressed the question if cells undergo an effective random motion in connected cell assemblies and if directed flow is influencing their characteristic movements. We tracked single cell nuclei and calculated the mean square displacement for flowing and resting cell sheets. For better comparability, the individual underlying drift velocity was subtracted from each cell track taken under flow, resulting in centered traces. The MSD showed a subdiffusive behavior for cells moving in a resting confluent layer for scales longer than a typical cell diameter. The cells seems to be caged by their neighbors since an exchange of positions rarely occurs. Cells in flowing tissues were not restricted to subdiffusive motion. Here, diffusive behavior is observed beyond scales of one cell area, denoting an enhanced mobility of cells within the layer.

The observed directed cell migration acted to balance the present density gradient. The question how cells can sense the local density and adapt their migration behavior accordingly, however, is still unanswered. Mechanisms such as contact inhibition of locomotion, impact of leader cells and plithotaxis have been discussed in literature [132]. The described coordinated noise on short time scales observed in our experiments in combination with enhanced cell mobility in flowing sheets may play a role in gradient sensing. Randomly arising bursts of coordinated cell migration and active feedback can lead to balancing of gradients. The de-

crease of frequency and occurrence of vortex formation under flow suggests that the rotational collective cell migration turns directional.

5.2 Alignment of cell division axes in directed epithelial cell migration [M2]

In this manuscript [M2], we addressed the question to what extent cell division events are influenced by directed cell migration. We used the same setup as described in the previous chapter and confined expanding cell sheets of MDCK cells in three-dimensional PEG-DMA channels. The experiments were accompanied by particle based computer simulations in co-operation with Jens Elgeti. Again, particle image velocimetry (PIV) analysis and automated nucleus detection were used to describe velocity fields and local cell density. Cell division events were evaluated by manually identifying and marking the coordinates of the two daughter cells in the fluorescence images directly after cell division (see Fig. 5.6).

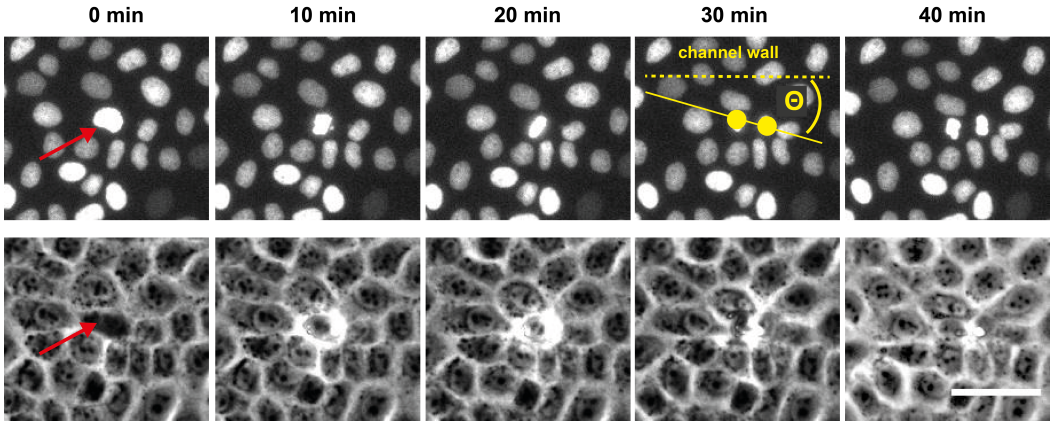

Figure 5.6: Time course of a cell division event in a flowing MDCK sheet. *The dividing cell (marked by the red arrow) contracts and rounds up as seen in the brightfield images (lower row). Due to chromatin condensation, the cell nucleus shrinks to an elongated shape exhibiting a very bright fluorescent signal (fluorescence images, upper row). For division axis identification, the coordinates of the two daughter cells are collected in the first image of separated nuclei. The angle between the channel walls and the cell division axis is denoted as* Θ.

As described before, the cell sheet invaded the channels at constant speed, independently of the channel widths. The flow profile resembled a plug-flow and exhibited an increasing average velocity from the channel entrance towards the leading edge. The flow profile perpendicular to the channel walls showed finite slip boundary conditions from the confinement since the velocity decreases towards the walls by a factor of three. The length of the decay corresponds to one or two cell diameters, respectively. The main characteristics were reproduced by the simulations, however, the effect of decreasing velocity towards the bulk is much smaller and the simulations yield a almost perfect plug-flow profile in y-direction of the channel. The

density distribution with low densities at the front and higher in the bulk found in the experiments was well described by modeling.

After characterizing the predominant flow of the growing cell sheet, we focused on the orientation of cell division axis within the cell layer. Reffay *et al.* found orientated cell division and polarity along formed fingers following specialized leader cells [95]. Beyond these border instabilities, neither the work of Reffay *et al.* nor the paper published by Poujade *et al.* showed evidence that cell division events are ordered inside the cell bulk [89, 95].

In order to determine the level of orientation, we calculated a simplified nematic order tensor S_x^d which denotes an isotropic distribution for $S_x^d = 0$ and perfect alignment for $S_x^d = 1$. For the bulk, we found typical orders in the range of 0 to 0.5, displaying a distinct orientation in the direction of the flow. Again, simulation results were in good agreement with the experimental findings, however, discrepancies at the borders were noticed. The correlation between the predicted tensile stress in advancing cell layers from literature [111, 123, 129] and the division axis was evaluated by calculating the strain rate tensor from the PIV data. We found that the main axis of the tensor was aligned with the direction of the channel as well, however, a much smaller degree of order was reported. This observation, nonetheless, supported the assumption that the cell division axis self-organizes in the direction of the maximal principal stress. On these large scales, it seemed contradictory that the x-component of the flow field decreased with increasing distance to the leading edge while the degree of alignment of the division axis increased. In the case of orientation of division axis due to mechanical stresses, the cell division axis should adapt to the local flow gradients. We evaluated the average order of divisions in directions of the flow gradients and found a clear correlation between the divisions and the strain rate tensor.

In order to be capable of distinguishing the influence of cellular flow on the orientation of cell division axis from possible effects of the borders, we investigated cell division events in resting tissues. Cells were uniformly seeded over the whole channels resulting a confluent monolayer of MDCK cells. In the absence of global flow, the cell division axis was strongly aligned with the channels walls, however, the near perfect order declined rapidly over one to two cell diameters to isotropic distributions in the middle of the channel. As consequence, we can assume that the observed alignment of cell division axis within flowing cell sheets was mainly caused by the global orientation of motility.

Further investigation of the distribution of cell division events revealed an increased number of divisions directly at the channels walls (also in the range of one to two cell diameters). This effect was accompanied by increased cell density and division rates at the borders. We found a small divergent flux of cells perpendicular to the channel walls which, however, was not reproduced by the simulations. The phenomenon of increased proliferation at the borders of confinements has already been reported in literature [79].

Manuscript 1 [M1]

Flow and diffusion in channel-guided cell migration

Anna-Kristina Marel[1], Matthias Zorn[1], Christoph Klingner[1], Roland Wedlich-Söldner[2], Erwin Frey[3] and Joachim Oskar Rädler[1]

[1]Fakultät für Physik and Center for NanoScience, Ludwig-Maximilians-Universität, Geschwister-Scholl-Platz 1, 80539 München, Germany

[2]Institute of Cell Dynamics and Imaging, University of Münster, Von-Esmarch-Strae 56, 48149 Münster, Germany

[2]Fakultät für Physik, Arnold Sommerfeld Center and Center for NanoScience, Ludwig-Maximilians-Universität, Theresienstrae 37, 80333 München, Germany

Submitted to 'Biophysical Journal'

Running head: Channel-guided cell migration

Flow and diffusion in channel-guided cell migration

Anna-Kristina Marel [†, ✱, ○], Matthias Zorn [†, ✱, ○], Christoph Klingner [†],

Roland Wedlich-Söldner [‡], Erwin Frey [§, ✱] and Joachim O. Rädler [†, ✱, *]

[†] Fakultät für Physik & Center for NanoScience, Ludwig-Maximilians-Universität,

Geschwister-Scholl-Platz 1, 80539 München, Germany

[‡] Institute of Cell Dynamics and Imaging, University of Münster,

Von-Esmarch-Straße 56, 48149 Münster, Germany

[§] Fakultät für Physik, Arnold Sommerfeld Center & Center for NanoScience, Ludwig-Maximilians-Universität,

Theresienstraße 37, 80333 München, Germany

[✱] Nanosystems Initiative Munich, Schellingstraße 4, 80799 München, Germany

[*] Joachim O. Rädler, Fakultät für Physik, LMU, Geschwister-Scholl-Platz 1, 80539 München

Phone: +49-(0)89-2180-2437 ; Fax: +49-(0)89-2180-3182

E-mail: raedler@lmu.de

[○] These authors contributed equally to this work

Abstract

Collective migration of mechanically coupled cell layers is a notable feature of wound healing, embryonic development and cancer progression. In confluent epithelial sheets, the dynamics have been found to be highly heterogeneous, exhibiting spontaneous formation of swirls, long-range correlations and glass-like dynamic arrest as a function of cell density. In contrast, the flow-like properties of one-sided cell-sheet expansion in confining geometries are not well understood. Here, we study the short- and long-term flow of Madin-Darby canine kidney (MDCK) cells as they move through microchannels. Using single-cell tracking and particle image velocimetry (PIV), we found that a defined stationary cell current emerges in such a pipe-like structure when data are averaged over characteristic spatial and temporal scales. The averaged flow-field exhibits a velocity gradient in the direction of migration and a plug-flow-like profile across the advancing sheet. From the density gradient and the speed of front propagation, we extract the collective diffusion coefficient using the Fisher-Kolmogorov model. To connect diffusive transport to underlying cellular motility, we studied single cell trajectories and occurrence of vorticity. We discovered that the directed large-scale cell flow alters fluctuations in cellular motion at short length scales: vorticity maps show a reduced frequency of swirl formation in channel flow compared to resting sheets of equal cell density. Furthermore, under flow, single-cell trajectories showed persistent, long-range random-walk behavior superimposed on drift, whereas cells in resting tissue did not show significant displacements with respect to neighboring cells. Our work thus suggests that the mechanism of diffusion-like long-range transport is configured by short-range random bursts of correlated motion.

Keywords: collective cell dynamics, single-cell analysis, vorticity, Fisher-Kolmogorov equation

Introduction

The phenomenon of collective cell migration is a prominent element of embryonic development, wound healing and cancer metastasis. Unlike single cells, which migrate in a random-walk-like fashion in the absence of external cues, the members of multicellular assemblies are physically connected, and can communicate by mechanochemical signaling and via the extracellular environment (1–3). Even in the absence of external cues, such as physical forces or chemical gradients, groups of identical cells exhibit characteristic collective motion, which remains poorly understood. In recent years, increasing efforts have been made to formulate mechanistic principles that can account for the dynamics of cohesive cell sheets (4). There is increasing evidence that cell migrations in developing tissue, under homeostatic conditions as well as in artificially designed experiments, exhibit universal behavior. Two-dimensional sheets of epithelial cells have long been a model system for the study of cell migration. The so-called wound-healing assay convincingly demonstrates the fluid-like behavior of epithelial cell sheets. At least two mechanisms are thought to be responsible for the directional motion of cells towards the advancing edge of the cell monolayer. Firstly, leader cells protrude from the cell front, drawing rows of mechanically coupled follower cells after them (5–8). Secondly, mechanical force transmission has been proposed to maintain directional flow of cells (9). Although the existence of leader cells is indisputable, the mechanism by which forces are transmitted, and its range of action, are still under debate. Furthermore, there is no experimental evidence bearing on the issue of whether and, if so, how cell layers further behind the leading front of a migrating cell sheet follow a density gradient. In addition, dynamic heterogeneity and kinetic arrest complicate the picture of collective motion: cellular dynamics in confluent epithelial cell layers exhibit anomalously large fluctuations of traction forces (10), strong spatial and temporal correlations in migration velocity (11, 12) and spontaneous formation of swirls not seen in ordinary fluids (13). A key determinant of cellular dynamics is the overall cell density. Cellular systems seem to exhibit glass-like kinetic arrest, with the appearance of mobile clusters that grow in size, as a function of increasing cell density (13). Furthermore, the average rate of mitosis within

migrating cell sheets is a function of cell density or cell size. Complete arrest of mitosis occurs when the average cell area falls below a critical value (14). From a theoretical perspective, two-dimensional cell monolayers resemble foam-like solids with a characteristic junctional network and packing geometry (15). Several models, such as agent based models (12, 16) or continuum models (8, 17), have been used in attempts to capture the physical aspects of cell assemblies. In a recent paper, Ranft et al. showed that, owing to the remodeling induced by cell division and apoptosis, the homeostatic state can be effectively described as a viscoelastic fluid (18). This model implies diffusive motion, which is a prerequisite for reaction-diffusion-type models that have previously been used to describe interface propagation and closure processes in wound healing assays (19–24). Apart from cell division, active migration of individual cells sparked by intrinsic stimuli must also be considered. This biological activity is evidenced by force mapping and leads to collective processes that are coordinated over multicellular groups. In a mechanical analogy to a tug-of-war scenario, neighboring cells join forces to transmit stress from cell to cell (9). However, little is known about how local cell migration activity is coordinated. In this context, a mechanism named plithotaxis has been proposed that forces cells to migrate along orientations of minimal intercellular shear stress (25). Plithotaxis is believed to provide a guidance cue that allows cells to migrate towards the open end of a cell sheet.

In order to scrutinize and challenge theory on cell migration, various assays have been developed to quantify cell behavior in microstructured environments (26–28). Most recently, Vedula et al. studied cell migration on microstructured stripes (29). They observed that a decrease in the width of the strips is accompanied by an overall increase in the speed of the migrating cell sheet. Moreover, large-scale vortices over ten cell lengths appeared on wide strips, whereas a contraction-elongation type of collective motion was observed on narrow strips. We carry this approach forward to ask what drives cellular flow through an artificial pipe-like microstructure in the absence of external chemical cues. Flow of an ordinary viscous fluid through a pipe requires the presence of a pressure gradient and follows a parabolic flow profile known as Hagen-Poissieulle's law. For non-Newtonian, polymeric or liquid crystalline fluids, more complex flow profiles emerge due to non-linear coupling (30). For

cellular monolayers there is as yet no experimental evidence for a defined flow profile, and a kinematic description of how cells that are hundreds of cell layers away from the leading edge sense density gradients is also lacking.

Here we study the flow of MDCK cell sheets through microfabricated channels made of poly(ethylene glycol)-dimethacrylate (PEG-DMA). In the first part of the paper, we show by means of particle image velocimetry (PIV) analysis that, at sufficiently large time and length scales, a stationary flow profile emerges. Cell flux is directed along the cell density gradient in the channel. Both the cell flux balance and the stationary cell density profile are consistent with the reaction-diffusion-type Fisher-Kolmogorov equation, with an effective collective diffusion constant D_c = 1150 ± 120 μm²/h, superimposed on a density independent constant drift velocity v = 9 ± 2 μm/h In the second part, we analyze the occurrence of short-term coordinated rotational migration by calculating the vorticity map at any instant. The lifetime of spontaneous swirls is about 15 min, with left-handedness and right-handedness being equally frequent. Most interestingly, the strength of the vorticity field decreases with increasing cell density and for cell sheets undergoing directional flow compared to confluent layers at comparable cell density. In contrast, the two-dimensional mean-squared displacement of single-cell trajectories is higher in migrating cell sheets than in resting confluent cell layers. Finally, we discuss how diffusion-like transport at large length scales is related to active correlated migration at short scales.

Results and Discussion

Directed cell migration was achieved by confining expanding cell sheets within microchannels (see Fig. 1*A*). We fabricated poly(ethylene glycol)-dimethacrylate (PEG-DMA) microchannels of different widths ranging from 100 to 300 μm using micromolding into capillaries (MIMIC). Briefly, the microchannels were created using a preformed PDMS stamp deposited on a petri dish. This stamp was filled with PEG-DMA, which was then polymerized by UV illumination, and cells were seeded in

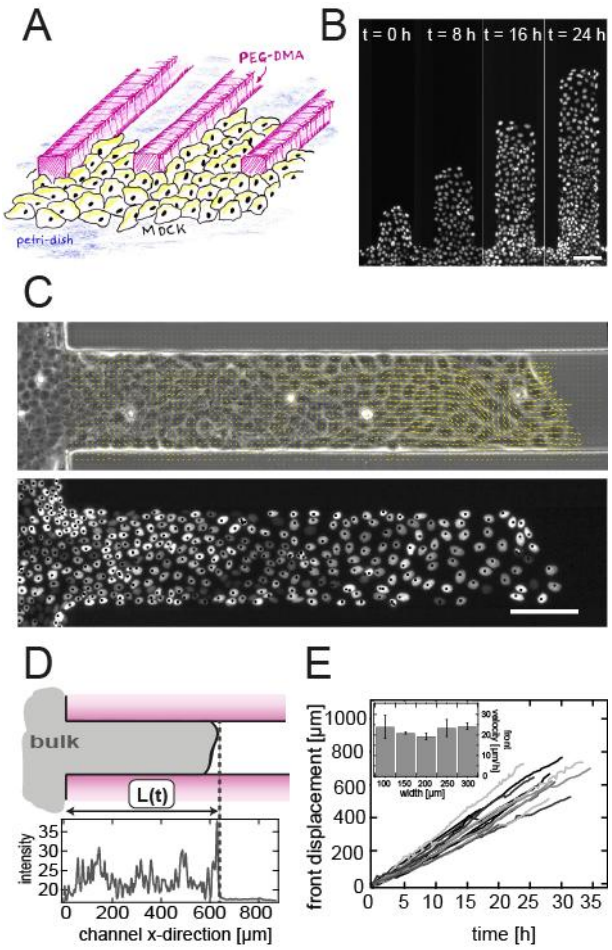

Fig.1. Migration of MDCK cells, expressing fluorescence-labeled nuclear H2B, in PEG-DMA microstructures. (A) Once within the microstructures, migration of the cells is constrained by the channel walls, as indicated in the schematic drawing (the scale bar corresponds to 100 µm). (B) The progression of stably transfected MDCK cells with fluorescently labeled nuclei along the channels is monitored by time-lapse microscopy (scale bar: 50 µm). (C) The velocity field is mapped by PIV analysis using bright-field images. Fluorescence images taken at the same time point are used to determine the cell density by locating individual cell nuclei. (D) The tip of the cell front is detected by the summed intensity spectrum along the y-direction of the bright-field images. The sharp drop in intensity corresponds to the moving cell front. (E) Linear front displacement for channels of varying widths. The invading fronts advance at a constant velocity that is essentially independent of the channel width. In the main plot, channel width is indicated on a gray scale from light grey (100 µm) to black (300 µm). Average velocities over all channels of the same width are plotted in the inset.

front of the PDMS block. When the cell layer reached a confluent level, the migration experiment was initiated by removing the PDMS stamp, thus opening the channels. The spreading cell sheet invaded the interstitial, channel-like areas of the microstructures that are composed of the PEG-DMA walls bordering the bare petri-dish surface (see Movie S1 in the Supporting Material). Sheet expansion was monitored by both bright-field and fluorescence time-lapse microscopy. We used a

stably transfected MDCK cell line expressing mCherry-labeled H2B histones, which results in clearly defined fluorescence signals localized to cell nuclei (Fig. 1*B* and Movie S2). Computer-aided localization of the labeled nuclei enabled us to follow the spatiotemporal evolution of the cell density. The bright-field images were used for PIV analysis, as well as for the definition of the leading edge (Fig. 1*C*, *D*; see also Movie S3, S4 and S5). As shown in Fig. 1*D*, *L(t)*, the distance of the cell front from the channel entrance, was measured. For all channel widths tested, the leading edge was found to advance continuously over the entire observation time of up to 35 h. The average velocity of the front was determined to be $v = 22 \pm 5$ μm/h, and the time courses showed that it was approximately constant and essentially independent of the channel width (see Fig. 1*E*). The number of cells entering the channel scaled linear with the channel width as wells as demonstrated in Figure S2. The values obtained are in good agreement with the results reported by Vedula et al. (29). Note that we used channel dimensions in the upper range of those in the work of Vedula et al. (29), where only a weak dependence of the front velocity on stripe widths was observed.

Flow-field analysis

As shown in Fig. 2*A*, the flow field of the invading cell sheet obtained from the PIV analysis exhibited strong spatial and temporal fluctuations. Nevertheless, a net flux along the direction of the trench could be discerned (see top-left corner image of Fig. 2*A*), and successive application of spatial coarse-graining and time-averaging revealed a smooth directional flow. The homogeneous flow field exhibited an increase in flow velocity from the rear to the front of the invading cell sheet (see Fig. 3*C*). Simultaneously, a flat flow profile across the width of the channel was observed (see Fig. 3*A*). A steep velocity gradient across about two cell columns separated this plug-like flow from the channel walls (see Fig. 3*B*). In order to determine how fluctuations were averaged out as a function of length and time scale, we plotted the variance of the vertical flow component against the coarse-graining length and averaging time, respectively (see Fig. 2*B*). Within the limits of accuracy of the measurement, this flow component was found to fluctuate around a mean value negligibly close to zero. Plots of the dependence of the variance of vertical flow on temporal and spatial averaging

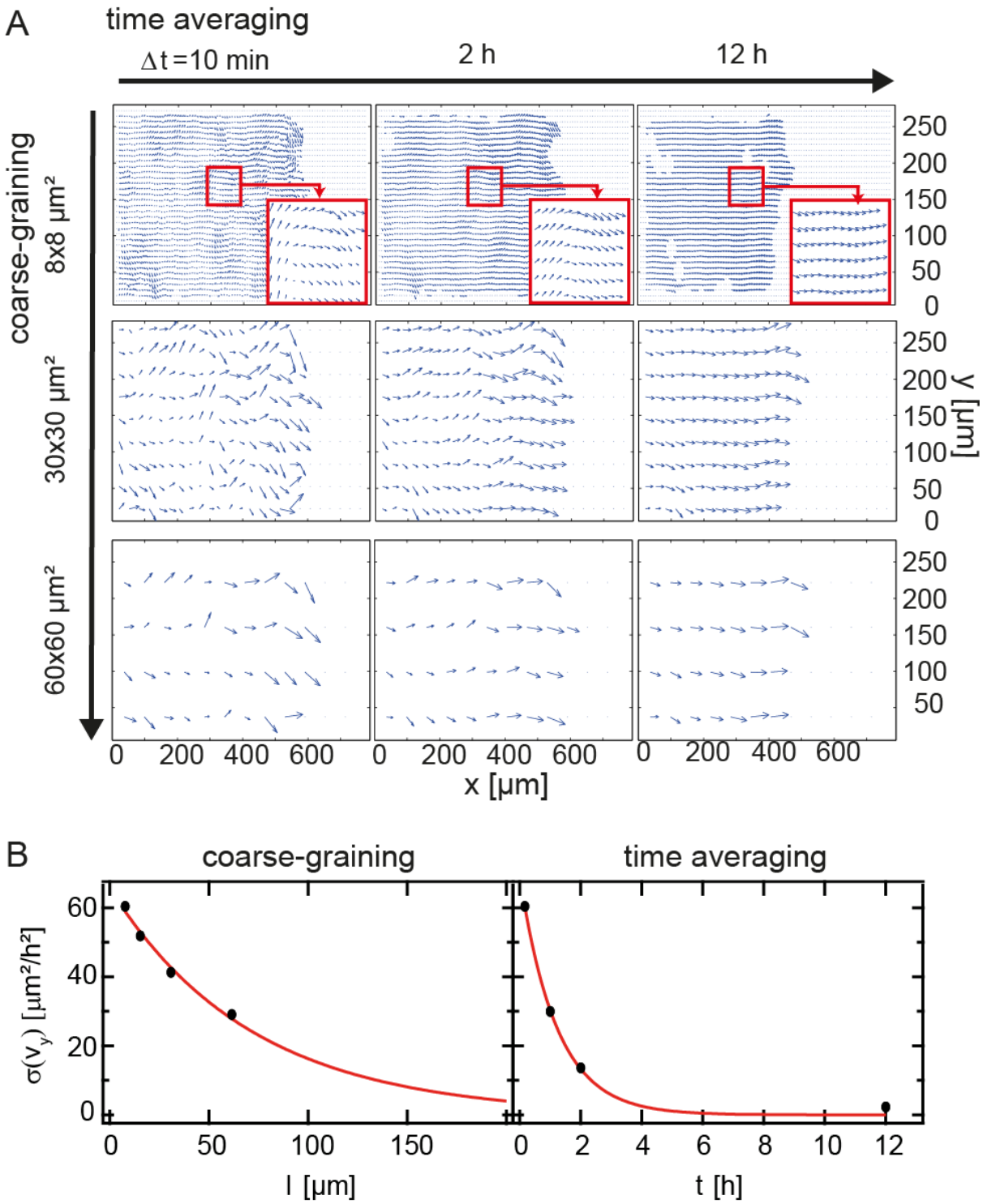

Fig. 2. Smoothing of the velocity field by spatial and temporal averaging. (A) The original PIV vector field (top left) is averaged over time taking vector fields 1 h (middle column) or 6 h (right column) before and after t = 0 into account, respectively, for every grid point. Alternatively, the original vector field is coarse-grained, averaging over 4x4 neighboring vectors (middle row) or 8x8 neighboring vectors (bottom row). While the original velocity field shows fluctuations, each averaging process results in smoother, more homogeneous fields. A combination of coarse-graining and time-averaging clearly reveals the existence of a plug flow within the limits of local and temporal fluctuations. (B) Dependence of the variance in the v_y velocity component on coarse-graining length and averaging time. Fitting of exponential decay curves yields characteristic correlation lengths and times.

could be fitted to exponential decay curves, yielding values of l_c = 70 µm for the length scale, and a characteristic averaging time of t_c = 1.2 h, over which the amplitudes drop to 1/e of their original values (see Fig. 2*B*). Note that the coarse-graining length scale is of the same order as the 80 - 100 µm correlation length determined for coordinated cell movement at comparable cell density (13). The characteristic time t_c can be interpreteted as the corresponding correlation time of the fluctuations in the cellular migration patterns and has not been reported so far. Note that this time scale is considerably shorter than the doubling time t_d = 25.2 ± 4.2 h that represents another characteristic time scale in systems of cells.

Cell flux density and diffusion

The average cell flow was directed towards the tip of the invading cell sheet and hence towards regions of lower cell density, i.e. along an established cell density gradient. We therefore tested whether the cell flux follows a linear Onsager relation equivalent to Fick's first law of diffusion, which states that the flux *J* is proportional to the slope of the density gradient.

$$J = -D_c \frac{dc}{dx} + J_0 \qquad [1]$$

Here, D_c is the collective diffusion coefficient and *dc/dx* the density gradient, whereas J_0 describes a possible underlying, density independent drift. The cell flux density *J* was determined by measuring the cell density *c* and the flow velocity *v*, according to $J = c \cdot v$. To this end the channel area was dissected into 50 µm wide observation windows starting at the position of the front. Cell density was measured by automated counting of stained nuclei (see Fig. 4*A*). The flow velocity was assessed by PIV analysis and the *x*-components were averaged for each stripe sector. As a representative example, Fig. 4*B* shows the cell density and velocity for two windows, 200 and 350 µm away from the front, respectively, in one channel. Note the strong temporal fluctuations in the time courses of both local cell density and cell flow velocity. The time-averaged values, however, clearly indicated a decrease in cell density and an increase in velocity towards the leading edge, as already seen in the

coarse-grained PIV analysis (see Fig. 2*A*) and as also demonstrated in Fig. S3 and S4. The rates of cell

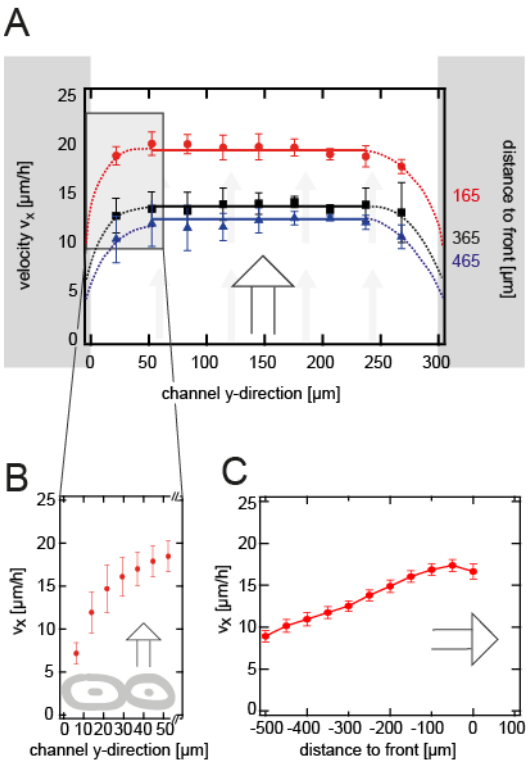

Fig. 3. Velocity profiles parallel and perpendicular to the channel walls. (A) Coarse-grained profiles of the v_x component (parallel to the walls) taken across the channel (perpendicular to the walls) for three levels at different distances from the front, averaged over three 300 µm wide channels. A plug flow is clearly visible across the channel, with the exception of the outermost cell layers (around two cell diameters wide), where a slight decrease in velocities is visible. Note, however, that the coarse-grained data do not extend all the way to the channel walls. (B) The profile immediately adjacent to the channel walls was examined in more detail using non-coarse-grained PIV fields, and reveals a sharp drop in velocities at the edge over a distance equivalent to approximately two cell diameters. (C) Velocity profile parallel to the channel walls as a function of distance from the front, averaged over 14 channels of different widths. The plot shows that velocity increases linearly with decreasing distance from the leading edge. The foremost point shows a slight decrease, though this is likely due to inaccuracies in the PIV analysis at the edge of the cell sheet, possibly compounded by the fact that the channel is not filled over its entire width.

influx into and eflux from the chosen stripe region appeared to be equal within experimental uncertainty. In order to test whether cell flux was driven by the cell density gradient, the density gradient and corresponding cell flux were determined for four pairs of observation windows 150 µm apart (ranging from 100 µm to 400 µm away from the leading edge). Whether these value pairs follow a linear correlation is not immediately apparent when examining all data points. A trend becomes clear, however, after separating the data points depending on their absolute cell density (see Fig. 4*C*). While the cell flux is indeed driven by density gradients, this effect appears to be

density dependent. To confirm such a dependency, the linear correlation between cell flux and density gradient is analyzed statistically, while excluding points of successively higher densities. The threshold density c_t is increased step by step and the Pearson product-moment correlation coefficient r calculated each time for all pairs of flux and density gradient values obtained from absolute densities above c_t. The resulting correlation coefficient depends sigmoidally on the chosen threshold density (see Fig. 4*D*). The Onsager relation (see Eq.[1]) was then fitted to all pairs of J and $-dc/dx$ values stemming from densities above a cutoff density c_{cut} = 0.0022 [cells/µm²] determined as the threshold density for which the sigmoidal fit of the correlation coefficient reached half of its maximum height. This determined density corresponds well to the critical density necessary for the emergence of collective behavior as reported by Doxzen et al. (12). Whereas the cell flux and density gradient show no significant correlation for all data points obtained below (and at) c_{cut} (r = 0.10 with a p-value of p = 0.63), there is a linear correlation above this value (r = 0.45 with a p-value of p=0.01). A constant offset $J_0 = (24 \pm 3)\cdot 10^{-3}\,(\mu m \cdot h)^{-1}$, which must be interpreted as a density independent drift term, remained when carrying out the linear fit in this regime. For the average cell density of 0.0026 cells/µm² in the evaluated area, this flux corresponds to an underlying migration velocity of 9 ± 2 µm/h. Since the underlying velocity is independent of the density, there must be a preexisting external direction, which might be determined by the leading edge or conditions at the channel entrance (see Fig S1 in the Supporting Information). Within the framework of our theoretical approach, no mechanism is provided for the origin of drift. The cell flux due to a cell density gradient, however, is well described and the slope of the fit yielded an effective collective diffusion coefficient D_c = 1500 ± 500. Thus, even if this description is insufficient to completely explain the observed cell motion, it captures the density dependent mass transport and gives a good initial assessment of the collective diffusion. In principal, an additional flux term due to cell proliferation is expected for long observation times. At the relatively short length scale of our flux analysis this contribution remained within the noise level. Modelling the cell density profile along the entire channel, however, requires incorporation of cell profliferation as shown in the next section.

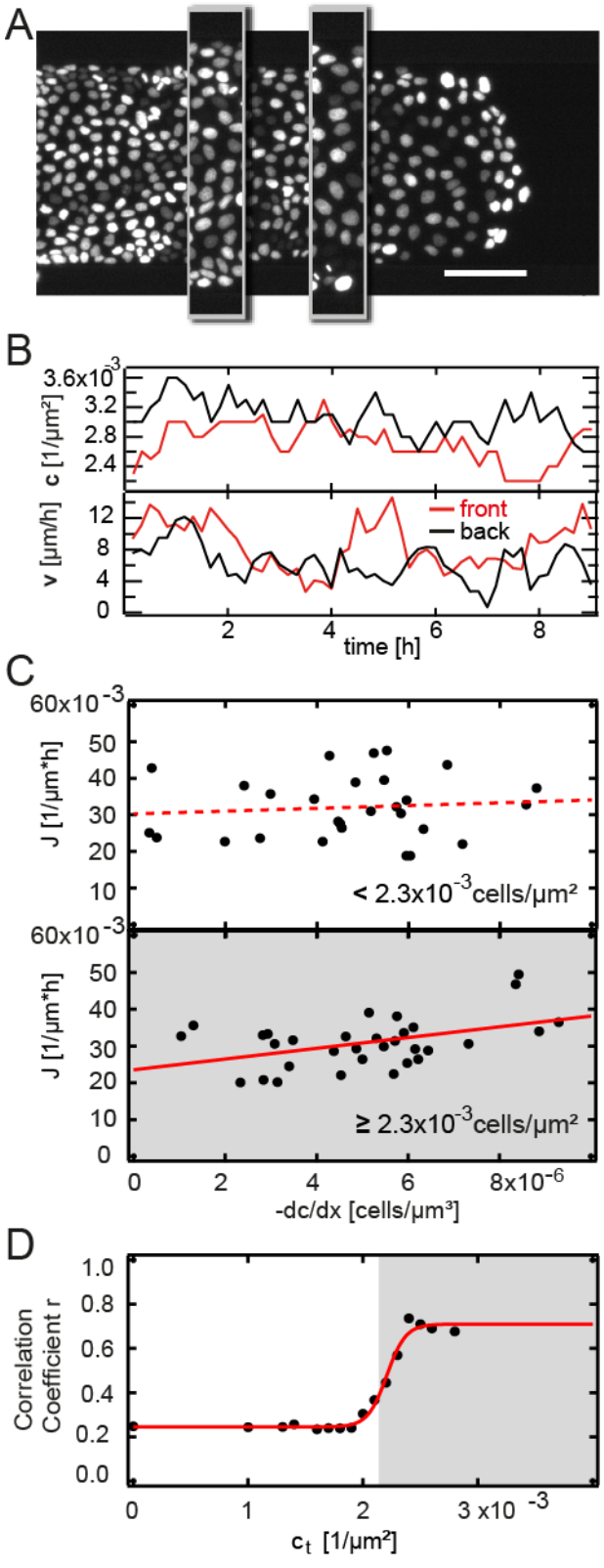

Fig. 4. Flux behavior in a migrating MDCK monolayer. (A) The local flux density is calculated from the local cell density and the averaged flow velocity. Cell flux was determined for overlapping sets ('bins') of three contiguous windows, spanning a fixed distance of 150 µm and extending 200, 250 and 300 µm away from the leading edge respectively. Insets show selected windows of 50-µm width, 200 µm and 350 µm away from the front (scale bar corresponds to 100 µm). (B) Time courses of cell density (*c*) and velocity (*v*) for one representative measurement on a 250 µm wide channel and one bin

combination. Strong temporal fluctuations were observed. (C) Comparision of the scatter plots for average cell densities lower than 0.002 cells/µm² and higher than 0.002 cells/µm². The cell flux correlates hardly with the density gradient for lower cell densities (r = 0.09). In contrast, by neglecting data points of average cell densities lower than 0.002 cells/µm², a correlation coefficient of r = 0.46 was calculated for cell flux and density gradient. The linear fit yields a slope corresponding to the collective diffusion coefficient D_c = 1600 ± 500 µm²/h. (D) Evaluation of the correlation coefficient *r* between the cell flux and density gradient reveals a considerably dependence on the average cell density.

Reaction-Diffusion Model

For the description of the evolution of the cell density profile along the channel, we use the most general continuum model which includes diffusion-like transport and cell proliferation by logistic growth. The corresponding reaction-diffusion equation is the Fisher-Kolmogorov equation (31)

$$\frac{\partial c}{\partial t} = D_c \nabla^2 c + \lambda c(1 - \frac{c}{K}). \qquad [2]$$

Here D_c denotes the effective diffusion constant, λ the growth rate, and *K* the carrying capacity, respectively. The Fisher-Kolmogorov equation can be analytically solved and leads to travelling wave solutions with constant front speed $s = \sqrt{4D\lambda}$ (32). In case of diffusion plus drift, Eq. 2 describes the profile in the co-moving frame. In experiment, as seen in Fig. 5*A*, the time sequence of invading experimental cell density profiles showed an evolution from an initially steep profile towards an ever shallower stationary profile. Cell density profiles were obtained by collecting the number of cells counted in 50-µm wide bins along the x-direction of the channel. The representative dataset reported in Fig. 5*A* derives from a channel of 300 µm width observed for 22 h (elapsed time is represented by the color code from dark blue to deep red). Figure 5*B* shows the late-stage, stationary density profiles from different experiments transformed into the moving frame, i.e. with the coordinate origin at the leading front. Due to the different length scales of the two regimes, in this scaling the quick density drop close to the cell front becomes inconspicuous. The averaged profile (black crosses) agrees with the travelling-wave profile predicted by Eq. [2] with the exception of the sharp drop at the leading edge. Here, the asymptotical theoretical solution is incapable of describing

the discrete end of the connected cell sheet. Note that for the displayed fit, both the collective

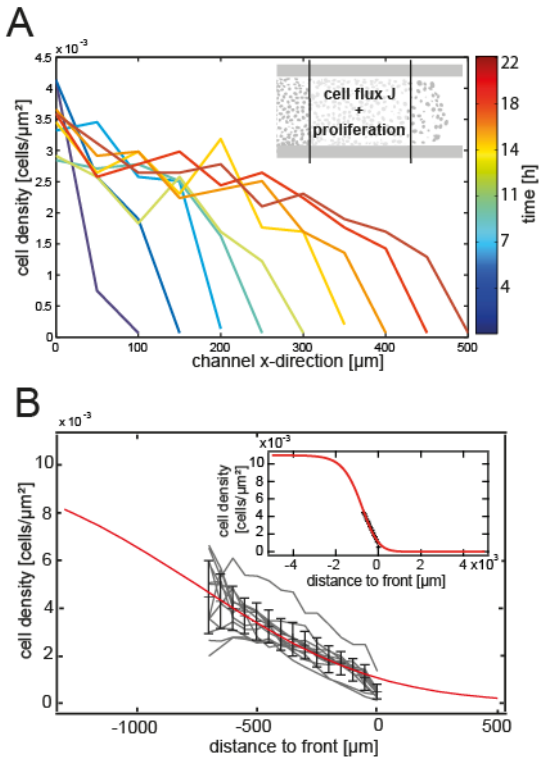

Fig. 5. The time evolution of the cell density can be interpreted as a traveling wave. (A) Development of the cell density profile over time. As the cell front migrates into the channel, the density profile reaches a steady state of an approximately constant shape that propagates in x-direction. The inset highlights the factors of expansion, namely cell flux and proliferation. (B) Density distributions at the final time point for measurements (at which point cells have penetrated at least 750 µm into the channel) plotted against their distance from the cell front (gray traces) and the averaged curve (black crosses). The analytical solution of the Fisher-Kolmogorov equation is fitted to the averaged distribution of the cell densities (solid red line). When the growth rate λ is set to the value actually observed (0.028 h^{-1}), the fit results in a diffusion constant D_c = 1140 ± 120 µm²/h on the order of the collective diffusion coefficient determined by Fick's law, and a maximum cell density K = 0.011 ± 0.0003 cells/µm². The inset shows an expanded view.

diffusion coefficient D_c and the carrying capacity K were free fit parameters. Only the growth rate λ = 0.0283 ± 0.0005 h^{-1} was fixed, as it could be measured independently from the time course of the exponentially increasing cell number in a confluent monolayer confined in the same kind of channel (see Supporting Material). The resulting carrying capacity, K = 0.01 ± 0.0003 cell/µm^2, is in good agreement with values given in the literature (14, 33), however, the cell densities of the invading cell fronts are clearly smaller and settled only in the front part of the fitting curve. We assume the travelling wave in the described system penetrates the cell bulk outside the channels since the

leading edge had to bridge a distance of approximately 2000 µm before reaching the entrance of the channels (see Fig. S1), meaning the densities in the unobserved area before the channel would fall higher on the theoretical curve. The measured collective diffusion coefficient D_c = 1150 ± 120 µm²/h agrees well with the value obtained from the density flux *J* in the previous section. The obtained parameters are not arbitrary. Significant changes to one of the fit parameters (D_c or K) quickly causes the shape of the theoretical curve to diverge significantly from the empirical data points as well as cause the second fit parameter to also be driven to values inconsistent with expected values for D_c or K. The traveling wave solution of the Fisher-Kolmogorov equation also predicts a constant front speed $s = \sqrt{4D\lambda}$ in the resting frame. Using the values given above, we obtained s_{th} = 11 µm/h, for the front speed in the moving frame. Only after adding the previously determined constant drift velocity of v = 9 µm/h determined in the previous section for a total speed s_{tot} = 20 µm/h is a good agreement with the experimentally determined value (s_{exp} = 22 ± 5 µm/h) achieved.

Vorticity analysis

Spontaneous vortex formation is a hallmark of collective cell migration (11). We therefore assessed the incidence of vortex formation in flowing and resting cell sheets by calculating the vorticity from the PIV vector fields (an example of a vector field of a resting MDCK sheet is depicted in Movie S6). As shown in Fig. 6*C*, we used coarse-graining with a lattice size of about one cell diameter and calculated the curl at each site from the perpendicular component of the relative velocity of the neighboring sites, as depicted in the Figure (for details see Materials and Methods in the Supporting Material). Figure 6*C* displays representative vorticity heatmaps for both resting confluent cells (vertically arranged heatmaps), and cells invading the microchannels (horizontally arranged heatmaps). For the time evolution of vorticity heatmaps, see Movie S7 and S8 in the Supporting Material. The plot is ordered with respect to the local cell density for better comparison. Note that white squares in the heatmap indicate grid points where no vorticity value could be calculated due to the velocity map lacking a reliable velocity value on at least one surrounding grid point. As seen from the heatmaps of confluent cell sheets without flow, vorticity increases with decreasing cell density.

This effect is also demonstrated in a quantitative fashion in the Supporting Material (see Fig. S5). The

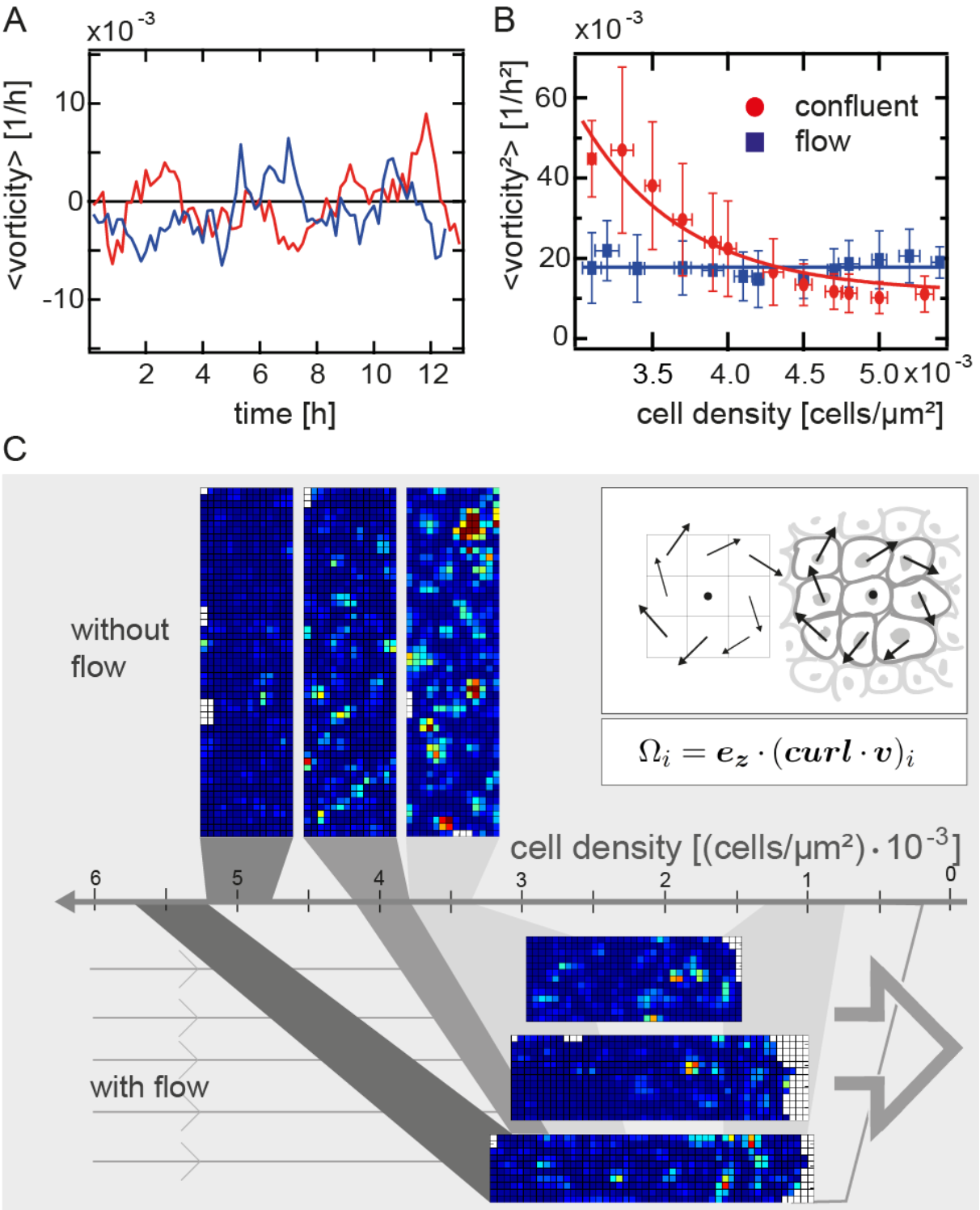

Fig. 6. Vortex formation in representative confluent resting and flowing cell sheets. (A) There is no preference for formed vortices to rotate clockwise (negative vorticity values) or counter-clockwise (positive vorticity values), irrespective of whether cells are under flow or not. (B) Squared vorticity as a function of cell density for both the confluent case (red) and the case with flow (blue). The vorticity decreases with increasing density. At low cell densities, the values for the vorticity with flow are lower than those observed at the same densities when flow is absent. This indicates that both, a flow and an increasing density, suppress vortex formation (lines are guides to the eye). (C) Heatmaps of

the squared vorticities, displaying the effect of density and flow. Red squares indicate high rotational activity (see Supporting Material), while dark blue squares mark regions of low vorticity Ω, which is calculated by means of an algorithm from the relative velocities (obtained from the coarse-grained PIV analysis) of a given point and its eight nearest neighbors (schematically displayed in the inset). In the absence of flow, the density of cells in the channel increases and the amount of vortices decreases until the squared vorticity has dropped close to zero over the whole area. Even at lower densities (1-4x10^{-3} cells/µm²), the cells with flow show lower overall vorticity than in the least dense confluent case (3.5x10^{-3} cells/µm²). Due to the gradient in density present in flowing cell sheets, however, vortices still form near the leading edge.

frequency of vortex formation in invading cell sheets is consistently lower than in resting confluent cell layers at the same cell density. Most strikingly, the high degree of vortex formation seen at a density of 3.5·10^{-3} cells/μm^2 in resting cells was not observed in areas of equivalent cell density in flowing cell sheets. Nevertheless, vortices were mostly found at the leading edge, where very low cell densities of about 1·10^{-3}cells/μm^2 were reached. The density dependence is summarized in Fig. 6*B*, where the averaged and squared vorticity is plotted versus cell density. As seen in Fig. 6*A*, these vortices were strongly fluctuating and short lived. The sense of rotation can be left-handed or right-handed and was found to be equally distributed within the accuracy of the measurement both in resting confluent layers and under flow. The heatmaps indicated vortex sizes of up to about six cell diameters, which is in good agreement with the results obtained by Vedula et al. (29). Characteristic lifetimes of about 15 ± 1 min for vortices were obtained from a time correlation of the vorticity (see Fig. S6). Note that such a short lifetime implies a short path length of the collective angular rotation, which corresponded to effective collective rotations within the limited angular range of 9° (dark red squares in the heatmap, see Fig. S7). Again, this measured time scale is much smaller than the cells' doubling time.

Single-cell motility

The motility of single cells in a growing cell sheet was studied using single-cell tracking. We asked whether cells undergo effectively random motions in connected cell monolayers and if in the case of cellular flow in channels directional cell migration is superimposed to diffusive motion. Representative trajectories for resting confluent cells, as well as for cells in flowing cell sheets, are

shown in Fig. 7*A*. In the latter case, we subtracted an average drift velocity from individual cell traces.

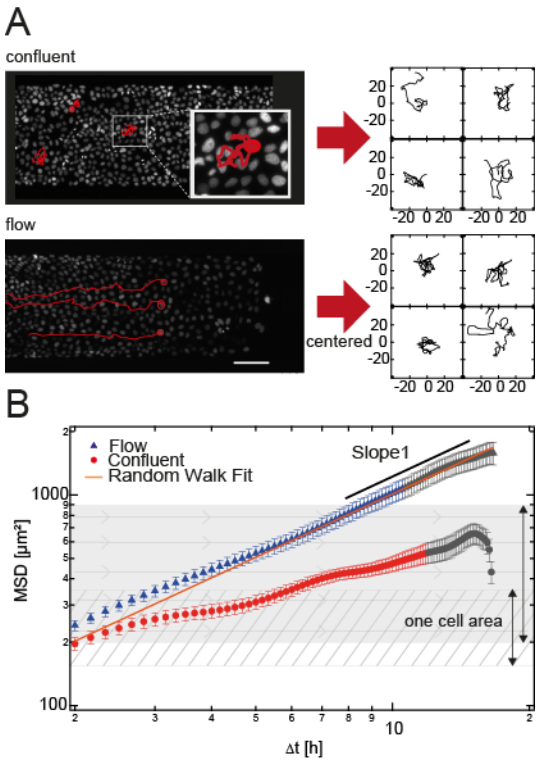

Fig. 7. Single-cell tracks for confluent and flow data. (A) Individual cell nuclei were tracked over time and representative traces are displayed in the lower panel. For better comparability, tracks obtained from the flow data are centered by subtracting one defined velocity vector from every time step, resulting in a track uniformly expanded in the x-direction. In both cases, single cell tracks show random motion. (B) MSD analysis reveals qualitative differences in individual cell behavior under flow compared to resting sheets. In the case without directed collective migration, motility appears to be subdiffusive above the scale of one cell area (indicated by the hatched area). In contrast, under flow, the behavior of individual cells can be seen to remain diffusive even on scales much larger than the cell area (indicated by the upper section of the shaded box) by comparing the slope in the log-log plot to a slope of 1 (black line). A random walk fit (orange line) describes the MSD values under flow well, particularly for large time scales. Error bars indicate standard errors. Due to increasing unreliability at longer time scales, the average MSD tracks were grayed out once the standard deviation of the individual measurements reached 70 % (resting case) and 90 % (flowing case) of the calculated mean values, respectively.

This drift velocity is chosen so that the average displacement from the initial track point is zero in x-direction (for details see Supporting Material). As there was no directed motion perpendicular to the channel at long time scales, the tracks were only centered parallel to the walls. The random cell motion under flow, corrected for drift, is shown in the lower panel of Fig. 7*A*, which indicates that the drift correction yielded centered and symmetric random motion comparable to the random walks seen for cells in resting layers. Firstly, under flow, there seems to be a slight difference between the

one-dimensional MSD parallel and perpendicular to the channel (data not shown), with the parallel component showing values about 1.4 times as large as the perpendicular component, albeit at the same slope. No such effect is present in the resting case. This effect is small and both hard to grasp as well as hard to separate from possible artifacts in the centering algorithm. The calculated two-dimensional mean square displacement meanwhile revealed clear differences for the flowing and resting case (see the log-log plot in Fig. 7*B*). In the long time- and length-scale regime, which describes cell displacement over more than one cell length, only the MSD scaling under flow showed a slope close to 1. In contrast, the MSD for cells in confluent monolayers exhibited subdiffusive behavior and did not significantly exceed the area of a single cell. This implies that, in resting tissue, single cells are caged at a length scale of a cell body length and local cell swaps or cell translocations across the next neighbors rarely occur. In flowing tissue, however, there seems to be sufficient tissue remodeling to allow single cells to carry out effectively random walks exceeding several cell body lengths. It is worthwhile noting here that the self-diffusion constant D_{flow} = 25.3 ± 0.1 μm^2/h, which we extracted from single-cell tracking, are in good agreement with the self-diffusion constant obtained from the dynamic structure factor of a velocity field in MDCK monolayer (13).

Conclusion

Whether or not collective cell migration should be considered as a cellular flow depends largely on whether a phenomenological transport theory is capable of describing experimentally observed features of the phenomenon. Conventional cell migration experiments are not tailored to quantitatively probe cell flow, but novel microstructuring techniques allow the design of artificial environments to corroborate the concept of cellular hydrodynamics. In particular, defined boundary conditions can be created by using microstructured surfaces that confine cell migration to defined geometries. In this study, we investigated the flow field of MDKC cells advancing through microfabricated channels with side walls made of the cell-repellent polymer PEG-DMA on a petri-dish surface. In this setting, which resembles a classical pipe-flow experiment, we found defined characteristics in the long-term flow profile and short-range dynamics. The current exhibited a

velocity gradient in the direction of flow and a flat plug-flow-like profile across the channel. At the channel walls, however, a short-reaching velocity decay over only about two cell layers is found. In the direction of flow, the cell density profile could be approximately described by the Fisher-Kolmogorov equation invoking an effective collective diffusion constant of $D_c \approx 1200\ \mu m^2/h$ and a constant migration velocity of 9 µm/h, though a constant, underlying migration velocity of 9 µm/h independent of the cell density remained unexplained. Effects of the leading edge are the most likely cause of this drift term, but its origin cannot be thoroughly elucidated without further study. The nature of the macroscopic diffusive transport remains unclear until the underlying mesoscopic mechanisms are uncovered. In solid matter, single atom diffusion is typically faster than collective diffusion. In contrast, here we found that rates of single-cell self-diffusion were lower than the observed long-range effective diffusion by two orders of magnitude.

Moreover, as seen in our experiments, the tendency to follow a density gradient was strongly perturbed by active local cell motion, including the formation of spontaneous swirls. Under these circumstances, it is difficult to assume a gradient-sensing mechanism. In the MDCK monolayer, a 2.5% relative change in cell density would need to be sensed over a distance equivalent to the length of a typical cell body. Hence, mechanisms that extend the action over larger distances are needed. It is likely that the correlated, but at large scales random, active migration accounts for balancing of cell density gradients by diffusion. The coordinated migration exhibited a length scale $l_c = 70\ \mu m$ and a time scale $t_c = 1.2$ h. If we consider these bursts of collective motion as an effective displacement of cell mass over distance l_c , then random bursts will yield diffusive transport with $D_{rb} = l_c^2/4t_c = 1000\ \mu m^2/h$, which is in good agreement with the measured collective diffusion constant $D_c = 1200\ \mu m^2/h$. Hence, collective migration provides a plausible mechanism that evens out cell density gradients at large scales. A second hint of a role for active coordinated noise in diffusive transport is given by the fact that the frequency and strength of vorticity decreased under flow, while the mean-square displacement of single cells increased. Increasing mean-square displacement under flow is well known in colloidal systems that show shear thinning (34). In a simplified view, cages that

restrict single-cell diffusion are broken up under flow conditions. Likewise, collective rotational cell migration in the resting confluent state is non-directional and does not require freely accessible space. Under flow, these vortices might break out and evolve into advances of coordinated directional cell migration. Note that the disappearance of vortices and the emergence of modes of directed contraction-relaxation-based migration were also described by Vedula et al. in the case of stripes that were narrower than the correlation length (29). Taken together, our experiments support the notion that a hydrodynamic theory of cellular matter as given by the Fisher-Kolmogorov equation is compatible with the expansion of epithelial monolayers under confinement at large length and time scales. In this case diffusive transport is promoted by active collective dynamics, which is driven by short-scaled bursts of coordinated migration with length scale l_c, rather than single cell motion. In contrast, a description at length scales shorter than l_c, as is the case e.g. in narrow channels or fibers, requires refined kinetic agent-based modeling of active motion. Here, particular features of cell-cell coupling and of individual cell dynamics will play a more important role. Migration studies in defined geometries, together with a theory of active cellular flow, provide a framework for quantitative studies on collective cell motion, a phenomenon that is instrumental in underpinning multicellular dynamics and structure formation in biology.

Materials and Methods

PEG-DMA microstructures were fabricated using a PDMS mold designed to form microchannels of varying widths (approximately 100 to 300 µm) (26). Cells were seeded in front of the PDMS stamp, which was initially left in place to prevent them from entering the channels. After removal of the PDMS, cells began to migrate into the opened channels, and the expansion of the tissue was followed by time-lapse microscopy. Particle image velocimetry (PIV) analysis and image analysis was used to evaluate the velocity field and the density distribution, and for single-cell tracking. (For a detailed description of the procedures see the Materials and Method section in the Supporting Material)

Acknowledgements

Financial support by the Deutsche Forschungsgemeinschaft (DFG) via SFB 1032, the Excellence Cluster 'Nanosystems Initiative Munich' (NIM) and the Center for NanoScience (CeNS) is gratefully acknowledged.

References

1. Gillespie, P.G., and R.G. Walker. 2001. Molecular basis of mechanosensory transduction. Nature. 413: 194–202.

2. Rørth, P. 2009. Collective cell migration. Annu. Rev. Cell Dev. Biol. 25: 407–29.

3. Friedl, P., and D. Gilmour. 2009. Collective cell migration in morphogenesis, regeneration and cancer. Nat. Rev. Mol. Cell Biol. 10: 445–57.

4. Vedula, S.R.K., A. Ravasio, C.T. Lim, and B. Ladoux. 2013. Collective cell migration: a mechanistic perspective. Physiology (Bethesda). 28: 370–9.

5. Petitjean, L., M. Reffay, E. Grasland-Mongrain, M. Poujade, B. Ladoux, et al. 2010. Velocity fields in a collectively migrating epithelium. Biophys. J. 98: 1790–800.

6. Reffay, M., L. Petitjean, S. Coscoy, E. Grasland-Mongrain, F. Amblard, et al. 2011. Orientation and polarity in collectively migrating cell structures: statics and dynamics. Biophys. J. 100: 2566–75.

7. Poujade, M., A. Hertzog, J. Jouanneau, P. Chavrier, B. Ladoux, et al. 2007. Collective migration of an epithelial monolayer. Proc. Natl. Acad. Sci. U. S. A., 104:15988-93

8. Mark, S., R. Shlomovitz, N.S. Gov, M. Poujade, E. Grasland-Mongrain, et al. 2010. Physical model of the dynamic instability in an expanding cell culture. Biophys. J. 98: 361–70.

9. Trepat, X., and J.J. Fredberg. 2011. Plithotaxis and emergent dynamics in collective cellular migration. Trends Cell Biol. 21: 638–46.

10. Trepat, X., M.R. Wasserman, T.E. Angelini, E. Millet, D.A. Weitz, et al. 2009. Physical forces during collective cell migration. Nat. Phys. 5: 426–430.

11. Angelini, T.E., E. Hannezo, X. Trepat, J.J. Fredberg, and D.A. Weitz. 2010. Cell Migration Driven by Cooperative Substrate Deformation Patterns. Phys. Rev. Lett. 104: 1–4.

12. Doxzen, K., S.R.K. Vedula, M.C. Leong, H. Hirata, N.S. Gov, et al. 2013. Guidance of collective cell migration by substrate geometry. Integr. Biol. (Camb). 5: 1026–35.

13. Angelini, T.E., E. Hannezo, X. Trepat, M. Marquez, J.J. Fredberg, et al. 2011. Glass-like dynamics of collective cell migration. Proc. Natl. Acad. Sci. U. S. A. : 1–6.

14. Puliafito, A., L. Hufnagel, P. Neveu, S. Streichan, A. Sigal, et al. 2012. Collective and single cell behavior in epithelial contact inhibition. Proc. Natl. Acad. Sci. U. S. A. 109: 739–44.

15. Farhadifar, R., J.-C. Röper, B. Aigouy, S. Eaton, F. Jülicher, et al. 2007. The influence of cell mechanics, cell-cell interactions, and proliferation on epithelial packing. Curr. Biol. 17: 2095–104.

16. Basan, M., J. Elgeti, E. Hannezo, W.-J. Rappel, and H. Levine. 2013. Alignment of cellular motility forces with tissue flow as a mechanism for efficient wound healing. Proc. Natl. Acad. Sci. U. S. A. 110: 2452–9.

17. Arciero, J.C., Q. Mi, M.F. Branca, D.J. Hackam, and D. Swigon. 2011. Continuum model of collective cell migration in wound healing and colony expansion. Biophys. J. 100: 535–43.

18. Ranft, J., M. Basan, J. Elgeti, J.-F. Joanny, J. Prost, et al. 2010. Fluidization of tissues by cell division and apoptosis. Proc. Natl. Acad. Sci. U. S. A. 107: 3–5.

19. Simpson, M.J., Treloar, K.K., Binder, B.J., Haridas, P., Manton, K.J., et al. 2013. Quantifying the roles of cell motility and cell proliferation in a circular barrier assay. J. R. Soc. Interface 82: 20130007

20. Sengers, B.G., C.P. Please, M. Taylor, and R.O.C. Oreffo. 2009. Experimental-computational evaluation of human bone marrow stromal cell spreading on trabecular bone structures. Ann. Biomed. Eng. 37: 1165–76.

21. Sengers, B.G., C.P. Please, and R.O.C. Oreffo. 2007. Experimental characterization and computational modelling of two-dimensional cell spreading for skeletal regeneration. J. R. Soc. Interface. 4: 1107–17.

22. Maini, P.K., D.L.S. McElwain, and D.I. Leavesley. 2004. Traveling wave model to interpret a wound-healing cell migration assay for human peritoneal mesothelial cells. Tissue Eng. 10: 475–82.

23. Savla, U., L.E. Olson, and C.M. Waters. 2004. Mathematical modeling of airway epithelial wound closure during cyclic mechanical strain. J. Appl. Physiol. 96: 566–74.

24. Sherratt, J. A, and J.D. Murray. 1990. Models of epidermal wound healing. Proc. Biol. Sci. 241: 29–36.

25. Tambe, D.T., C.C. Hardin, T.E. Angelini, K. Rajendran, C.Y. Park, et al. 2011. Collective cell guidance by cooperative intercellular forces. Nat. Mater. 10: 469–75.

26. Marel, A.-K., S. Rappl, A. Piera Alberola, and J.O. Rädler. 2013. Arraying Cell Cultures Using PEG-DMA Micromolding in Standard Culture Dishes. Macromol. Biosci. : 1–8.

27. Riahi, R., Y. Yang, D.D. Zhang, and P.K. Wong. 2012. Advances in wound-healing assays for probing collective cell migration. J. Lab. Autom. 17: 59–65.

28. Nikolić, D.L., A.N. Boettiger, D. Bar-Sagi, J.D. Carbeck, and S.Y. Shvartsman. 2006. Role of boundary conditions in an experimental model of epithelial wound healing. Am. J. Physiol. Cell Physiol. 291: C68–75.

29. Vedula, S.R.K., M.C. Leong, T.L. Lai, P. Hersen, A.J. Kabla, et al. 2012. Emerging modes of collective cell migration induced by geometrical constraints. Proc. Natl. Acad. Sci. U. S. A. : 1–6.

30. Guyon, E. 2001. Physical Hydrodynamics. OUP Oxford.

31. Murray, J.D. 2002. Mathematical Biology: I. An Introduction. Springer.

32. Griffiths, G., and W.E. Schiesser. 2010. Traveling wave analysis of partial differential equations: numerical and analytical methods with MATLAB and Maple. Access Online via Elsevier.

33. Rosen, P., and D.S. Misfeldt. 1980. Cell density determines epithelial migration in culture. Proc. Natl. Acad. Sci. U. S. A. 77: 4760–3.

34. Eisenmann, C., C. Kim, J. Mattsson, and D. A. Weitz. 2010. Shear Melting of a Colloidal Glass. Phys. Rev. Lett. 104: 035502.

Supporting Information

Flow and diffusion in channel-guided cell migration

Anna-Kristina Marel[†,¤,○], Matthias Zorn[†,¤,○], Christoph Klingner[†], Roland Wedlich-Söldner[‡], Erwin Frey[§,¤] and Joachim O. Rädler[†,¤,*]

SI Materials and Methods

Fabrication of microstructures and cell seeding. Poly(ethylene glycol)-dimethacrylate (PEG-DMA) microstructures were fabricated as described previously [1]. The masters used for polydimethylsiloxane (PMDS) molding were fabricated by conventional photolithography under cleanroom conditions. The PDMS prepolymer solution (Sylgard 184, Dow Corning, USA) was mixed with the curing agent in a 10:1 ratio (w/w) and degassed for 15 min. The mixture was deposited on top of the master, degassed for a further 15 min, and cured at 70 °C for 4 h. The molded stamp was then peeled off and trimmed, opening the channels at one end of the structure while leaving the other end blocked by a narrow barrier of PDMS at the other end. Immediately after activation of the PDMS by exposure to argon plasma (Diener Electronic, Nagold, Germany) for 30 s, the stamp was placed in close contact with a hydrophilic ibidi µ-dish (ibidi, Martinsried, Germany). A small drop of a freshly prepared 2 % (v/v) solution of the photoinitiator 2-hydroxy-2-methylpropiophenone in PEG-DMA (Mn = 550; both purchased from Sigma-Aldrich, Germany) was then spotted in front of the open ends of the channels, and the structures were filled spontaneously by capillary force-induced flow. The process was visually controlled under a microscope to ensure complete filling of the channels and formation of proper edges. The PEG-DMA was then polymerized for 10 min by irradiation with a UV-ozone cleaning system (UVOH 150 LAB, FHR, Ottendorf, Germany), and the structured surfaces were stored at 50 °C in a drying oven (Binder GmbH, Tuttlingen, Germany) overnight. Before cell seeding, the microstructures (with the PDMS stamps still in place) were

sterilized with 80 % ethanol for 5 min, washed three times with PBS, and covered with cell medium. Cells were seeded in front of the PDMS stamp at the closed end of the channels, and grown to confluence in a humidified atmosphere containing 5 % CO_2 at 37 °C overnight. The PDMS stamp was removed to open the PEG-DMA channels and bare the protected surface of the petri-dish which is the substrate for the migrating cell sheets. The sample was washed with fresh medium to remove non-adherent cells, and the attached cell layer began to expand towards the uncovered structures. Samples were then incubated under culture conditions until the cell front reached the entrance to the channels (typically after 2 days).

Cell culture. Doubly transfected Madin-Darby canine kidney cells (MDCK) cells stably expressing EGFP-labeled Lifeact and mCherry-labeled histone 2B were cultured in Dulbecco's Modified Eagle Medium, supplemented with 10 % fetal bovine serum (FBS), 20 mM L-glutamine, high levels of glucose (4.5 g/l) and 110 mg/l pyruvate. Cells were incubated at 37 °C in a humidified atmosphere (5 % CO_2) and grown to 80-90 % confluence before trypsinization.

Time-lapse microscopy. Migrating cell sheets were monitored by time-lapse microscopy using a motorized Nikon Eclipse Ti epifluorescence microscope equipped with a temperature-controlled mounting frame and a CCD camera (Model Clara E from Andor Technology). Image acquisition was controlled by μ-Manager open-source software and both bright-field and fluorescence images were taken every 10 min. An ibidi heating stage (ibidi GmbH, Martinsried, Germany) was used to maintain a constant temperature of 37 °C. For the measurements, cell medium was replaced by CO_2-free Leibovitz´s L15 medium, supplemented with 10 % FBS.

Visualization of cell nuclei and evaluation of cell density. Stably expressing MDCK Lifeact/H2B cells exhibited bright fluorescence localized to the cell nucleus. The fluorescence signals emanating from cell nuclei were detected using the 'find maxima' function of the open-source software ImageJ (National Institutes of Health, Bethesda, MD, USA). The appropriate threshold was adjusted manually for each movie. Using ImageJ macros written in-house, cell nuclei were evaluated in every frame,

enabling the total cell number to be determined at every time point. Based on comparisons with manual cell counts, the relative error of the 'find maxima' function was found to be under 6 %. Cell density profiles were obtained by collecting the detected cell nuclei in 50-µm wide bins along the x-direction of the channel. Using customized Matlab scripts, cell density profiles were compiled for every time point of the measurement.

Identification of the cell front. The displacement of the cell front was followed by scanning the intensity (summed in the y-direction) of bright-field images along the length of the channels. The resulting spectra showed a sharp drop in intensity immediately followed by a flat baseline, indicating the position of the cell front and the adjacent area still free of cells, respectively. A custom-written Matlab script (The MathWorks, Natick, MA) was used to detect this sharp drop by first calculating the sum over ten adjacent intensity values and subtracting it from the sum over the next ten adjacent intensity values shifted to the left from the original interval. After dividing the difference by the first of the two sums, the quotient was compared to a chosen threshold value. This process was repeated by shifting the two intervals by one pixel to the left until the quotient exceeded the threshold for the first time. The center of the whole area interrogated was defined as the position of the front. The result was plotted as a line to the movie and outliers were identified visually. Values due to outliers were deleted for appropriate time points and the resulting gaps were closed by linear interpolation.

Particle image velocimetry (PIV). Velocity fields of the moving cell layers were mapped by PIV analysis using the MatPIV software package for Matlab (The MathWorks, Natick, MA), with some minor modifications. The size of the interrogation window was 32x32 pixels (21x21 µm), with 62.5 % overlap in a single iteration. The resulting velocity vectors were filtered with a signal-to-noise ratio filter, a global histogram operator, a peak height filter and a local filter (all included in the MatPIV package) to produce smoother vector fields.

Coarse graining and time averaging. Velocity fields resulting from the PIV analysis were averaged in time and/or space. A customized Matlab script calculated the average over 2x2, 4x4 or 8x8

neighboring vectors for the coarse-graining process, placing the resulting vector on a grid point at their center. For the time averaging, a second customized script calculated the average over the vectors on a distinct grid point for all the frames in the period of observation. An average value is only calculated for grid points where a measured value was obtained at all time points, whereas grid points with no velocity values after filtering and interpolation are completely excluded. This ensures all average values are really based on the intended amount of time points, but can lead to small areas where there are no vectors that appear as white holes in the time averaged velocity fields.

Flux determination. For cell flux calculations, the cell front was chosen as the reference point. The local cell flux density was estimated from the local cell density and the averaged x-component of the flow velocity. The cell bulk was divided into 50-µm wide windows starting from the actual current position of the front. Cell flux was determined for overlapping sets ('bins') of three contiguous windows, spanning a fixed distance of 150 µm and extending 200, 250 and 300 µm away from the leading edge respectively. The cell density is averaged over several hours (from 3 to 15 h, depending on the channel) for all bins, starting at the point when the cell sheet had penetrated to a depth of 500 µm into the channel. The density gradient was calculated for all bins by linearly fitting the averaged cell density values of the selected outer windows as well as the intermediate ones. The slope gives the *dc/dx* values, which were plotted against the averaged cell density flux *J* obtained from the two selected outer windows. Due to the three combinations of outer windows, three pairs of values were obtained for every channel. The diffusion constant D_c corresponds to the slope of the plot of *J* against *dc/dx*.

Fit of the Fisher-Kolmogorov equation. The averaged density profile was fitted with the analytical solution of the Fisher-Kolmogorov equation (see equation S1) taken from [2].

$$c(x,t) = K \cdot \left\{ \left[1 + \exp\left[-\frac{5}{6} \cdot \lambda + \sqrt{\frac{\lambda}{6D_c} \cdot (x + 400)} \right] \right] \right\}^{-2} \qquad \text{[Eq. S1]}$$

Here, *K* denotes the carrying capacity of the system, D_c is the collective diffusion coefficient and lambda is the growth rate, which is fixed to 0.0283 h^{-1} as determined by Eq. S5. While the x-offset can be varied, 400 was chosen as it led to the best agreement of the fit shape with the empirical data points while keeping both yielded fit parameters (D_c and K) within the expected range.

Analysis of vorticity. The vorticity was derived from the flow fields by a customized Matlab script after coarse graining. The spatial averaging (30x30 µm²) was chosen in such a manner that each grid point approximately corresponded to the area of one actual cell. For each grid point i (located at $\mathbf{r}_i$), the relative velocity $\mathbf{v}_{ij}=\mathbf{v}_j-\mathbf{v}_i$ of each of the eight nearest-neighbor grid points j (located at r_j) was projected onto the vector $\mathbf{r}_{i,j}=\mathbf{e}_z \times \mathbf{r}_{i,j}$, and divided by the squared distance of the relative position vector $r_{i,j}=\mathbf{r}_j-\mathbf{r}_i$. Given the definition $\mathbf{e}_z=\mathbf{e}_x \times \mathbf{e}_y$, the resulting vorticity Ω obtained after averaging over all neighbors (see equation S2) is positive for counter-clockwise rotation [3].

$$\Omega_i = e_z \cdot (curl \cdot v)_i \qquad \text{[Eq. S2]}$$

For the heatmaps generated, the direction of rotation was irrelevant and the vorticity values obtained were squared, providing an image of the distribution of magnitudes. This whole process was repeated for each time point, resulting in a movie of the chronological formation and decay of vortices.

Single-cell tracking. The trajectories of individual cells used for MSD analysis were traced automatically with the software OPEN BOX (Informationssysteme Schilling, Munich, Germany).

The chosen particle is located in each image with an implemented Gaussian correlation algorithm at pixel precision. After application of a median filter (3x3 square), each image was correlated with the previous image, choosing a reasonable maximum velocity per frame based on the observed speed of cells in the experiment.

Drift correction. Cell tracks obtained from the flowing cell sheets were centered by subtracting a constant drift velocity from each time step. This drift velocity is obtained by comparing how centered the resulting tracks are in dependence on the chosen subtracted velocity. For each cell track, an individual drift speed is chosen so that for the resulting, corrected track, the average displacement of all track points from the initial track point in x-direction is zero.

Determination of mean squared displacement (MSD). Mean squared displacement analysis was performed with a customized Matlab script, calculating the squared displacement (d^2) between each point in the cell track and the point Δt later, averaging over all possible starting points t_0 in time, and repeating the process for all larger Δt.

$$< d^2 >=< (\boldsymbol{X}_i(t_0 + \Delta t) - \boldsymbol{X}_i(t_0))^2 >_i \qquad \text{[Eq. S3]}$$

Here, $\mathbf{X}_i(t)$ denotes the track position of cell i at a given point in time t and $<\cdot>_i$ indicates the ensemble average over all cells.

Cell doubling time. Cells were homogenously seeded on top of PEG-DMA channels and grown to confluence. Further proliferation was followed by time-lapse microscopy. Labeled nuclei were identified using the 'find maxima' function of the open source program ImageJ for every time point. Exponential cell growth given by

$$N(t) = N_0 \cdot e^{\lambda t} \qquad \text{[Eq. S4]}$$

where N is the cell number and λ is the growth rate, was confirmed by the linear increase of the logarithmic representation for different channel widths. The growth rate was calculated to be λ = 0.0283 ± 0.0005 h^{-1}. The corresponding doubling time t_D was calculated using equation S5:

$$\lambda = \frac{ln2}{t_D} \qquad \text{[Eq. S5]}$$

In the present case, we obtained a doubling time of t_D = 25.2 ± 4.2 h for a confined MDCK monolayer in a state of equilibrium.

Figures:

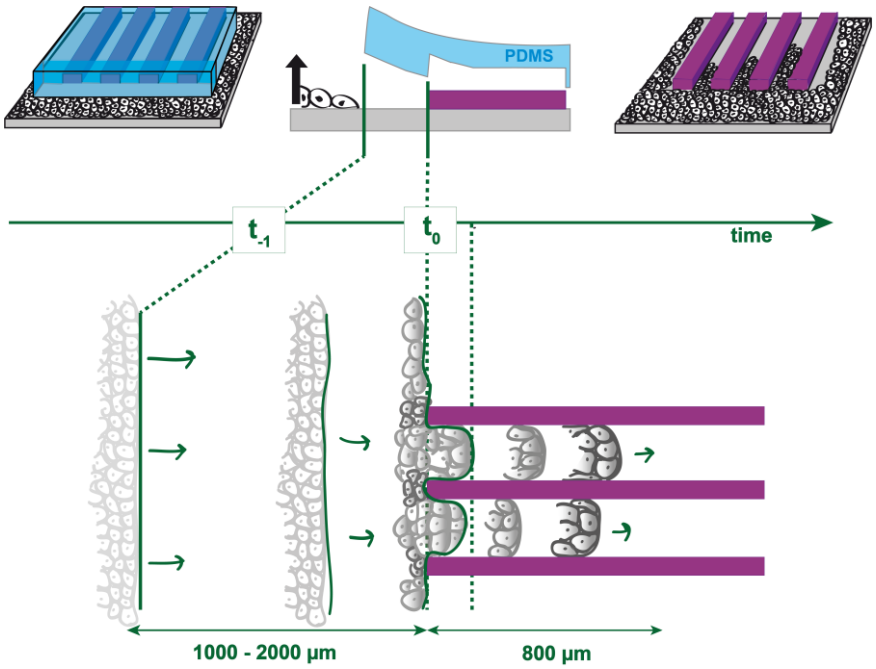

Fig.S1. Description of the experimental time course. Cells are grown in front of the PDMS stamp which protects the microchannels from cell adhesion. The PDMS mold is removed at time t_{-1} releasing a straight cell front of the confluent MDCK monolayer. The sheet starts to expand towards the microstructured PEG-DMA channels, bridging a gap of 1000 to 2000 µm. Measurements were started when the cell front reaches the channel entrances (t_0). Note that the cell density is decreased in comparison to the location of the initial release. We observed cell crowding at the cross section of the channel walls, however, cells tend to glide along the PEG-DMA entering either of the channels. We followed cell sheet invasion up to a penetration length of approxemately 800 µm.

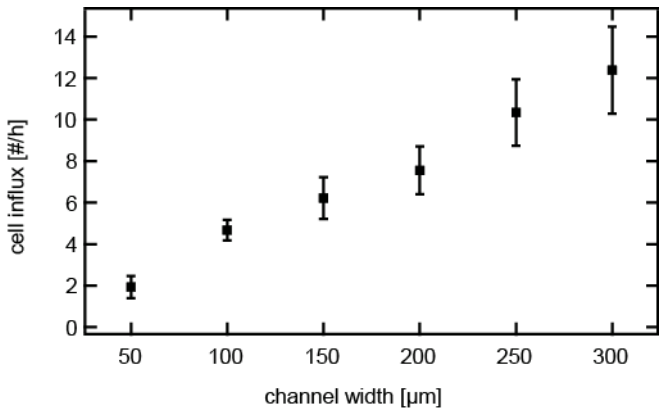

Fig. S2. Rates of cell influx were determined by analysis of a kymograph at the channel entrance. A one-line kymograph was generated over the whole movie, and the number of cells passing the line was established by counting fluorescently labeled nuclei. The average number of cells crossing the line per hour was calculated. The plot shows that cell flux increases linearly with channel width.

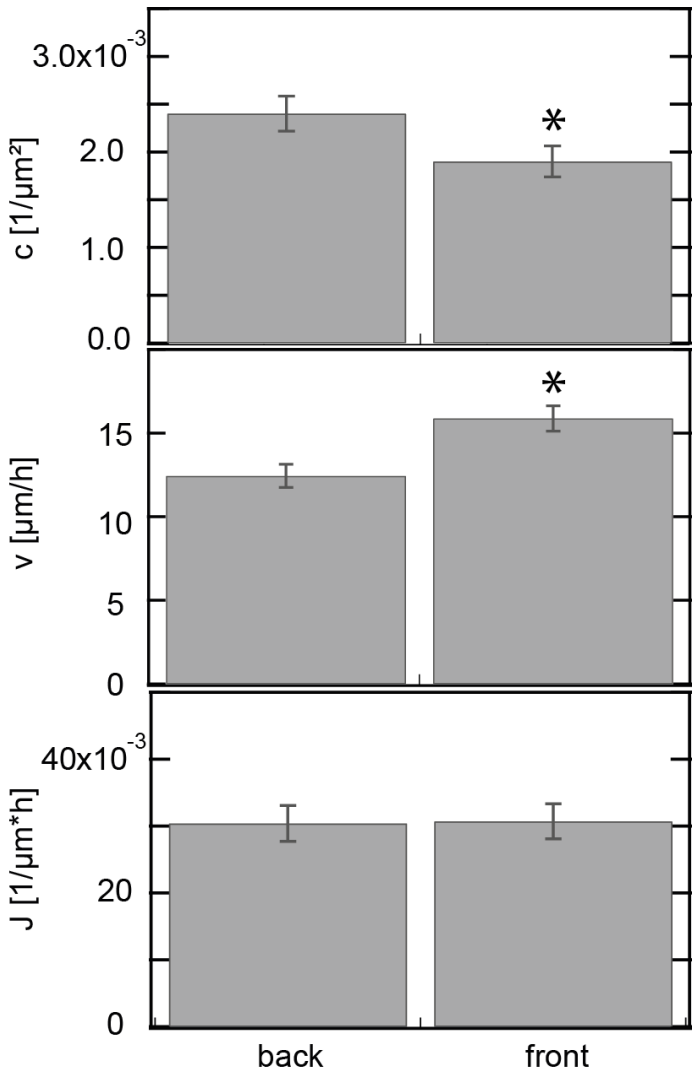

Fig. S3. Average cell densities, velocities and cell fluxes close to the cell front (200 µm) and farther back (350 µm from cell front). Analysis of the time averaged quantities in both positions, averaged over all measurements, revealed that the cell density at the front was statistically significantly lower than further back, while the cell velocity was significantly higher. The cell flux appears to be about equal. Statistical significance was determined with a paired student t-test and significance assumed for $p \leq 0.01$. Error bars depict standard errors.

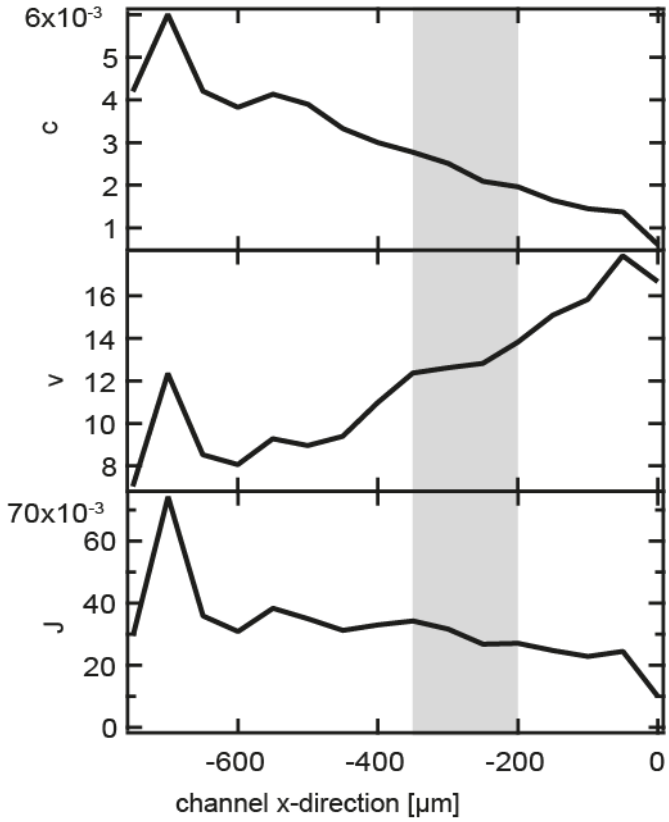

Fig. S4. Time-averaged profiles along the channel for cell density (c, in cells per µm²), local velocity (*v*, in µm/h) and cell density flux (*J*, in 1/µm²·h). Values are averaged with respect to the position of the front. The example shown is for a channel of 200-µm width and all time points of invasion deeper than 500 µm were considered. The shaded zone highlights the area of one pair of bins (bins 4 and 7) that were used to determine the diffusion constant in Fig. 4*D*. In the shaded areas, note the gradients in density and velocity, as well as the relative constancy of the flux rate.

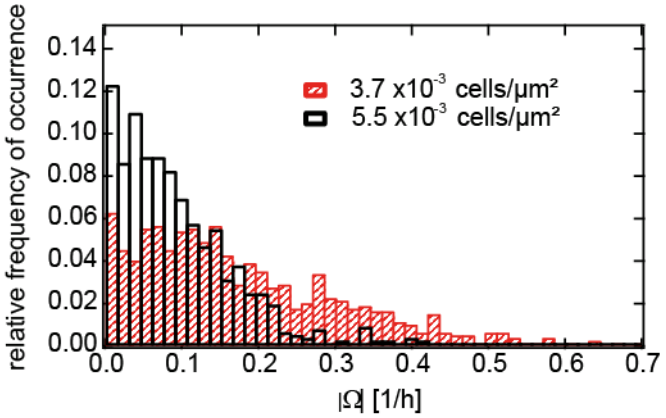

Fig. S5. Distribution of vorticity magnitudes. The magnitude of vorticity of a confluent, confined monolayer was calculated for every grid point for one time point of low (red) and high (black) cell density. Since the frequency of vortex formation decreases with increasing cell density, the distribution gets narrower as vorticity magnitudes decrease.

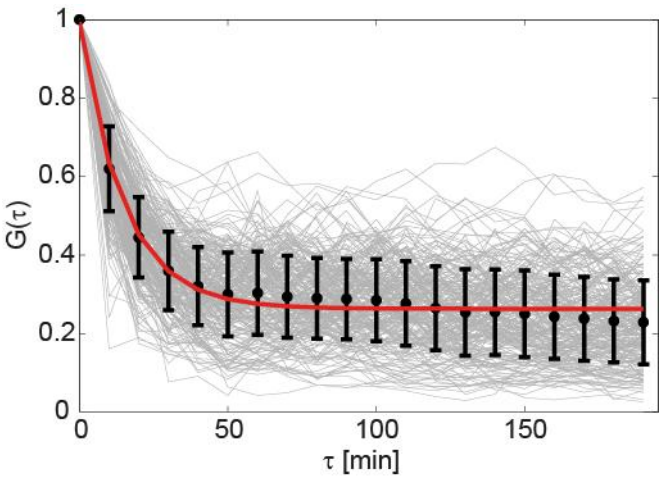

Fig. S6. Relaxation time of vortices in confluent cell layers. The standardized correlation *G(τ)*, corresponding to the normalized autocorrelation function on each grid point, was calculated as:

$$G(\tau) = \frac{\langle \Omega(t) \cdot \Omega(t+\tau) \rangle}{\langle \Omega^4 \rangle}$$

where Ω is the vorticity. The gray traces correspond to the time evolution of individual coordinates. The average over all curves is indicated by the black points. An exponential decay curve was fitted (red curve) to these mean values, yielding a relaxation time of t_R=15 min (defined as the interval over which *G(τ)* has drops to 1/e of the difference between *G(0)* and the non-zero asymptotic value of *G(τ)* for large τ).

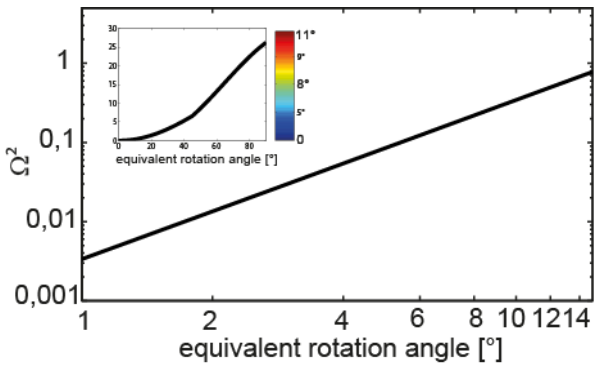

Fig. S7. Equivalent rotation angle corresponding to squared vorticity values (Ω^2). The vorticity value for each rotation angle is calculated from the displacement and relative velocities for eight neighboring cells that rotate by precisely that amount around a center point, collectively and in unison. This yields an approximate measure of the relationship between the squared vorticity values plotted in the heatmaps and the angular magnitude of the rotation actually performed by the cells. The main plot displays the range of rotation angles found in experiments on a logarithmic scale, while the insert shows the full range from 0 to 90° rotation. The nonlinear color scale relates these values to the colors used in the heatmaps in Figure 6.

Supporting References

1. Marel, A.-K., Rappl, S., Piera Alberola, A., and Rädler, J. O., 2013. Arraying Cell Cultures Using PEG-DMA Micromolding in Standard Culture Dishes. Macromol. Biosci., 1–8.

2. Griffiths, G., and Schiesser, W.E. 2010. Traveling Wave Analysis of Partial Differential Equations: Numerical and Analytical Methods with Matlab and Maple. Academic Press.

3. Heidemann, R., Zhdanov, S., Sütterlin, K. R., Thomas, H. M., and Morfill, G. E., 2011. Shear flow instability at the interface among two streams of a highly dissipative complex plasma. EPL, 96: 15001.

Movies (frame rate: 1/10 min, video is played at 10 frames per second)

Movie S1: Brightfield images of MDCK cells migrating into a PEG-DMA channel (scale bar: 50µm)

Movie S2: Migration of MDCK cells with fluorescently labeled cell nuclei into a PEG-DMA channel (scale bar: 50µm)

Movie S3: Detection of the leading edge of MDCK cells migrating into a PEG-DMA channel (scale bar: 50µm)

Movie S4: Brightfield images of migrating MDCK cells overlaid by calculated velocity field (scale bar: 50µm)

Movie S5: Velocity field of MDCK cells migrating into a PEG-DMA channel (scale bar: 50µm)

Movie S6: Velocity field of a resting MDCK sheet inside a PEG-DMA channel (scale bar: 50µm)

Movie S7: Magnitude of vorticites of migrating MDCK cells (size of the squares: 30x30 µm)

Movie S8: Magnitude of vorticites of resting MDCK cells (size of the squares: 30x30 µm)

Manuscript 2 [M2]

Alignment of cell division axes in directed epithelial cell migration

Anna-Kristina Marel[1], Nils Podewitz[2], Matthias Zorn[1], Joachim Oskar Rädler[1] and Jens Elgeti[2]

[1]Fakultät für Physik, Ludwig-Maximilians-Universität, Geschwister-Scholl-Platz 1, 80539 München, Germany
[2]Theoretical Soft Matter and Biophysics, Institute of Complex Systems (ICS-2), Forschungszentrum Jülich, 52425 Jülich, Germany

Submitted to 'New Journal of Physics'

Alignment of cell division axes in directed epithelial cell migration

Anna-Kristina Marel[1,3], Nils Podewitz[2,3], Matthias Zorn[1], Joachim Oskar Rädler[1], and Jens Elgeti[2†]

[1]Fakultät für Physik, Ludwig-Maximilians-Universität, Geschwister-Scholl-Platz 1, 80539 München, Germany

[2] Theoretical Soft Matter and Biophysics, Institute of Complex Systems, Forschungszentrum Jülich, 52425 Juelich, Germany

E-mail: `j.elgeti@fz-juelich.de`

Abstract. Cell division is an essential dynamic event in tissue remodeling during wound healing, cancer and embryogenesis. In collective migration, tensile stresses affect cell shape and polarity, hence, the orientation of the cell division axis is expected to depend on cellular flow patterns. Here, we study the degree of orientation of cell division axes in migrating and resting epithelial cell sheets. We use microstructured channels to create a defined scenario of directed cell invasion and compare this situation to resting but proliferating cell monolayers. In experiments, we find a strong alignment of the axis due to directed flow while resting sheets show very weak order. The observed effects are reproduced by computer simulations based on a mesoscopic particle approach.

[3]These Authors contributed equally to this work.

PACS numbers: 87.19.xj,87.19.R-,87.55.Gh

Submitted to: *New J. Phys.*

1. Introduction

The positioning and orientation of the cell division axis is a key element during the development of multicellular organisms and to maintain the functionality of the tissue. Many examples of pattern formation have been found in the developing embryo depending on emerging anisotropies in cell division, such as the imaginal wing disc of Drosophila [1]. These observations imply that the understanding of cell division orientation is fundamental. Single cell experiments have shown that the orientation of the cell division plane is determined by many factors such as cell shape, cell polarity and the spatial distribution of the extracellular matrix [2, 3, 4]. The orientation of cell division within tissues, however, is less well studied. Madin-Darby canine kidney (MDCK) cells are a widely used model system to study growing motile tissues [5, 6, 7, 8]. This epithelial cell line exhibits strong cell-cell junctions and grows as a polarized and continuous monolayer in culture [9, 10]. Cell division usually occurs within the plane of the epithelium, producing two daughter cells that remain within the cell sheet [11]. Cells continue to divide at confluent level with decreasing division rates until a maximum density is reached [7]. At the same time, cell motility is reduced with increasing cell density, displaying a glass-like transition in cellular behavior [12]. In general, directed cell migration can be initiated by introducing a model wound in the cell sheet, creating a new, free surface [8]. Cells spontaneously start to migrate and proliferate in order to close the gap, displaying striking features like the formation of fingers [13] and leader-cells [8]. During collective migration of cell sheets, forces are exerted on the substrate, leading to the development of a global tensile stress within the layer [14]. Individual cells react to generated stresses by changing their shape to elongated architectures or rearranging within the tissue in order to locally reduce the stresses. The orientation of the mitotic spindle is predicted to self-organize during cell division due to mechanical forces. As early as 1884, Oscar Hertwig proposed a simple concept, known as the "long axis rule", implying that the axis of the spindle lies in the direction of the longest axis of the cell, cutting this axis transversely [15]. As a consequence, the possible correlation between emerging forces during collective migration and cell division orientation is an interesting issue. Poujade *et al.* investigated the orientation of cell divisions in the central region of expanding, stripe shaped MDCK monolayers, finding no preferred direction of the division axis [8]. At the rim of the expanding culture, however, finger formation promotes strong correlation of cell division axis and polarity with the main finger direction as proven by Reffay *et al.* [6]. A majority of the motility phenomena were explained recently by a simple mechanical model of growth [16] combined with a local orientation mechanism of cellular motility that does not require any alignment force from the neighboring cells, or chemical gradients to determine the direction of cell migration. This simple model was able to reproduce the glassy transition for confluent monolayers, finger formation at invading fronts, and the tension in expanding cell sheets [17].

In this work, we study the orientation of cell division axes in flowing and resting

epithelial monolayers and compare the experimental results to a computational model. We use microstructured channels to create a directional cell flow of migrating and proliferating cells. The distribution and orientation of the cell division events as a function of cell density and distance to the leading edge were analyzed. We demonstrate that cell divisions are significantly oriented by the emergent cell flow in contrast to the scenario of cells in resting, confluent monolayers within the same channels. Computer simulations based on the algorithm developed by Basan et al. [17] are able to reproduce the experimental results qualitatively, without further adaption of the parameters. Both the experimental data as well as simulations suggest a tight coupling between the direction of collective cell migration and the orientation of the cell division axis.

2. Results

In order to study the influence of directed cell growth on the orientation of cell division axes, we confine expanding epithelial cell sheets in microchannels. Using micromolding in capillaries, the cell-repellent polymer poly(ethylene glycol)-dimethacrylate (PEG-DMA) is shaped by a structured polydimethylsiloxane (PMDS) mold and cross-linked by UV irradiation [18]. Madin-Darby canine kidney (MDCK) cells are grown to confluence in front of the mold. After removal of the PDMS, the cells start to migrate into the three dimensional PEG-DMA channels of different widths ranging from 200 µm–300 µm, corresponding to approximately fifteen to twenty cell diameters (see Figure 1). The expansion of the cell sheets is followed by time lapse microscopy over 10 h–35 h. We use stably transfected MDCK cells expressing mcherry labeled 2B histones, resulting in bright and located fluorescence of cell nuclei. Thus, the cell density can be identified by automated counting of cell nuclei. The local velocity field is determined by particle image velocimetry (PIV) analysis.

We compare the experimental results to particle based computer simulations. The model, as described in Ref. [17], is used without any parameter modifications. In short, cells are represented by two point particles, which interact with particles of other cells like sticky, soft colloids. The particles of one cell repel each other and cell division is initiated when a critical distance is reached. Additionally, cells can be in a non-motile or motile state. By switching into the motile state with a constant rate, cells pull in a random direction with a constant motility force. The rate of turning non-motile is dependant on the alignment of the motility force with the cell velocity (alignment results in lower rate than non-alignment).

2.1. Flow and density profiles in invading cell sheets

We study the orientation of cell division axes in confined, growing MDCK monolayers experimentally. First, we characterize the flow profile of the invading sheets for different channel widths (see Figure 1). The displacement of the leading edge is monitored by the analysis of the averaged intensity profile of the brightfield images. The leading cell

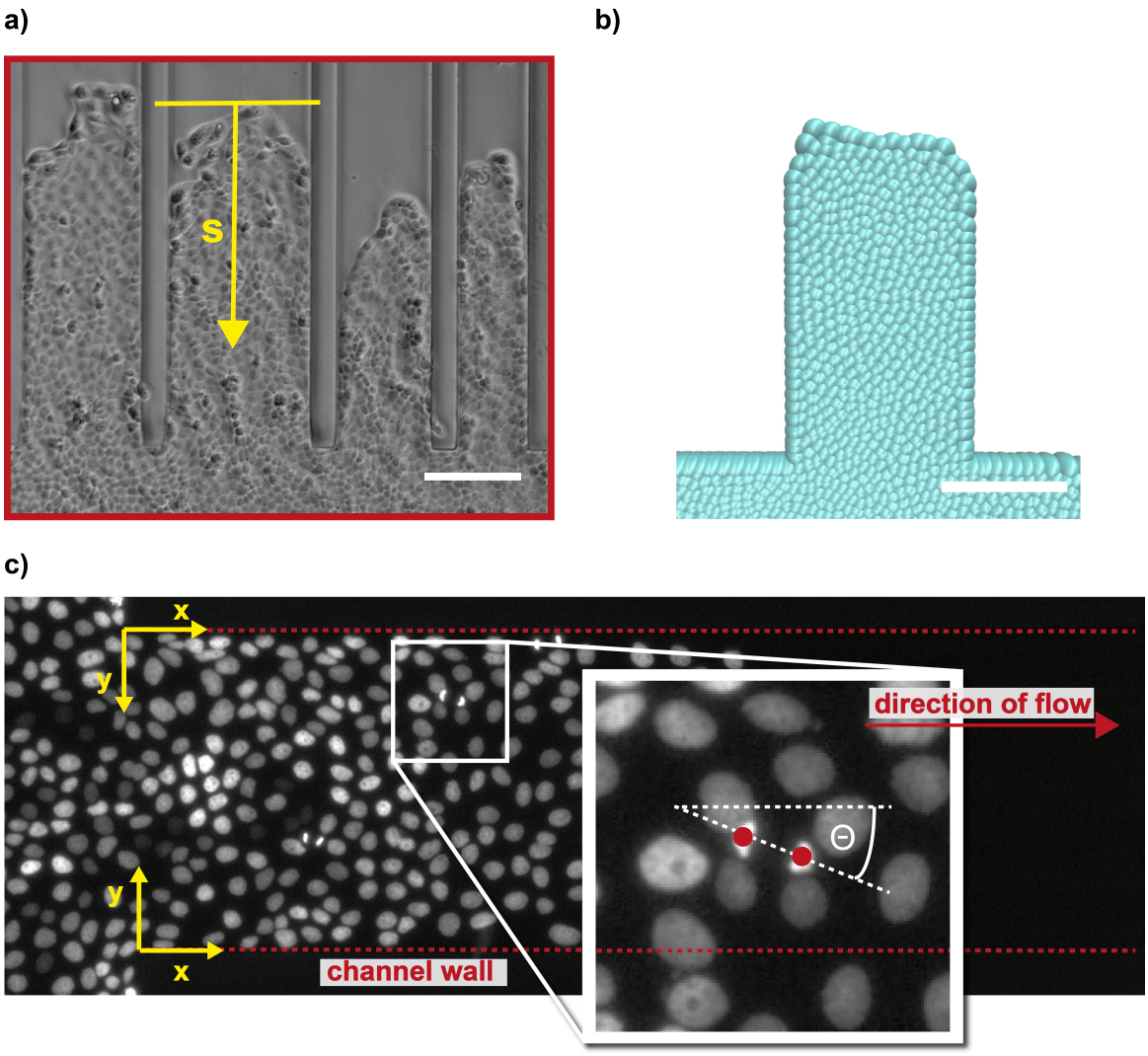

Figure 1. Cell sheets invading channels in experiment and simulation. a) Growing cell monolayers are confined by three-dimensional PEG-DMA microchannels. MDCK cells expand into channels of different widths. The x-coordinate runs along the channel from the entrance towards the front, s measures the distance from the front, while y is the distance from the wall. See also supplementary movies. (Scale bar corresponds to 200 µm) **b)** Computer simulation of cell proliferation and invasion into a narrow channel. (Scale bar corresponds to 200 µm) **c)** The cell division axis **d** is defined as the vector between the nuclei of the two daughter cells. The angle Θ denotes the deviation between the division axis and the x-direction of the channel.

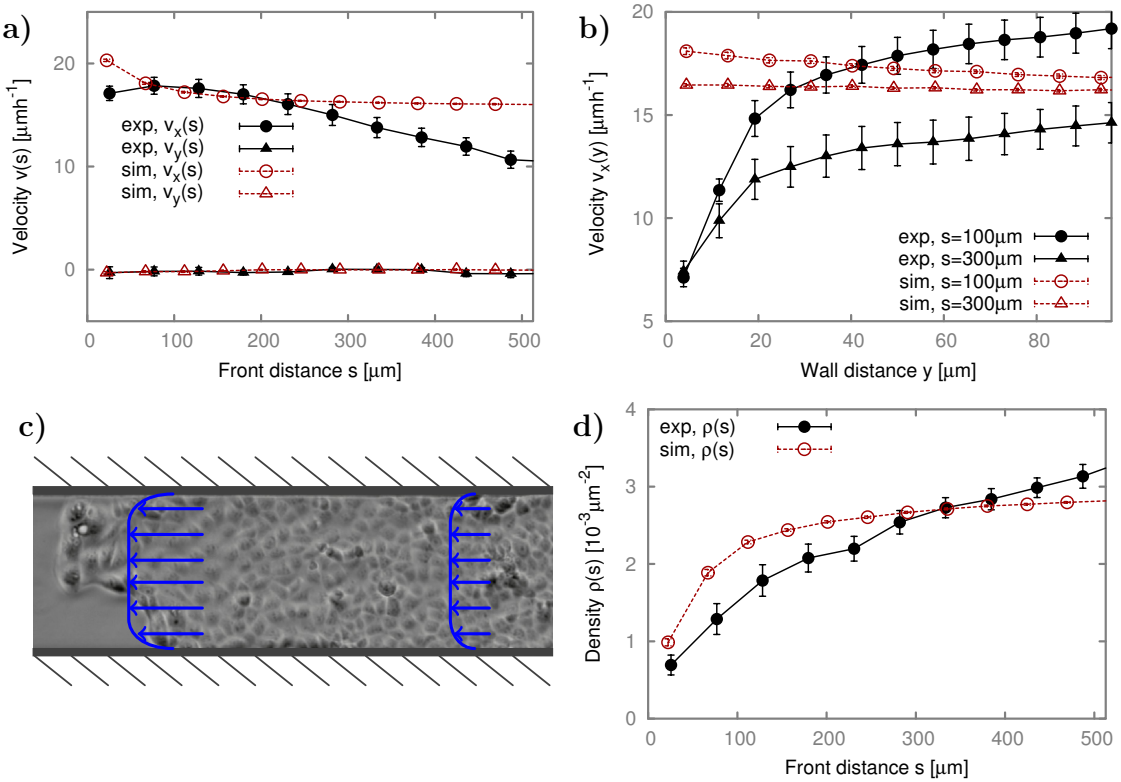

Figure 2. Velocity profiles and density distribution in invading cell sheets. **a)** Cellular velocity v_x as a function of the distance s to the front, as determined by PIV. The speed maximum is behind the front. Note, however, that the PIV analysis has a higher error closer to the interface. **b)** Velocity profiles as a function of distance from the wall y for different distances from the front s. **c)** Sketch of the velocity profiles at different distances from the front for an invading cell sheet. **d)** Cell density ρ as a function of the distance s to the front.

front advances at a constant speed of about $(22 \pm 5)\,\mu m/h$, independent of the channel width and invasion length. Additionally, a clear increase of the average velocity from bulk towards the front of the invading cell sheet is measured as shown in Figure 2a. The flow component in y-direction of the channel is negligible. Perpendicular to the channel walls, a flow profile is observed which is neither parabolic nor a simple plug flow (Figure 2b). The local velocity is reduced by a factor of three from the center of the channel towards the walls, referring to finite slip boundary conditions. During the expansion of the cell colony, a density gradient developed along the channels with increasing cell densities from about 1 cell per $1000\,\mu m^2$ at the front to 2.5 cells per $1000\,\mu m^2$ roughly $400\,\mu m$ behind the front (see Figure 2d).

The simulations show a constant invasion velocity, independent of channel width and penetration length, in agreement with the experimental results. The velocity profiles along the channels displays the same trends as observed in the experimental data, however, simulations yield an almost perfect plug flow profile across the channels. The density profile on the other hand is consistent between simulations and experiments (see

Figure 2d). The similarity in the density profile shape as well as the constant invasion velocity suggest these quantities as units of measure to rescale the simulation results to physical units (for detailed information see Materials and Methods).

2.2. Orientation of the cell division axis

The question we asked is to what extent cell division events are affected by the emergent flow in the expanding cell sheets. The axes of individual cell divisions are determined by identifying the position of the two daughter cells directly after division. The angle between the division axis and the x-direction of the channel is denoted with θ as described in Figure 1c. The orientation of the cell division $\boldsymbol{d}$ is represented by a (mirror-symmetric) axis, and thus best described by the nematic order tensor

$$Q_{ij} = 2 < d_i d_j > -\delta_{ij}, \tag{1}$$

which is often used in the context of liquid crystals. The indices i and j represent the spatial directions. The order of one orientation relative to another, however, can be described by a simple scalar quantity:

$$S_b^a = 2 < \boldsymbol{a} \cdot \boldsymbol{b} > -1 \tag{2}$$

with the unit vectors $\boldsymbol{a}, \boldsymbol{b}$ for the two directions. Here, we define divisional order relative to the x-axis of the channel

$$S_x^d = e_x Q e_x = 2 < \cos^2\theta > -1. \tag{3}$$

$S_x^d = 0$ characterizes isotropy, while $S_x^d = 1$ reflects perfect alignment of the cell division axis with the x-axis as illustrated in Figure 3a.

We find a significant alignment of the cell division axis in the bulk of the invading cell sheet, displaying order in the range of $S_x^d = 0.2$ to 0.5 (see Figure 3b). Towards the leading edge, however, the order parameter drops to negative values, indicating an orientation of the axis perpendicular to the channel. This phenomenon of division axis alignment perpendicular to the expansion direction (i.e. in the plane of the front), can also be seen in the videos of the experiments (see supporting information).

Computer simulations are able to quantitatively reproduce the orientation of cell division axes. We find deviations close to the boundaries of the cell sheet (at the leading edge and the channel walls) between experiment and model, however, if boundaries are not taken into account, agreement is quantitative (see Figure 3b, note that order is dimensionless, and thus without adjustable parameters or units).

It is known from literature [14, 19, 20] that a tensile stress is built up in advancing cell layers. As no direct stress measurements are accessible from the experimental data, we focus instead on the strain rate tensor

$$E_{ij} = \frac{1}{2}\left(\frac{\mathrm{d}v_i}{\mathrm{d}x_j} + \frac{\mathrm{d}v_j}{\mathrm{d}x_i}\right). \tag{4}$$

In fluids (and most often in complex fluids as well), the stress tensor is directly proportional to the strain rate tensor. This tensor gives the deformation rates in

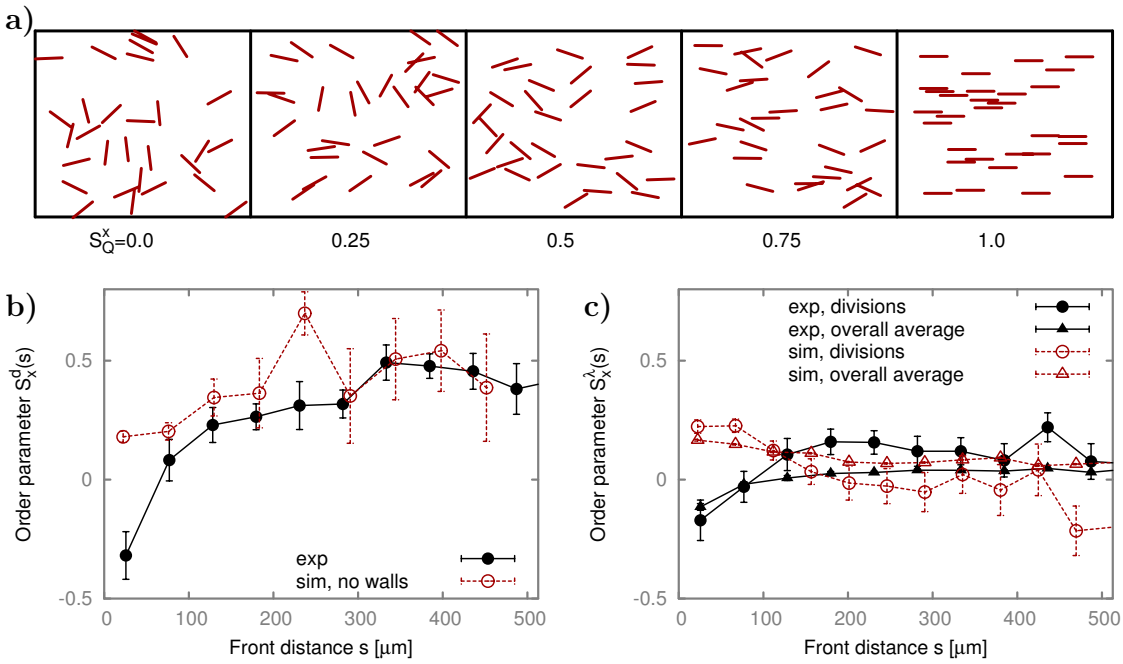

Figure 3. The order of division axis in flowing cell sheets. a) Visualization of the order parameter. $S^d_x = 0$ is isotropic, while $S^d_x = 1$ is perfect alignment of the cell division axis with the x-axis. **b)** Orientation of division axis with respect to the x-axis S^d_x as a function of the front distance s. "sim, no walls" displays the order in the simulations if particles closer than 42 µm to the walls are excluded from the evaluation. **c)** Orientation of the eigenvector of the greatest eigenvalue of the velocity gradient tensor S^λ_x with respect to the x-axis, as a function of the front distance s at division sites and as average over all positions.

all directions at each point and is symmetric by construction. The eigenvector λ, belonging to the larger eigenvalue λ_1 of the diagonalized tensor, gives the direction of largest extensile flow (or least contractile flow) and will be called "main axis". The difference between the largest and the smallest eigenvalue $p = \lambda_1 - \lambda_2$ is the dipolar flow contribution, while the sum of the two is the divergence of the flow. Figure 2a shows a positive divergence behind the front, which is thus indicative of an expanding tissue (instead of a cell inflow from the channel entrance). The main axis of the strain rate tensor is evidence for the main axis of stress via the coupling between strain rate and stress tensor. We find the main axis of the strain rate tensor to be aligned with the x-axis, in particular at the points of division (see Figure 3c). The degree of order, however, is much smaller than the orientation of the division axis. Our observations support the assumption that the cell division axis self-organizes in the direction of the maximal stress.

2.3. Boundary effects on cell division orientation

The orientation of the cell division axis shows a strong alignment with the main direction of the flow, however, we can not exclude an extensive effect of the channels wall

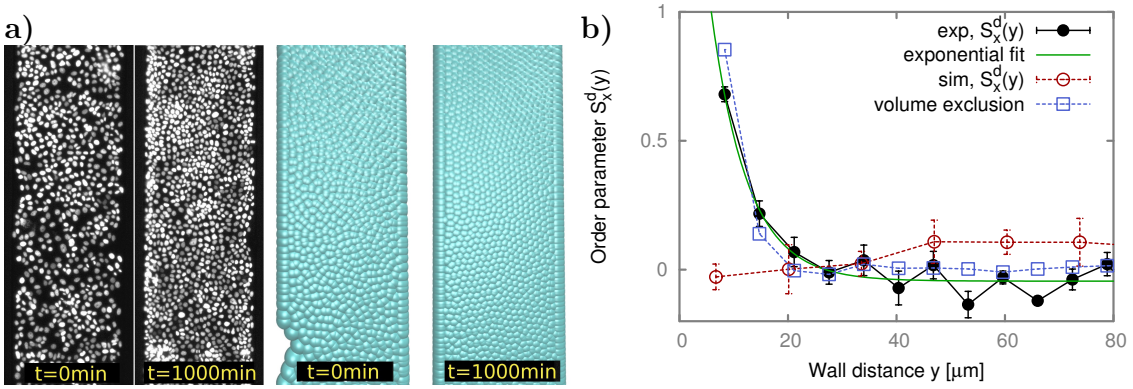

Figure 4. The order of cell division axes in resting cell sheets. a) Cells are seeded uniformly over the channel forming a confluent monolayer. During subsequent growth, divisions and velocities are tracked. Snapshots at early and late times for experiments and simulations are shown (channel width is 300 µm for the experiment and 270 µm for the simulation. The density is $2.6/1000\,\mu m^2$ at $t = 0$ min and $4.4/1000\,\mu m^2$ at $t = 1000$ min in both cases. **b)** Order parameter S_x^d between the division- and the x-axis as a function of distance y to the wall. Note that $+1$ corresponds to perfect alignment, while -1 indicates perpendicular alignment to the x-axis and 0 reflects isotropic orientation.

influencing cell division events. In order to separate influences on the cell division axis generated by cell flow from boundary effects, we generated a closer-to-equilibrium scenario of non-flowing tissues within identical PEG-DMA channels. Confined cell monolayers are prepared by uniform cell seeding over the whole microstructures. Cells sediment and adhere solely inside the three-dimensional channels due to the cell-repellent properties of PEG-DMA (Figure 4a). A confluent and resting MDCK monolayer is formed and analyzed in terms of cell division events, cell density effects and the local velocity fields.

The order parameter S_x^d indicates a nearly isotropic distribution of the cell division axis orientation for the bulk of the channels (Figure 4b). Cell division events close to the PEG-DMA walls, however, show almost perfect order and are strongly aligned with the confinement. This effect declines over roughly one cell layer and is well described by the assumption of total randomness in cell division orientation under constraint. In order to verify this assumption and compare it to the experimental data, we randomly draw center of mass positions and division angles from uniform distributions with a fixed daughter distance of $l = 16\,\mu m$. We define a division axis as the line connecting the positions of two daughter cells. All events, where the resulting division axis penetrates the wall, are discarded (see Appendix A for details). Therefore, the range of possible orientations at distances smaller than the average distance between daughter cells decreases, i.e. leading to an increased alignment of the division axis with the wall. The resulting divisional order is shown in Figure 4b and demonstrates a very good agreement with the experimental data.

The particle based simulations reproduce the random orientation of cell division axes in

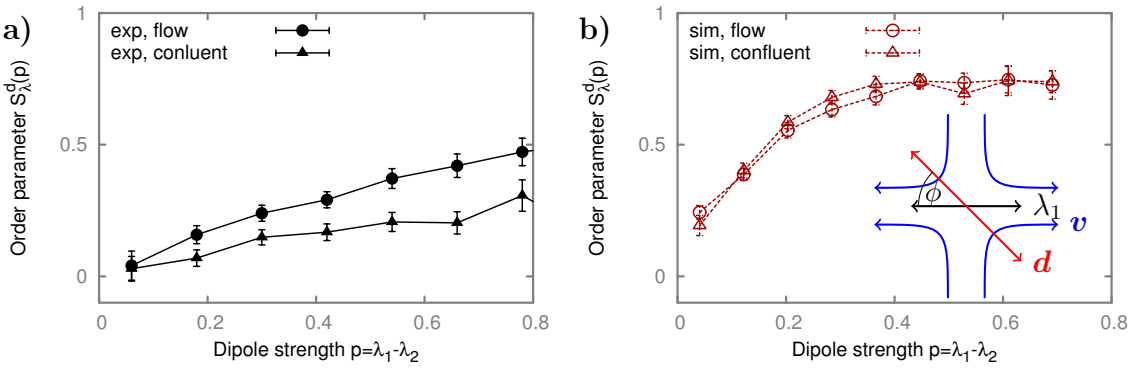

Figure 5. Alignment of divisions with local flow gradients. Degree of alignment of the division axis $\boldsymbol{d}$ with the flow gradient, represented by the eigenvector to the greatest eigenvalue λ_1 of the strain rate tensor, as a function of the dipolar strength of the velocity gradient $p = \lambda_1 - \lambda_2$, for experiments **a)** and simulations **b)**. Error bars are standard error of mean, calculated from all division events. The inset in **b)** shows a sketch of a division axis and the eigenvector of the drawn velocity field.

the bulk of the cell sheet, and, contrary to the experimental observations, show unbiased cell divisions close to the channel walls. Based on the observations in the resting cell monolayer, we can conclude that the observed alignment of the cell division axis in flowing cell sheets is mainly caused by the global orientation of cell flow.

2.4. Cell division orientation and local flow fields

So far, the divisional order has only been examined on large scales. Cells, however, have no known mechanism of sensing large scale variables like their distance from the front of the sheet. Thus, the order should only depend on *local* variables. In this section, we study the dependence of division axis alignment on measurable local variables.

Due to broken Galilean invariance, symmetry allows for the orientation of the division axis by the velocity vector which would not be possible without an underlying substrate. Note, that while the degree of alignment with the $x-$axis increases with distance from the front, the $x-$velocity decreases. This contradicts assumptions of flow aligning divisions, as opposed to flow gradients. Furthermore the average order between the local velocity vector and the division axis is only 0.16 ± 0.014 for the flow experiments, and 0.06 ± 0.014 for the no-flow experiments (errors are standard deviation of mean). We interpret the (small) positive correlation in the flow experiments as a common cause correlation as both the local velocity vector and the division axis are on average parallel to the $x-$axis. As discussed above, it is known that mechanical stresses orient cellular divisions. Moreover, this is a requirement in theoretical works explaining fluidization of tissues due to cellular division [21], which suggest treating tissues as fluids on time scales greater than the division time. It thus stands to reason that cellular divisions should be oriented by local flow gradients, which we investigate in the remainder of the

section. To study correlations between the local flow gradients and division orientation, we calculate the average order of divisions in direction of the flow gradients:

$$S_\lambda^d = 2 < \cos^2 \phi > -1, \tag{5}$$

where ϕ is the angle between the division axis, and the eigenvector corresponding to the largest eigenvalue of the strain rate tensor (see Figure 5). We find a clear correlation with an average value of $S_\lambda^d = 0.29 \pm 0.67$ between divisions and the strain rate tensor in the invading cell sheets. Indeed, the degree of alignment scales linearly with the dipolar strength of the strain rate tensor, defined as the difference of the largest and smallest eigenvalue. In confluently plated, resting cells, the degree of alignment to the local flow gradient is also present but smaller ($S_\lambda^d = 0.15 \pm 0.71$).

Closer analysis of the local velocity field reveals that division events seem to be overall contractile, with $< \mathrm{div}(v) >= -0.10\,\mathrm{h}^{-1}$ for the flow experiments and $< \mathrm{div}(v) >= -0.11\,\mathrm{h}^{-1}$ for confluently plated cells. In contrast, the overall flow field in the bulk showed positive divergence for flow experiments (see Figure 2). For the confluently plated cells the overall divergence is close to zero. Furthermore, fluctuations are large with a standard deviation of $\sigma = 0.34\,\mathrm{h}^{-1}$ in both experiments. With over 2500 observed divisions, the mean is still clearly statistically significant, should, however, be taken with care. More intuitively, the divisions have a strong positive dipolar flow field with $< \partial_\parallel v_\parallel - \partial_\perp v_\perp >= 0.16\,\mathrm{h}^{-1}$ on average in the flow experiments and $< \partial_\parallel v_\parallel - \partial_\perp v_\perp >= 0.07\,\mathrm{h}^{-1}$ on average in the confluently plated cells (where $\parallel$ and $\perp$ denote parallel and perpendicular direction to the division axis respectively). Fluctuations are large, however, with a standard deviation of $\sigma = 0.36\,\mathrm{h}^{-1}$ and $\sigma = 0.38\,\mathrm{h}^{-1}$ respectively. Note, that we calculate derivatives (see Materials and Methods for details) as close to the moment of division as possible by choosing the frame just prior the appearance of the daughters. At the moment of division, cells round up and subsequently respread into the tissue, which might bias the results. By choosing an excluded area larger than the cell, when calculating the gradients, we avoid the directed motion inside the dividing cell. Studying the same quantities two or three frames earlier shows significant differences. In the invasion experiments, for example, $< \mathrm{div}(v) >$ changes from $0.18\,\mathrm{h}^{-1}$ in the frame where the daughters appear to $-0.38\,\mathrm{h}^{-1}$ 40 min earlier. Investigating the flow gradients along the cells trajectory prior to the division event in a more detailed study, will enable examination of the growth and orientation phase.

The simulations show an even stronger alignment with the local flow gradient, independent of global flow. Here, cell divisions align with the least compressional or most tensional direction, since the model consists only of physical forces, which orient the cell in a way that on average it grows in the direction of least resistance. Furthermore, this underlines the close correlation between the eigenvalues and eigenvectors of the strain rate tensor and the principal stresses. The divergence at division sites is positive for the simulations, although the fluctuations are large ($< \mathrm{div}(v) >= 0.04\,\mathrm{h}^{-1}$, $\sigma = 0.20\,\mathrm{h}^{-1}$ for confluent and $< \mathrm{div}(v) >= 0.06\,\mathrm{h}^{-1}$, $\sigma = 0.27\,\mathrm{h}^{-1}$ for invading cells). As in the

experiments, the dipole moment is similarly positive, independent of the global flow ($< \partial_\parallel v_\parallel - \partial_\perp v_\perp >= 0.16\,\mathrm{h}^{-1}$, $\sigma = 0.24\,\mathrm{h}^{-1}$ for no flow and $< \partial_\parallel v_\parallel - \partial_\perp v_\perp >= 0.15\,\mathrm{h}^{-1}$, $\sigma = 0.33\,\mathrm{h}^{-1}$ for invading sheets).

3. Conclusion

In this article, we have studied the influence of emerging flow in collective cell migration on the orientation of cell division axes. Expanding epithelial cell sheets were confined in microstructured PEG-DMA channels and flow characteristics were determined by PIV analysis. The tracking of single cell division events was facilitated by stable nuclei staining of the MDCK cells, which additionally provides the basis for automated investigation of the cell density. We correlated flow fields, division events and cell density and managed to extract many quantitative features of tissue migration. Experimental results were compared to particle based computer simulations, which were able to reproduce striking features of tissue growth in a recent publication [17].

The cell monolayers invaded the channels at a constant front speed with a well defined flow profile. A density gradient, with low densities at the leading edge and higher ones in the bulk, developed. We found a strong alignment of the orientation of the cell division axis with the direction of the observed flow.

In order to distinguish phenomena caused by the cell flow from boundary effects of the channel walls, we generated resting cell sheets within the same PEG-DMA microchannels. In this scenario, cell division axes were randomly oriented, supporting our suggestion that the emergent flow in migrating monolayers was the main influence on the direction of cell division.

The simulations reproduced the observed phenomena of decreasing cell density towards the leading edge and emergent flow profiles. The alignment of cell division axes with the direction of cell flow as well as random distribution of the orientation of cell division axes in resting cell sheets were captured well by this mesoscopic model.

The orientation of cell division axes in flow fields could be of significant relevance for growing tissues in wound healing and development. It seems natural that an expanding tissue will orient individual cell divisions in the direction of expansion in order to reduce the principal stress. We could quantify this assumption by showing a strong alignment between the cell division axis and the direction of expansion. The presented approach of measuring cellular flow and cell division events can be easily adopted to several adherent cell lines in order to prove the universality of our reported results.

4. Materials and Methods

4.1. Experimental proceedings

In this study, we analyzed the flow behavior and orientation of the cell division axis in confined MDCK cell sheets invading PEG-DMA microchannels. During the experimental procedure, we prepared the microstructured surfaces with standard cell

culture dishes as substrates, followed by cell seeding (for better illustration, see Figure 6). The PEG-DMA channels were shaped by the PDMS mold as perfect negative replica and the cell-repellent polymer was cross-linked by radical polymerization, forming a three-dimensional, dense network. The microstructures were uncovered by the removal of the PDMS stencil, however, to protect the microstructured area from initial cell attachment, the PDMS mold remained on top of the structures during cell seeding. The cells were grown to confluent level around the covered structures forming a proper edge at the border of the PDMS. After removal of the PDMS, the substrate consisted of free-standing PEG-DMA walls that guided the expanding cell sheets as both chemical and physical barrier. The free surface presented to the cells was the untreated petri-dish. The channels exhibited a height of approximately 15 µm and a length of several millimeters, however, we only monitored the cell sheet expansion to a penetration depth of up to 700 µm. In order to ensure the rightful ascription of the observed effects to the emergent flow in collectively migrating MDCK cells as opposed to effects of the PEG-DMA confinement, we created resting cell sheets within the same kind of microchannels. In this case, the PDMS mold was removed *before* cell seeding to bare the channels to sedimenting cells.

4.1.1. Preparation of PEG-DMA microchannels. Three-dimensional poly(ethylene glycol)-dimethacrylate (PEG-DMA) channels were prepared according to the protocol described previously [18]. Briefly, a polydimethylsiloxane (PDMS) mold that features channels with 200 µm, 250 µm and 300 µm widths and approximately 15 µm height was created by curing the prepolymer against a master prepared by conventional soft lithography. Therefore, the prepolymer solution (Sylgard 184, Dow Corning, USA) was carefully mixed with the curing agent in a 10:1 ratio (w/w) and degassed for 15 min. The mixture was deposited on top of the master followed by an additional degassing step for 15 min to avoid bubble formation. Next, the polymer was cured at 70 °C for 4 h. The molded stamp was peeled off and cut in a way so that the channels were protected by a small barrier of PDMS on one end of the structure since the other end of the channels were open. The PDMS was activated by argon plasma (Diener Electronic, Nagold, Germany) for 30 s. Immediately after the treatment, the stamp was placed upside down in close contact with a hydrophilic ibidi µ-dish (ibidi, Martinsried, Germany). A solution of PEG-DMA (Mn = 550) containing 2 % (v/v) of the photoinitiator 2-hydroxy-2-methylpropiophenone (both purchased from Sigma-Aldrich, Germany) was freshly prepared. A small drop was deposited in front of the open ends of the channels and the structures were filled spontaneously by capillary force induced flow. The process was visually controlled under a microscope to ensure complete filling of the channels and the formation of proper edges. Once the PEG-DMA filled out the whole channel, it was polymerized by the use of an UV-ozone cleaning system (UVOH 150 LAB, FHR, Ottendorf, Germany) with a wavelength ranging from 185 nm–546 nm and a power of $> 50\,\mathrm{mW/cm^2}$ for 10 min. The structures were stored in a drying oven (Binder GmbH, Tuttlingen, Germany) overnight at 50 °C. Immediately before cell seeding, samples were

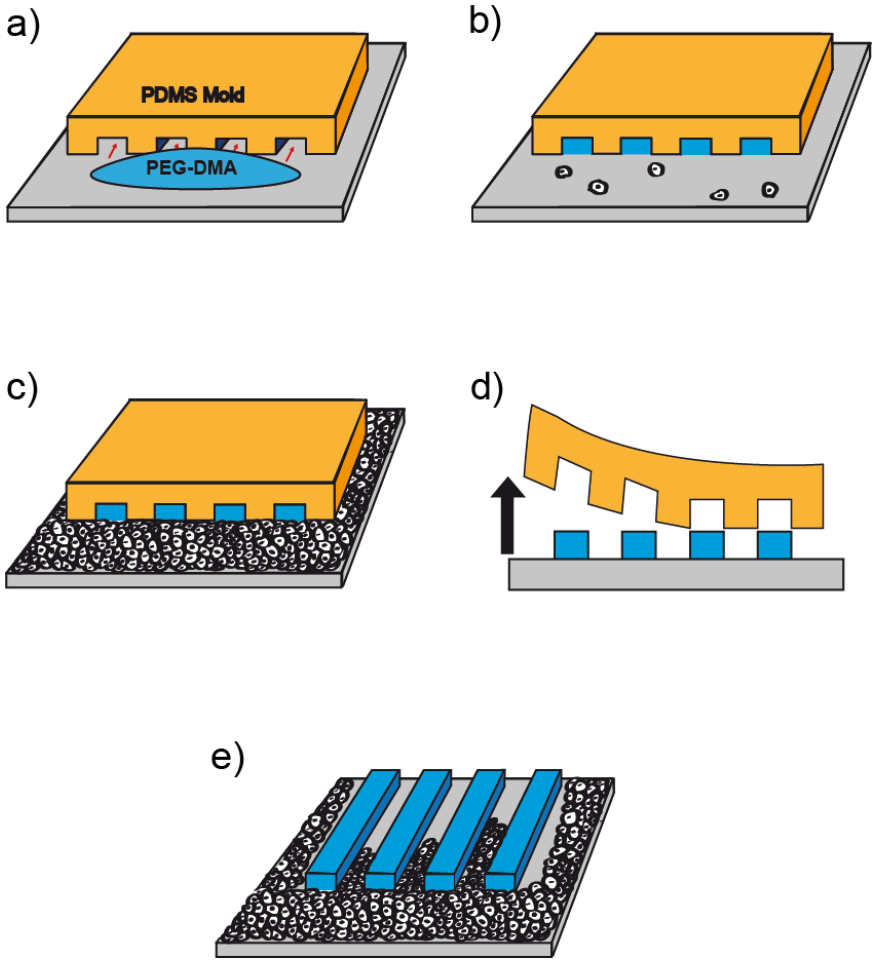

Figure 6. Illustration of the experimental proceeding. a) The PDMS mold is filled with the fluid polymer PEG-DMA by capillary force induced flow. **b)** After cross-linking the PEG-DMA by radical polymerization, the PDMS mold remains on the microstructures during cell seeding, protecting the channels from cell adhesion. **c)** The cells grow to a confluent level under culture conditions, forming a proper edge at the border of the PDMS mold. **d)** Finally, the PDMS is removed and the cell sheet starts to penetrate the PEG-DMA microchannels **e)**.

sterilized with 80 % ethanol for 5 min, washed three times with PBS and covered with cell medium while the PDMS mold still remained on top of the structures to protect the channels from cell adhesion.

4.1.2. Experiments with global flow. Cells were trypsinized and centrifuged at 1000 rpm for 3 min. The cell pellet was resuspended in medium and cells were seeded in front of the PDMS stamp. Then, cells were grown to confluence overnight under culture conditions. The PDMS stamp was removed to bare the protected PEG-DMA channels and the sample was washed with fresh medium to eliminate dead cells. The cell layer started to expand towards the microchannels. Samples were stored under culture condition until the cell front reached the entrance of the channels (typically after 2 d). For time-lapse

measurements, the medium is replaced with CO_2 independent Leibovitz's L15 medium, supplemented with 10 % FBS.

4.1.3. Measurements of non-flowing cell sheets. To prepare confluent cell layers within the PEG-DMA microchannels, cells were seeded all over the uncovered structures. In this case, the PDMS mold was removed after storing the samples overnight in the drying oven. The bare channels were sterilized analogously to the protected ones with 80 % ethanol for 5 min, followed by three washing steps with PBS. After cell trypsination, centrifugation and resuspension, cells were seeded all over the whole petri-dish. The non-fouling properties of PEG-DMA prevented cell adhesion on top of the channel walls, and consequentially, cells adhered exclusively inside the channels. The sample was stored under culture condition until confluence was reached. For time-lapse measurements, the medium is replaced with CO_2 independent Leibovitz's L15 medium, supplemented with 10 % FBS.

4.2. Cell culture and microscopy.

Doubly transfected Madin-Darby canine kidney cells (MDCK) cells with lifeact (EGFP) and H2B (mcherry) were kindly provided by Dr. Wedlich-Söldner of the Max Planck Institute of Biochemistry. Cells were routinely cultured in Dulbeccos Modified Eagle Medium, supplemented with 10 % fetal bovine serum (FBS), 20 mmol L-Glutamine, high-glucose level (4.5 g/l and 110 mg/l pyruvate). Cells were kept at 37 °C in a humidified atmosphere, 5 % CO_2 level. Cell migration within the channels was followed by time-lapse microscopy by using an epifluorescence motorized Nikon Eclipse Ti microscope equipped with an ibidi heating stage (ibidi GmbH, Martinsried, Germany) and a CCD camera (model Clara E from Andor Technology). Image acquisitions were controlled through µ-Manager open source software. Brightfield and fluorescence images were taken at 10 min intervals using a 10× objective. Cells were maintained at 37 °C using a temperature-controlled mounting frame.

4.3. Image analysis

4.3.1. Determination of cell division events. Cell division events were identified from the fluorescence images of labeled cell nuclei. The position of the daughter cells were marked manually using the open source software ImageJ (National Institutes of Health, Bethesda, MD, USA). The detection was carried out immediately after cell division meaning in the fist image where the daughter cells appeared. The difference between these two coordinates was defined as the cells division axis $\mathbf{d} = \mathbf{x_1} - \mathbf{x_2}$. The angle θ between $\mathbf{d}$ and the x-axis $\mathbf{e_x}$ was inferred from their dot product as $\mathbf{d} \cdot \mathbf{e_x} = |\mathbf{d}||\mathbf{e_x}| \cos\theta$. The same applies to the angle ϕ between $\mathbf{d}$ and the eigenvector of the greatest eigenvalue of the velocity gradient tensor λ. These angles were then used to calculate the according order parameters S_x^d and S_λ^d.

4.3.2. Calculation of cell density. For cell density determination, positions of all stained cell nuclei ($\mathbf{x_i}$) were captured using the 'find maxima' function of ImageJ with a manually adjusted threshold for every movie. The relative error was determined to be below 6 % by manual cell counting. In this two-dimensional system of a cell monolayer, the density ρ was defined as number of cells per area. Thus, the density was calculated from the cell nuclei positions $\mathbf{x_i}$ for any area A as follows: $\rho = \int_A \delta(\mathbf{x} - \mathbf{x_i})\,\mathrm{d}\mathbf{x} / \int_A \mathrm{d}\mathbf{x}$. For the experimental data, a bin width of 80 px ($\sim 50\,\mu$m) in x or s direction and a width of 12 px ($\sim 8\,\mu$m) in y direction was chosen. In the case of the simulations, the binning was varied along x or s between 21 µm and 42 µm and along y a width of 8.4 µm was chosen.

4.3.3. Detection of front displacement. To follow the displacement of the cell front, the intensity value for each pixel of the brightfield images was determined. The intensities of the pixels across the channel (in y-direction) were summed for every column obtaining a graph of summarized intensities along the channel (in x-direction). The spectra showed a sharp drop in intensity, corresponding to the position of the leading edge. A custom Matlab script (The MathWorks, Natick, MA) was used to detect this sharp drop by first calculating the sum over the intensity values of ten adjacent pixels and subtracting it from the sum over the ten adjacent intensity values shifted one pixel to the left from the original interval (meaning from the cell-free surface in the channel towards the advancing cell front). This difference was divided by the first of the two sums, and the quotient compared to a chosen threshold value. This process was repeated, shifting the intensity value intervals for both sums by one pixel to the left each time until the quotient exceeds the threshold for the first time, marking the point we defined as the front. The result was compared to the original movie and outliers were identified visually and deleted. The emerging gap was closed by linear interpolation.

4.3.4. PIV analysis. Velocity fields were mapped by PIV analysis using the MatPIV software package for Matlab (J Kristian Sveen: `http://folk.uio.no/jks/matpiv/`, GNU general public license), with some slight, custom modifications. The size of the interrogation window was 32×32 pixels, i.e. 21×21 µm, with 62.5 % overlap in a single iteration. The resulting velocity vectors were filtered with a Signal-to-Noise ratio filter, a global histogram operator, a peak height filter and a local filter (all included in the MatPIV package) to produce smoother vector fields. Vectors removed by the filtering process were replaced by linear interpolation from the surrounding vectors, as long as there were at least five neighbors remaining that were not excluded by the previous step. Requiring this minimal number of neighbors prevented the analysis from interpolating into the region ahead of the leading edge of the cell sheet.

4.3.5. Calculation of velocity field derivations. Spatial derivatives were obtained by using a plain fitting method. A plane was fitted through all v_x that lie within a certain radius r_c of a point $\mathbf{x_i}$. The gradient of the resulting plane in x and y direction then

corresponds to $\partial v_x/\partial x$ and $\partial v_x/\partial y$, respectively. The same procedure was run for v_y to get $\partial v_y/\partial x$ and $\partial v_y/\partial y$. For a chosen radius r_c that only includes the 4 nearest neighbors, the derivatives exactly matched the ones obtained by a finite differences method. By changing r_c, the area over which the derivatives were averaged could easily be adjusted. Furthermore, this method allowed the definition of a second radius $r_s < r_c$ of excluded points, in order to omit the velocities of the cell itself in the gradient calculation. The plane fitting was done with a linear least squares algorithm. This transformed the problem into a linear system of equations, which was solved by applying the LU decomposition algorithm implemented in the GNU Scientific Library (GSL). The choice of r_c and r_s, within reasonable limits, did not change the qualitative behavior of the results. In this work, we set $r_s = 11\mu m$ and $r_c = 23\mu m$. This choice approximately calculates the derivatives on the scale of the cells neighbors.

From the derivatives, the strain rate tensor E_{ij} (see equation 4) was calculated. The eigenvalues and corresponding eigenvectors of this symmetric 2x2 matrix were then obtained through the characteristic polynomial. Furthermore, with the unit vectors $\mathbf{n}$ parallel to $\mathbf{d}$ and $\mathbf{n}_\perp$ perpendicular to $\mathbf{d}$, the strain rate tensor E_{ij} was used to calculate $\partial_\parallel v_\parallel = \mathbf{n}^\mathbf{T} E \mathbf{n}$ and $\partial_\perp v_\perp = \mathbf{n}_\perp^\mathbf{T} E \mathbf{n}_\perp$.

4.4. Computer simulations

Growth of motile tissues is modeled as presented in Ref. [17]. In brief, cells are represented by two point-particles, that repel each other with a growth force B. When a critical size is reached, the cells divide with a rate k_d. The apoptosis rate was set to zero since experimental data showed an insignificant number of cell deaths. Mechanical interactions between the cells is achieved through a soft volume exclusion and an adhesion force, which basically resembles soft sticky spheres. Energy dissipation and random noise is introduced by a DPD thermostat that acts between the particles of one cell as well as between different cells. Cell motility is introduced as a simple two state model, in which each cell can be either in a motile or non motile state. A non motile cell changes state with a rate k_{wake}, in which case a uniformly distributed random motility direction is chosen. The transition rate from the motile into a non motile state depends on whether the motility direction is aligned with the cell velocity (k^+) or not ($k^- > k^+$). Motile cells pull against a background friction with a predefined motility force in the motility direction.

In order to resemble the experimental conditions as close as possible, we confined the cells in a rectangular box with a channel connected at one side (see Figure 1b). The rectangular box acts as a reservoir and is initially covered by a confluent cell layer. We chose the reservoir dimensions as three times the channel width perpendicular to the channel and one times the channel width parallel to it. To approximate the finite slip boundaries in the experiments, reflective boundary conditions were used. The cells of the confluent simulations were initially distributed randomly over the whole channel with a predefined density of 2.3 cells per $1000\,\mu m^2$.

In order to obtain the velocity gradient, we directly used the individual velocity of each particle as input to the plane fitting algorithm instead of calculating an average velocity on a grid, following the PIV analysis.

4.4.1. Units. A prominent problem of mesoscale simulations is their relation to real units. Computer simulations rely on contracting time and length scales, in order to make them feasible [22]. This naturally leads to discrepancies if one tries to compare all involved time and length scales. Thus, taking the model cells as one cell length for example is overinterpreting the model. Instead, one has to carefully choose how to relate simulation with experimental results. In order to reproduce mesoscopic continuum properties, we choose our rescaling quantities on a mesoscopic level. The length unit is chosen such, that the density of cells in the bulk matches. This gives us a length scale to convert simulation lengths to real lengths by $l_0 = 42\,\mu\text{m}$. For the time unit we use the the fact that both experiments and simulations lead to a robust constant invasion velocity, independent of channel width and invasion length. With the length scale already defined, this gives us a timescale of $t_0 = 0.11\,\text{h}$ to convert simulation times into real time units.

The parameters used in the simulations are the same as in Ref. [17].

4.5. Error estimation

Unless otherwise noted, error bars are standard deviation of mean, where averages over one channel are considered as one experiment. For example, the density profile in Figure 2 is calculated for different distances from the front for several channels. First, the cell densities are determined and related to the actual front position in every frame. We obtain an averaged density profile for each channel by averaging the densities of corresponding distances from the front over time. Subsequently, each channels profile is considered as one measurement from which we obtain mean and standard error of mean. We have no indication of systematic error of any kind.

Acknowledgments

We would like to thank Christoph Klingner and Dr. Wedlich-Söldner for kindly supplying stably transfected MDCK cell lines. Financial support by the DFG via SFB 1032, the Excellence Cluster NIM and the Center for NanoScience is gratefully acknowledged.

Appendix A

In the absence of global flow, the alignment of the cell division axis $\boldsymbol{d}$ with the channel walls declines rapidly from near perfect order at the walls to isotropic distributions

towards the middle of the channel within the distance of one to two cell diameters (see Figure 4a). The division anisotropy can be fitted by an exponential decay

$$S_x^d(y) = \exp\left(-\frac{y - y_0}{\xi}\right) + S_0, \tag{6}$$

with an offset describing a minimal distance from the wall $y_0 = (6.2 \pm 0.7)\,\mu\text{m}$, the average bulk order $S_0 = -0.04 \pm 0.02$ and the decay length $\xi = (6.7 \pm 1.3)\,\mu\text{m}$. The ordering effect of the boundary is consistent with an isotropic orientation of cell division under constraint. In a "volume exclusion model" we assume an average distance between the two daughter cells at divisions of $l = 16\,\mu\text{m}$, which corresponds to the experimentally measured distance, and draw the center of mass and division angle randomly from uniform distributions. This defines the positions of the two daughter cells. If one of these positions lies within the wall, the division event is discarded. This simple model can reproduce the order as a function of distance from the wall (see the "volume exclusion" in Figure 4b), showing a clear influence of the channel walls on the orientation of the cell division axis of the first cell row at the walls while the residual bulk order is essentially zero.

References

[1] Bittig, T., Wartlick, O., Kicheva, A., González-Gaitán, M., and Jülicher, F., New Journal of Physics **10** (2008) 063001.

[2] Théry, M. et al., Proceedings of the National Academy of Sciences of the United States of America **103** (2006) 19771.

[3] Minc, N., Burgess, D., and Chang, F., Cell **144** (2011) 414.

[4] Théry, M. et al., Nature cell biology **7** (2005) 947.

[5] Vedula, S. R. K. et al., Proceedings of the National Academy of Sciences of the United States of America (2012) 1.

[6] Reffay, M. et al., Biophysical journal **100** (2011) 2566.

[7] Puliafito, A. et al., Proceedings of the National Academy of Sciences of the United States of America **109** (2012) 739.

[8] Poujade, M. et al., Proceedings of the National Academy of Sciences of the United States of America **104** (2007) 15988.

[9] Wegener, J., *Cell Junctions*, Encyclopedia of Life Sciences. Nature Publishing Group (2002), 2002.

[10] Bacallao, R. et al., The Journal of cell biology **109** (1989) 2817.

[11] Reinsch, S. and Karsenti, E., The Journal of cell biology **126** (1994) 1509.

[12] Angelini, T. E. et al., Proceedings of the National Academy of Sciences of the United States of America (2011) 1.

[13] Petitjean, L. et al., Biophysical journal **98** (2010) 1790.

[14] Trepat, X. et al., Nature Physics **5** (2009) 426.

[15] Hertwig, O., Jenaische Zeitschrift (1884).

[16] Basan, M., Prost, J., Joanny, J.-F., and Elgeti, J., Physical Biology **8** (2011) 026014.

[17] Basan, M., Elgeti, J., Hannezo, E., Rappel, W.-J., and Levine, H., Proceedings of the National Academy of Sciences of the United States of America **110** (2013) 2452.

[18] Marel, A.-K., Rappl, S., Piera Alberola, A., and Rädler, J. O., Macromolecular bioscience (2013) 1.

[19] Serra-Picamal, X. et al., Nature Physics **8** (2012) 628.

[20] Tambe, D. T. et al., Nat Mater **10** (2011) 469.
[21] Ranft, J. et al., Proceedings of the National Academy of Sciences of the United States of America **107** (2010) 3.
[22] Padding, J. T. and Louis, A. A., Physical Review E **74** (2006) 031402.

6 Investigation of Single Stem Cell Fate in Microstructured Environments

50 million cells die every second in the adult human body. All these cells of different function have to be replaced in homeostasis. Stem cells are a specialized cell type taking care of the balanced supply of new cells. They have the unique capacity to differentiate into a magnitude of specialized cells and are highly capable of self-renewing, maintaining the stem cell pool throughout the lifetime of the organism [126, 137]. During embryogenesis, embryonic stem cells (ES) give rise to all tissues in the body, hence, ES cells are defined as pluripotent. In the adult organism, undifferentiated somatic stem cells are found throughout the body in different tissues [10, 44, 51], however, they only exist in small numbers (e.g. for hematopoitic stem cells, only one in thousands of cells in the bone marrow is a stem cell [105]). Generally, these cells are lineage-restricted (multi- or unipotent) meaning that they only differentiate into a minimum of specialized cells of the somatic tissue they reside in. The main function of stem cell is to support tissue repair by replenishing cells that died due to injury or disease as well as the replacement of non-dividing cells such as blood cells. Due to these regenerative properties, stem cells have become increasingly interesting for clinical applications [138].
Within the tissue, stem cells reside in specialized areas called stem cell niches [62, 76]. These microenvironments regulate stem cell fate and therefore balance the the proportion of quiescent and activated cells, maintaining a constant pool of slowly dividing cells. In the case of, for instance, an injury, cells are activated, exit the stem cell niches and start extensive proliferation to ensure the regeneration of the tissue. Within the niches cells are exposed to a wide range of molecular and cellular signals including soluble chemokines like cytokines or growth factors, as well as insoluble parameters like transmembrane receptors or ligands. Additionally, physical properties of the surrounding mircoenvironment, such as matrix mechanics and topological surface architecture, as well as mechanotransducted forces resulting in certain cell shapes and geometries, play an important role in regulating stem cell fate [121]. In order to promote a detailed understanding of the regulatory processes in stem cell niches, artificial microenvironments have been designed, allowing the spatial and temporal control of biophysical and biochemical cues. These regulatory signals can be supplied precisely and delivered by means of biomaterials and specific influence on stem cell fate can be studied [64]. Various techniques have been developed to mimic natural stem cell niches, including

microfluidic approaches, co-culture scenarios and micropatterning methods [58]. The concept of microwell arrays enables the simultaneous observation of cells under the same experimental conditions and high throughput measurements can be achieved [21, 75, 94]. Hydrogel-based microwells are suitable to imitate physiological surface properties and substrate stiffness [36]. To probe the molecular mechanism of cell differentiation, experiments are typically conducted on cell populations and the responses are averaged across the entire cell assembly. Since stem cell populations were found to be very heterogeneous, this approach causes problems by not considering events like apoptosis or changes regarding kinetics of the cell cycle or differentiation steps. Furthermore, differentiated progenitor cells within the population may distort the analysis by rapid growth [64]. Presently, it is unclear if the heterogeneity of stem cell populations is an intrinsic feature of stem cells themselves or evolves due to purification problems, however, the knowledge about the exact molecular control of cell differentiation is essential for therapeutic applications. The observation of individual cells is also facilitated by microwell arrays that, besides mimicking the natural stem cell environment, can also separate cells at single cell level. Another aspect of stem cell analysis is the development of non-invasive methods to determine cell differentiation. For most of the analytical techniques, cells are killed by fixation and subsequent fluorescence staining. Continuous long-term observations at single cell level provide the opportunity to follow changes in cellular states during stem cell fate and differentiation [106], however, the implementation of long-term time-lapse microscopy and subsequent image analysis requires a broad technical understanding and is still challenging. Hence, the quest for platforms where stem cell differentiation can be studied over long time scales at the single cell level is furthermore continuing.
We developed a PEG-DA microwell array were single stem cell were trapped and followed by time lapse microscopy. The time point of differentiation was detected by monitoring the change of Brownian motion at the transition of the non-adherent to the adherent state of the cells. Since the analysis of motion is based on brightfield images, no fluorescent labeling was required.

Hematopoietic stem cells differentiate into all types of blood cells

Hemaotopoietic stem cells (HSC) are multipotent and can regenerate all of the hematopoitic cell lineages by having the potential to differentiate into both the myeloid and the lympoid progenitor. Additionally, HSCs have a high regenerative capacity since they can generate at least one HSC daughter cell by asymmetric cell division or even two HSC daughters by symmetric cell division [108]. HSCs are mainly located in the bone marrow but can also be found in umbilical cord blood and, more rarely, in peripheral blood. The morphology of these non-adherent cells exhibits a rounded shape with low cytoplasm-to-nucleus ratio. HSCs differentiate either into a common myeloid progenitor or a common lymphoid progenitor (see Fig. 6.1). This first differentiation step takes place in the bone narrow. Multiple committed progenitors are generated over various steps in the myeloid as well as in the lymphoid lin-

eage and migrate into the blood stream. There, the final differentiation into thrombocytes, erythrocytes, basophils, neutrophils and eosinophils for the myeloid lineage and natural killer cells for the lymphoid lineage, occurs, respectively. The formation of monocytes that migrate to specific tissues is an additional way of progenitor differentiation. Monocytes mature into interstitial dendritic cells, macrophages or microglial cells depending on the location and the external stimulation by different cytokines and interleukins. Likewise, plasmacytoid dendritic cells and lymphocytes are generated in tissue coming from the lymphoid lineage.

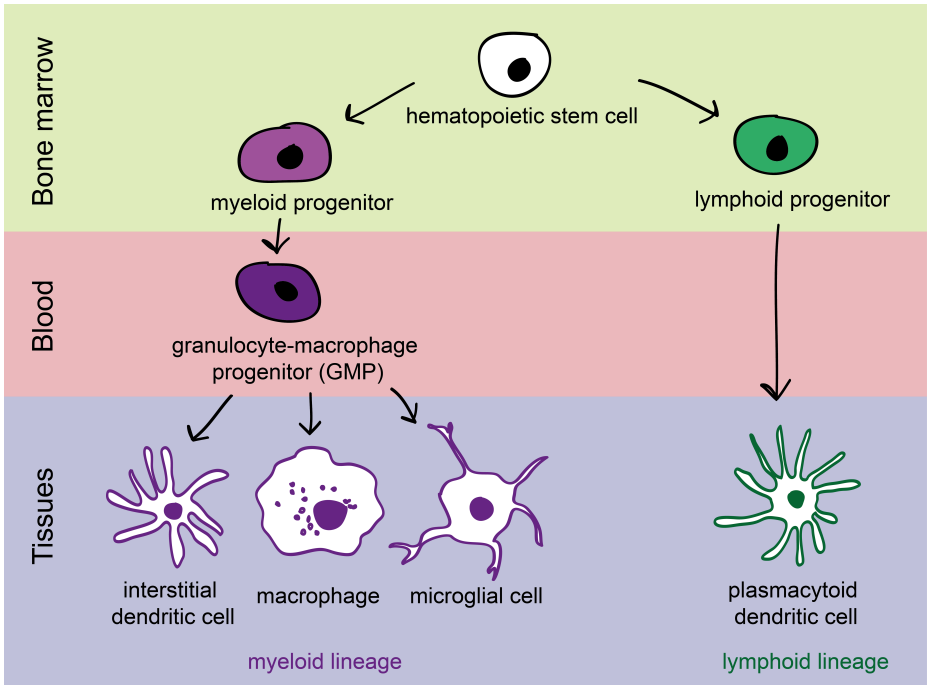

Figure 6.1: Hematopoietic stem cells (HSC) can differentiate into both the myeloid or lymphoid lineage of blood cells. *The multipotent HSCs differentiate into either a myeloid (purple) or lymphoid (green) progenitor. The myeloid progenitor is able to migrate from the bone marrow into the blood stream where it differentiates into a granulocyte-macrophage progenitor (GMP) that differentiates farther into interstitial dendritic cells, macrophages or microglial cells depending on the actual tissue. The lymphoid progenitor can directly differentiate into the plasmacytoid dendritic cell. The diagram only shows a selection of the possible differentiation pathways.*

6.1 Marker Free Detection of Stem Cell Differentiation by Brownian Motion Analysis in μ-Wells [M3]

We combined the ability of spatial control given by microstructued surfaces with non-invasive motion analysis to probe the kinetics of stem cell differentiation. PEG-DA microwells were used to trap single granulocyte-macrophage progenitor (GMP) cells. The well size was adjusted in a way that on one hand free diffusion of the non-adherent GMP's is ensured and, on the other hand, double occupied wells rarely occur. Cells were seeded uniformly over the

structured surfaces and settled into the wells. During the whole measurement, cells remained within the spatial confinement and were followed by time lapse microscopy. The microstructured surface enables the observation of hundreds of individual cells in parallel under the same conditions revealing the heterogeneous behavior of the population.
We probed the differentiation of granulocyte-macrophage progenitor (GMP) cells into macrophages after the addition of the cytokine macrophage colony-stimulation factor (M-CSF). The cells passed through three stages of adhesion levels from non-adhesive GMP cells that become semi-adherent while keeping a rounded shape to fully spread out macrophages. The cellular motion was automatically tracked from out-of-focus phase-contrast images which rendered fluorescent labeling unnecessary. We observed distinct mobility behavior depending on the present stage of the cells: non-adherent GMP's diffuse freely within the wells utilizing the whole available area while semi-adherent cells stayed more or less fixed. After differentiation, macrophages spread on the well bottom covering most of the area.
For time-lapse experiments, the image acquisition interval was adjusted to a 3 min time interval due to the theoretical assumptions for Brownian motion in confinement and the resolution of our setup. The Brownian motion was characterized by the mean squared displacement (MSD) of the cell. The MSD for confined motion exhibit a plateau value P for large timescales where the particle senses the barrier. The obtained MSD traces for individual cells show the expected time course and calculated dimensions of the confinement from the observed plateau values are in good agreement with the actual microwell sizes.
The technical challenge was to detect the transition from the non-adherent to the semi-adherent stage of the cells. Since the non-adherent cells diffuse freely inside the wells, we examined the displacement (ΔR) of the cells between two sequent frames expecting a distinct reduction of the displacement for adherent cells which remain at one position. In order to show the dispersion of the movements on short time scales, the temporal standard deviation σ_i was calculated for five successive time points and then shifted by one frame. The transition from non-adherent to the adherent state is indicated by a permanent decrease of the deviation below a certain threshold as verified by the cumulative sum.
By means of this algorithm, we were able to monitor the heterogeneity of the time point of transition at the single cell level. Cells were treated with M-CSF being in the same condition, however, the time point of differentiation varied over several hours. Our results are in good agreement with recent works [99], however, the presented setup allowed high-throughput measurements with precise time-resolution.

Manuscript 3 [M3]

Marker Free Detection of Stem Cell Differentiation by Brownian Motion Analysis in Micro-Wells

Farzad Sekhavati[1],Max Endele[2], Susanne Rappl[1], Anna-Kristina Marel[1], Timm Schröder[2] and Joachim Oskar Rädler[1]

[1]Fakultät für Physik, Ludwig-Maximilians-Universität, Geschwister-Scholl-Platz 1, 80539 München, Germany
[2]Institute of Stem Cell Research, Helmholtz Zentrum München, Ingolstädter Landstr. 1, 85764 Neuherberg, Germany

Manuscript for submission to Integrative Biology

Integrative Biology

Dynamic Article Links ►

Cite this: DOI: 10.1039/c0xx00000x

www.rsc.org/xxxxxx

ARTICLE TYPE

Marker Free Detection of Stem Cell Differentiation by Brownian Motion Analysis in Micro-Wells

Farzad Sekhavati,[a] Max Endele,[b] Susanne Rappl,[a] Anna-Kristina Marel,[a] Timm Schroeder,[b] and Joachim O. Rädler*[a]

Received (in XXX, XXX) Xth XXXXXXXXX 20XX, Accepted Xth XXXXXXXXX 20XX
DOI: 10.1039/b000000x

The kinetics of stem cell differentiation at single cell level is an essential clue for unraveling the underlying decision making circuits. In the case of granulocyte macrophage progenitor (GMP) cells differentiation into macrophages is accompanied by the expression of lineage-specific markers as well as a transition from a non-adherent to adherent cell morphology. Here, we introduce a label-free approach for acquiring the time distribution of the adherence transitions of hundreds of cells in parallel. We trapped single cells in arrays of micro-wells and used phase contrast time-lapse movies to distinguish non-adherent cells from adherent ones by analysis of Brownian motion. The technique allowed us to follow the differentiation of primary bone marrow-derived bipotent GMPs into macrophages. Adherent cells were observed beginning 4 hours after addition of the cytokine M-CSF and approached 80% of the population within the first 20 hours. The Brownian motion analysis proved to be a sensitive and robust tool to determine the cell adherence transition and could be used to monitor label-free cell differentiation at the single cell level in high throughput.

Introduction

Single cell studies have increasingly been used in biological and biophysical characterization of micro-organisms. In contrast to population studies, which describe the average behavior of a cell colony, single cell studies examine the genuine dynamics of individual cells in response to external trigger[1]. Experiments range from early signaling and protein transcriptions to cell division and cell fate choices[2]. Single cell analysis elucidated the phenotypic heterogeneity in isogenic populations. Stem cell fate decisions are prominent examples of heterogeneous system responses. The unique capability to transform into many kinds of cells makes them the prime candidates for regenerative medicine. A single cell analysis of hematopoietic stem cell decision making will help understanding the regulatory motives with potential impact in medical treatment. Within hematopoietic differentiation, multipotent hematopoietic stem cells (HSCs) give rise to several lineage restricted progenitors, which ultimately produce all the different mature blood cell types[3]. The bipotent granulocyte macrophage progenitor (GMP) population gives rise to the monocyte/macrophage (M) and the granulocyte (G) lineage[4]. In vitro, GMPs can be instructed towards M or G by the cytokines macrophage colony stimulating factor (M-CSF) or granulocyte colony stimulating factor (G-CSF), respectively[5]. Cells induced by M-CSF were found to become adherent due to the expression of the surface protein Mac-1[6].

In recent years it has been recognized that for single cell analysis of stem cells in particular there is a need to develop microscopy platforms culturing isolated cells with precise control over mechanical and chemical properties of the micro-environment[2,7]. Population studies of stem cells have shown that the signaling molecules[8] and mechanical properties of the environment[9,10] have great impact on the fate of stem cells [11]. Microfluidic devices offer a highly accurate and flexible platform for this purpose including cell screening and micro-environmental patterning[12,13]. For most primary cells, and more generally non-adherent cells, isolation and tracking proves to be difficult and time-consuming[14,5]. Various microfluidic approaches have been developed to hold cells in place and to facilitate long-term experiments. Active systems use e.g. hydrodynamic forces to create single-cell traps at the end of microchannels[15] or cell-sized-semi-circle barriers [16], while passive system e.g. micro-arrays of semi-3D micro-wells topologically trap the cells on the surface[17]. In such devices single cell observation time is limited by cell division and the use of fluorescent markers tracking the various cell properties of interest. Fluorophore instability, bleaching, background noise, and phototoxicity effects limit the application of fluorescence microscopy[7]. A label free technique, which do not rely on these factors, is highly beneficial for time-lapse imaging of cells.

[a] *Faculty of Physics, Ludwig-Maximilians-University, Munich, Germany. Fax: +49-(0)89-2180-3182; Tel: +49-(0)89-2180-2438; E-mail: raedler@lmu.de*
[b] *Research unit Stem Cell Dynamics, Helmholtz Zentrum München, Munich, Germany*
† Electronic Supplementary Information (ESI) available: [details of any supplementary information available should be included here]. See DOI: 10.1039/b000000x/

Here we introduce a novel approach to follow the fate of isolated cells over time without labeling them. The technique exploits the Brownian motion of single cells to determine their state of adhesion. Image analysis is used to resolve the heterogeneity of adherence transition times at single cell level. Cells are confined to arrayed micro-wells and their motion is tracked over time using phase contract microscopy. We investigated the differentiation of granulocyte-macrophage progenitors in response to the cytokine M-CSF. We compare the transition timing of adherence with the expression time course of the fluorescently tagged LysM, that up regulates upon differentiation to macrophage. We find that the adherence transition precedes the appearance of the fluorescent marker but follow the general behavior observed by Rieger et. al[5,18]. We demonstrate the use of the label free technique to robustly detect the adherence transition and discuss its potential for following differentiation kinetics.

Results

Micro-structure fabrication

We fabricated microstructure patterns on a tissue culture plastic (TCP) substrate and mounted under a channel (I-Luer sticky slide, ibidi, Germany) with height of 400 µm. The micro-pattern consists of an array of semi-3D micro-wells with 12 µm height. We have tested well diameter range from 20 to 50 µm and selected for highest probability of single cell coverage and no-change in duplication time compare to bulk. The division time is used as an indication that the cell growth is not affected by micro-well constraint[7]. For the granulocyte macrophage cells with average diameter of 15 µm, an array of micro-wells with a diameter of 35 µm did not alter the division time of cells[19]. The micro-array pattern is fabricated from cell-repellant PEGDA polymer on a tissue culture plastic substrate[20]. Every slide contains an array of 45×750 micro-wells. The low height of channel and consequently thinner medium layer on top of cells, compared to common cell-culture flasks, reduces the fluorescence background noise while still supplying enough nutrient for up to two-day experiment.

Cells in micro-wells

GMPs were instructed towards M lineage by adding macrophage colony stimulating factor (M-CSF) cytokine[5]. A concentration of 20 µg/ml M-CSF cytokine was added to GMP medium just prior to seeding. Cells are seeded into the channel and subsequently sediment into the micro-wells by gravitational force (Fig.1.a). The adherence of a cell to the surface has three separated states. A freely moving state of non-adherent cell, an adherent states and finally the flattened out state which cells spread on the surface (Fig.1.b). The differentiation of GMPs to macrophages also goes through this three stages (Fig.1.b). GMPs are non-adherent and freely float around the well over time. In the presences of M-CSF cytokine GMPs differentiate to macrophages and express surface proteins and adhere to the TCP[5]. In adherent state, they keep their spherical shape while holding to the substrate. After full development, macrophage flattens out and spread on the substrate, flattened state.

Non-adherent cells diffuse freely within the well, their motion extends over the whole area of a micro-well. Semi-adherent cells adhere to the surface and stop their free motion. Fully adherent cell spread on the substrate and start their active crawling motion. Fig.1.c. shows a phase-contrast image of a representative cell at three stages. The overlaid tracks show the position of the center of cell over 24 hours color codes are time. For the purpose of differentiation detection, we followed the position of cells until before division or transition to final state. State III was observed to confirm that the cell successfully reach the fully developed macrophage state, this could happen in the same generation or after division.

In non-adherence state, while most of the cells span the whole well area, for some, a tendency of staying at the proximity of the wall was observed. These cells show a smaller difference in motion between two states, however this motion regime change is still distinguishable.

Time-lapse imaging

Time-lapse microscopy with an inverted Axiovert 100M Zeiss microscope was employed. We have benefited from the out-of-focus phase-contrast image, in which cells have bright centers. This accelerates cell-recognition in image processing. Every 3 minutes one image of sample every 3 minutes for 24 hours produced a time-lapse sequence of cell motion (Fig.2.a). The time interval is calculated according to the theory of Brownian motion in confinement (more detail in SI). An interval of 3 minutes for 15 µm cell corresponds to 3-4 µm motion, which equals ~2-3 pixel resolution in our microscopy setup.

Cell centers are tracked with an in-house ImageJ[21] plug-in. The software locates the micro-well array and automatically choose the occupied wells with single cell in initial frame. The center of cell is tracked in subsequent frames until division. For more details on recognition algorithm see supplementary information. Fig.2.b shows an example of one cell with micro-well (red) and cell contour (green) recognized by software. Fig.2.c is the resulted trajectory of center of the cell. All the occupied wells have been processed simultaneously, which decrease the time for analysis.

A fluorescent image was taken with 3 hours interval. We have a LysM:EGFP marked cells which up-regulate GFP protein after commitment to M or G cell line. The fluorescent image was taken every 3 hours from each position, however at every scan interval (3 minutes) fluorescent image of one set of positions were taken. Hence we have data of different positions at 3 minutes intervals.

Confined Brownian motion in micro-wells

We used the mean square displacement (MSD) of cell motion for characterization of its Brownian motion. Short time-scale part of MSD graph which is linear, indicates the free diffusion characteristics of particle such as diffusion coefficient. At larger time-scales, MSD graph reaches a plateau value which indicated the influences of confinement on motion. We have used the equation of MSD plot for a sphere in confinement for our cells. [22]. In micro-wells we have a symmetry in x and y direction which further simplifies the equations and lets us look at the motion in radial direction. The clearance (L) between the cell with diameter of d_{cell} in a micro-well with the diameter of d_{well}, is $L = d_{well} - d_{cell}$ and according to Kusumi et al. formula, the plateau value (P) is $P = L^2/6$.

MSD graph of a set of 10 individual GMPs is shown in Fig.3.a.

They exhibit the characteristic shape of MSD for a confined Brownian motion with the plateau value corresponding to the clearance between cell diameter and well diameter. Lines are the fit from theoretical equation (more detail in SI). Fig.3.b shows the images of three cells corresponding to three colored lines in Fig.3.a. The diameter of cell derived from plateau of MSD graph (inset of Fig.3.a) and image (values in Fig.3.b) agree with each other. The out of focus image shrinks the diameter of cell, hence the difference between the two values.

Transition point from non-adherent to adherent state

The discrimination between non-adherent and adherent state is an indication of the differentiation time point for a primary cell. We measured the displacement of cells between two subsequent frames ($\Delta R = |R_{i+1}-R_i|$) (Fig.4.a). The displacement depends on the diffusion coefficient and physical constrains of motion. A non-adherent cell freely diffuses inside the well, hence having a large displacement compared to non-moving adherent cell. Fig.4.a shows exemplary displacement of 8 cells and the difference between non-adherent state in the beginning and adherent state at the end. For a high-throughput parallel investigation of single cells, it's important to automatically detect this transition point.

The standard deviation of displacement over a rolling time-window of 5 frame, σ_5, was used for automatic determination of the transition point. The standard deviation σ is an indicator of variation in motion of a particle during the course of time-window. A threshold value was chosen in such a way that after adherence σ_5 value drops below it. This value is manually chosen for one cell and used for all experiment. The time-point that σ persistently drops below threshold is taken as transition point (red circle in Fig.4.b) It is possible that σ_5 drops temporarily below the threshold before the actual transition point. To discard these points we look at the persistency of adherence motion. If the algorithm finds more than one transition point it automatically increases the persistency time until only one transition point is found.

The cummulative sum (cusum) algorithm was used to confirm the transition point detection. Cusum algorithm checks the global behavior of a system until each time-point and reports if there is a persistent regime change in the system[23,24]. Using this algorithm we were able to confirm the transition points reported from standard deviation technique. The cusum and standard deviation algorithm are described in detail in SI.

Heterogeneity in adherence point

Differentiation of hematopoietic stem cell has a stochastic dynamics[25,26] with each individual cell showing variability in behavior (e.g. Fig.4.a). With the help of micro-well array we are able to capture the behavior of up to two thousand cells in parallel. The transition point detection technique was used to find the adherence events of 538 cells in parallel. This point is an indication of differentiation of non-adherent GMP to adherent macrophage cell. Fig.5.a shows the time-distribution of single cell adherence over 30 hours. All the cells were cultured under the same condition. The observation started 4 hours after addition of the M-CSF to the progenitors. Around 40% of cells were adherent by the start of imaging. The number of adherence event drops exponentially over the time and before the first division 80% of cells adhered to the TCP substrate. The average division time is within the reported division time of GMPs (12-22 hours[19]) The fluorescent images was investigated to mark the onset of GFP signal from each cell. The longer times represent the signal from daughter cells. Fig.4.b shows the percentage of adherent (black) and fluorescent cells (red) over the course of 48 hours. We have observed that the GFP onset generally occurs later than the adherence event. Fig.5.c shows the correlation between this two events, where cells first become adherent and later turn on their GFP signal.

DISCUSSION

Our study demonstrates that arrays of micro-wells allow for single cell analysis of the transition from a non-adherent to an adherent state by exploiting Brownian motion as reporter. GMPs exhibit heterogeneous timing in both the adhesion transition as well as differentiation at single cell level. As shown by Rieger et al.[5] the transition into the adherent state precedes the expression of the LysM:eGFP marker protein. Our study, which reproduces these data quantitatively with high temporal resolution and high statistics, is in alignment with the earlier study. The single cell motion analysis introduces a robust label-free method for high-throughput detection of the adherence transition and hence is potentially capable to eliminate the need for fluorescence markers. To this end in future work the micro-wells need to be functionalized with specific antibodies in order to unambiguously discriminate for the expression of surface molecules that relate to adherence and binding of cells to the micro-well surface. In this case time-resolved studies on single cell surface protein expression could be carried out without any adverse effect of intense illumination for fluorescence imaging. The time-interval of phase contrast imaging in our study was several minutes which could be further reduced. Potentially, Brownian motion analysis allows resolving single molecule binding as shown by Wong et al. for latex particles [27]. Hence single cell adhesion arrays open up the possibility of single surface molecules studies on living cells as for example for protein and membrane characterization[22,28,27] and quantitative evaluation of number of adhesion bonds. There is no principle limitation on the observation time in our approach other than cell division. The setup addresses concerns about suitable growth condition, CO_2 incubation, temperature control and the perfusion with fresh medium[29]. We believe that the highly parallel Brownian motion analysis of single cells is a powerful high-throughput label-free method, which is particularly promising for the time-resolved investigation of differentiation and the detection of changes in cell surface properties in general.

Methods

Device fabrication

Our microfluidics devices are based on inert PEG-DA (polyethyleneglycol diacrylate)[30]. The stencil of micro-well array is fabricated on a standard tissue culture plastic which attached to the bottom of an I-Luer sticky slide from ibidi (ibidi, Munich, Germany). I-Luer sticky slide has a 400 µm high channel which can be accessed with two inlets on two ends.

The fabrication is the same as was already described[20]. In short,

The PDMS precursor is mixed with curing agent with 10:1 (Sigma-Aldrich) ratio. It is degassed for 15 mins, poured on a patterned silicon wafer. After subsequent degassing step for 15 mins, PDMS is cured for ~3 hours in 50°C oven. The PDMS mold is peeled off from the wafer and cut along the structures forming an open network. Then both PDMS and plastic substrate were plasma treated with argon plasma for 30 second, afterward the structures in PMDS brought into contact with the substrate surface. A drop of PEGDA polymer (polymer solution containing 2% of photoinitiator 2-hydroxy-2-methylpropiophenone (v/v) (Sigma-Aldrich, Germany)) is placed at the open side of PMDS mold. The empty space of the mold is filled with PEGDA due to capillary force induced flow. In subsequent step, the polymer is cured under UV light for 15 minutes. PDMS mold is removed and the PEDGA patterned substrate further cured overnight in 50°C oven. The substrate then sonicated with Ethanol for 10 minutes followed with a 10 minutes sonication in DI-water. Afterward, it is blow dried and attached to the ibidi I-Luer sticky slide and kept in sterile condition.

Cell preparation

FACS purification of GMPs[4] from LysM:EGFP mice[31] was performed as described[5]. Briefly, femurs, tibiae, humeri, hip bones and vertebrae from 8-12 week old mice were isolated, crushed in ice cold 2% FCS/PBS, and filtered through a 40 µm filter (BD). For erythrocyte lysis, cells were re-suspended in ACK buffer (Lonza) for 2 min. Cells were then stained with biotinylated antibodies against lineage markers (B220, CD3e, CD19, CD41, CD11b, Gr-1, Ter119 (all eBioscience)) followed by incubation with streptavidin-coated magnetic beads (Roth). After magnetic lineage depletion, cells were stained with Streptavidin-APC-eFluor780, c-kit-PE-Cy7, CD34-eFluor660 (all eBioscience), Sca-1-Pacific Blue (Biolegend) and CD16/32-PE (BD) for at least 30 min on ice. Cell sorting was done on a FACSAriaIII (Becton Dickinson). Sorted GMPs were re-suspended in SFEM (Stem Cell Technologies) containing 20µg/ml of M-CSF. The time-lapse imaging started 4 hours after sorting and addition of cytokine.

The cells are seeded into the channel and further settle down into the micro-well arrays with gravitational forces. The slide is incubated at 37°C inside chamber with 5% CO_2 and high humidity. The chamber is on the stage of an inverted microscope which takes phase-contrast images of 100 positions every 3 minutes with 10X magnification; this covers the whole area of channel.

Acknowledgement

We hereby thank Christian Meggle for developing the image processing software. This work has been funded by the Deutsche Forschungs-gemeinschaft (DFG) via SFB1032, the Excellence Cluster ‘‘Nano-systems Initiative Munich (NIM)’’, the Center for NanoScience (CeNS) Munich via International Doctorate Program NanoBioTechnology (IDK-NBT), and graduate school of Quantitative Bioscience Munich (QBM).

References

1. F. S. O. Fritzsch, C. Dusny, O. Frick, and A. Schmid, *Annu. Rev. Chem. Biomol. Eng.*, 2012, **3**, 129–155.
2. D. G. Spiller, C. D. Wood, D. A. Rand, and M. R. H. White, *Nature*, 2010, **465**, 736–45.
3. S. H. Orkin and L. I. Zon, *Cell*, 2008, **132**, 631–644.
4. K. Akashi, D. Traver, T. Miyamoto, and I. L. Weissman, *Nature*, 2000, **404**, 193–7.
5. M. M. A. Rieger, P. P. S. Hoppe, B. B. M. Smejkal, A. C. Eitelhuber, and T. Schroeder, *Science (80-.).*, 2009, **325**, 217–218.
6. C. J. Flaim, D. Teng, S. Chien, and S. N. Bhatia, *Stem Cells Dev.*, 2008, **17**, 29–39.
7. I. Kurth, K. Franke, T. Pompe, M. Bornhäuser, and C. Werner, *Integr. Biol. (Camb).*, 2009, **1**, 427–34.
8. J. M. Karp, J. Yeh, G. Eng, J. Fukuda, J. Blumling, K.-Y. Suh, J. Cheng, A. Mahdavi, J. Borenstein, R. Langer, and A. Khademhosseini, *Lab Chip*, 2007, **7**, 786–94.
9. A. J. Engler, S. Sen, H. L. Sweeney, and D. E. Discher, *Cell*, 2006, **126**, 677–689.
10. X. Mu, W. Zheng, J. Sun, W. Zhang, and X. Jiang, *Small*, 2013, **9**, 9–21.
11. H. Yin and D. Marshall, *Curr. Opin. Biotechnol.*, 2012, **23**, 110–119.
12. K. D. Kokkaliaris, D. Loeffler, and T. Schroeder, *Curr. Opin. Hematol.*, 2012, **19**, –.
13. A. C. Rowat, J. C. Bird, J. J. Agresti, O. J. Rando, and D. A. Weitz, *Proc. Natl. Acad. Sci.*, 2009, **106**, 18149–54.
14. S. L. Faley, M. Copland, D. Wlodkowic, W. Kolch, K. T. Seale, J. P. Wikswo, and J. M. Cooper, *Lab Chip*, 2009, **9**, 2659–64.
15. H. Kim, R. E. Cohen, P. T. Hammond, and D. J. Irvine, *Adv. Funct. Mater.*, 2006, **16**, 1313–1323.
16. S. Kobel and M. Lutolf, *Biotechniques*, 2010, **48**, ix–xxii.
17. T. Springer, G. Galfré, D. S. Secher, and C. Milstein, *Eur. J. Immunol.*, 1979, **9**, 301–6.
18. M. A. Rieger and T. Schroeder, *Cell Cycle*, 2009, **8**, 4019–4020.
19. D. Metcalf, *Proc. Natl. Acad. Sci. U. S. A.*, 1980, **77**, 5327–30.
20. A.-K. Marel, S. Rappl, A. Piera Alberola, and J. O. Rädler, *Macromol. Biosci.*, 2013, **13**, 595–602.
21. W. S. Rasband, .
22. A. Kusumi, Y. Sako, and M. Yamamoto, *Biophys. J.*, 1993, **65**, 2021–2040.
23. E. S. Page, *Biometrika*, 1954, **41**, 100–115.
24. G. A. Barnard, *J. R. Stat. Soc. Ser. B (* …, 1959, **21**, 239–271.
25. D. Dingli, A. Traulsen, and J. M. Pacheco, *Cell Cycle*, 2007, **6**, 461–466.
26. J. L. Abkowitz, S. N. Catlin, and P. Guttorp, *Nat. Med.*, 1996, **2**, 190–197.
27. W. P. Wong, V. Heinrich, and E. Evans, *Mater. Res. Soc. Symp. Proceeding*, 2004, **790**, P5.1.1–P5.1.12.
28. A. Sonnleitner, G. J. Schütz, and T. Schmidt, *Biophys. J.*, 1999, **77**, 2638–2642.
29. T. Schroeder, *Nat. Methods*, 2011, **8**, S30–5.
30. A. Khademhosseini, J. Yeh, S. Jon, G. Eng, K. Y. Suh, J. A. Burdick, and R. Langer, *Lab Chip*, 2004, **4**, 425–30.
31. N. Faust, F. Varas, L. M. Kelly, S. Heck, and T. Graf, *Blood*, 2000, **96**, 719–26.

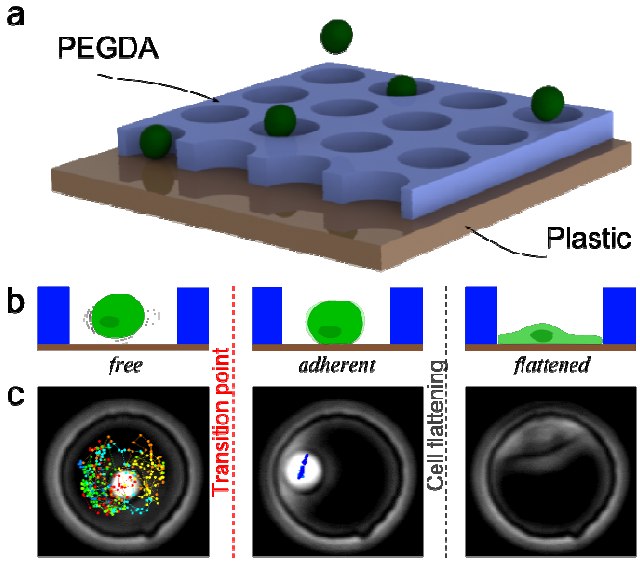

Fig.1 a) schematic view of cell settling into the micro-wells due to gravitational forces. b) Schematic drawing of the three states of adherence: freely moving, adherent and flattened out. c) Corresponding phase contrast image of non-adherent GMP cells which differentiates to adherent macrophage and later flattens out on the surface. Transition point is the time at which the cell enters the adherent state.

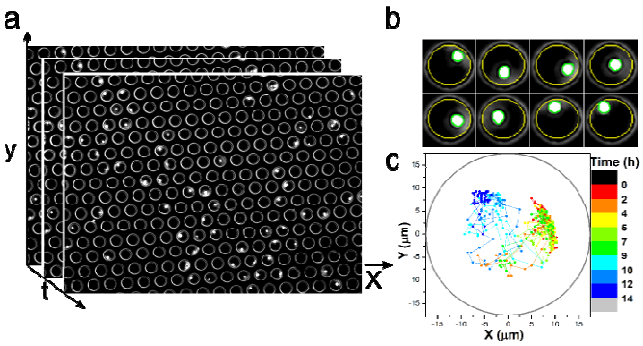

Fig.2 a) 3 frames form time-lapse phase contrast images of one field of view with 10X magnification. It contains ~250 wells and 50 single cells. b) Selected frames of a time-sequence of phase contrast image of one well. Contours are detected automatically, the yellow contour indicates the micro-well and green contour indicated the center of the cell. c) Trajectory of the center of cell over 14 hours, color codes are time, This cell adheres to the surface at around 12 hours.

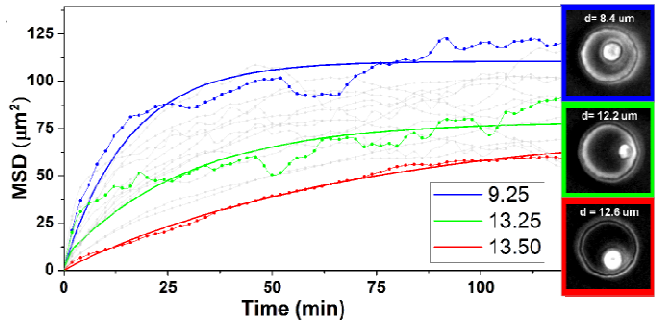

Fig.3 a) Mean square displacement of cell-centre, dots are experimental points and the dashed line corresponds to the fit from theory 19 (SI) the different plateau value is an indication of cell diameter. The corresponding images of cells for think lines are shown with the diameter calculated from image

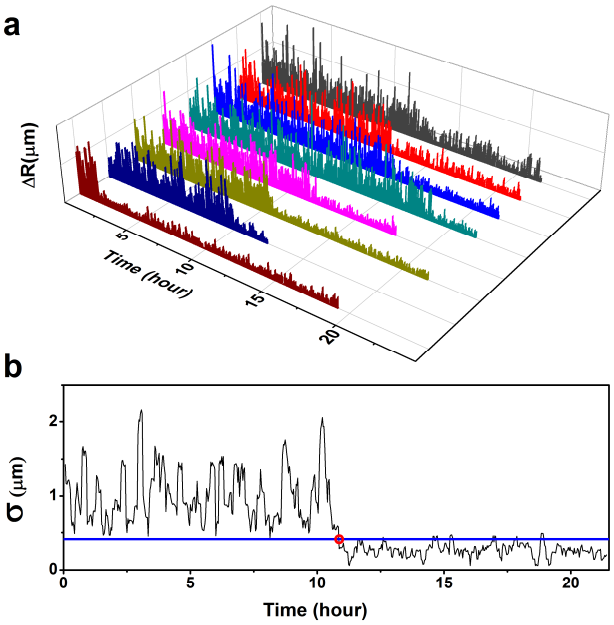

Fig.4 a) Displacement-time graph of a set of 8 single cells, showing a non-adherent GMP cell turns into an adherent macrophage. b) Evolution of the standard-deviation σ over a rolling time window of 5 frames.

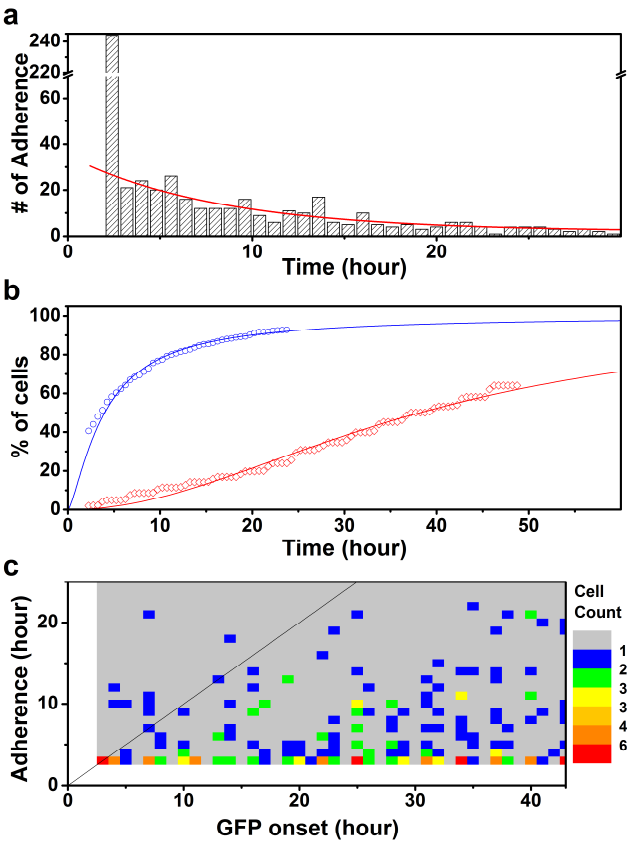

Fig.5 a) Histogram of time of adherence indicating the differentiation of GMP to macrophage (data are from 538 single cells). b) Adherence of macrophage (blue) and GFP expression in differentiated M cell (red) c).

Supplementary Information:

Marker Free Detection of Stem Cell Differentiation by Brownian Motion Analysis in Micro-Wells

Microfluidic optimization

It is known that for adherent cells the shape of confinement induces change in normal behavior of cell[1,2], to our knowledge there has not been a report on behavior of suspension cells in micro-pattern confinement. However, we have checked the apoptosis and doubling rate for diameters of 15 to 50 µm of micro-well. For our 15 µm cells we did not see any change in behavior due to confinement for diameters larger than 30 µm. Well geometry is also optimized to have high probability of single-cell trapping. The diameter of 35 µm is more than two times the average cell diameter which provides enough clearance to resolve cell motion in micro-well. The micro-well depth is 15 µm, at this depth the cells do not wash away from inside the well, and at the same time they cannot stack on top of each other.

Calculation the proper time interval

Considering the cell-size and the calculated diffusion coefficient we estimated the time interval needed for an optimal resolution in Brownian motion of cell. Here we approximated the cell with a sphere.

Diffusion equation for sphere at room temperature:

$$@T = 37℃ \rightarrow D = \frac{K_b T}{6\mathrm{r}\pi\eta} = \frac{1.4\times10^{-23}\times310}{6\mathrm{r}\pi\eta} = 2.30\times10^{-22}\frac{1}{\eta r}(N.m) \quad \text{SI.Eq.1}$$

Approximating the diffusion coefficient of medium with water:

$$\eta_{water@35℃} = 0.7225\mathrm{mPa.s} \rightarrow D \approx 3.18\times10^{-19}\frac{1}{r}(m^3/s) \quad \text{SI.Eq.2}$$

And the diameter of the cell is 10-15 µm:

$$r \approx 8\,\mu\mathrm{m} \rightarrow D = 4\times10^{-14}(m^2/s) = 0.04(\mu m^2/s) \quad \text{SI.Eq.3}$$

Writing the mean-square displacement equation:

$$x^2 \geq q_i\, Dt \quad \text{SI.Eq.4}$$

where q depends on diffusion dimension, in our case is 2D and q = 4. We need around 3 minutes to scan the whole chip (more than 100 position) for this time the approximate Brownian motion of cell in the medium compared to the spatial resolution of microscope at 10 times magnification (0.65 µm/pixel) is:

$$@t = 3\mathrm{min}: \ \mathrm{x} = \sqrt{4\mathrm{Dt}} = \sqrt{4\times4\times10^{-14}\times180} = 5.4\,\mu\mathrm{m} \equiv 8\,pixels \quad \text{SI.Eq.5}$$

Mean square displacement

The mean square displacement (MSD) of any movement indicated the characteristics of that motion such as diffusion coefficient, confinement etc. For free motion MSD is a straight line with the slope which indicated the diffusion coefficient. For Brownian motion in confinement, MSD reaches a

maximum value which corresponds to the confinement size. Kusumi et. al.[3] showed that in this case the equation for MSD-Δt is

$$MSD = \left\langle x^2 \right\rangle = \frac{L_x^2}{6} + \frac{16L_x^2}{\pi^4} \sum_{n=1(odd)}^{\infty} \frac{1}{n^4} \exp\left\{ \frac{-1}{2} \left(\frac{n\pi\sigma_x}{L_x} \right)^2 t \right\} \quad \text{SI.Eq.6 [Eq11a in [3]]}$$

$$\left\langle x^2 \right\rangle = \frac{L_x^2}{6} + \frac{16L_x^2}{\pi^4} \sum_{n=1(odd)}^{\infty} \frac{1}{n^4} \exp\left\{ \frac{n^2}{L_x^2} \alpha t \right\} \quad \text{SI.Eq.7}$$

$$\alpha = \frac{(\pi\sigma_x)^2}{2}$$

$$\sigma_x = 2D_x$$

Where, L is the clearance value between the cell and confinement (inset in Fig.SI.1). Same formula applies to *y* direction. At large *t* value the formula converge to $L^2/6$. Fig.SI.1. shows a schematic MSD graph. The red fit gives the diffusion constant of cell in the confined area and blue fit is the plateau line.

Micro-wells are symmetrical in x and y direction (L_x=L_y=L) and for 2 dimensional diffusion $\sigma_r^2 = 4D$.

$$MSD_r = MSD_x + MSD_y \quad \text{SI.Eq.8}$$
$$L_r = L_x + L_y$$

Substituting the SI.Eq.7 in SI.Eq.8 we conclude that the formula for *r* direction is the same as *x* direction.

To implement SI.Eq.11 as a fit in OriginPro (OriginLab, Northampton, MA) we expand the summation up to the first 5 expressions for *r* direction:

$$\left\langle r^2 \right\rangle = \frac{L_r^2}{6} + \frac{16L_r^2}{\pi^4} \left\{ \exp\left(\frac{\alpha}{L_r^2} t \right) + \frac{1}{3^4} \exp\left(\frac{9\alpha}{L_r^2} t \right) + \frac{1}{5^4} \exp\left(\frac{25\alpha}{L_r^2} t \right) + \frac{1}{7^4} \exp\left(\frac{49\alpha}{L_r^2} t \right) + \frac{1}{9^4} \exp\left(\frac{81\alpha}{L_r^2} t \right) \right\} \quad \text{SI.Eq.9}$$

Temporal standard deviation

Standard deviation is a measure of dispersion of motion. Temporal standard deviation (σ_t) indicate the dispersion in a define time-domain (t) and is calculated from SI.Eq.10, where N is the N^{th} point of temporal standard deviation. The transition point from high motility to low or no-motility can be detected with σ_t. To automatically observe the change in cell motion we sampled the displacement over an arbitrary number of 5 consequent frames. This indicates the displacement dispersion in a 15 minutes window. The highest persistence crossovers of σ_5 from a threshold value to lower value is marked as the transition point.

$$\sigma_t = \sqrt{\frac{1}{t-1}\sum_{N}^{N+t}(x_i - \bar{x})^2} \quad \text{SI.Eq.10}$$

Cusum algorithm

Cusum is the cumulative sum of differences between successive values *k* and a reference value Q [4], SI.Eq. 11.

$$\text{cusum}_i = (Q_i - k) + \text{cusum}_{i-1} \quad \text{SI.Eq.11}$$

In our experiment, k is the consequent displacement ΔR of cell from position R_i to R_{i+1} and Q is the global mean value of displacement, since the mean-dispersion of non-adherent cell (the actual reference) is not known initially. This means that cusum plot will have a constant slope for each state of cell inside the well, and instead of looking at the deviation from horizontal line [5], we look at the change in slope. The change in slope of cusum-plot indicates a change in the regime of random motion. We have used a partial linear fit to cusum plot and reported the slope-change values as possible transition points. The highest value of slope-change is reported as actual transition point. The cusum method had in most cases confirmed the results of standard deviation approach, and in discrepancy points, the correct point was chosen manually by the user.

Image processing

Initially the images have been corrected for instability in microscope x-y motion with "Image stabilizer" plug-in[6] for imageJ software. There is a small change in average image intensity over time which is corrected with a "Bleach Correct" [7] macro.

For cell tracking and image analysis a Java based plug-in for ImageJ software is developed. To facilitate the image detection we have used an out-of-focused phase-contrast image. Cells in focal plane of phase-contrast image have a bright rings for the cell boundary, while out-of-focus image results in bright spots for cells.

In short, the software identifies the well array by thresholding the image and fitting a smooth circle on the recognized well and automatically detects the wells that are filled with single cell. Next, the program goes through all the frames and tracks the position of center of the cell with respect to the center of the well. The cell recognition algorithm is also based on an automatic threshold value recognition. The position list is imported to a Matlab code for further analysis, such as σ_5, cusum, transition point, cell-size calculation.

The bright cells are efficiently detected with a thresholding algorithm in image processing step.

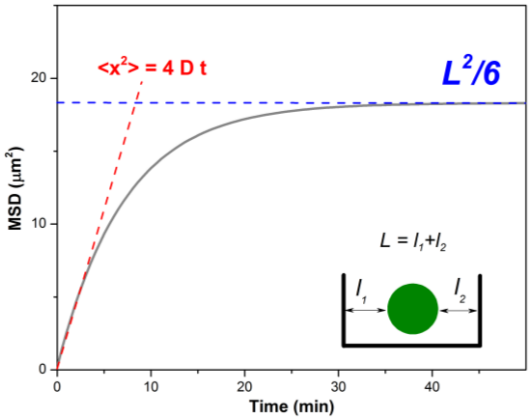

Fig.SI.1. Schematic of mean square displacement of spherical particle in a two-wall confinement.

References of supplementary information

1. N. J. Sniadecki, R. a Desai, S. A. Ruiz, and C. S. Chen, *Ann. Biomed. Eng.*, 2006, **34**, 59–74.
2. L. E. Dike, C. S. Chen, M. Mrksich, J. Tien, G. M. Whitesides, and D. E. Ingber, *In Vitro Cell. Dev. Biol. Anim.*, 1999, **35**, 441–8.
3. A. Kusumi, Y. Sako, and M. Yamamoto, *Biophys. J.*, 1993, **65**, 2021–2040.
4. E. S. Page, *Biometrika*, 1954, **41**, 100–115.
5. G. A. Barnard, *J. R. Stat. Soc. Ser. B (…*, 1959, **21**, 239–271.
6. K. Li, 2008.
7. J. Rietdorf, 2005.

7 Conclusion and Outlook

In this work we investigated the dynamics of collectively migrating cells sheets. By confining small cell group in microstructures, we were able to gain deeper insights into the coordinated motion of epithelial cell sheets. The viscoelastic relaxation time for small patches was determined experimentally for the first time and in good agreement with predictions from literature. The fluid-like behavior of expanding cell sheets was characterized in terms of fluctuations of the emerging velocity field, formation of a density gradient and vorticities. The diffusive behavior of single cells as well as collective diffusive motion was investigated and combined with the reaction-diffusion model of Fisher-Kolmogorov which has been applied in literature as model to describe growing cell fronts. In our work, we determined the individual parameters of the equation in independent experiments for the first time and were able to show that this model applicable to our system.

In this last chapter, we give a short overview of some preliminary experiments and ongoing projects that evolved from the preceding work.
The definition of a cell layer by means of the voronoi tesselation is motivated by the hope of better comparability of experimental data with theoretical description of cell layers based on the vertex model. The enhancement of PEG-DMA microwells towards specialized environments presenting defined ligands or protein to cells represents a further step on the way of detailed resolution of stem cell differentiation. Lastly, we show that the utilization of PEG-DMA microstructures is not limited to biological applications and can serve as templates for the spatial alignment of organic semiconductors.

Voronoi diagrams describe continuous cell layers

A Voronoi diagram divides a space into regions of Voronoi cells arranged to corresponding sites and their nearest neighbors. The regions are obtained by the intersection of the half-spaces between adjacent points generating convex polygons. Voronoi diagrams have been used to describe surfaces or volumes by meshing [61] and occurs in both, chemical and physical systems [23]. In the field of cell biology, Voronoi tessellation have been adopted to model tissues and their dynamics [13, 50, 72, 73, 78]. We want to generate Voronoi tessellations from nuclei labeled epithelial monolayers in order to describe the cellular network. The Voronoi

diagram may be used to translate experimental data into theoretical models such as the vertex model [27] making obtained results more comparable. Additionally, analysis of cell shape and adjacency becomes easily accessible. We tested to what extent the Voronoi tessellation is able to reproduce a confined cellular network by comparing labeled cell membranes with the diagram (see fig. 7.1). We found relatively good agreement of the Voronoi tessellation and the cell membranes within the cell sheet, however, we observe considerably deviations at the border.

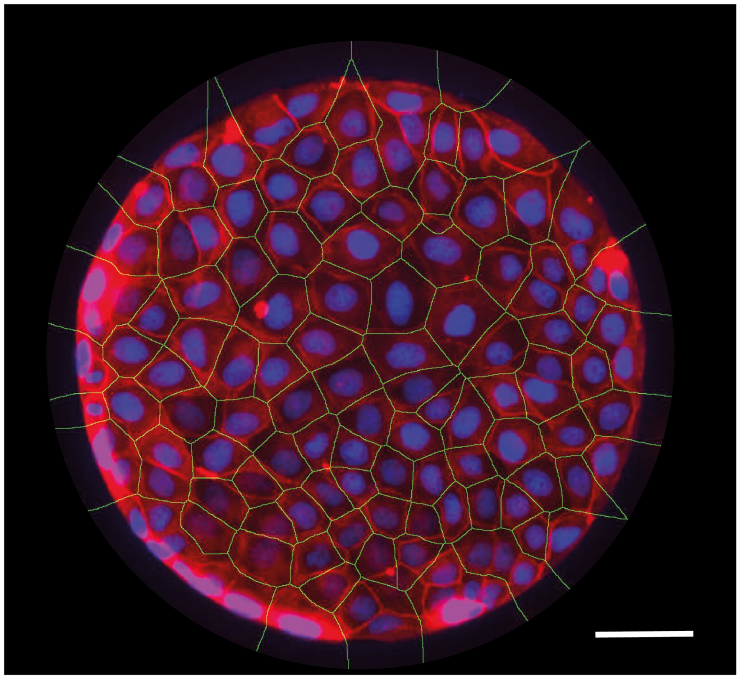

Figure 7.1: A Voronoi diagram of nuclei labeled MDCK cells in confinement *The labeled nuclei of the small cell group (blue) are the base for a Voronoi tessellation (thin yellow lines). Due to labeling of the cell membrane (red) the real position of the cell outline can be compared to the generated Voronoi network.*

Functionalized microwells present specialized ligands to stem cells

The introduced method of label-free detection of stem cell differentiation by analysis of the Brownian motion of the cells can be extended to identify the expression of surface markers. The bottom of the microwells can be functionalized in a way that bounded ligands or antibodies are presented to the cell, leading to the immobilization of the cell once the corresponding receptors or antigens are expressed. Lipid monolayers can be prepared on hydrophobic plastic surfaces and the insertion of head-modified lipids with a biotin group is easily achieved by mixing the lipids before deposition. We were able to produce fluorescently labeled SOPC monolayers which were restricted to the bottom of PEG-DA microwells as seen in figure 7.2. Once biotinylated lipids are present in the layer, the binding sites can be saturated with

avidin or derivatives. The bounded avidin again acts as linker to biotinylated ligands or antibodies which are then in consequence immobilized on the surface via this molecular chain. Once the related receptor or antigen is present at the outer cell membrane, it is linked to its counterpart. The cell sticks to the surface changing the Brownian motion behavior which can be detected by our algorithm. It is known from stem cells that they express new surface proteins during differentiation, macrophages produces the antigen Mac-1 for instance [116]. This technique might be able to detect the expression of surface proteins at the single molecule level and, in this case, contributes to still higher time resolution of the heterogeneity of stem cell differentiation.

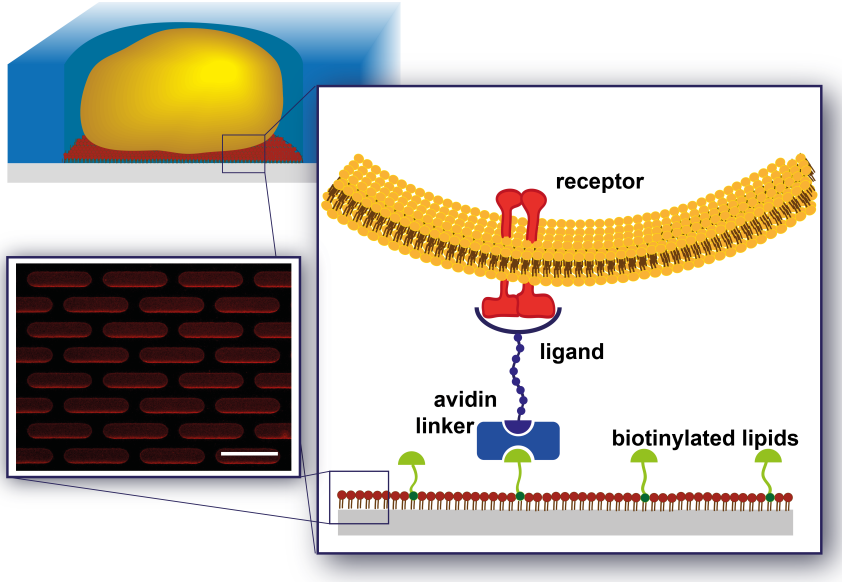

Figure 7.2: The expression of surface markers are detected by functionalized microwells. *The bottom of the PEG-DA microwells is modified with a lipid monolayer containing small percentage of biotinylated lipids. Via an avidin linker, an applicable ligand can be bound to the surface detecting the expression of related receptors by binding. The fluorescence image shows a PEG-DA microstructure modified with a fluorescently labeled lipid monolayer (scale bar corresponds to 100 µm).*

PEG-DMA membranes as templates for semiconductors

Organic semiconductors have found application in state of the art electronics over the last decades. Whereas some properties, important for high performance technology like CPUs, are inferior with respect to well established classic semiconductors, they show tremendous promise for specific applications. As organic polymers and small molecules are relatively weakly bound by Van-der-Waals forces, thin organic films are highly flexible, opening new possibilities and directions for medical and everyday life electronics, such as sensors, LEDs and photovoltaics. Furthermore, their easy synthesis and low temperature production are

following the economic and ecologic trend.

Two prominent materials in the class of small organic molecules are pentacene and C60. They show good hole and electron conductivity, respectively and have found a wide range of applications [81]. We deposited crystalline thin films and hetero junctions under UHV conditions in order to manufacture electronic devices such as thin film transistors and solar cells. The optimization of these devices as well as the investigation of charge transport phenomena within the semiconductors and at their interfaces requires good control over device and junction geometry. Hence there is a need for precise and small structured shadow masks for film deposition that are easily to remove. We used thin PEG-DMA membranes for precise spatial deposition of pentacene on a silicon surface. The pentacene bound exclusively on the uncovered areas of the surface exhibiting sharp edges and expected thickness of the film as measured by AFM (see fig. 7.3). The future challenge is to reduce the size of the pattern to areas smaller than 2 µm in order to achieve PN-interfaces of lateral geometry in small microchannels.

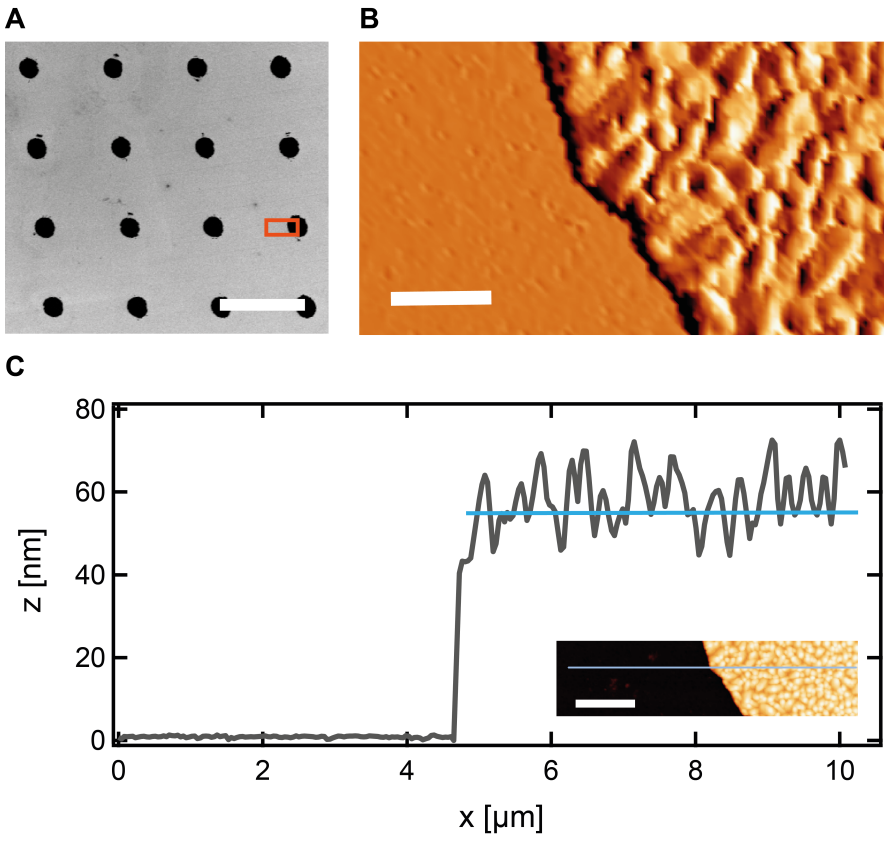

Figure 7.3: Thin PEG-DMA membranes act as templates for pentacene deposition *(A) The REM image shows small islands of evaporated pentacene on a silicon surface (scale bar corresponds to 100 µm). (B) The edges of the pentacene layer are sharp as demonstrated by the AFM amplitude image of a region such as marked with the small insert in A (scale bar corresponds to 700 nm). (C) The thickness of the pentacene film is determined to 58 nm by the profile from the AFM height pictograph (scale bar corresponds to 2 µm).*

Bibliography

[1] M. Abercrombie und J.E. Heaysman, *Experimental cell research* **6** (1954), 293.

[2] R.J. Adrian, *Experiments in Fluids* **39** (2005), 159.

[3] B. Alberts, D. Bray, K. Hopkin, A. Johnson, J. Lewis, M. Raff, K. Roberts und P. Walter: *Essential Cell Biology.* 3. Auflage. Garland Science, März 2009.

[4] T.E. Angelini, E. Hannezo, X. Trepat, J.J. Fredberg und D.A. Weitz, *Physical Review Letters* **104** (2010), 1.

[5] T.E. Angelini, E. Hannezo, X. Trepat, M. Marquez, J.J. Fredberg und D.A. Weitz, *Proceedings of the National Academy of Sciences* (2011), 1.

[6] attc at http://www.lgcstandards atcc.org/, .

[7] R. Bacallao, C. Antony, C. Dotti, E. Karsenti, E.H. Stelzer und K. Simons, *The Journal of cell biology* **109** (1989), 2817.

[8] M. Basan, J. Elgeti, E. Hannezo, W.J. Rappel und H. Levine, *Proceedings of the National Academy of Sciences* **110** (2013), 2452.

[9] M. Basan, T. Risler, J.F. Joanny, X. Sastre-Garau und J. Prost, *HFSP journal* **3** (2009), 265.

[10] A.P. Beltrami, K. Urbanek, J. Kajstura, S.M. Yan, N. Finato, R. Bussani, B. Nadal-Ginard, F. Silvestri, A. Leri, C.A. Beltrami et al. , *New England Journal of Medicine* **344** (2001), 1750.

[11] E. Berthier, E.W.K. Young und D. Beebe, *Lab on a chip* **12** (2012), 1024.

[12] M. Block, E. Schöll und D. Drasdo, *Physical Review Letters* **99** (2007), 3.

[13] M. Bock, A.K. Tyagi, J.U. Kreft und W. Alt: *Generalized voronoi tessellation as a model of two-dimensional cell tissue dynamics.*, Band 72, Oktober 2010.

[14] D. Bray: *Cell movements: from molecules to motility.* Garland Pub, 2001.

[15] A. Brú, J. Pastor, I. Fernaud, I. Brú, S. Melle und C. Berenguer, *Physical Review Letters* **81** (1998), 4008.

[16] D.E. Bruns, *Biochemical Pharmacology* **38** (1989), 73.

[17] B. Brutovsky, D. Horvath und V. Lisy, *Physica A* **387** (2008), 839.

[18] M. Charnley, M. Textor, A. Khademhosseini und M.P. Lutolf, *Integrative biology* **1** (2009), 625.

[19] E.A. Codling, M.J. Plank und S. Benhamou, *Journal of the Royal Society, Interface* **5** (2008), 813.

[20] B.L. Coomber und A.I. Gotlieb, *Arteriosclerosis* **10** (1990), 215.

[21] M. Cordey, M. Limacher, S. Kobel, V. Taylor und M.P. Lutolf, *Stem cells* **26** (2008), 2586.

[22] J. Davies: *Mechanisms of Morphogenesis.* Elsevier Science, 2005.

[23] B. De Lacy Costello, N. Ratcliffe, A. Adamatzky, A.L. Zanin, A.W. Liehr und H.G. Purwins, *International Journal of Bifurcation and Chaos* **14** (2004), 2187.

[24] C. Dombrowski, L. Cisneros, S. Chatkaew, R.E. Goldstein und J.O. Kessler, *Physical Review Letters* **93** (2004), 098103.

[25] D. Drasdo, S. Hoehme und M. Block, *Journal of Statistical Physics* **128** (2007), 287.

[26] D. Falconnet, G. Csucs, H.M. Grandin und M. Textor, *Biomaterials* **27** (2006), 3044.

[27] R. Farhadifar, J.C. Röper, B. Aigouy, S. Eaton, F. Jülicher und J.C. Ro, *Current biology* **17** (2007), 2095.

[28] A. Fick, *Annalen der Physik* **170** (1855), 59.

[29] D.A. Fletcher und P.L. Geissler, *Annual review of physical chemistry* **60** (2009), 469.

[30] A. Folch, B.H. Jo, O. Hurtado, D.J. Beebe und M. Toner, *Journal of biomedical materials research* **52** (2000), 346.

[31] G. Forgacs, R. Foty, Y. Shafrir und M. Steinberg, *Biophysical Journal* **74** (1998), 2227.

[32] R.A. Foty, G. Forgacs, C.M. Pfleger und M.S. Steinberg, *Physical review letters* **72** (1994), 2298.

[33] P. Friedl und D. Gilmour, *Nature reviews. Molecular cell biology* **10** (2009), 445.

[34] J.P. Garrahan, *Proceedings of the National Academy of Sciences* **108** (2011), 4701.

[35] M. Ghibaudo, A. Saez, L. Trichet, A. Xayaphoummine, J. Browaeys, P. Silberzan, A. Buguin und B. Ladoux, *Soft Matter* **4** (2008), 1836.

[36] S. Gobaa, S. Hoehnel, M. Roccio, A. Negro, S. Kobel und M.P. Lutolf, *Nature methods* **8** (2011), 949.

[37] N.S. Gov, *Proceedings of the National Academy of Sciences* **104** (2007), 15970.

[38] N.S. Gov, *Nature materials* **10** (2011), 412.

[39] K. Guevorkian, M.J. Colbert, M. Durth, S. Dufour und F. Brochard-Wyart, *Physical Review Letters* **104** (2010), 218101.

[40] C. Guillot und T. Lecuit, *Science* **340** (2013), 1185.

[41] H. Haga, C. Irahara, R. Kobayashi, T. Nakagaki und K. Kawabata, *Biophysical journal* **88** (2005), 2250.

[42] J.M. Harris: *Poly(Ethylene Glycol) Chemistry: Biotechnical and Biomedical Applications*. Springer, 1992.

[43] J.M. Harris und Zalipsky: *Poly(ethylene glycol): chemistry and biological applications*. ACS symposium series. American Chemical Society, 1997.

[44] S.E. Haynesworth, J. Goshima, V.M. Goldberg und A.I. Caplan, *Bone* **13** (1992), 81.

[45] O. Hertwig, *Jenaische Zeitschrift* (1884).

[46] B.D. Hoffman und J.C. Crocker, *Annual review of biomedical engineering* **11** (2009), 259.

[47] J.H. Hoh und C.A. Schoenenberger, *Journal of cell science* **107** (1994), 1105.

[48] A.L. Hook, H. Thissen und N.H. Voelcker, *Trends in biotechnology* **24** (2006), 471.

[49] M. Huergo, M. Pasquale, A. Bolzán, A. Arvia und P. González, *Physical Review E* **82** (2010), 1.

[50] D. Hutchison, J.C. Mitchell, G. Bebis und R. Boyle: *Advances in Visual Computing*, 1973.

[51] T.N. Ignatova, V.G. Kukekov, E.D. Laywell, O.N. Suslov, F.D. Vrionis und D.A. Steindler, *Glia* **39** (2002), 193.

[52] A. Janshoff und S. Künneke, *European Biophysics Journal* **29** (2000), 549.

[53] R.S. Kane, S. Takayama, E. Ostuni, D.E. Ingber und G.M. Whitesides, *Biomaterials* **20** (1999), 2363.

[54] J.M. Karp, J. Yeh, G. Eng, J. Fukuda, J. Blumling, K.Y. Suh, J. Cheng, A. Mahdavi, J. Borenstein, R. Langer und A. Khademhosseini, *Lab on a chip* **7** (2007), 786.

[55] K.E. Kasza, A.C. Rowat, J. Liu, T.E. Angelini, C.P. Brangwynne, G.H. Koenderink und D.A. Weitz, *Current opinion in cell biology* **19** (2007), 101.

[56] H. Kim, R. Cohen, P. Hammond und D. Irvine, *Advanced Functional Materials* **16** (2006), 1313.

[57] P. Kollmannsberger und B. Fabry, *Annual Review of Materials Research* **41** (2011), 75.

[58] Kshitiz, D.H. Kim, D.J. Beebe und A. Levchenko, *Trends in biotechnology* **29** (2011), 399.

[59] K.P. Landsberg, R. Farhadifar, J. Ranft, D. Umetsu, T.J. Widmann, T. Bittig, A. Said, F. Jülicher und C. Dahmann, *Current biology* **19** (2009), 1950.

[60] B.A. Langowski und K.E. Uhrich, *Langmuir* **21** (2005), 10509.

[61] B. Lévy und Y. Liu, *ACM Transactions on Graphics* **29** (2010), 1.

[62] L. Li und T. Xie, *Annu. Rev. Cell Dev. Biol.* **21** (2005), 605.

[63] C.C. Liang, A.Y. Park und J.L. Guan, *Nature protocols* **2** (2007), 329.

[64] M.P. Lutolf, P.M. Gilbert und H.M. Blau, *Nature* **462** (2009), 433.

[65] P.K. Maini, D.L.S. McElwain und D.I. Leavesley, *Tissue engineering* **10** (2004), 475.

[66] K.M. Malinda, G.S. Sidhu, K.K. Banaudha, J.P. Gaddipati, R.K. Maheshwari, A.L. Goldstein und H.K. Kleinman, *Journal of immunology* **160** (1998), 1001.

[67] M. Marchetti, J.F. Joanny, S. Ramaswamy, T. Liverpool, J. Prost, M. Rao und R.A. Simha, *arXiv preprint arXiv:1207.2929* (2012).

[68] A.K. Marel, A. Piera Alberola und J.O. Rädler, *Biophysical Reviews and Letters* **7** (2012), 15.

[69] A.K. Marel, S. Rappl, A. Piera Alberola und J.O. Rädler, *Macromolecular bioscience* **13** (2013), 595.

[70] S. Mark, R. Shlomovitz, N.S. Gov, M. Poujade, E. Grasland-Mongrain und P. Silberzan, *Biophysical journal* **98** (2010), 361.

[71] M. Martin, *Journal of the National Cancer Institute* **101** (2009), 914.

[72] G.A. Meijer, J.A. Belien, P.J. van Diest und J.P. Baak, *Journal of Clinical Pathology* **50** (1997), 365.

[73] F.A. Meineke, C.S. Potten und M. Loeffler, *Cell proliferation* **34** (2001), 253.

[74] N. Minc, D. Burgess und F. Chang, *Cell* .

[75] H.C. Moeller, M.K. Mian, S. Shrivastava, B.G. Chung und A. Khademhosseini, *Biomaterials* **29** (2008), 752.

[76] K.A. Moore und I.R. Lemischka, *Science* **311** (2006), 1880.

[77] J. Murray: *Mathematical Biology: I. An Introduction*. Interdisciplinary Applied Mathematics. Springer, 2002.

[78] T. Nagai und H. Honda, *Philosophical Magazine B* **81** (2001), 699.

[79] C.M. Nelson, R.P. Jean, J.L. Tan, W.F. Liu, N.J. Sniadecki, A.a. Spector und C.S. Chen, *Proceedings of the National Academy of Sciences of the United States of America* **102** (2005), 11594.

[80] D.L. Nikolić, A.N. Boettiger, D. Bar-Sagi, J.D. Carbeck und S.Y. Shvartsman, *American journal of physiology. Cell physiology* **291** (2006), C68.

[81] S.J. Noever, S. Fischer und B. Nickel, *Advanced Materials* (2012).

[82] E. Ostuni, R. Kane, C.S. Chen, D.E. Ingber und G.M. Whitesides, *Langmuir* **16** (2000), 7811.

[83] K. Park, L.J. Millet, N. Kim, H. Li, X. Jin, G. Popescu, N.R. Aluru, K.J. Hsia und R. Bashir, *Proceedings of the National Academy of Sciences* **107** (2010), 20691.

[84] R. Paul, P. Heil, J.P. Spatz und U.S. Schwarz, *Biophysical journal* **94** (2008), 1470.

[85] L. Petitjean, M. Reffay, E. Grasland-Mongrain, M. Poujade, B. Ladoux, A. Buguin und P. Silberzan, *Biophysical journal* **98** (2010), 1790.

[86] R.J. Petrie, A.D. Doyle und K.M. Yamada, *Nature reviews. Molecular cell biology* **10** (2009), 538.

[87] H.M. Phillips und M.S. Steinberg, *Proceedings of the National Academy of Sciences* **64** (1969), 121.

[88] R. Poincloux, O. Collin, F. Lizárraga, M. Romao, M. Debray, M. Piel und P. Chavrier, *Proceedings of the National Academy of Sciences* **108** (2011), 1943.

[89] M. Poujade, E. Grasland-Mongrain, a. Hertzog, J. Jouanneau, P. Chavrier, B. Ladoux, A. Buguin und P. Silberzan, *Proceedings of the National Academy of Sciences of the United States of America* **104** (2007), 15988.

[90] B. Pratt, A. Harris, J. Morrow und J. Madri, *The American journal of pathology* **117** (1984), 349.

[91] R. Prebiotic, *Nature* **376** (1995), 581.

[92] A. Puliafito, L. Hufnagel, P. Neveu, S. Streichan, A. Sigal, D.K. Fygenson und B.I. Shraiman, *Proceedings of the National Academy of Sciences* **109** (2012), 739.

[93] J. Ranft, M. Basan, J. Elgeti, J.F. Joanny, J. Prost und F. Jülicher, *Proceedings of the National Academy of Sciences of the United States of America* **107** (2010), 3.

[94] A. Ranga und M.P. Lutolf, *Current opinion in cell biology* **24** (2012), 236.

[95] M. Reffay, L. Petitjean, S. Coscoy, E. Grasland-Mongrain, F. Amblard, A. Buguin und P. Silberzan, *Biophysical journal* **100** (2011), 2566.

[96] S. Reinsch und E. Karsenti, *The Journal of cell biology* **126** (1994), 1509.

[97] R. Riahi, Y. Yang, D.D. Zhang und P.K. Wong, *Journal of laboratory automation* **17** (2012), 59.

[98] A.J. Ridley, M.a. Schwartz, K. Burridge, R.a. Firtel, M.H. Ginsberg, G. Borisy, J.T. Parsons und A.R. Horwitz, *Science (New York, N.Y.)* **302** (2003), 1704.

[99] M.A. Rieger, P.S. Hoppe, B.M. Smejkal, A.C. Eitelhuber und T. Schroeder, *Science* **325** (2009), 217.

[100] P. Rorth, *Annual review of cell and developmental biology* **25** (2009), 407.

[101] O. Roure, A. Saez, A. Buguin, R.H. Austin, P. Chavrier, P. Silberzan und B. Ladoux, *PNAS* (2005).

[102] S. Sandersius, C. Weijer und T. Newman, *Physical biology* **8** (2011), 045007.

[103] U. Savla, L.E. Olson und C.M. Waters, *Journal of applied physiology* **96** (2004), 566.

[104] T. Schreier, E. Degen und W. Baschong, *Research in experimental medicine* **193** (1993), 195.

[105] T. Schroeder, *Cell stem cell* **6** (2010), 203.

[106] T. Schroeder, *Nature methods* **8** (2011), S30.

[107] M.a. Schwartz und D.W. DeSimone, *Current opinion in cell biology* **20** (2008), 551.

[108] J. Seita und I.L. Weissman, *Wiley interdisciplinary reviews. Systems biology and medicine* **2** (2010), 640.

[109] B.G. Sengers, C.P. Please und R.O.C. Oreffo, *Journal of the Royal Society, Interface* **4** (2007), 1107.

[110] B.G. Sengers, C.P. Please, M. Taylor und R.O.C. Oreffo, *Annals of biomedical engineering* **37** (2009), 1165.

[111] X. Serra-Picamal, V. Conte, R. Vincent, E. Anon, D.T. Tambe, E. Bazellieres, J.P. Butler, J.J. Fredberg und X. Trepat, *Nature Physics* **8** (2012), 628.

[112] H.W. Shim, J.H. Lee, T.S. Hwang, Y.W. Rhee, Y.M. Bae, J.S. Choi, J. Han und C.S. Lee, *Biosensors & bioelectronics* **22** (2007), 3188.

[113] M.J. Simpson, K.K. Treloar, B.J. Binder, P. Haridas, K.J. Manton, D.I. Leavesley, D.S. McElwain und R.E. Baker, *Journal of The Royal Society Interface* **10** (2013).

[114] R. Singhvi, A. Kumar, G.P. Lopez, G.N. Stephanopoulos, D.C. Wang, G.M. Whitesides und D.E. Ingber, *Science* **881** (1993), 1992.

[115] B. Slater, C. Londono und A.P. McGuigan, *BioTechniques* **54** (2013), 87.

[116] T. Springer, G. Galfré, D.S. Secher und C. Milstein, *European journal of immunology* **9** (1979), 301.

[117] M. Steinberg und T. Poole, *Cell behavior* (1982), 583.

[118] M. Stoker und H. Rubin, *Nature* (1967), 171.

[119] L. Subiza, S. Albertos, I. Bru und A. Bru, *Biophysical Journal* **85** (2003), 2948.

[120] K.Y. Suh, M.C. Park und P. Kim, *Advanced Functional Materials* **19** (2009), 2699.

[121] Y. Sun, C.S. Chen und J. Fu, *Annual review of biophysics* **41** (2012), 519.

[122] a. Szabó, R. Unnep, E. Méhes, W.O. Twal, W.S. Argraves, Y. Cao und a. Czirók, *Physical biology* **7** (2010), 046007.

[123] D.T. Tambe, C.C. Hardin, T.E. Angelini, K. Rajendran, C.Y. Park, X. Serra-Picamal, E.H. Zhou, M.H. Zaman, J.P. Butler, D.A. Weitz, J.J. Fredberg und X. Trepat, *Nat Mater* **10** (2011), 469.

[124] M. Théry, V. Racine, A. Pépin, M. Piel, Y. Chen, J.B. Sibarita und M. Bornens, *Nature cell biology* **7** (2005), 947.

[125] M. Théry, V. Racine, M. Piel, A. Pépin, A. Dimitrov, Y. Chen, J.B. Sibarita und M. Bornens, *Proceedings of the National Academy of Sciences of the United States of America* **103** (2006), 19771.

[126] J.E. Till und E.A. McCulloch, *Radiation research* **14** (1961), 213.

[127] X. Trepat und J.J. Fredberg, *Trends in cell biology* **21** (2011), 638.

[128] X. Trepat, G. Lenormand und J.J. Fredberg, *Soft Matter* **4** (2008), 1750.

[129] X. Trepat, M.R. Wasserman, T.E. Angelini, E. Millet, D.a. Weitz, J.P. Butler und J.J. Fredberg, *Nature Physics* **5** (2009), 426.

[130] S. Vedel, S. Tay, D.M. Johnston, H. Bruus und S.R. Quake, *Proceedings of the National Academy of Sciences* **110** (2013), 129.

[131] S.R.K. Vedula, M.C. Leong, T.L. Lai, P. Hersen, A.J. Kabla, C.T. Lim und B. Ladoux, *Proceedings of the National Academy of Sciences of the United States of America* (2012), 1.

[132] S.R.K. Vedula, A. Ravasio, C.T. Lim und B. Ladoux, *Physiology* **28** (2013), 370.

[133] P. Vitorino und T. Meyer, *Genes & development* **22** (2008), 3268.

[134] J. Wegener, (2004).

[135] J. Wegener, A. Janshoff und H.J. Galla, *European biophysics journal* **28** (1999), 26.

[136] D.B. Weibel, W.R. Diluzio und G.M. Whitesides, *Nature reviews. Microbiology* **5** (2007), 209.

[137] I.L. Weissman, *Cell* **100** (2000), 157.

[138] I.L. Weissman, *Science* **287** (2000), 1442.

[139] G.M. Whitesides, E. Ostuni, S. Takayama, X. Jiang und D.E. Ingber, *Annual review of biomedical engineering* **3** (2001), 335.

[140] E.B. Wilson, (1924).

[141] C.W. Wolgemuth, *Society* **4** (2011).

[142] D. Wright, B. Rajalingam, S. Selvarasah, M.R. Dokmeci und A. Khademhosseini, *Lab on a chip* **7** (2007), 1272.

[143] J. Wu, M. Zhang, L. Chen, V. Yu, J. Tin-Yum Wong, X. Zhang, J. Qin und W. Wen, *RSC Advances* **1** (2011), 746.

[144] Y. Xia und G.M. Whitesides, *Annual review of materials science* **28** (1998), 153.

[145] M.L. Yarmush und K.R. King, *Annual review of biomedical engineering* **11** (2009), 235.

[146] X.M. Zhao, Y. Xia und G.M. Whitesides, *Journal of Materials Chemistry* **7** (1997), 1069.

Ich danke euch für die schöne Zeit!